Modelling of defects in ingot forging
with the finite element flow formulation

Christiansen, Peter

Publication date:
2014

Document Version
Publisher's PDF, also known as Version of record

Modelling of defects in ingot forging

PhD Thesis

$$(EIv'')'' = q - \rho A \ddot{v}$$

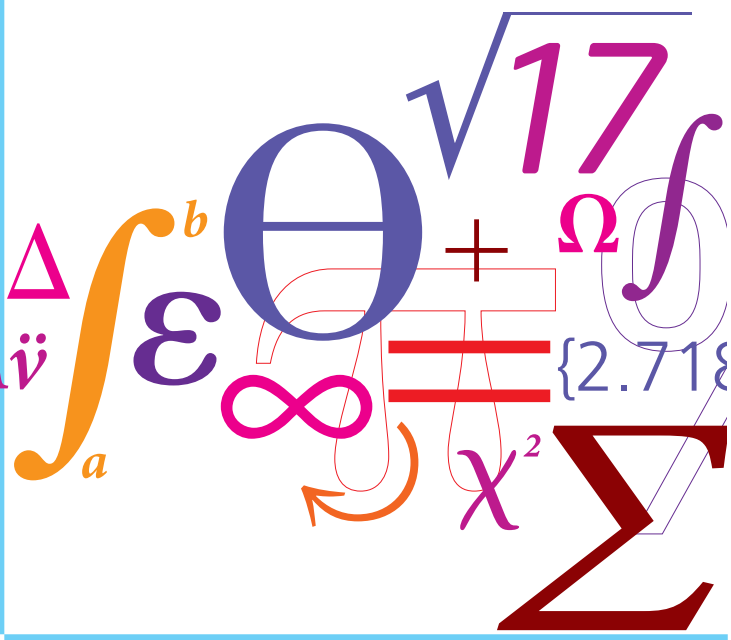

Peter Christiansen
February 2014

DTU Mechanical Engineering
Department of Mechanical Engineering

Modelling of defects in ingot forging

- with the finite element flow formulation

Peter Christiansen

Ph.D-student
M. Sc. Peter Christiansen
Department of Mechanical Engineering, Section for Manufacturing Engineering
Technical University of Denmark

Main Supervisor
Professor, Ph.D Jesper Henri Hattel
Department of Mechanical Engineering, Section for Manufacturing Engineering
Technical University of Denmark

Co-supervisor
Professor, Dr. Tech. Niels Bay
Department of Mechanical Engineering, Section for Manufacturing Engineering
Technical University of Denmark

Mentor
Professor, Habilitation Paulo António Firme Martins
Instituto Superior Tecnico
University of Lisbon

Funding
The work is supported by the Strategic Research Center "REWIND - Knowledge based engineering for improved reliability of critical wind turbine components", Danish Research Council for Strategic Research, grant no. 10-093966

Preface

This thesis summarizes some of the findings by the author during his Ph.D-study in the period 15-02-2011 to 14-02-2014. During this period, the author has been member of the Process Modelling Group, part of the Institute of Mechanical Engineering at the Technical University of Denmark.

The author wishes to thanks all current and former members of the Process Modelling Group for contributing to a nice, humerous and friendly everyday atmosphere. Especially the leader of the Process Modelling Group, Professor, Ph.D Jesper Henri Hattel, is always an inspiration with constant questions that leads to gained knowledge and new ideas.

The author will like to assign a special thanks to Dr. Ing. Petr Kotas, former member of the Process Modelling Group and now Magma Gießereitechnologie GmbH, for providing contacts to industry, without which this project would not have been possible.

Professor, Dr. Technic Niels Bay from the Metal Forming and Joining Group have always been ready with constructive critisism, suggestions and sharing his comprehensive knowledge regarding metal forming operations. He is always ready when the author needs some inspiration regarding the interpreting of plots and proof-reading of articles. His effort is greatly acknowledged.

During the author's external research visit at the Instituto Superior Tecnico, Lisbon, Portugal in the autumn of 2012, he was welcomed by Professor, Dr. Habilitation Paulo António Firme Martins and his research group like being one of their own. Besides of the experimental work, Paulo Martins also shared his comprehensive knowledge regarding the finite element flow formulation and metal forming in general with the author. This collaboration was continued during Prof. Martins' sabbatical in Denmark in the spring of 2013, and the author hopes that all his questions may have tricked an idea or two for Prof. Martins also. Without his effort, the project would not have been so successful.

February 14$^{\text{th}}$, 2014

Peter Christiansen

Abstract

The present report presents an investigation of the ingot forging process with special emphasis on modelling the influence of die geometry on the soundness of the ingot after hot forging. An investigation on how to model damage was also performed.

The influence of the lower die angle is quantified experimentally by utilizing down-scaled lead model ingots (billets) being compressed by a tool with different lower die angles. Centreline defects, occurring due to the ingot casting processes, was modelled by drilling holes through the centreline of the cast billets. The experiments showed a marked influence on centreline hole closure by the lower die angle. Of the utilized lower die angles, a 120° lower die gave the largest hole closure when applying the same press stroke for all the experiments. The performed experiments were compared with both 2D and 3D FEM simulations. Both simulations were found to mimic the experiments reasonably correct. Therefore both models were subsequently applied for further investigations of the influence of the lower die angle on the evolution of centreline defects.

2D FEM single stroke simulations of ingots having different hardening behaviour yielded an approximately constant lower die angle of 130°-140° giving rise to the largest centreline porosity closure regardless of material hardening behaviour applied. Friction was found only to have a minor influence on the optimum.

Multi stroke forging operations have also been modelled since the ingot forging process consists of many forging strokes. Two different approaches to quantify ductile damage were applied: uncoupled ductile damage and a porous plasticity model. Lower die angles ranging from 60° to 180° with 30° intervals were used in the simulations. When applying the uncoupled normalized Cockcroft & Latham ductile damage criterion, a lower die angle of 120° was found to be best. "Best" is evaluated using a simple average of damage and effective plastic strain measures. When applying porous plasticity as a model for the description of damage, a 90° lower die angle was found to be best closely follow by the applied, larger lower die angles.

A preliminary investigation of the influence of feed size was performed. Only two different lower die angles of 120° and 180° were utilized with either 400mm or 800mm feed. Damage was modelled with porous plasticity while at the same time also computing normalized Cockcroft & Latham damage. It was found that when evaluating damage only by relative density; feed size and lower die angle did not influence whether the hot forging process was successful or not. This is in disagreement with the general understanding of the ingot forging process. When evaluating ductile damage by the normalized Cockcroft & Latham criterion, marked differences were predicted depending on the lower die angle applied. The damage is also affected by the feed size, indicating that the smallest of the two feed sizes should be utilized together with the 120° lower die in practice. These findings are in close agreement with the general understanding of the ingot forging process.

Therefore porous metal plasticity should not be used solely when evaluating the soundness of the final, forged ingot based on FEM simulations.

Based on an analysis of forming fracture limit diagrams combined with uncoupled ductile damage criteria, it was found that the normalized Cockcroft & Latham criterion is most suited for modelling damage in bulk metal forming, if the forming fracture limit diagram can be described by a straight line having a slope of -1/2. A damage criterion independent of slope is presented. Often the forming fracture limit diagram consists of two straight lines intersecting one another in the principal strain space along a line corresponding to uniaxial tension. If the slopes of the two lines are -1/2 and -1, which is often encountered in practice, an uncoupled ductile damage criterion is introduced which predicts the same damage value at fracture along both lines. A physical mechanism giving rise to different formability limits, depending on the applied stress state, is introduced. Further investigations of the mechanisms governing ductile fracture is still needed in order to confirm or reject the proposed damage criterion and damage mechanism.

Resumé (in danish)

Nærværende rapport opsummerer en række undersøgelser vedrørende bloksmedning. Hovedtemaet er undersøgelse af smedeværktøjsgeometriens indflydelse på kvaliteten af blokstøbningen efter varmsmedning. Der er også foretaget en analyse af, hvordan duktil skade modelleres.

Smedeværktøjets geometriske udformnings indflydelse på lukning af centerlinieporøsiteter er blevet undersøgt ved brug af nedskalerede blyemner, der smedes med et værktøj med forskellige vinkler mellem smedeværktøjsfladerne. Centerlinieporøsitet er modelleret ved at bore langsgående huller gennem de cylindriske blyemner. Eksperimenterne viser, at ud af de eksperimentelt anvendte vinkler, opnås størst lukning, for en given slaglængde, ved at anvende en vinkel på 120°. Eksperimenterne sammenholdes med både 2D og 3D FEM beregninger. Begge modeller viser overensstemmelse med eksperimenterne. Derfor anvendes begge modeller til videregående undersøgelser.

2D FEM modeller bruges til at undersøge om den optimale smedeværktøjsgeometri er afhængig af emnemateriale og friktion. Der anvendes kun en sammenpresning af emnet i simuleringerne. En vinkel på 130°-140° giver den største lukning af en centerlinieprøsitet for en given slaglængde, uanset hvilket af de modellerede emnematerialer der anvendes. Friktion har kun en mindre indflydelse på den optimale vinkel.

Flertrins smedeoperationer er også blevet modelleret, eftersom bloksmedningsprocessen består af en lang række smedeoperationer. To forskellige metoder til modellering af duktil skade anvendes: en ukoblet duktil skadesmekanikmodel og en porøs plasticitetsmodel. Værktøjsgeometrivinkler mellem 60° og 180°, med 30° interval, bruges ved modelleringen. Når skade modelleres med det ukoblede, normaliseret Cockcroft & Latham skadeskriterium, indikerer simuleringerne, at en 120° vinkel giver bedst resultat. "Bedst" evalueres ved hjælp af et simpelt gennemsnit af ækvivalent plastisk tøjning og duktil skade. Såfremt porøs plasticitet bruges som skadesmodel, er 90° bedst, dog tæt fuldt af de andre, større vinkler.

En indledende undersøgelse af betydningen af steplængden imellem smedningen af to blokstøbningstværsnit er også foretaget. To forskellige vinkler på 120° og 180° anvendes. Steplængder på 400mm eller 800mm anvendes. Duktil skade modelleres ved hjælp af porøs plasticitet samtidig med, at duktil skade også udregnes ved hjælp af det normaliserede Cockcroft & Latham kriterium. Når skade modelleres alene ved hjælp af porøs plasticitet, har valg af vinkel og steplængde kun mindre indflydelse på, om blokstøbningen forudsiges at være succesful eller ej. Dette er i modstrid med den gængse forståelse af bloksmedning. Når man også inddrager Cockcroft & Latham skadeskriteriet, er der udtalte forskelle på den modellerede skade. Simuleringerne antyder, at den mindste af de simulerede vinkler og den mindste steplængde resulterer i mindst skade. Dette er i bedre overensstemmelse med den gængse forståelse af bloksmedningsprocessen. Derfor

bør modellering af duktil skade ikke kun foretages ved hjælp af porøs plasticitet, når der foretages FEM simuleringer af bloksmedning.

Ud fra en analyse af formbarhedsdiagrammer for brud sammenholdt med en række ukoblede duktile skadeskriterier findes det, at det normaliserede Cockcroft & Latham kriterium er bedst egnet til modellering af duktil skade i smedeoperationer, hvis formbarhedsgrænsen er defineret ved en ret linie med hældning -1/2. Et skadeskriterium, der er uafhængigt af hældingen af formbarhedsgrænsen, præsenteres også. Ofte kan formbarhedsgrænsen beskrives ved to rette linie med hældninger på henholdsvis -1/2 og -1, krydsende hinanden i et hovedtøjningsdiagram langs en linie beskrevet ved enakset træk. Et skadeskriterium, der forudsiger en konstant værdi langs en sådan formbarhedsgrænse, præsenteres. Der foreslås en fysisk mekanisme for duktil skade baseret på revnevækst, der forklarer, hvorfor forskellig formbarhed opnås afhængig af spændingssituationen. De opstillede hypoteser vedrørende skadeskriterium og revnevækst kræver yderligere undersøgelser for at kunne be- eller afkræftes.

Contents

Nomenclature

A	Constant in Zener-Hollomon hardening	$[-]$
A	Function in porous plasticity model	$[-]$
A	Amplitude factor for friction modelling	$[-]$
A_0	Initial cross sectional area	$[m^2]$
A_i	Cross sectional area after stroke i	$[m^2]$
A_{final}	Final hole area ratio	$[-]$
$A_{initial}$	Initial hole area ratio	$[-]$
A_{nom}	Nominal contact area	$[m^2]$
B	Function in porous plasticity model	$[-]$
B_{ij}	Left Cauchy-Green deformation tensor	$[-]$
$\mathbf{B}$	Strain-rate matrix	$\left[\frac{1}{s}\right]$
$\mathbf{B}$	Left Cauchy-Green deformation matrix	$[-]$
C_{ij}	Right Cauchy-Green deformation tensor	$[-]$
$\mathbf{C}$	Right Cauchy-Green deformation matrix	$[-]$
$\mathbf{C}^T$	Kronecker delta on vectorial form	$[-]$
C	Accumulated ductile damage vaule	$[Unit\, dependent\, on\, function]$
C	Strength coefficient	$\left[\left(\frac{N}{m^2}\right)\right]$
C_{11}	Coefficient	$[rad]$
C_{12}	Coefficient	$[rad]$
C_{21}	Coefficient	$[rad]$
C_{22}	Coefficient	$[rad]$
$\mathbf{D}$	Diagonal matrix	$[-]$
$\mathbf{D}$	Rate of deformation	$\left[\frac{1}{s}\right]$
D	Damage parameter	$[-]$
$\mathrm{D}_{\mathrm{ingot}}$	Diameter of ingot	$[m]$
E_{ij}	Green-Lagrange strain tensor	$[-]$
E	Young's modulus	$[Pa]$
F	Friction force between contacting bodies	$[N]$
F_x	Horizontal force	$[N]$
$\mathbf{F}$	Deformation gradient	$[-]$
$\mathbf{F}^{el}$	Elastic deformation gradient	$[-]$
$\mathbf{F}^{pl}$	Plastic deformation gradient	$[-]$
$\dot{\mathbf{F}}$	Rate of deformation gradiens	$\left[\frac{1}{s}\right]$
G	Energy release rate	$\left[\frac{J}{m^2}\right]$
H	Height of rectangular ingot	$[m]$
I_1	First invariant of stress tensor	$\left[\left(\frac{N}{m^2}\right)^2\right]$
I_2	Second invariant of stress tensor	$\left[\left(\frac{N}{m^2}\right)^2\right]$

$\mathbf{I}$	Identity matrix	$[-]$
J_1	First invariant of deviatoric stress tensor	$\left[\left(\frac{N}{m^2}\right)^2\right]$
J_2	Second invariant of deviatoric stress tensor	$\left[\left(\frac{N}{m^2}\right)^2\right]$
J_3	Third invariant of deviatoric stress tensor	$\left[\left(\frac{N}{m^2}\right)^2\right]$
K	Penalty factor (volumetric viscocity)	$\left[\frac{N}{m^2}s\right]$
K_I	Stress intensity factor mode I	$\left[\frac{N}{m^{3/2}}\right]$
K_{II}	Stress intensity factor mode II	$\left[\frac{N}{m^{3/2}}\right]$
k_ω	Porosity growth rate constant	$[-]$
$\mathbf{K}$	Global stiffness matrix	$\left[\frac{kg}{s}\right]$
$\mathbf{K}^D$	Deviatoric stiffness matrix	$\left[\frac{kg}{s}\right]$
$\mathbf{K}^H$	Hydrostatic stiffness matrix	$\left[\frac{kg}{s}\right]$
$\mathbf{L}$	Differential operator matrix	$\left[\frac{1}{m}\right]$
$\mathbf{L}$	Velocity gradient	$\left[\frac{1}{s}\right]$
L	Lode parameter	$[-]$
L	Contact length	$[m]$
$\mathrm{L_{die}}$	Length of forging die	$[m]$
N	Normal force between contacting bodies	$[N]$
N_i	Interpolating functions	$[-]$
N^e	Number of finite elements	$[-]$
$\mathbf{N}$	Interpolating functions matrix	$[-]$
$\mathbf{P}_o$	Point in material	$[m]$
$\mathbf{P}_1$	Point in material	$[m]$
Q	Activation energy	$\left[\frac{mol}{J}\right]$
$\mathbf{Q}_\mathrm{o}$	Point in material	$[m]$
$\mathbf{Q}_1$	Point in material	$[m]$
R	Gas constant	$\left[8.3145\frac{J}{mol\cdot K}\right]$
R	Relative density	$[-]$
$\mathbf{R}$	Rotation matrix	$[-]$
$\dot{\mathbf{R}}$	Rate of rotation	$\left[\frac{rad}{s}\right]$
S_{ij}	Deviatoric stress	$\left[\frac{N}{m^2}\right]$
S	Surface of domain	$[m^2]$
S_N	Standard deviation of nucleation of particles	$[-]$
S^e	Surface of finite element	$[m^2]$
T	Temperature	$[^oK]$
T_{liq}	Liquidus temperature	$[^oC]$
$T_{Pouring}$	Pouring temperature	$[^oC]$
T_{sol}	Solidus temperature	$[^oC]$
$\mathbf{U}$	Right stretch matrix	$[-]$
$\dot{\mathbf{U}}$	Stretch rate	$\left[\frac{1}{s}\right]$
V	Volume of domain	$[m^3]$
V	Velocity in hodograph	$\left[\frac{m}{s}\right]$

V	Velocity	$\left[\frac{m}{s}\right]$
V_0	Initial volume	$[m^3]$
V_1	Final volume	$[m^3]$
$\mathbf{V}$	Left stretch matrix	$[-]$
$\dot{\mathbf{V}}$	Stretch rate	$\left[\frac{1}{s}\right]$
V_{Voce}	Strain hardening constant in Voces law	$[-]$
V^e	Volume of finite element	$[m^3]$
W_i	Weight factors	$[-]$
$\mathbf{W}$	Continuum spin	$\left[\frac{1}{s}\right]$
X_i	Tensor with coordinates	$[m]$
$\mathbf{X}$	Vector/matrix with coordinates	$[m]$
dX_i	Infinitesimal tensor	$[m]$
$d\mathbf{X}$	Infinitesimal vector	$[m]$
a	Slope of fracture line	$[-]$
a	Half crack length	$[m]$
a_o	Constant in Oyane damage model	$[-]$
$a_{drawing}$	Slope of fracture line in drawing region	$[-]$
$a_{stretching}$	Slope of fracture line in stretching region	$[-]$
d_i	Displacement tensor	$[m]$
$\mathbf{d}$	Displacement vector	$[m]$
$d\mathbf{p}$	Plastically deformed configuration of body	$[m]$
$\dot{e}_{ij}^{pl}$	Deviatoric plastic strain rate tensor	$\left[\frac{1}{s}\right]$
f	Porosity density	$[-]$
f	Variable in porous plasticity	$[-]$
$\mathbf{f}$	Force vector	$[N]$
f_N	Fraction of porosity nucleating particles	$[-]$
$f\left(\sigma_{ij}\right)$	Yield function	$\left[\frac{N}{m^2}\right]$
$g\left(d\varepsilon_{ij}^{pl}\right)$	Function of incremental plastic strain tensor	$[-]$
k	Pure shear flow stress	$\left[\frac{N}{m^2}\right]$
k_I	Local stress intensity factor mode I	$\left[\frac{N}{m^{3/2}}\right]$
k_{II}	Local stress intensity factor mode II	$\left[\frac{N}{m^{3/2}}\right]$
l_a^0	Initial distance between elliptic porosities	$[m]$
m	Strain rate exponent	$[-]$
m_f	Friction factor	$[-]$
n	Exponent in Oyane damage model	$[-]$
n	Strain hardening exponent	$[-]$
n	Constant in Zener-Hollomon hardening	$[-]$
p	Indentation pressure	$\left[\frac{N}{m^2}\right]$
p_m	Mean stress	$\left[\frac{N}{m^2}\right]$
q_1	Constant in GTN-model	$[-]$
q_2	Constant in GTN-model	$[-]$
q_3	Constant in GTN-model	$[-]$
u_i	Velocity	$\left[\frac{m}{s}\right]$
$\mathbf{u}$	Element velocity vector	$\left[\frac{m}{s}\right]$

$\ddot{u}_i$	Accelerations	$\left[\frac{m}{s^2}\right]$
v	Relative sliding velocity	$\left[\frac{m}{s}\right]$
v_o	Cut-off value for friction modelling	$\left[\frac{m}{s}\right]$
$\mathbf{v}$	Nodal point velocity vector	$\left[\frac{m}{s}\right]$
$\mathbf{v}$	Velocity vector	$\left[\frac{m}{s}\right]$
$\mathbf{v}^e$	Element nodal point velocity vector	$\left[\frac{m}{s}\right]$
w_i	Weight functions	$[-]$
x_i	Tensor with coordinates	$[m]$
$\mathbf{x}$	Vector/matrix with coordinates	$[m]$
dx_i	Infinitesimal tensor	$[m]$
$d\mathbf{x}$	Infinitesimal vector	$[m]$
y	Distance in slipline field	$[m]$
α	Constant in Zener-Hollomon hardening	$[-]$
α	Stress ratio	$[-]$
α_1	Stress ratio	$[-]$
α_2	Stress ratio	$[-]$
β	Temperature sensitivity	$[^oK]$
γ	Crack propagation angle	$[rad]$
$\triangle$	Deformation zone geometry parameter	$[-]$
δ_{ij}	Kroneckers delta	$[-]$
$\dot{\varepsilon}_{ij}$	Strain rate tensor	$\left[\frac{1}{s}\right]$
$\dot{\boldsymbol{\varepsilon}}^{pl}$	Plastic strain rate vector	$\left[\frac{1}{s}\right]$
$\dot{\bar{\varepsilon}}^{pl}$	Effective plastic strain rate	$\left[\frac{1}{s}\right]$
$\dot{\varepsilon}_M$	Mean strain rate of matrix material	$\left[\frac{1}{s}\right]$
$\dot{\varepsilon}_V^{pl}$	Volumetric plastic strain rate	$\left[\frac{1}{s}\right]$
ε_0	Prestrain	$[-]$
ε_1	First principal strain	$[-]$
ε_2	Second principal strain	$[-]$
ε_3	Third principal strain	$[-]$
ε_{ij}^{pl}	Plastic strain tensor	$[-]$
$d\varepsilon_{ij}^{pl}$	Plastic strain increment	$[-]$
$\bar{\varepsilon}^{pl}$	Effective plastic strain	$[-]$
$d\bar{\varepsilon}^{pl}$	Effective plastic strain increment	$[-]$
ε^C	Fracture strain at plane strain tension loading	$[-]$
$\bar{\varepsilon}^C$	Effective plastic strain at fracture	$[-]$
ε_f	Convergence tolerance forces	$[-]$
ε_M	Mean strain of matrix material	$[-]$
ε_{max}^{pl}	Maximum plastic in-plane strain	$[-]$
ε_{min}^{pl}	Minimum plastic in-plane strain	$[-]$
ε_{max}^{C}	Maximum in-plane plastic strain at fracture	$[-]$
ε_{min}^{C}	Minimum in-plane plastic strain at fracture	$[-]$
ε_N	Mean strain for nucleation of porosities	$[-]$
ε_V	Convergence tolerance velocities	$[-]$
ζ	Natural coordinate	$[-]$
η	Natural coordinate	$[-]$

η	Factor relating flow stress of fully dense and porous material	$[-]$
θ	Angle of rotations	$[rad]$
$\dot{\theta}$	Rotation rate	$\left[\frac{rad}{s}\right]$
$d\lambda$	Plastic multiplier	$\left[\frac{m^2}{N}\right]$
$\dot{\lambda}$	Plastic multiplier rate	$\left[\frac{m^2}{Ns}\right]$
μ	Friction coefficient	$[-]$
ξ	Natural coordinate	$[-]$
π	Functional	$\left[\frac{J}{s}\right]$
ρ	Density	$\left[\frac{kg}{m^3}\right]$
ρ_o	Full density	$\left[\frac{kg}{m^3}\right]$
ρ	Strain ratio	$[-]$
ρ_1	Strain ratio	$[-]$
ρ_2	Strain ratio	$[-]$
σ_a	Largest principal stress in porosity deformation direction	$\left[\frac{N}{m^2}\right]$
σ_b	Smallest principal stress in porosity deformation direction	$\left[\frac{N}{m^2}\right]$
σ_{ij}	Cauchy stress tensor	$\left[\frac{N}{m^2}\right]$
$\sigma_{ij,j}$	Partial derivatives of Cauchy stress tensor	$\left[\frac{N}{m^3}\right]$
$\bar{\sigma}$	Effective stress	$\left[\frac{N}{m^2}\right]$
σ_o	Flow stress	$\left[\frac{N}{m^2}\right]$
$\tilde{\sigma}_o$	Apparent flow stress	$\left[\frac{N}{m^2}\right]$
σ_∞	Saturation stress	$\left[\frac{N}{m^2}\right]$
σ_i	Principal stresses	$\left[\frac{N}{m^2}\right]$
σ_e	Mises stress	$\left[\frac{N}{m^2}\right]$
σ_f	Flow stress of porous material	$\left[\frac{N}{m^2}\right]$
σ_m	Mean (hydrostatic) stress	$\left[\frac{N}{m^2}\right]$
σ_M	Flow stress of fully dense material	$\left[\frac{N}{m^2}\right]$
σ_{max}	Maximum in-plane stress	$\left[\frac{N}{m^2}\right]$
σ_{min}	Minimum in-plane stress	$\left[\frac{N}{m^2}\right]$
σ_n	Normal stress to surface	$\left[\frac{N}{m^2}\right]$
σ_{nom}	Nominal stress	$\left[\frac{N}{m^2}\right]$
σ_{real}	Real stress	$\left[\frac{N}{m^2}\right]$
σ_y	Initial flow stress	$\left[\frac{N}{m^2}\right]$
τ_i	Surface tractions	$\left[\frac{N}{m^2}\right]$
$\boldsymbol{\tau}$	Surface tractions vector	$\left[\frac{N}{m^2}\right]$
τ	Friction stress	$\left[\frac{N}{m^2}\right]$
$\tau*$	Modified friction stress	$\left[\frac{N}{m^2}\right]$
ϕ	Angle of rotation	$[rad]$
$\triangle\phi$	Angle of rotation	$[rad]$

1 Introduction to shaft manufacturing

1.1 Introduction

In this chapter an overview of the processes related to the manufacturing of large shafts is given. The purpose is to give the reader an introduction to the entire process involved in the manufacturing. The main emphasis is on the casting and forging process involved in manufacturing the shaft.

Most of the pictures showing actual forging operations are courtesy to Vitkovice Heavy Machinery A/S.

1.2 Shaft manufacturing overview

1.2.1 Casting of ingot

The first step in the process of manufacturing an ingot is the ingot casting process. The ingot casting process consists of casting a large block of steel. The process is seen schematically in Fig. 1.1.

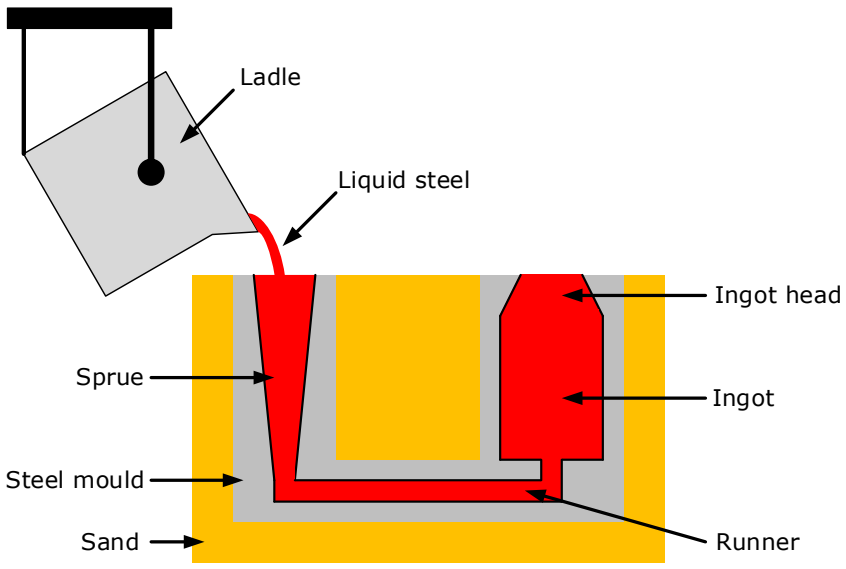

Fig. 1.1. Ingot casting.

The ingot casting process basically consists of liquid metal being poured from a ladle into a sprue, then the liquid metal runs into the ingot through a horizontal runner. The ingot is filled from the bottom all the way to the ingot head, which serves as feeder for the ingot during solidification.

Different ingots can have varying sizes depending on the sizes of the final components. As an example of a large ingot, Kawaguchi et al. [55] reports casting an ingot of 570 tons for making a flange for a pressure vessel in a nuclear power plant. The cast ingot can be seen in Fig. 1.2.

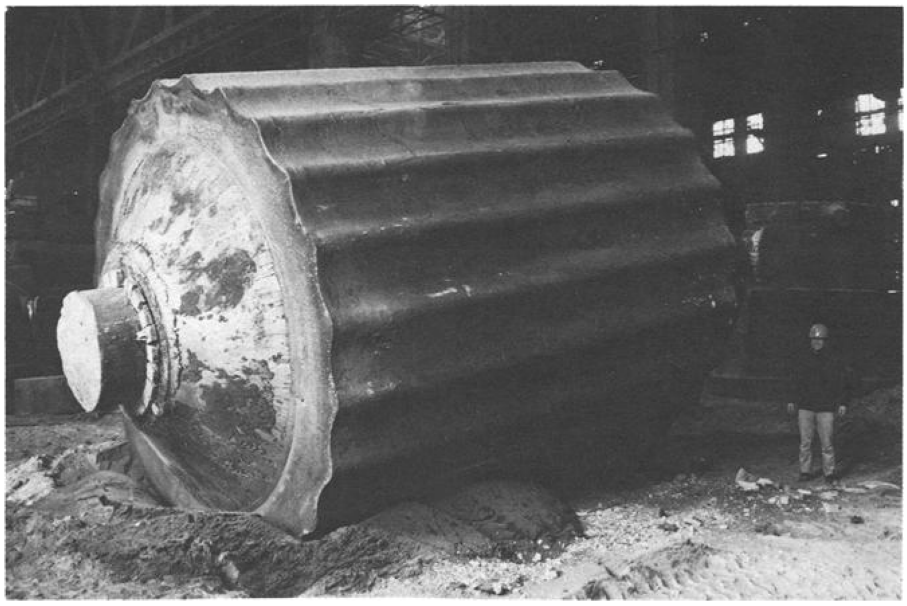

Fig. 1.2. 570 tons ingot cast by Kawasaki Steel Corporation. From Kawaguchi et al. [55].

From Fig. 1.2 it is seen that the cast ingot is not cylindrical but more "star" shaped. This is in order to increase the surface area and thereby reduce both heating and cooling time of the ingot.

After the ingot is solidified and cooled somewhat down, it is stripped from the mould and left to cool down in free air.

For a more elaborate description of the casting process and related defects, the reader is referred to Chapter 2.

1.2.2 Upset forging of ingot

After the ingot has been cast, it is hot forged. The first step of the hot forging process is an upsetting operation. The purpose of the upsetting operation is to produce a manipulator pin in one end of the ingot in order to handle the ingot during forging. The ingot is preheated before the upsetting operation. The upsetting operation can be seen in Fig. 1.3.

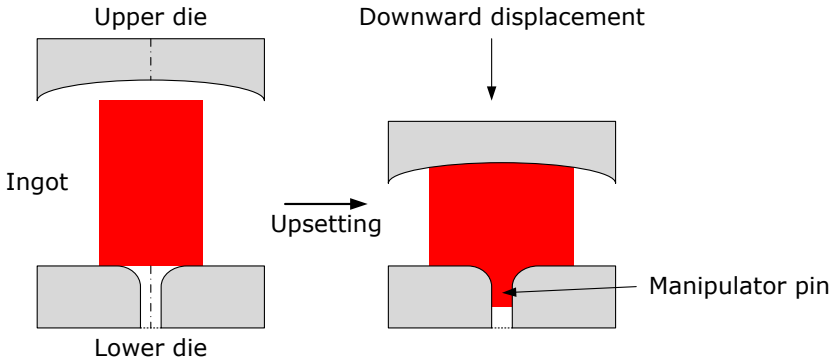

Fig. 1.3. Ingot upsetting.

In Fig. 1.3 a schematic representation of the upsetting operation is seen. The ingot is placed between a downward moving, spherically shaped upper die and a flat lower die with a centreline hole, in which the manipulator pin is extruded.

Besides forming the manipulator pin, the upsetting operation also has the objective to remove the scale on the surface. The scale originates from the casting and cooling process and breaks off in pieces during the upsetting operation. This minimizes the surface oxides present in subsequent forging operations.

(a) Cast and preheated ingot before upsetting.

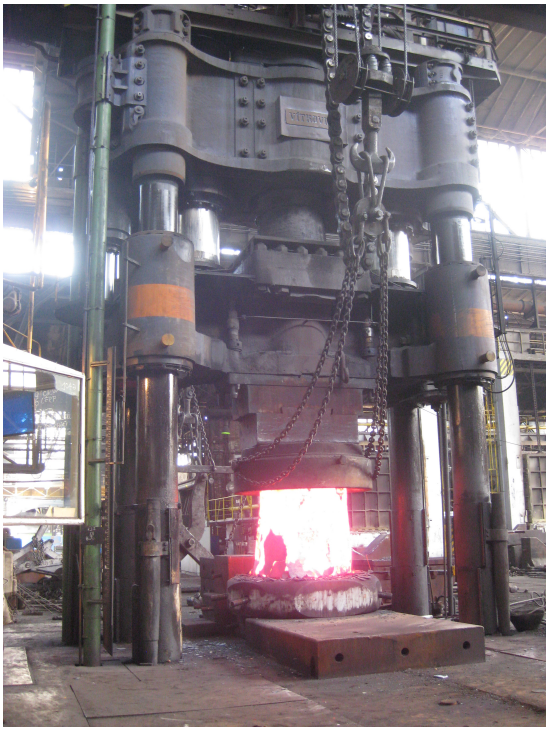

(b) Upsetting of ingot. Scale is peeling off.

Fig. 1.4. Ingot upsetting.

The ingot after upsetting, with extruded manipulator pin, can be seen in Fig. 1.5.

Fig. 1.5. Ingot after upsetting.

1.2.3 Open die forging of ingot

Following the upsetting operation, where the manipulator pin was formed and the scale was removed, the ingot is hot forged. The ingot is first reheated after the upsetting operation and then forged between a pair of dies. In the open die forging process the ingot is compressed several times between an upper die and a lower die. The ingot is rotated by the manipulator (labeled as Porter bar in Fig. 1.6a) in between each compression. Only one cross-section of the ingot is forged at a time. Thereby the process is different from a cogging operation of a square bar, where the bar is displaced longitudinally in-between each compression. Only after a cross-section of the ingot has been substantially hot forged, the ingot is displaced longitudinally in between the dies. The die pair usually consists of an upper flat die and a lower V-shaped die but in the early stage of the process the lower die can also be flat. The dies are also labeled as anvils in literature. The process can be seen in Fig. 1.6.

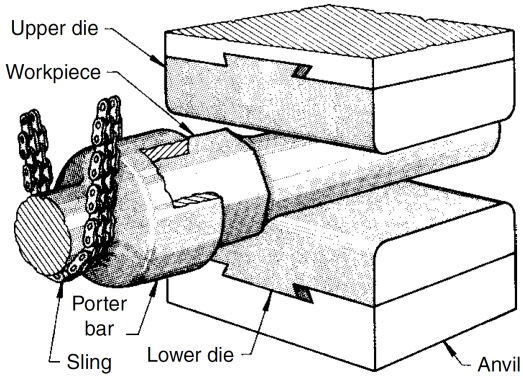

(a) Principle of open die forging. From Semiatin [88] p. 101.

(b) Real forging operation.

Fig. 1.6. Open die forging of ingot.

By continued forging, the ingot is gradually shaped into a shaft. When the final forging shape is reached, the forged shaft is cut-off from the rest of the ingot, see Fig. 1.7.

Fig. 1.7. Cutting off forged shaft from ingot.

1.2.4 Closed die forging of shaft

After the ingot has been forged into a shaft by open die forging, the shaft is axially compressed in a die to calibrate the shape. The die consists of several shorter die rings placed on top of each other hereby forming one complete die.

The process is seen in Fig. 1.8, Fig. 1.9 and Fig. 1.10.

(a) Inserting shaft into die.

(b) Lid is placed on top of shaft

Fig. 1.8. Closed die forging of shaft.

(a) Shaft after being compressed into die.

(b) Stripping of die.

Fig. 1.9. Closed die forging of shaft.

Fig. 1.10. Shaft after closed die forging.

After forging, the shaft is left to cool off before machining.

1.2.5 Turning of shaft

The forging operation is followed by turning on a lathe. This ensures better dimensional accuracy than the hot forging operation and removes the scale.

Fig. 1.11. Machining of shaft. Picture from Kelm Acubar.

1.2.6 Grinding and hardening of shaft

In order to increase the fatigue lifetime of the shaft, it is hardened and grinded after turning. The grinding process is seen in Fig. 1.12.

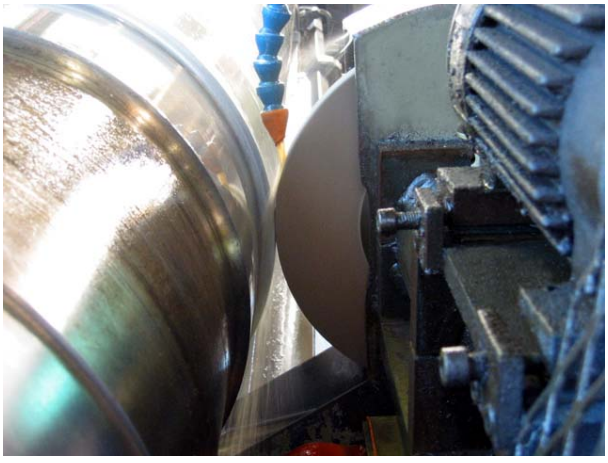

Fig. 1.12. Grinding of shaft. Picture from Bowe Machine Company.

1.3 Conclusion

From the listed number of processes it should be clear that the manufacturing of shafts is a complex process. In this presentation, the main focus was on the casting and especially the forging of the shaft. This, however should not be seen as reflecting these processes being more important than subsequent machining and hardening of the shaft. It is merely because the main focus of the project is on forging of the shaft.

2 Ingot casting and related defects

2.1 Introduction

The basis for the majority of forged steel parts are cast steel parts. The raw iron extracted from iron ores in the earth is the starting material for the foundry. The raw iron is melted, refined to remove impurities and unwanted chemical components, and thereafter cast to parts of different sizes. The size of each casting depends on the size of the final part. Two major types of these intermediate castings exists: Ingot casting and continuous casting. In ingot casting, individual blocks of metal are cast one by one or in small batches. In continuous casting, one long piece of metal is cast, hence the name continuous. The main principles of the two casting processes can be seen in Fig. 2.1. The process description, in this chapter, is based on Kalpakjian & Schmid [54], the heat flow is based on Hattel [43] and Fredriksson & Åkerlind [34], and the metallurgical part is based on Fredriksson & Åkerlind [34] and Porter et al. [80].

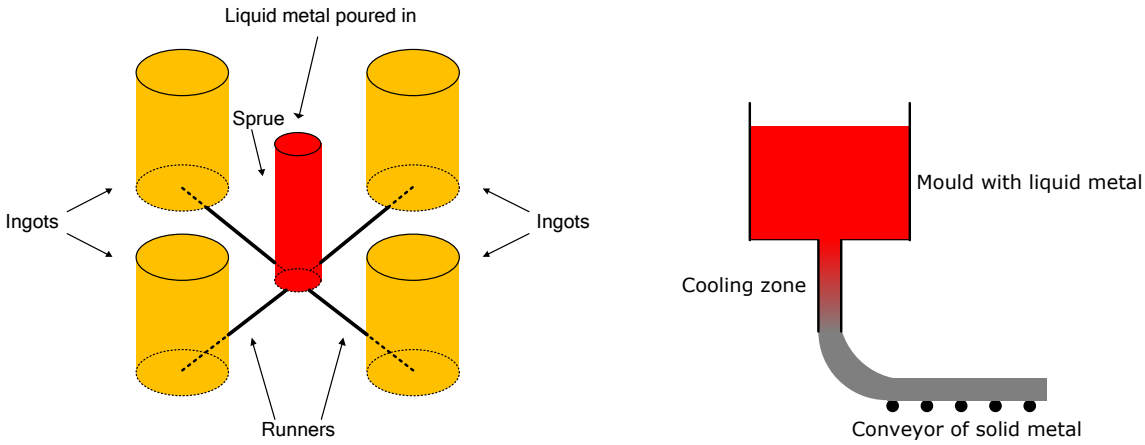

(a) Ingot casting. **(b)** Continuous casting.

Fig. 2.1. Main principles in ingot and continuous casting.

Continuous casting is the most used casting process for manufacturing of semi-finished metal goods. According to Kalpakjian & Schmid [54], continuous casting is less expensive than ingot casting and produces parts with more homogeneous properties. However ingot castings are still used as basis for manufacturing large components.

After casting, the metal part is subsequently shaped by plastic deformation. This is usually done through hot forging of ingots or hot rolling of continuous cast parts. The main purpose of the hot forging or rolling, besides that of obtaining the desired shape of the component, is to promote recrystallization of the metal. This recrystallization causes the cast metal structure, which is usually coarse, to become more refined and hereby improving the mechanical properties. At the same time, the induced deformation closes

internal defects such as porosities. The hot metal forming process is therefore important regarding the final mechanical properties of the part. However for accurate predictions of the influence of hot metal forming on the mechanical properties, a detailed description of the cast part is necessary. One needs to know which defects are present from the casting process in order to be able to evaluate, whether the metal forming operation minimizes them. Since shafts are large and therefore mainly produced by metal parts originating from ingot castings, the main focus in the chapter will concern ingot casting. The purpose is to give an overview of the ingot casting process and defects originating from the ingot casting process.

2.2 Ingot casting process

The basic principle of ingot casting can be seen in Fig. 2.2, an in the figure, four ingots are cast at the same time. It is common to cast several ingots together.

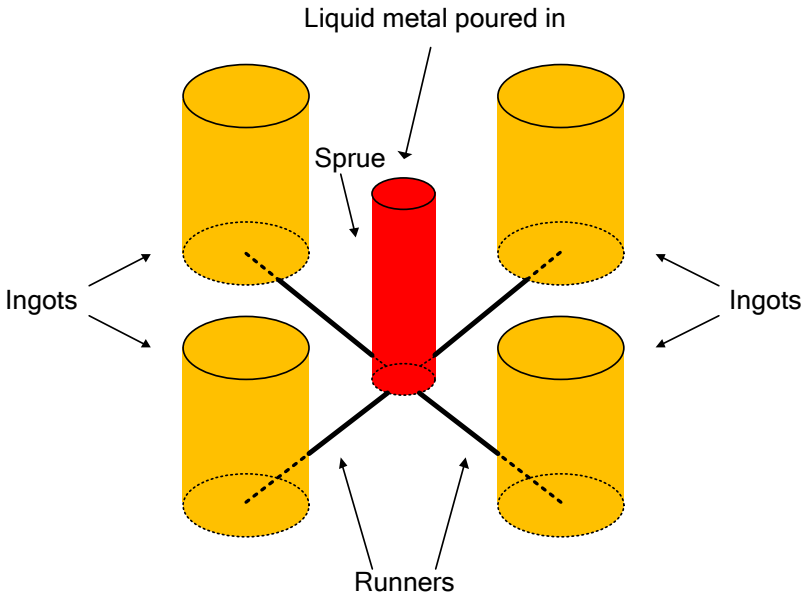

Fig. 2.2. Ingot casting process.

The liquid metal is poured into the sprue, where it flows down due to the gravitational force. The liquid metal then flows through the runners to the bottom of the ingots. The ingots are subsequently filled from the bottom, hence the name of this type of filling, which is "bottom filling". Each ingot has a feeder on the top, known as an "ingot head". Its purpose is to feed still liquid melt to the ingot, when it solidifies. A more detailed view of one ingot can be seen in Fig. 2.3.

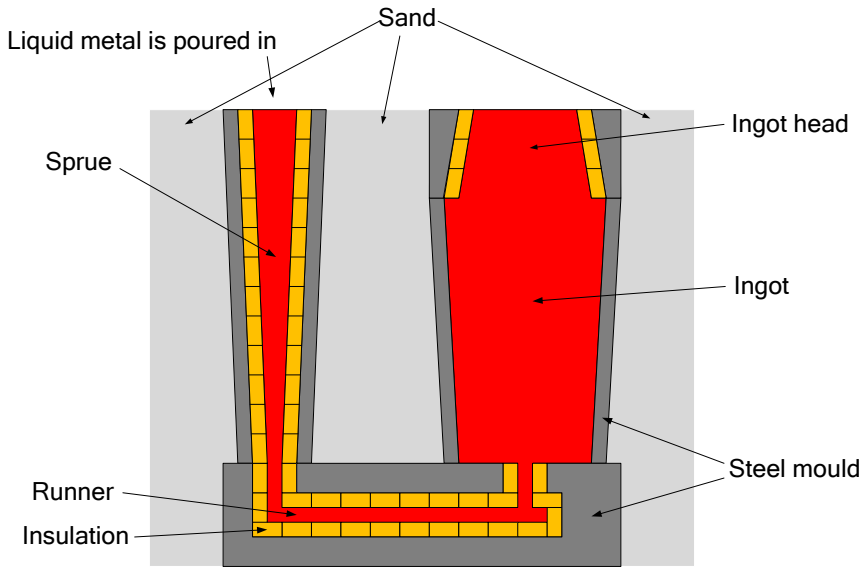

Fig. 2.3. Detailed view of ingot casting.

The filling of the ingot should be done in a steady manner in order to avoid turbulent flow and splashes of the liquid metal. If splashes occur, the metal will be oxidized by the surrounding air and result in a poor casting.

After filling of the ingot with liquid metal, it is left to solidify and cool off. It is especially during this stage, that most of the subsequent defects in the ingot manifest themselves. The defects can for instance be coarse microstructure with large and/or lamellar formed grains, segregation of the metal, porosity formation due to entrapped gas or improper feeding or inclusions due to the liquid metal reacting with the air or the mould. These defects will be treated in more detail later in the chapter.

2.3 Heat flow during casting

In order to better understand the casting process and the defect evolution associated with it, it is necessary to have knowledge regarding the cooling and solidification process. This calls for knowledge regarding the heat flow during the process and how the material responds to the cooling. This section will only concern a phenomenological description. For a mathematical description, the reader should consult specialized literature such as Hattel [43].

The basic physical principle governing any description of heat flow is that heat always flows from areas of high temperature to areas of low temperature. This means that the hot ingot will cool off while heating up the surrounding mould, which will transfer its heat to the surrounding air. A very simple example of such a heat flow in a sand casting process can be seen in Fig. 2.4.

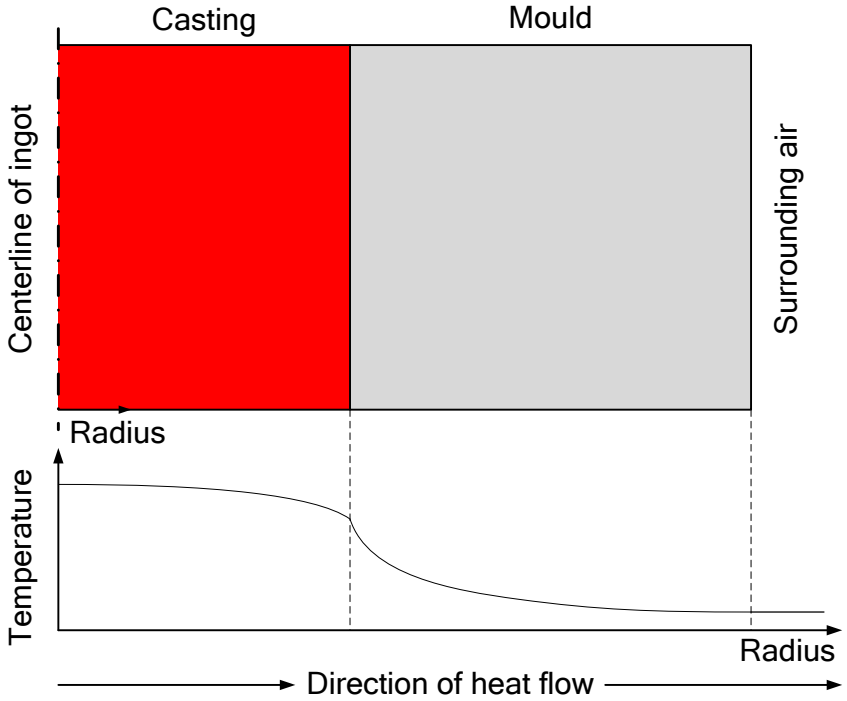

Fig. 2.4. Temperature profile during ingot casting in sand mould.

Fig. 2.4 shows sand casting of a cylinder, resembling an ingot. The heat flows from the hot ingot to the cold sand. The heat flow causes the ingot to cool down. This cooling gives rise to an internal temperature distribution in the ingot as function of radius R. The ingot is coldest at its outside, which is in contact with the sand mould. On the other hand, the sand mould starts to heat up due to the heat flow coming from the ingot. This gives rise to a temperature distribution through the sand mould, where it is hottest at the inside closest to the ingot, and coldest at the outside, which is in contact with the surrounding air. Fig. 2.4 also shows that the temperature profile is nonlinear through both the ingot and the sand mould.

After having established the cooling behavior of the metal, the next question is how the metal responds to the cooling. The most obvious effect of the cooling of the metal is that at some point, the metal starts to solidify, hence it changes phase from liquid to solid. This process is described in section 2.4.

2.4 Solidification of metals in casting processes

When a liquid metal is cooled down, it reaches a specific temperature, where the liquid starts to transform into a solid. This temperature is known as the liquidus temperature T_{liq}. When all the liquid metal has solidified, a temperature of the metal is reached called the solidus temperature T_{sol}. For some alloying compositions, the temperature at start of solidification is equal to the temperature at the end of solidification, but most often T_{liq} is larger than T_{sol}. The difference between the liquidus and the solidus temperature $(T_{liq} - T_{sol})$ is known as the miscibility gap. An example of a cooling curve for a metal can be seen in Fig. 2.5.

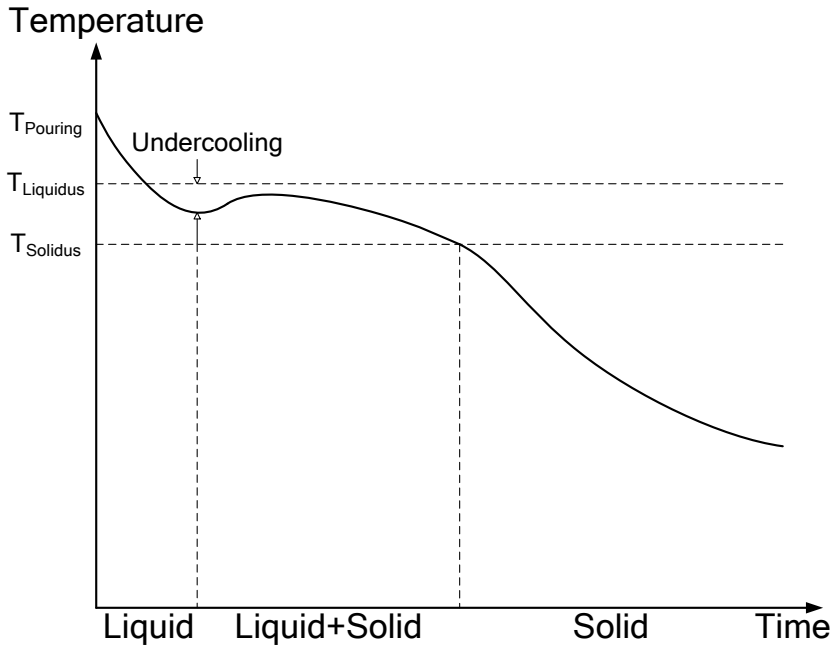

Fig. 2.5. Cooling curve for a metal.

Fig. 2.5 shows that the liquid metal is poured into the mould at the temperature $T_{Pouring}$. The liquid then starts to cool off. It does not start to solidify exactly when reaching the liquidus temperature T_{liq} but at some temperature lower than T_{liq}. Some undercooling is usually necessary in order to promote nucleation of solid metal particles in the liquid. When the liquid has started to solidify, latent heat from the phase transformation from liquid to solid is released. This causes the temperature to increase. When the casting continuous to cool off, eventually all liquid solidifies when T_{sol} is reached. Thereafter the solid casting cools off to ambient temperature. This cooling procedure is quite time consuming. For large ingots, the cooling time can be 24 hours.

2.5 Grain structure in castings

As mentioned in section 2.3, the casting cools off from the outside towards the center. From section 2.4 this implies that the first metal to solidify, is the metal in contact with the mould. Thereafter the solid grows through the liquid towards the center of the casting. This gives a special grain structure in the casting. At the mould-casting interface there is a narrow zone, known as the chill zone. The chill zone consists of equiaxed grains. Some of these grains are favorably oriented in terms of growth direction and grows into the liquid metal. Close to the casting-mould interface, where the numerical value of the temperature gradient is large, elongated grains are formed due to dendrite growth starting at the favorably oriented grains in the chill zone at the casting-mould interface. These grains are known as columnar grains. Closer to the center of the casting, equiaxed grains are formed due to lack of preferred growth direction. The grain structure, after solidification of the casting, can be seen in Fig. 2.6.

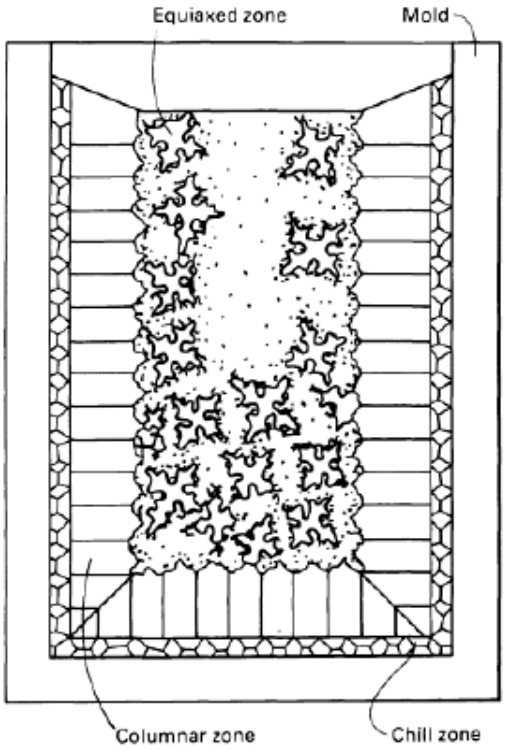

Fig. 2.6. Grain structure in ingot casting. From ASM Handbook Vol. 15 [6] p. 254.

A cast structure, as seen in Fig. 2.6, is normally considered to have less favorable metal structure. The columnar grains at the casting-mould boundary leads to mechanical anisotropy. The equiaxed grains formed closer to the center of the casting tends to be large due to the fact that they are formed at relatively low cooling rates. This implies that few grains are nucleated and the ones which are nucleated, grow and become large. This leads to a coarse microstructure with low mechanical strength. According to Anderson [4] p.238 a coarse microstructure, furthermore has less strength against cleavage fracture. Hence a coarse microstructure has less fatigue strength. These grain structure defects can, to some extend, be minimized during the casting process by adding inoculants to the molten metal before it is poured into the mould. The inoculants promote grain nucleation, and hereby a larger number of grains are formed, resulting in a part with more favorable mechanical properties.

2.6 Segregations in castings

Segregation is a phenomenon where there is a difference in the chemical composition throughout the casting, which originates from the solidification process. Segregations can occur both locally in the casting and as an overall difference in alloy composition in the casting. If there is a local variation in the chemical composition, the segregation is labeled microsegregation. Microsegregation occurs at sizes comparable to the grain or dendrite size in the casting. If there is an overall variation in chemical composition in

the casting, the segregation is labeled macrosegregation. Volumes of the casting, that after solidification has a content of alloying components lower than the average alloying component percentage, is labeled negatively segregated. Volumes of the casting, that after solidification has a content of alloying components larger than the average alloying component percentage, is labeled positively segregated.

2.6.1 Microsegregation

The principle of microsegregation is best explained qualitatively using a phase diagram. As an example the Fe-C diagram is used, see Fig. 2.7.

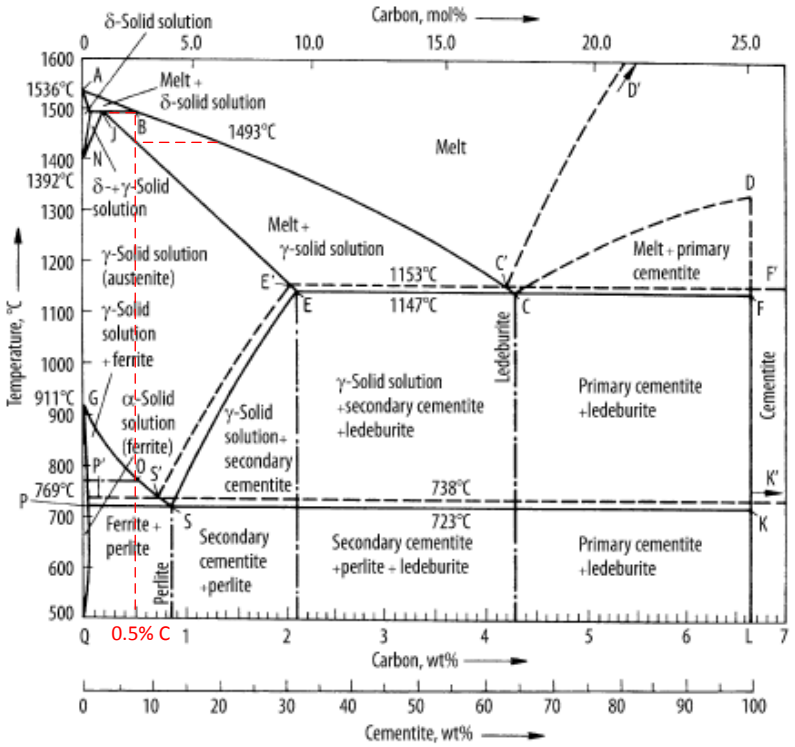

Fig. 2.7. Fe-C diagram. From Cardarelli [16].

A 0.5%-C steel is to be cast. When it starts to solidify, the first solid to form has a carbon content somewhat lower than the rest of the liquid, see Fig. 2.7 point J. As the solidification process continues, the liquid will therefore increase its carbon content since the solid formed has a lower carbon content than the liquid. Since the carbon content has much influence on the mechanical properties of steel, it is expected that segregated areas can have much different mechanical properties.

An example of microsegregation is the solidification of a liquid with small thermal gradients through the liquid. This is the case at the center of the ingot seen in Fig. 2.6. The small thermal gradient causes the grains to nucleate and grow approximately homogeneous as spheres. If there is no mixing of alloying elements in the formed solid due to diffusion, the center of the formed grains will be low in alloy content. As the grains grow, the last solidified layer of the grain will be more enriched in alloying elements than the previously formed layer. If there is no diffusion in the formed solid, the last liquid

to solidify will reach the eutectic composition (point C in Fig. 2.7), if the original liquid composition had a carbon content lower than the eutectic composition ($< \approx 4.3\%$). The solidification process can be seen in Fig. 2.8.

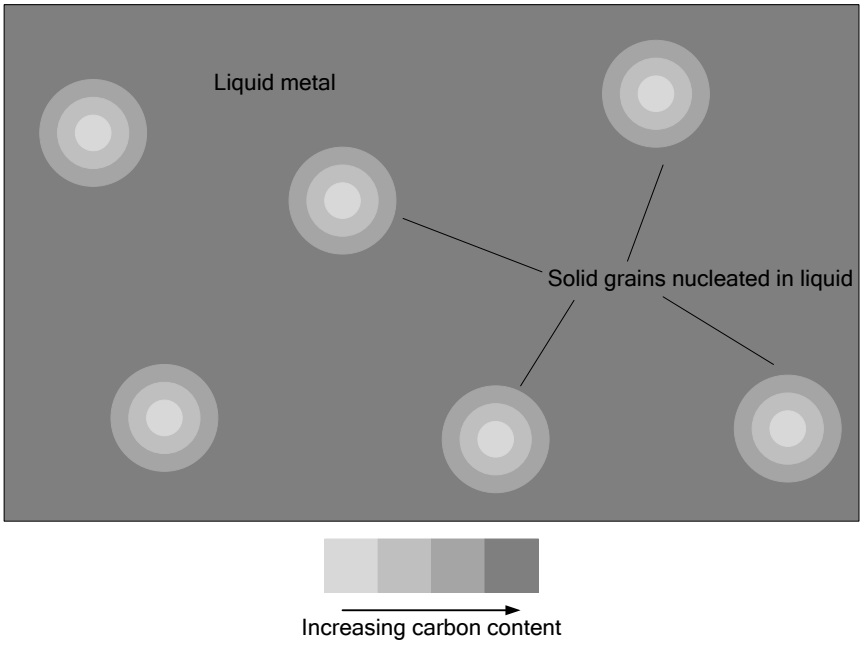

Fig. 2.8. Microsegregation resulting in equiaxed grain structure.

A similar phenomenon can occur if the grain growth is due to directional dendritic growth and not equiaxed grain growth. A principal figure of solidification by dendritic growth can be seen in Fig. 2.9.

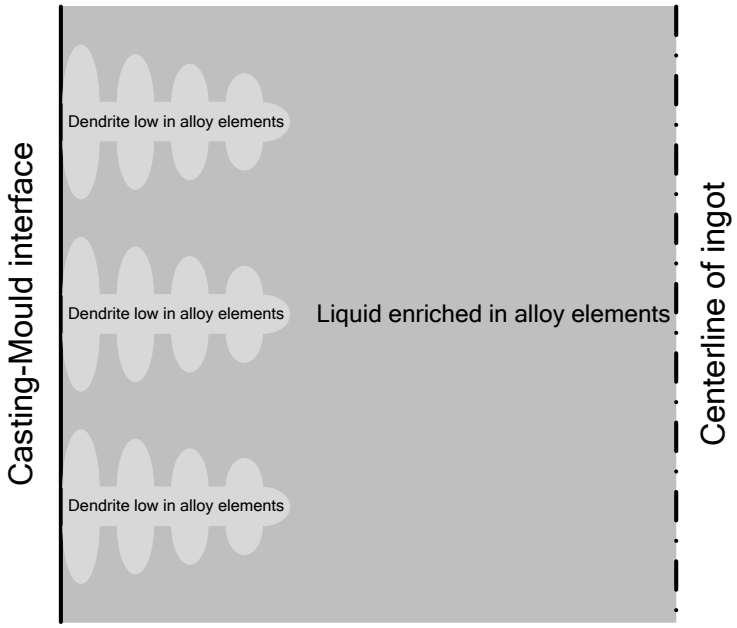

Fig. 2.9. Solidification by dendritic growth.

Fig. 2.9 shows that the dendrites start at the casting-mould interface, where the temperature gradient in the casting is largest, see Fig. 2.4. The dendrites grow into the liquid and forms the columnar grains seen in Fig. 2.6. It is unusual that the dendrites grow to the center of the ingot. Normally at some point, equiaxed grains are formed in the remaining liquid metal between the dendrite tips and the centerline of the casting.

Microsegregation can be minimized by heating the casting after it has been shaken out of the mould. By increasing the temperature of the casting afterwards, diffusion is increased and there will be a leveling of the alloying elements. Ideally this will continue until the alloying composition is the same everywhere. However this is only achievable on the local level. If diffusion should level out all differences in chemical composition throughout the casting, it would take a very long time due to the long distances the alloying elements should move due to diffusion. Therefore diffusion can only level out differences in chemical composition on a local level, hence only microsegregation, but not macrosegregation, can be minimized substantially by diffusion.

2.6.2 Macrosegregation

Macrosegregation is not directly related to the phase diagram as is the case for microsegregation. Macrosegregation has more to do with the internal phenomenon occurring in the casting during cooling and solidification. Four different phenomenon cause macrosegregation: shrinkage during solidification, density differences in the interdendritic liquid, density differences between the liquid and solid, and convection inside the casting.

Macrosegregation due to shrinkage can be explained using Fig. 2.10.

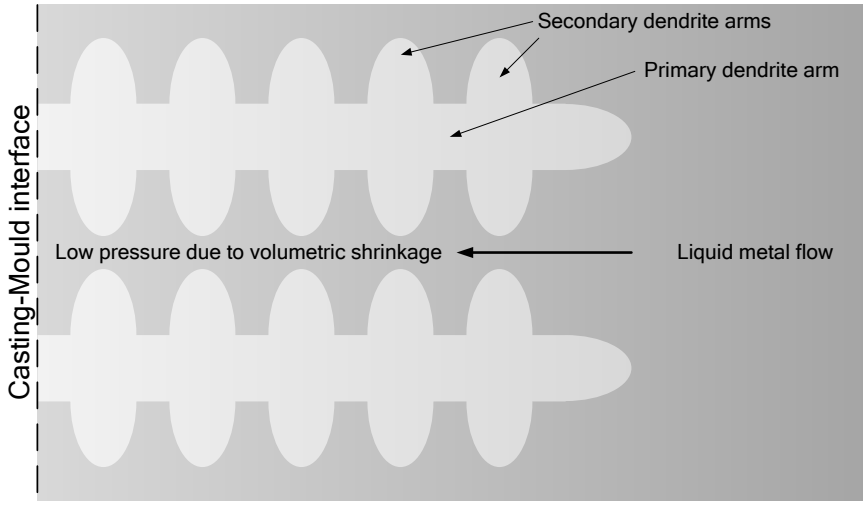

Fig. 2.10. Shrinkage macrosegregation principle.

Usually for metals, the density of the solid metal is larger than the density of the metal in the liquid state. This implies that the same mass of material occupies a larger volume in liquid state than in the solid state. This means that when the solid secondary dendrite arms grow into the liquid, a pressure drop due to volume shrinkage is occurring in between the two primary dendrite arms. Therefore liquid metal flows in between the primary dendrite arms from the alloy enriched liquid in front of the dendrites. This causes inverse segregation between the dendrites. The segregation is called inverse because it is

causing positive segregation at the casting-mould interface and not at the center of the casting, which is usually the positively segregated area.

Macrosegregation due to interdendritic liquid density differences is a phenomenon occurring due to gravitation. A metal alloy consists of minimum two and often more alloying components. If the alloying components have different densities, the components with high densities will be subjected to a larger gravitational force than the components with low density. Hence the dense elements sink down on top of the dendrite arms while the lighter elements flow upward and ends underneath the dendrite arms. The principle can be seen in Fig. 2.11.

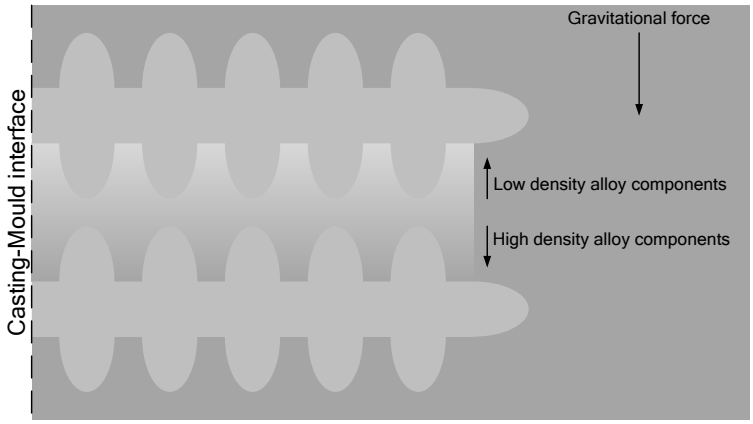

Fig. 2.11. Interdendritic macrosegregation due to density differences of the alloying components.

Macrosegregation due to density differences between liquid and solid occurs due to the density difference between liquid and solid metal phases. When a given metal mass solidifies, it shrinks and the density therefore increases. This causes the solid metal to sink to the bottom of the casting due to gravity. The situation can be seen in Fig. 2.12.

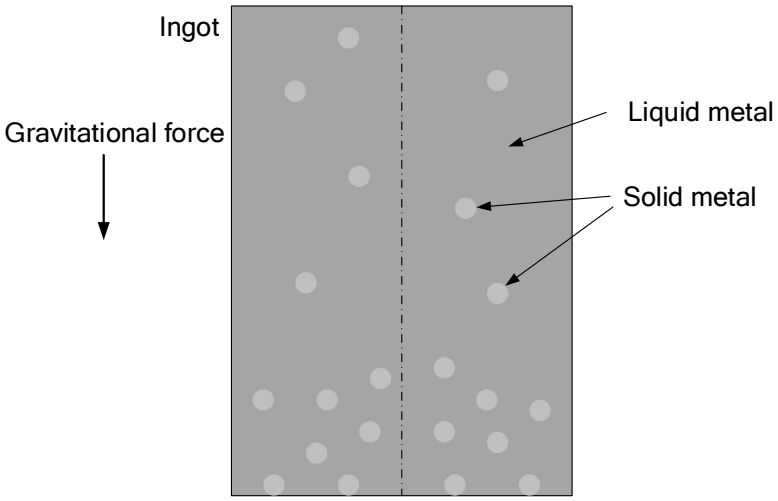

Fig. 2.12. Macrosegregation due to difference in density between liquid and solid metal phase.

Since the first solid to form has a lower alloying content than the solid solidifying later, the solid, which sinks to the bottom due to this segregation mechanism, will be low in alloy content. Therefore the bottom of the ingot will be negatively segregated.

Macrosegregation due to convection is caused by uneven temperature distribution through the ingot. Since density is temperature dependent and becomes smaller for increasing temperature, cold liquid metal will be more dense than hot liquid metal. This causes the cold liquid to sink to the bottom. Hot liquid will rise to the top of the ingot. Both of these internal mechanisms causes internal flow of liquid in the ingot. This internal flow gives rise to macrosegregation.

As it can be seen, macrosegregation is caused by a number of different mechanisms and since they all can occur at the same time, the net effects of the mechanisms are therefore coupled to one another. A typical example, of the net segregation result in a large ingot, can be seen in Fig. 2.13.

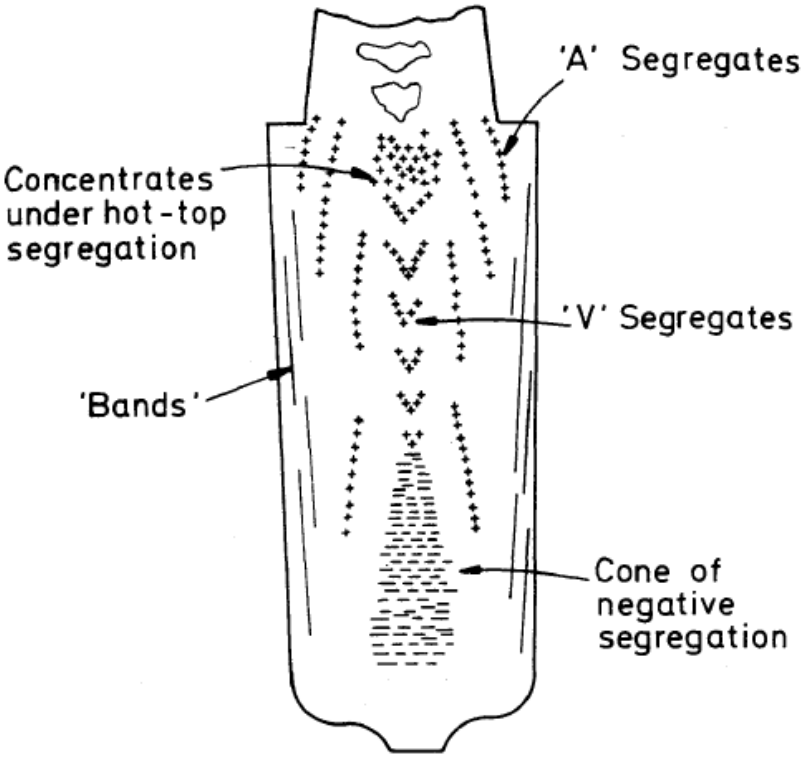

Fig. 2.13. Segregation pattern in a large ingot. (+) Positive segregation; (-) Negative segregation. From Flemings [33].

2.7 Porosity formation

Porosities are volumes in the casting where there are no material but holes. The porosities have a negative influence on the mechanical properties of the casting. They reduce the load carrying capacity of the casting since the size of the cross sectional area, that can carry the load, is reduced. An example of this principle is seen in Fig. 2.14.

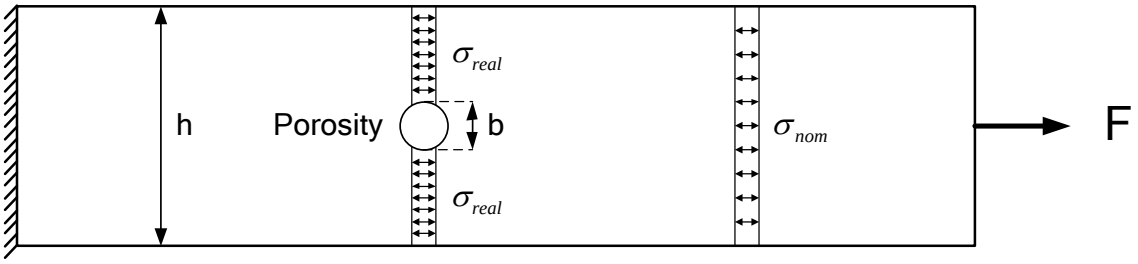

Fig. 2.14. Tensile test bar with internal porosity.

The tensile test bar, seen in Fig. 2.14, is loaded by a tensile force F at the right edge. The tensile test bar has the height h and the width w perpendicular to the plane of the figure. The nominal stress σ_{nom} can therefore be calculated as:

$$\sigma_{nom} = \frac{F}{hw} \tag{2.1}$$

However due to the porosity, which goes through the bar, located in the tensile bar, the load carrying area is reduced in a cross section close to the porosity. Ignoring any stress intensity phenomenon close to the porosity, the real stress, in the material in the cross section of the tensile test bar containing the porosity, can be calculated as:

$$\sigma_{real} = \frac{F}{(h-b)\,w} \tag{2.2}$$

hence when b increases, the real stress also increases in the section where the porosity is located. If the material is ductile, yielding may occur, but if the material is brittle, fracture may occur in the part. Porosities may also serve as sites for initiation of crack growth in cyclic fatigue. So therefore porosities should be minimized in the final part. There are two major causes of porosities in castings: gas and shrinkage. These two causes for the formation of porosities in castings will be explained in the following.

2.7.1 Porosity formation due to gases

Porosities due to gas originate from small bubbles of gas being entrapped in the casting during solidification. Normally the liquid metal is degassed before being poured into the casting. However this may not always remove all the entrapped gas bubbles in the liquid. Another source of gas bubbles may originate from the filling of the mould during pouring. Here gas may be dragged into the mould if the pouring is done in an unsteady manner. Gas may also form due to chemical reactions between the liquid metal and air. For instance carbon, which is an alloying element in many ferrous metals, may react with the oxygen in the air to form the gas carbonmonooxid (CO).

If there is some dew on the sides of the gating system or mould, the dew will evaporate when the liquid metal is poured into the casting. Thereby a gas of water vapor is formed inside the casting.

Another source of gas porosities in castings is due to nucleation of gas bubbles in the solid metal. The nucleation is due to a large difference in gas solubility in the liquid and solid state of the metal. Much more gas can be dissolved in the liquid phase than in the solid phase. An example of this is the Fe-H diagram seen in Fig. 2.15.

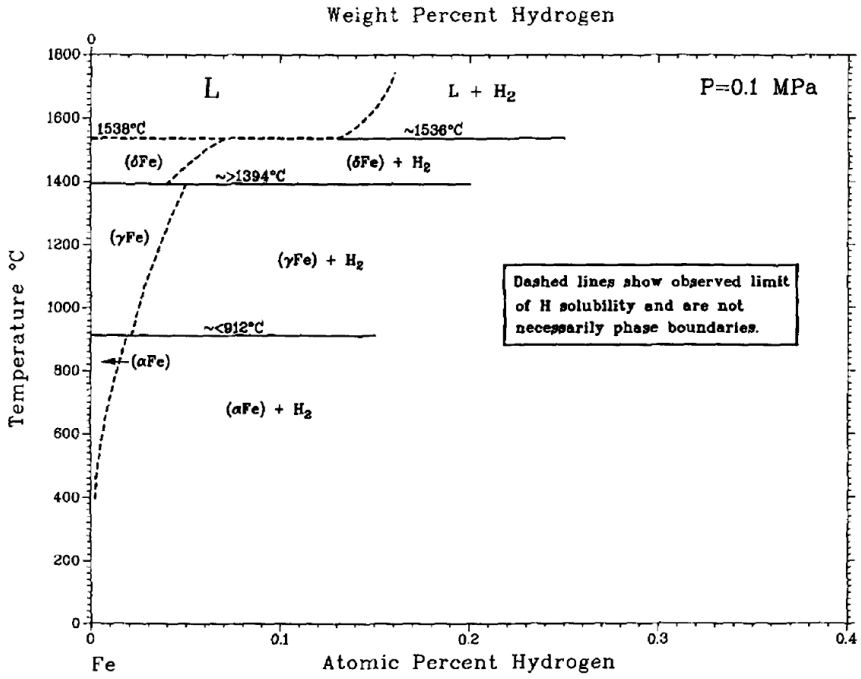

Fig. 2.15. Fe-H diagram. From San-Martin & Manchester [87].

Fig. 2.15 shows a marked solubility difference of hydrogen in the liquid and solid iron. This implies, that if there is hydrogen dissolved in the liquid metal before solidification, this hydrogen will be precipitated as gas when the metal solidifies. This causes the formation of gas porosities in the solid. The gas dissolved in the liquid can, to some extent, be removed by supplying degassing agents to the melt prior to pouring the liquid into the mould.

2.7.2 Porosity formation due to shrinkage

Porosities can also form due to volumetric shrinkage of the casting. It originates from the fact that most solids are more dense in the solid than in the liquid state. This implies that the same mass of metal occupies a larger volume in the liquid state than if it where in the solid state. In the ideal case, the casting would be free to contract during the solidification and cooling process, where the volumetric shrinkage occurs. However this is seldom the case. Therefore smaller or larger areas of the casting will be occupied not by metal but by porosity holes after solidification. This empty volume, formed during solidification, can, to some degree, be filled during formation with new liquid from feeders placed at suitable places. Such a feeder in ingot casting can be seen in Fig. 2.3, were it is labelled as ingot head. The idea behind feeding is that when the metal starts to solidify at the casting-mould interface, the interior of the casting is still liquid. This means that the empty volume formed by volumetric shrinkage can be filled by liquid melt from the interior of the casting. Hereby the formation of shrinkage porosities is suppressed. The idea is to change the location where solidification shrinkage takes place from the casting to the feeder. An example of an ideal solidification of an ingot can be seen in Fig. 2.16.

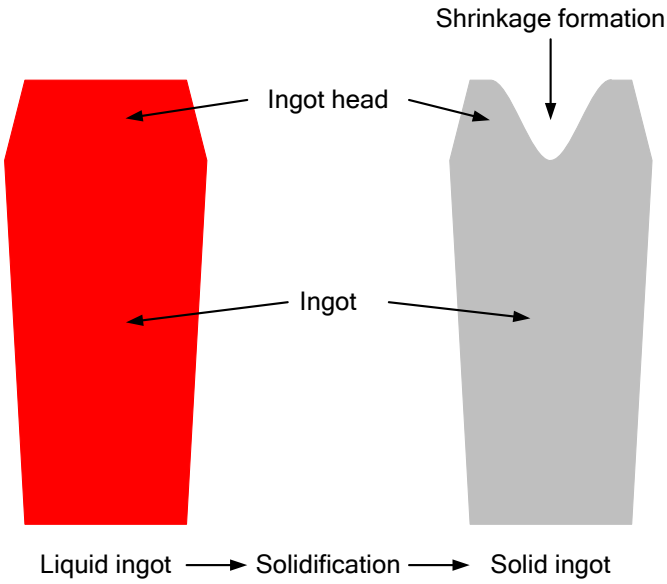

Fig. 2.16. Ideal solidification of ingot.

However this is a very ideal situation. Normally the feeding becomes more and more difficult due to solidification of the interior of the ingot. The partly solidified interior, with both liquid and solid metal, is called a mushy zone. This mushy zone reduces the free flow of liquid. The result is that the casting often will have few shrinkage porosities at the volumes that first solidified, and thereafter a gradual increase in shrinkage porosities, which maximizes at the volumes which solidified last. In ingot casting, the last solidifying volume is in the middle along the centerline. This gives rise to the shrinkage porosity profile seen in Fig. 2.17.

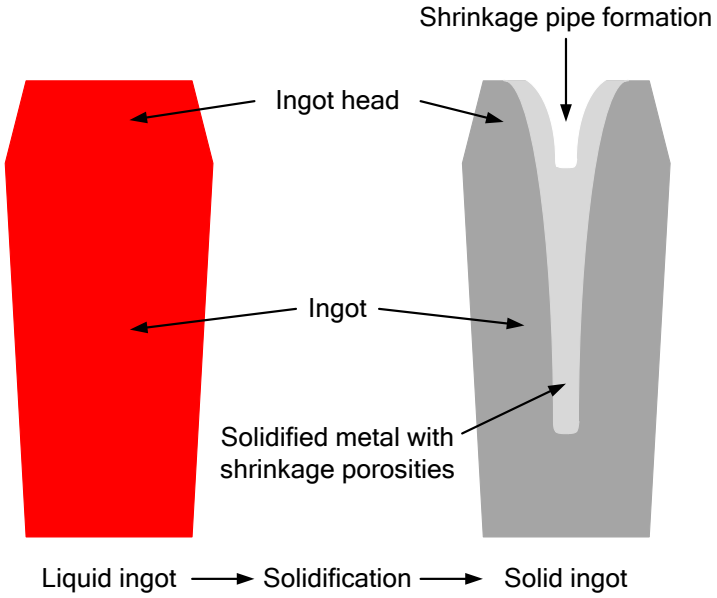

Fig. 2.17. Principal shrinkage porosity distribution in ingot casting.

As it can be seen from Fig. 2.17, it is to be expected that some volumes of the casting will contain porosities due to shrinkage although correct feeding has been applied.

2.8 Slag inclusions

Slags are unwanted chemical compounds in the casting. Often they are the product of oxygen degassing of the melt. Deoxidixing elements like Silicon, Manganese or Aluminium are added to the steel melt before pouring. The elements react with the oxygen dissolved in the melt to form ceramic compounds like SiO_2, MnO and Al_2O_3. Another common type of slag formed in ferrous alloys are Manganese sulfide (MnS). Manganese is often added to the melt to form the MnS slag, since it is relatively harmless compared to the alternative slag Iron sulfide (FeS). The formed ceramic compounds have a density smaller than the density of the melt. Hence ideally they should flow to the top of the melt due to buoyancy forces, and the slags could then be removed before pouring. However they may be prevented from flowing to the top by internal convection in the melt.

Another source of slag particles comes from the insulating brick material seen in Fig. 2.3. Usually the material is lime ($CaCO_3$). Due to erosion of the bricks during the filling, lime particles may flow into the casting.

Slags may also be formed when the liquid metal reacts with the surrounding air. This is especially prone to happen if splashes occur during the filling process. Since slag particles reduce the mechanical properties of the casting, slag formation should preferably be avoided. This can be done by shielding the melt from the surrounding air, which can be done by using an inert atmosphere of argon around the melt. Another way of removing slags is by using a so-called hot top. Instead of having insulating bricks around the ingot head, one can surround the ingot head with an exothermic material. An exothermic material is a material which burns when coming in contact with the melt. Hereby heat is generated by the combustion. This implies heating of the ingot head and this heating promotes internal convection inside the ingot, bringing slags to the top of the ingot head, and thereby removing them from the ingot.

2.9 Conclusion

As it will be clear from the chapter, there are many different defects that can occur during the manufacturing of ingot castings. Most of them can, to some degree, be prevented or minimized by good foundry practice. However it is not always that cast parts have the mechanical properties needed for a given application. It has been found that some of the defects originating from the casting process can subsequently be minimized by inducing mechanical deformation to the casting. This is reviewed in Chapter 6.

3 Metal hardening behaviour

3.1 Introduction

In metal forming operations it is commonly found that changes in strength occur during the metal forming operations. In cold metal forming, the flow stress is normally found to increase with deformation. This phenomenon is known as strain or work hardening. In hot metal forming, the flow stress of a given metal is mainly influenced by the temperature and strain rate, known as strain rate hardening. In hot metal forming, the hardening due to deformation is normally small due to the fast recrystallization rate at high temperature. In the intermediate temperature range, combinations of both strain hardening, strain rate hardening and recrystallization rate influence the overall flow stress during deformation.

In this chapter, some models are presented for hardening of metals during deformation.

3.2 Experimental findings regarding flow stress

From practical experience it is found that the flow stress of a metal varies depending on different parameters, see Section 3.1. As an example, different flow stress curves for steel 42CrMo4, which is a typical steel utilized for shafts, is presented to illustrate the flow stress behaviour at elevated temperatures. The flow stress data presented is from Spittel & Spittel [93].

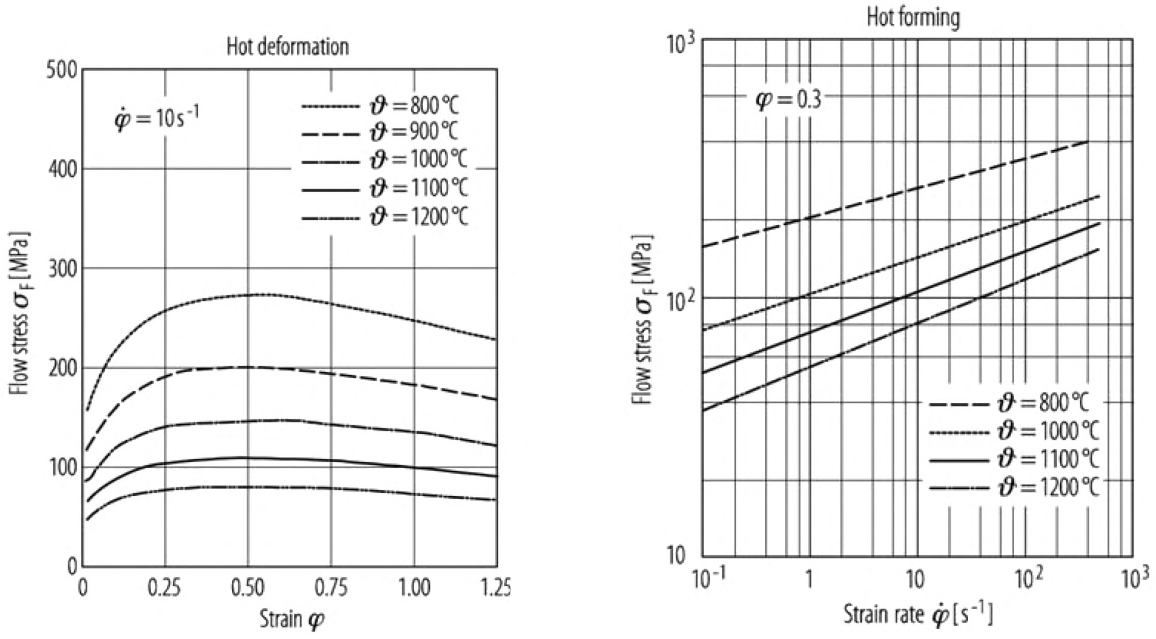

(a) Stress-strain curves. **(b)** Stress-strain rate curves.

Fig. 3.1. Flow stress curves for steel 42CrMo4.

From Fig. 3.1 it is seen that the flow stress increases with strain rate. It also increases with strain until a sudden point where it starts to decrease again. The flow stress decreases with increasing temperature. It should be noticed that the decline in flow stress at a sudden strain level is usually not encountered at room temperature, where the stress mainly increases, but the rate of increase decreases with the strain. The decline in flow stress noticed on the curves in Fig. 3.1a is due to the experiments not being performed isothermally. Due to the generated deformation heat, the temperature of the test specimen increases and thereby the flow stress decreases.

3.3 Flow stress models

Some different flow stress models, based on effective plastic strain $\bar{\varepsilon}^{pl} = \int \dot{\bar{\varepsilon}}^{pl} dt$, are introduced.

3.3.1 Strain hardening models

3.3.1.1 Ludwik hardening

Ludwik [68] proposed a model for strain hardening:

$$\sigma_0 = C \left(\bar{\varepsilon}^{pl}\right)^n + \sigma_y \tag{3.1}$$

where C is the strength coefficient, $\bar{\varepsilon}^{pl}$ is the effective plastic strain, n is the strain hardening exponent and σ_y is the initial flow stress. Ludwik hardening is suitable for metals having a marked initial flow stress.

3.3.1.2 Hollomon hardening

For metals with a small initial flow stress, for instance annealed metals, Hollomon [48] suggested the following strain hardening model:

$$\sigma_0 = C \left(\bar{\varepsilon}^{pl}\right)^n \tag{3.2}$$

Eq. 3.2 is much used in metal forming due to its simplicity. It is also often used in analytical models for metal forming operations. A plot of Hollomon hardening, with different values of the exponent n, can be seen in Fig. 3.2.

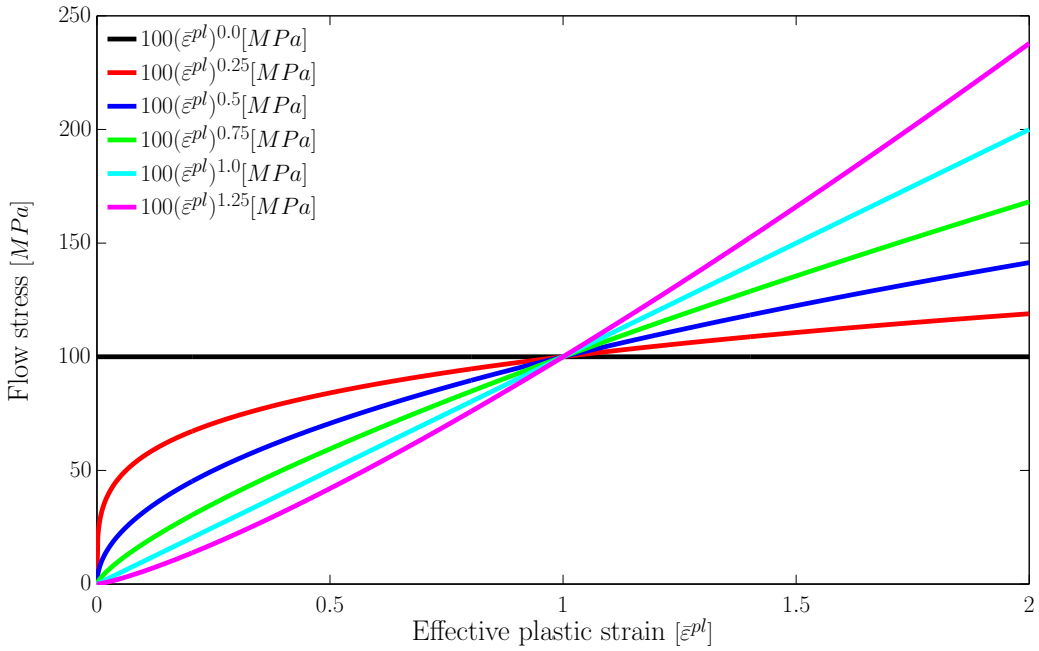

Fig. 3.2. Hollomon hardening.

It is seen in Fig. 3.2 that when the effective plastic strain $\bar{\varepsilon}^{pl}$ is in the interval 0-1, the flow stress, for a given $\bar{\varepsilon}^{pl}$, becomes lower as n increases.

The Ludwik model reduces to the Hollomon model if the initial flow stress $\sigma_y = 0$.

3.3.1.3 Swift hardening

For metals already having experienced some straining due to previous metal forming operations, Swift [96] introduced the model:

$$\sigma_0 = C\left(\bar{\varepsilon}^{pl} + \varepsilon_0\right)^n \tag{3.3}$$

where ε_0 is the prestrain from previous metal forming operations. The Swift model reduces to the Hollomon model if $\varepsilon_0 = 0$.

3.3.1.4 Voce hardening

Some metals may experience a saturation level where the flow stress does not increase with continued straining. Voce [99] presented the following model:

$$\sigma_0 = \sigma_y + (\sigma_\infty - \sigma_y)\left(1 - exp\left(-n_{Voce}\bar{\varepsilon}^{pl}\right)\right) \tag{3.4}$$

where σ_∞ is the stress at saturation and n_{Voce} is a fitting constant.

The four presented strain hardening models can be seen in Fig. 3.3.

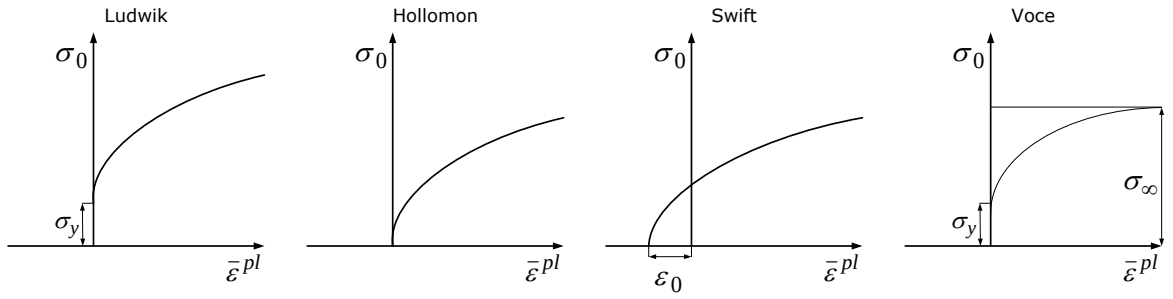

Fig. 3.3. Strain hardening models. Figure adopted from Wanheim et al. [103].

It should be noticed that for $n = 0$ all the models predict a constant flow stress. For $n = 1$ Ludwik, Hollomon and Swift predicts linear hardening with respect to the effective plastic strain.

3.3.2 Strain rate hardening

At high temperatures, the flow stress of a metal being deformed tends to increase with increasing speed of deformation, which is measured as the effective plastic strain rate $\dot{\bar{\varepsilon}}^{pl} = \sqrt{\frac{2}{3}\dot{\varepsilon}^{pl}_{ij}\dot{\varepsilon}^{pl}_{ij}}$.

3.3.2.1 Norton hardening

Norton [76] introduced a simple model for strain rate hardening:

$$\sigma_0 = C\left(\dot{\bar{\varepsilon}}^{pl}\right)^m \tag{3.5}$$

where m is the strain rate exponent.

3.3.3 Combined hardening

Attempts have also been made to describe the combined effect of both strain, strain rate and temperature on the flow stress.

3.3.3.1 Zener-Hollomon hardening

A model proposed by Zener & Hollomon [108] combines temperature and strain rate:

$$\sigma_0 = \frac{1}{\alpha} sinh^{-1}\left[\left(\frac{\dot{\bar{\varepsilon}}^{pl} exp\left(\frac{Q}{RT}\right)}{A}\right)^{\frac{1}{n}}\right] \tag{3.6}$$

where $\dfrac{Q}{R} = \beta$ is the temperature sensitivity, Q is the activation energy, R is the gas constant and α, A and n are constants.

A plot of Zener-Hollomon hardening can be seen in Fig. 3.4. The constants used are $\alpha = A = \beta = 1$. Both n and T are equal to 1 if they are not varied in the plot. The

purpose is to give a qualitative illustration of the change in flow stress by using different n and T, hence the curves are not supposed to model a real metal.

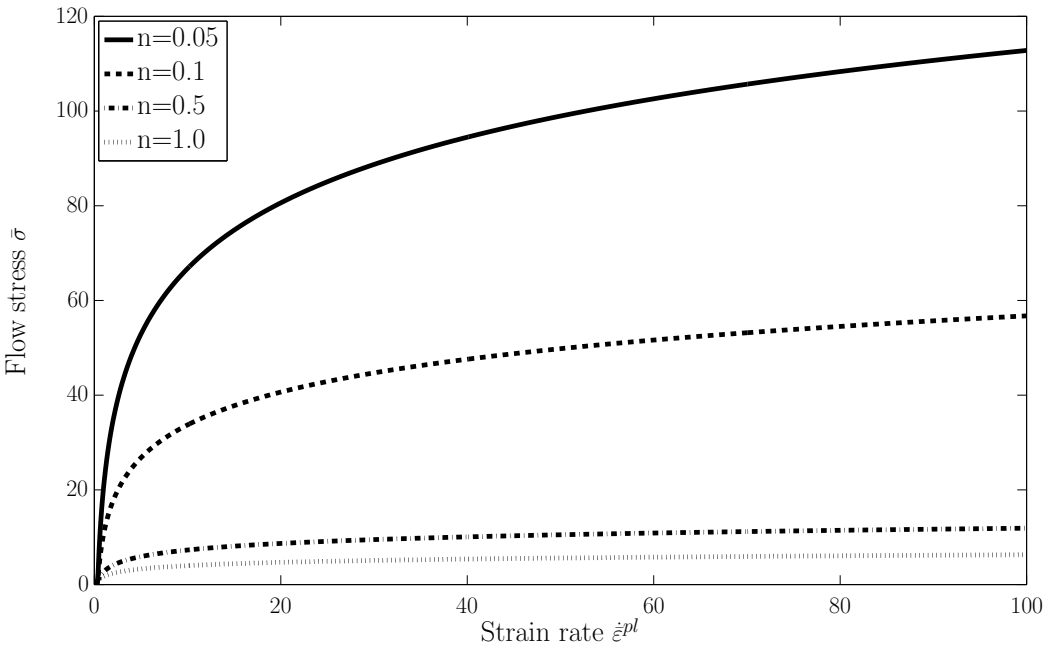

(a) Flow stress dependence on n.

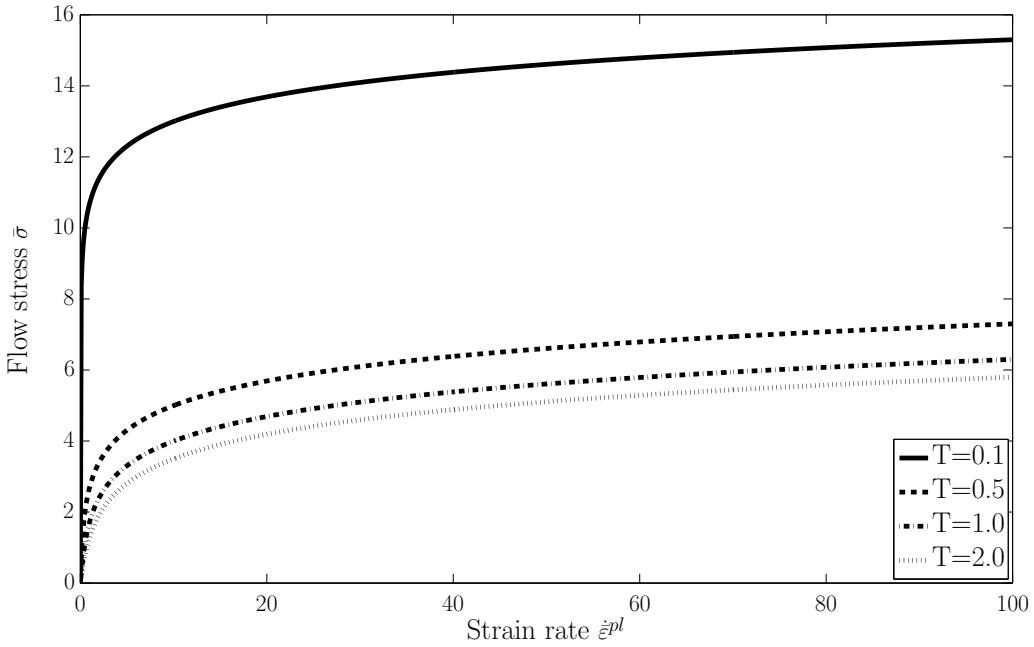

(b) Flow stress dependence on T.

Fig. 3.4. Qualitative plot of Zener-Hollomon hardening.

It can be seen from Fig. 3.4 that the Zener-Hollomon hardening model both predicts an increase of flow stress with increasing strain rate and a decrease of flow stress with increasing temperature.

3.3.3.2 Fields-Backofen hardening

Fields & Bachofen [32] introduced a model combining strain and strain rate hardening:

$$\sigma_0 = C \left(\bar{\varepsilon}^{pl}\right)^n \left(\dot{\bar{\varepsilon}}^{pl}\right)^m \tag{3.7}$$

Eq. 3.7 is compatible with both the Hollomon hardening (Eq. 3.2) and the Norton hardening (Eq. 3.5) behaviour.

3.3.3.3 Norton-Hoff hardening

By combining Hollomon (Eq. 3.2) and Norton (Eq. 3.5) hardening and adding a temperature dependent factor, Hoff [47] suggested the following model for the flow stress:

$$\sigma_0 = C \left(\bar{\varepsilon}^{pl}\right)^n \left(\dot{\bar{\varepsilon}}^{pl}\right)^m exp\left(\frac{\beta}{T}\right) \tag{3.8}$$

where β is the temperature sensitivity and T is the temperature in Kelvin. The Norton-Hoff equation is equal to Hollomon hardening (Eq. 3.2) if $m = 0$ and the temperature is constant. On the other hand Hollomon hardening may also be applied to high temperature metal forming operations if the variation in strain rates and temperature throughout the component being deformed is limited. Then $\sigma_0 = C \left(\bar{\varepsilon}^{pl}\right)^n \left(\dot{\bar{\varepsilon}}^{pl}\right)^m exp\left(\frac{\beta}{T}\right) \approx C_1 \left(\bar{\varepsilon}^{pl}\right)^n$.

A plot of Eq. 3.8 can be seen in Fig. 3.5. $C = n = m = \beta = 1$ so only different values of T are applied to evaluate the flow stress as function of strain rate.

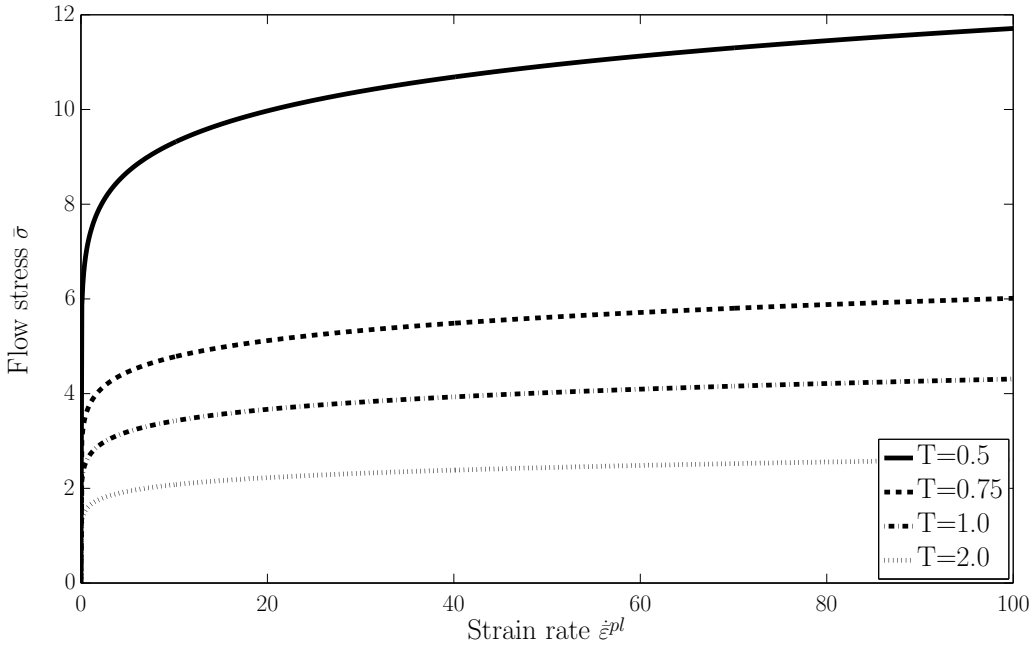

Fig. 3.5. Norton-Hoff hardening.

It is seen from Fig. 3.5 that the flow stress decreases with increasing temperature. Since the Norton-Hoff equation also includes the effective plastic strain it should in theory be

better suited for modelling work hardening than the Zener-Hollomon equation.

3.3.3.4 Hensel-Spittel hardening

Some metals experience strain softening after some straining. Hensel & Spittel [45] suggested the following expression:

$$\sigma_0 = C\left(\bar{\varepsilon}^{pl}\right)^n exp\left(A\bar{\varepsilon}^{pl}\right) exp(-\frac{\beta}{T}) \tag{3.9}$$

The flow stress predicted by the Hensel-Spittel equation can be seen in Fig. 3.6 for different temperatures. The constants used are $C = \beta = 1$, $A = -1$ and $n = 0.2$.

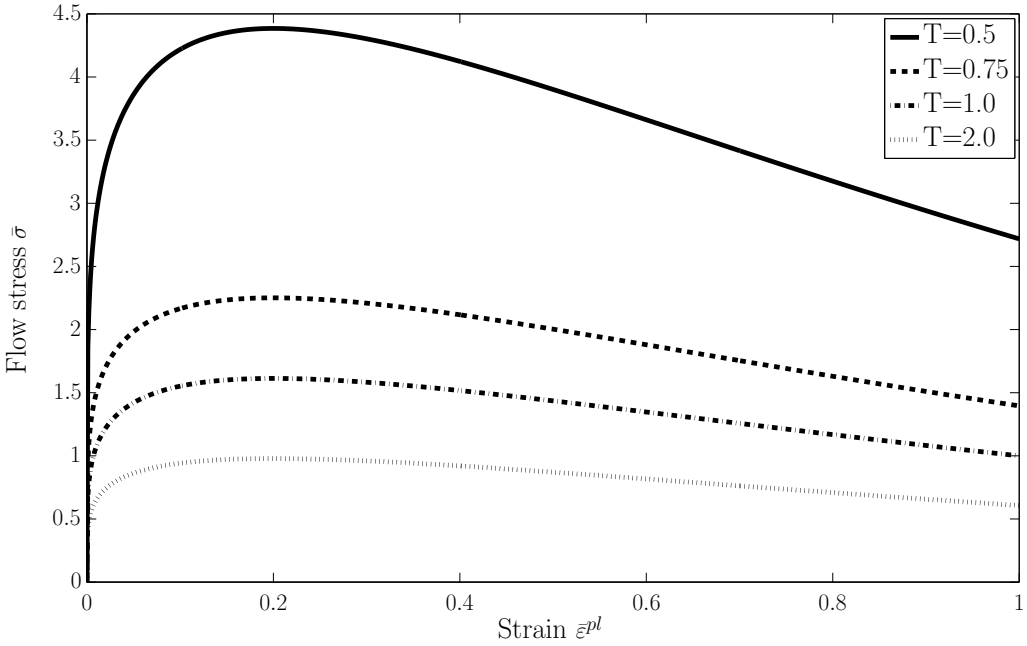

Fig. 3.6. Hensel-Spittel hardening.

Fig. 3.6 shows the flow stress increases until a maximum and then decreases again. The flow stress generally decreases with increasing temperature.

It should be noticed that several other models have been proposed for hardening of metals at high temperatures. Some are presented in Meyer et al. [72].

3.4 Flow stress data in DEFORM® database

The commercial software program DEFORM® contains a material library including flow stress data for steel 42CrMo4. Since DEFORM® is utilized for simulations in Chapter 11-Chapter 12, it is relevant to know which flow stress data that are contained in the DEFORM® material database. The flow stress data are given as table values and interpolation of these values generates the flow stress for a given combination of strain, strain rate and temperature. Flow stress data for steel 42CrMo4 corresponding to different strains, strain rates and temperatures are seen in Fig. 3.7-Fig. 3.9.

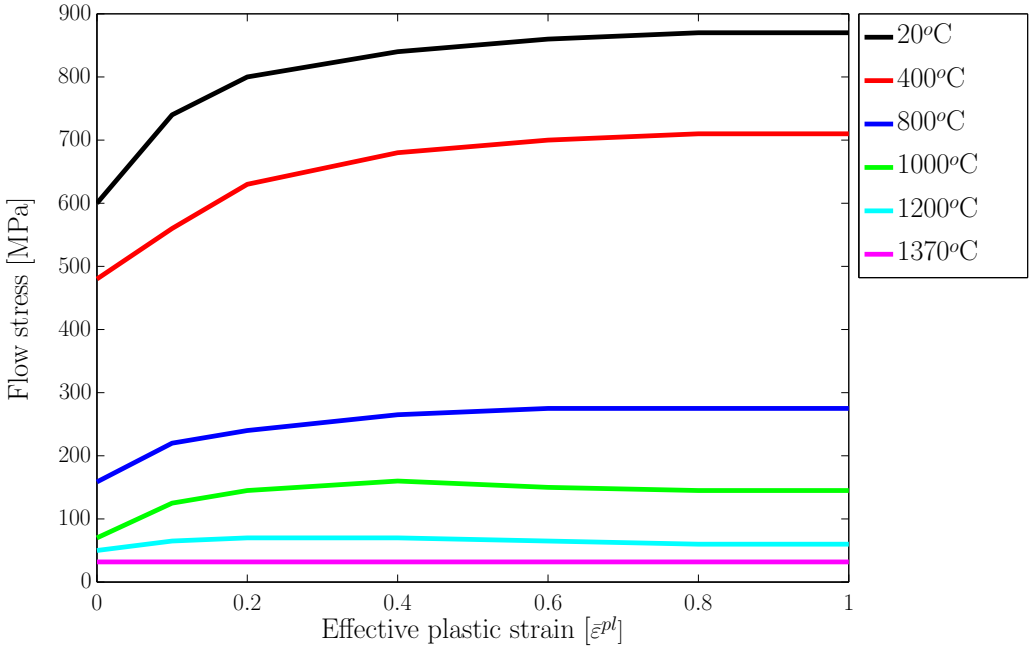

Fig. 3.7. Flow stress data for $\dot{\bar{\varepsilon}}^{pl} = 1.6/s$.

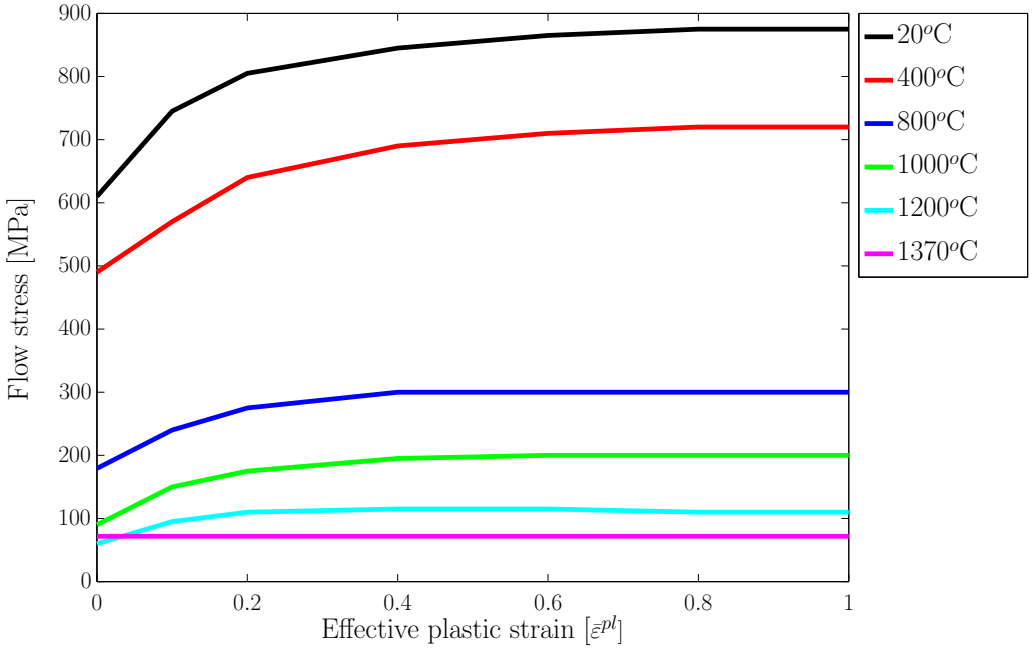

Fig. 3.8. Flow stress data for $\dot{\bar{\varepsilon}}^{pl} = 8.0/s$.

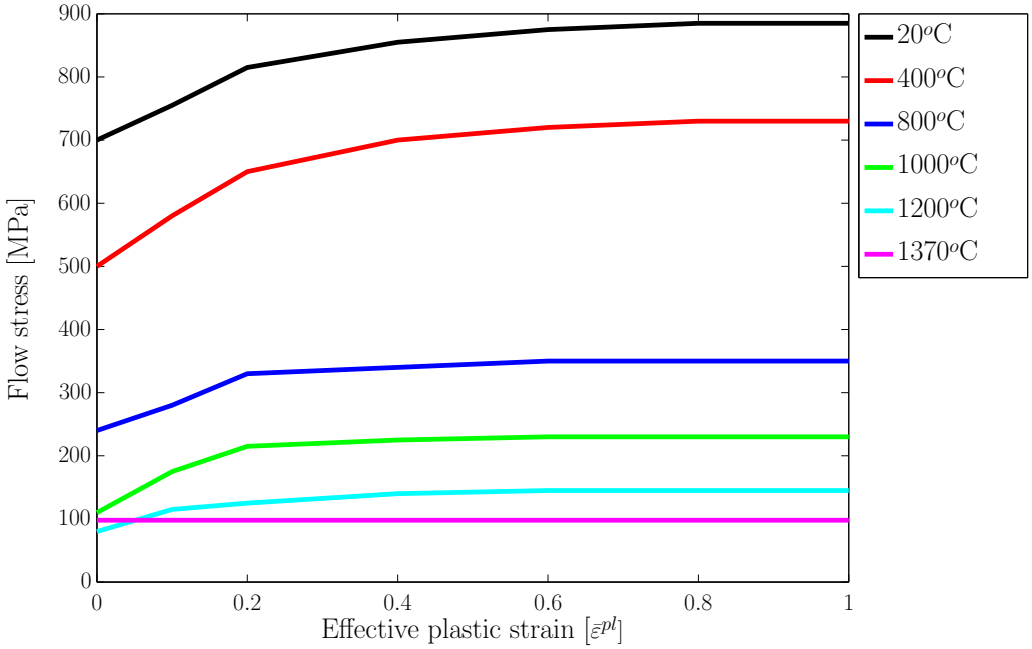

Fig. 3.9. Flow stress data for $\dot{\bar{\varepsilon}}^{pl} = 40.0/s$.

When comparing Fig. 3.7-Fig. 3.9 to Fig. 3.1a, reasonable agreement is seen. It therefore seems reasonable to apply the flow stress data from DEFORM® when performing simulations in DEFORM®. It is noticed that the flow stress data from DEFORM® does not decrease after some straining at elevated temperatures. This indicates that the tests have been performed isothermally.

3.5 Conclusion

A number of different hardening models have been presented. The models range from rather simple to more complex models. The advantage of simple models is their fairly ease of calibration based on experiments. However often these tests, such as uniaxial compression, have to be performed at experimental conditions similar to the ones experienced in the actual metal forming operation. For instance the flow stress behaviour of steel at 1200°C may be somewhat different than at 1000°C. Both temperatures may be encountered when forging large parts due to cooling on the outside of the part while the center region may experience constant temperature due to the heating by plastic work balancing the cooling to the surroundings. When also taking into account that metals experience strain rate dependent flow stress at high temperatures, the number of tests needed may increase rapidly. One solution to the problem is to perform tests at several temperatures and interpolate between data when performing numerical simulations. Another approach is to use a more advanced model taking into account more parameters. Many models of flow stress at high temperatures have been presented but are often limited to specific metals, temperature ranges or strain sizes.

4 Friction in metal forming

4.1 Introduction

A basic introduction to friction in metal forming is presented. The chapter introduces the basic concept of friction between bodies and some simple and commonly applied friction models. Some experimental findings regarding friction in hot forging are also presented.

4.2 Friction observed experimentally

A basic experiment illustrating friction is seen in Fig. 4.1.

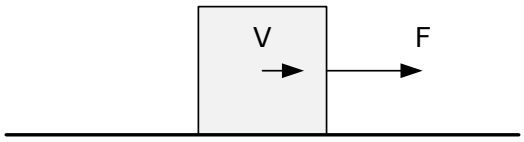

Fig. 4.1. Experimental observation of friction force.

In Fig. 4.1 a body is placed on a surface and it is noticed that a force F needs to be applied for maintaining the velocity V of the body. It is also observed that often a threshold force needs to be applied before any motion of the body occurs. This is called the static friction force. Often the static friction is disregarded in metal forming operations and this will also be the case in the present thesis.

Three early phenomenological observations (Amontons [3],Coulomb [24]) regarding friction forces are:

1. The friction force is directly proportional to the normal force between bodies (Amontons' first law).
2. The friction force is independent of the nominal area of contact between bodies (Amontons' second law).
3. The friction force is independent of sliding speed (Coulombs law).

4.3 Coulomb friction model

Amontons' first law have given rise to a friction model known as Coulomb friction:

$$F = \mu N \tag{4.1}$$

where F is the friction force, μ is the friction coefficient and N is the normal force.
If the nominal area of contact between the bodies is A_{nom}, Eq. 4.1 can be rewritten:

$$\begin{aligned} \frac{F}{A_{nom}} &= \mu \frac{N}{A_{nom}} \iff \\ \tau &= \mu \sigma_n \end{aligned} \tag{4.2}$$

where τ is the frictional shear stress and σ_n is the normal stress.
The friction coefficient μ may be dependent both on normal load, materials in contact and surface roughness according to Whitehead [106].

4.4 Constant friction model

The constant friction model, also known as the Tresca friction model, was proposed by Green [40]:

$$\tau = m_f k \tag{4.3}$$

where τ is the frictional shear stress, $0 \leq m_f \leq 1$ is the friction factor and k is the shear flow stress of the material with the lowest flow stress of the materials in contact. The limits of m_f indicate frictionless contact ($m_f = 0$) and full sticking ($m_f = 1$).

4.5 Applicability of the friction models

As an example of the two aforementioned friction models, an upsetting operation is used as illustration. Fig. 4.2 shows the analytically obtained friction shear stress τ when compressing a rigid-ideal plastic billet between rigid tools. v is the relative sliding velocity between billet and tools.

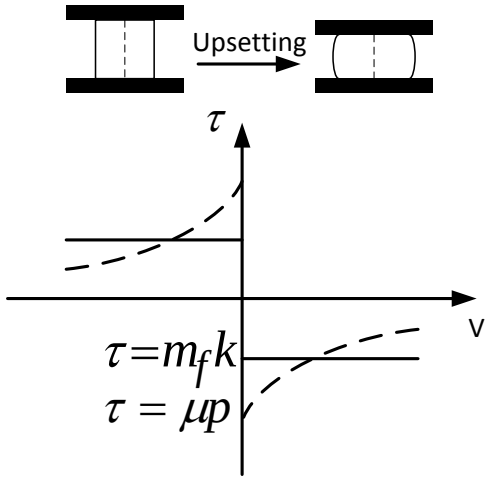

Fig. 4.2. Friction modelling in upsetting.

The centreline indicates the neutral plane. Due to Coulomb friction, an increasing normal stress between tool and billet is analytically predicted when moving from the

outer surface towards the centreline (for analytical solutions see for instance Wanheim et al. [104]). Therefore the frictional shear stress increases towards the centre when applying the Coulomb friction model. The constant friction model predicts the same numerical value of the friction shear stress across the entire surface where tool and billet are in contact. It was found in Bay & Gerved [11] that the normal pressure in upsetting does not increase monotonically towards the centreline but approaches a constant value. This illustrates that one should be careful about which friction model to apply.

It has however been found that the two aforementioned models are too simplistic for fully modelling frictional behaviour. In Bay & Gerved [11] it is in general recommended to apply Coulomb friction when $p/\sigma_o < 1.5$ and the constant friction model when $p/\sigma_o > 3$. More advanced friction models such as the Wanheim-Bay model (Wanheim et al. [102]) are not investigated in detail in the present work however a transition normal stress p^*/σ_o between Coulomb and the constant friction model is given in Zhang et al. [109]:

$$\frac{p^*}{\sigma_o} = \frac{1}{\sqrt{3}}\left(1 + \frac{\pi}{2} + arcos\left(m_f\right) + \sqrt{1 - m_f^2}\right) \tag{4.4}$$

Both Coulomb and the constant friction model are plotted in Fig. 4.3 with the transition between the models described by Eq. 4.4.

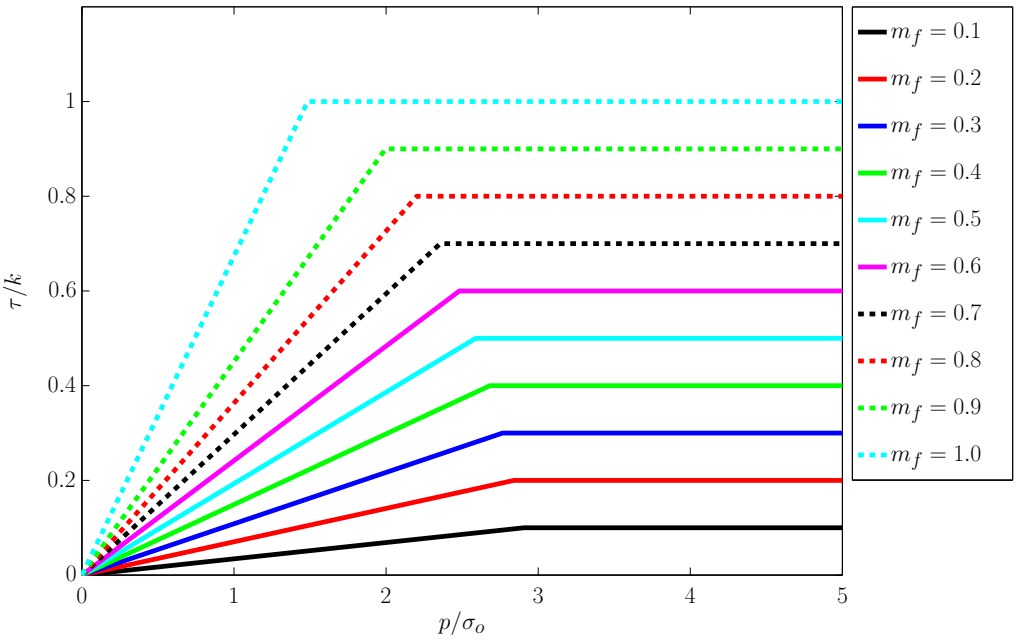

Fig. 4.3. Transition between Coulomb and constant friction model.

It can be seen from Fig. 4.3 that an increased friction factor m_f lowers the transition point p^*/σ_o, hence the constant friction model becomes applicable for a larger range of normal stresses when encountering high friction factors.

In order to avoid the abrupt change in friction in friction seen in Fig. 4.2 for $v = 0$ from $-\tau$ to τ, it is common in numerical codes to express the frictional stress as:

$$\tau* = A\tau \tag{4.5}$$

where $\tau*$ is the modified friction stress and A is an amplitude factor depending on the relative sliding velocity v:

$$A = \frac{2}{\pi} \arctan\left(\frac{\mid v \mid}{v_o}\right) \tag{4.6}$$

where $v_o \approx 1E-4$ is a small cut-off value. A plot of the constant friction model, with and without amplitude factor, is seen in Fig. 4.4.

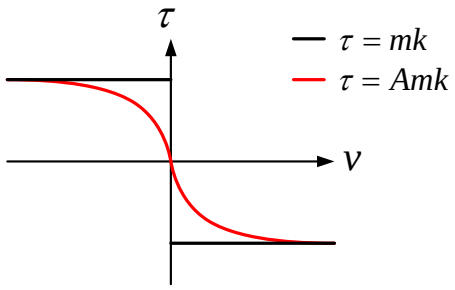

Fig. 4.4. Comparison of smooth and non-smooth transition of friction at $v = 0$.

Fig. 4.4 shows that the discontinuity in frictional stress is avoided by applying the amplitude A in the formulation for friction shear stress.

4.6 Friction in hot forging

Due to the high temperatures of the workpiece, traditional lubrication by oil is not possible. It is possible to apply lubricants such as graphite, but that is normally not done in ingot forging since lowering of friction is not an issue. Friction is in general quite high in hot forging, and the constant friction model is therefore most suitable to apply. Some suggested values of friction factors found in literature are:

Altan [1] p. 69 reports friction factors $0.7 < m_f < 1$ in hot forging of unlubricated steel.

Li et al. [67] did upsetting tests of cylindrical steel specimens at temperatures ranging from 1073°C to 1473°C and estimated the friction factor by inverse modelling of the barreling. Their results are seen in Fig. 4.5. Please notice that although it says friction coefficient in the figure, it is the friction factor m_f they are referring to, not the friction coefficient μ.

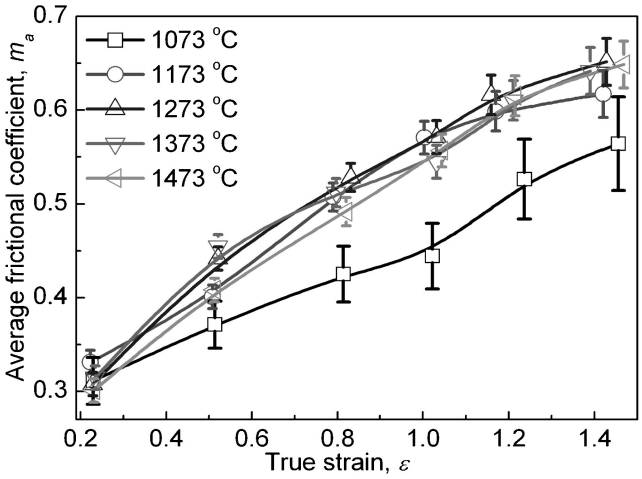

Fig. 4.5. Experimentally determined friction factors in hot forging. From Li et al. [67].

They found that the friction factor m_f is increasing with effective plastic strain. There is an increase in the size of the friction factor when increasing the temperature from 1073°C to 1173°C. Further increase of the temperature seems to have a minor influence on the size of the friction factor. It can be seen that the friction factor lies in the range $0.3 < m_f < 0.65$, depending on the effective strain.

4.7 Conclusion

Two commonly applied friction models have been presented. Based on theoretical analysis it is found that for hot forging, where friction can be considered to be large, the constant friction model is the most suitable of the two models presented.

Literature reports quite large friction factors to be present in hot forging of unlubricated steel.

5 Ingot forging - Process characteristics and theoretical analysis

5.1 Introduction

After casting the ingot, as described in Chapter 2, it is subsequently forged in order to obtain a shape closer to the final one, but the most important effect of the forging process is to minimize internal defects originating from the casting process. This defect minimization is described in Chapter 6. First, however, an introduction to the forging process, known as ingot forging, will be presented.

5.2 Ingot forging process

The ingot forging process is a process where a workpiece is placed between two dies and then compressed between them. A simple example of such a process is the upsetting operation seen in Fig. 5.1. A cylindrical workpiece, known as a billet, is placed between two dies. The lower die is stationary while the upper die is lowered in order to compress the billet. The dies are in literature sometimes labeled as anvils. This type of process is characterized as an upsetting operation.

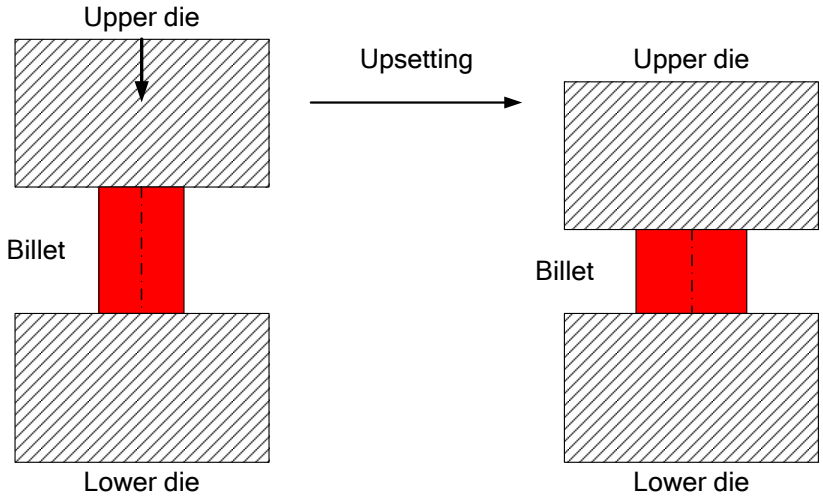

Fig. 5.1. Upsetting of cylindrical billet.

A more advanced open die forging operation is the forming of an ingot into a cylindrical shape, for instance a shaft. The process of forging an ingot into a shaft can be seen in

Fig. 5.2. The preheated ingot is placed between the dies, and the upper die is then lowered to compress the ingot. Thereafter the upper die is raised again, the ingot is rotated some angle around its centerline, and the upper die is lowered again. By continuing this process, the ingot is plastically deformed while maintaining a cylindrical shape, which can later be turned into the final shape on a lathe.

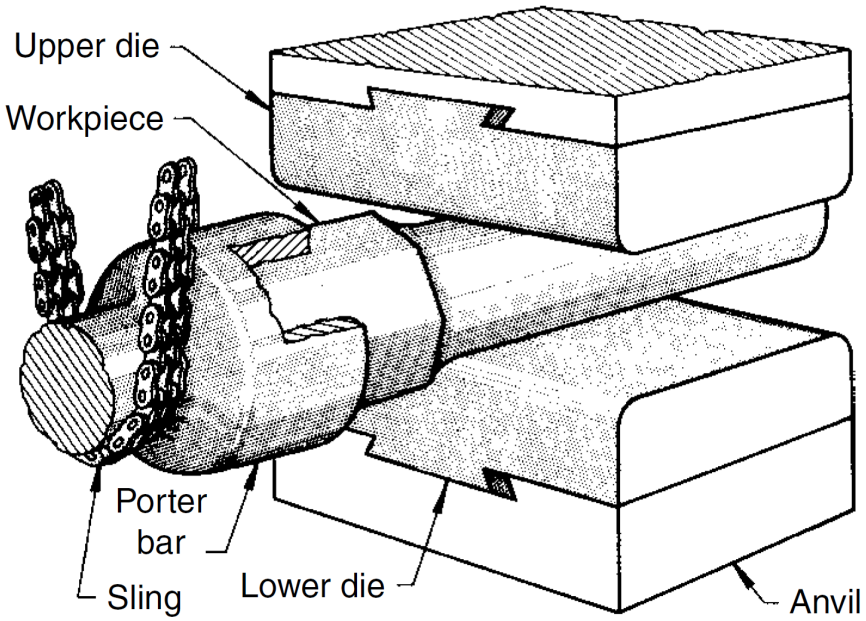

Fig. 5.2. Open die forging of an ingot into a cylinder. From Semiatin [88] p. 101.

An example from industry can be seen in Fig. 5.3. Here a shaft is produced by the Czech company Vitkovice Heavy Machinery a.s.

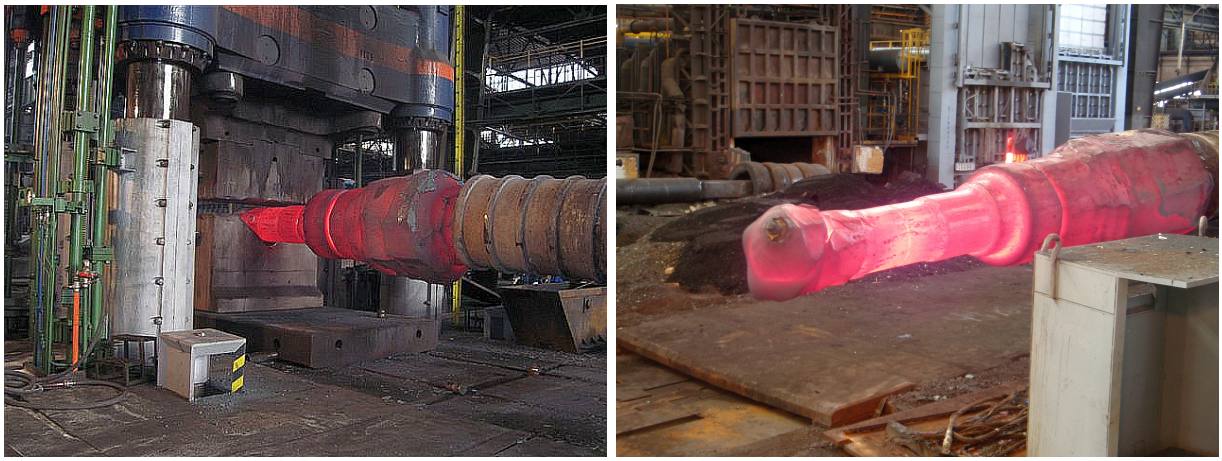

(a) Open die forging of a shaft. **(b)** One end of the ingot formed into a shaft.

Fig. 5.3. Ingot forging of shaft. Pictures are from Vitkovice Heavy Machinery a.s.

As it can be seen from Fig. 5.3, the ingots and shafts can be fairly large. It is possible to produce more than one shaft from an ingot. In this particular case, four shafts where made from one ingot. The ingot was preheated to 1200°C before the forging operation

was started. The ingot forging process is typically a fairly slow process. The handling of both the ingot and the press can be manually controlled or automatized by computer control.

5.3 Upper bound analysis of ingot forging

In order to obtain some knowledge regarding material flow in ingot forging, upper bound analysis may be applied. An upper bound field an a hodograph may be seen in Fig. 5.4.

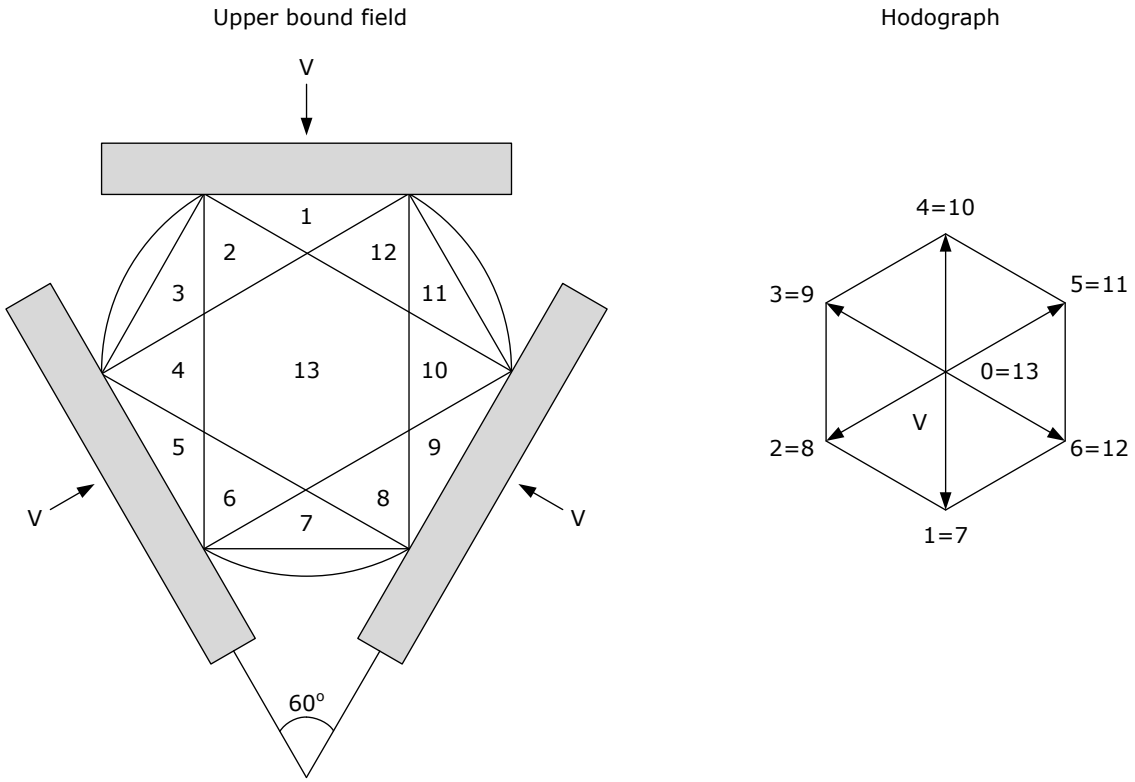

Fig. 5.4. Upper bound analysis of ingot forging. Figure adopted from Gouveia et al. [37] p. 244.

The upper bound analysis presented is a simplification of a real forging process. It is assumed that all the dies are moving towards the center of the ingot with the velocity V. This results in the formation of a dead zone numbered 13 in Fig. 5.4 in the center of the ingot. Therefore such a die layout is not suited for closure of centreline defects.

5.4 Characterization of the open die forging process by the deformation zone geometry parameter

An important parameter in ingot forging, according to Hosford & Caddell [49] p. 167, is the size of the deformation zone geometry. This is best illustrated in the forging process of a rectangular bar seen in Fig. 5.5. The forging process of compressing a bar locally between two dies is also known as a cogging operation. The deformation zone geometry is

described by the ratio of the height H of the workpiece and the contact length L between dies and workpiece.

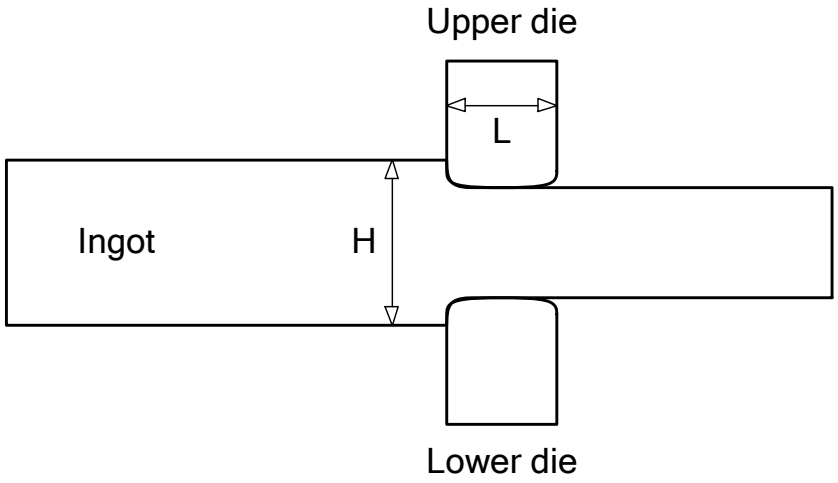

Fig. 5.5. Cogging operation.

In Fig. 5.5, two dies of width L are compressing a rectangular ingot with height H. The ratio H/L is used to characterize the deformation zone geometry and is labeled Δ:

$$\Delta = \frac{H}{L} \tag{5.1}$$

If the deformation zone geometry parameter Δ has a low value, the deformation is characterized by being fairly homogeneous. On the other hand a large deformation zone geometry gives rise to inhomogeneous deformation. This can be seen in Fig. 5.6, which shows the slipline field for a cogging operation depending on Δ.

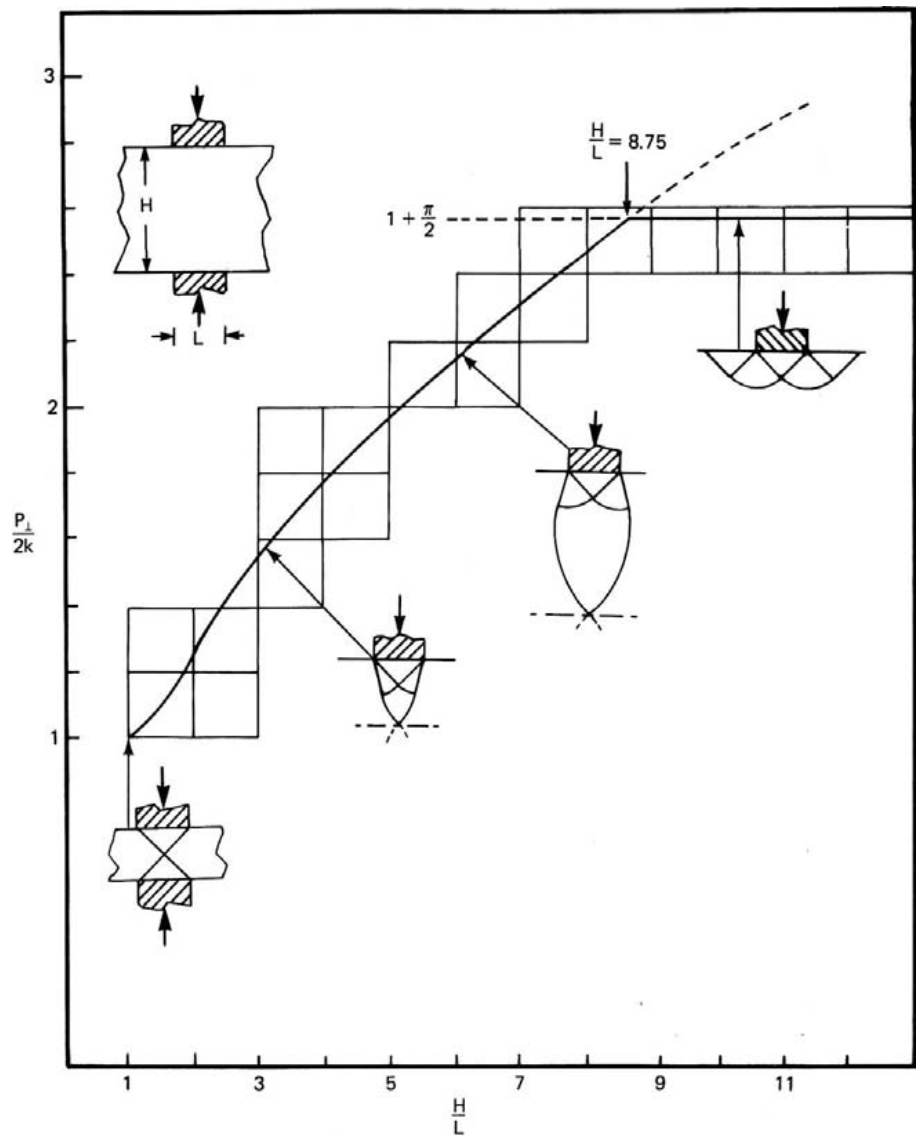

Fig. 5.6. Slipline field in cogging operation depending on deformation zone geometry parameter $\Delta = \dfrac{H}{L}$. From Hill [46] p. 257.

From Fig. 5.6 it is seen that the deformation pattern changes from a cross formed deformation field to an indentation-like field when increasing Δ. As Δ increases, the deformation becomes more inhomogeneous resulting in increased internal damage. To ensure sound forgings Δ should be kept as small as possible. Therefore large dies should be used compared to the size of the workpiece. The size of Δ is however, downwards limited by the required forging force and size of dies practical to handle.

5.5 Slipline analysis of deformation zone

For a more clear understanding of the indentation process, a slipline analysis is conducted. The nomenclature and method follows the description in Hosford & Caddell [49] chapter 10, which the reader should consult for a full review of the slipline method.

First a general slipline field for plane strain frictionless indentation is drawn and can be seen in Fig. 5.7.

m, n	$\Delta\phi$	y	x
0, 0	0	1.0	0
0, 1	$\frac{\pi}{12}$	1.225	0.2930
0, 2	$\frac{\pi}{6}$	1.366	0.6380
0, 3	$\frac{\pi}{4}$	1.414	1.000
0, 4	$\frac{\pi}{3}$	1.366	1.366
0, 5	$\frac{5\pi}{12}$	1.225	1.7071
0, 6	$\frac{\pi}{2}$	1.000	2.000
1, 1	0	1.605	0
1, 2	$\frac{\pi}{12}$	1.915	0.404
1, 3	$\frac{\pi}{6}$	2.120	0.904
1, 4	$\frac{\pi}{4}$	2.195	1.471
1, 5	$\frac{\pi}{3}$	2.116	2.070
1, 6	$\frac{5\pi}{12}$	1.873	2.659
2, 2	0	2.440	0
2, 3	$\frac{\pi}{12}$	2.885	0.584
2, 4	$\frac{\pi}{6}$	3.195	1.335
2, 5	$\frac{\pi}{4}$	3.311	2.222
2, 6	$\frac{\pi}{3}$	3.185	3.190
3, 3	0	3.640	0
3, 4	$\frac{\pi}{12}$	4.306	0.870
3, 5	$\frac{\pi}{6}$	4.780	2.021
3, 6	$\frac{\pi}{4}$	4.965	3.414
4, 4	0	5.43	0
4, 5	$\frac{\pi}{12}$	6.45	1.325
4, 6	$\frac{\pi}{6}$	7.18	3.118
5, 5	0	8.16	0
5, 6	$\frac{\pi}{12}$	9.73	2.055
6, 6	0	12.37	0

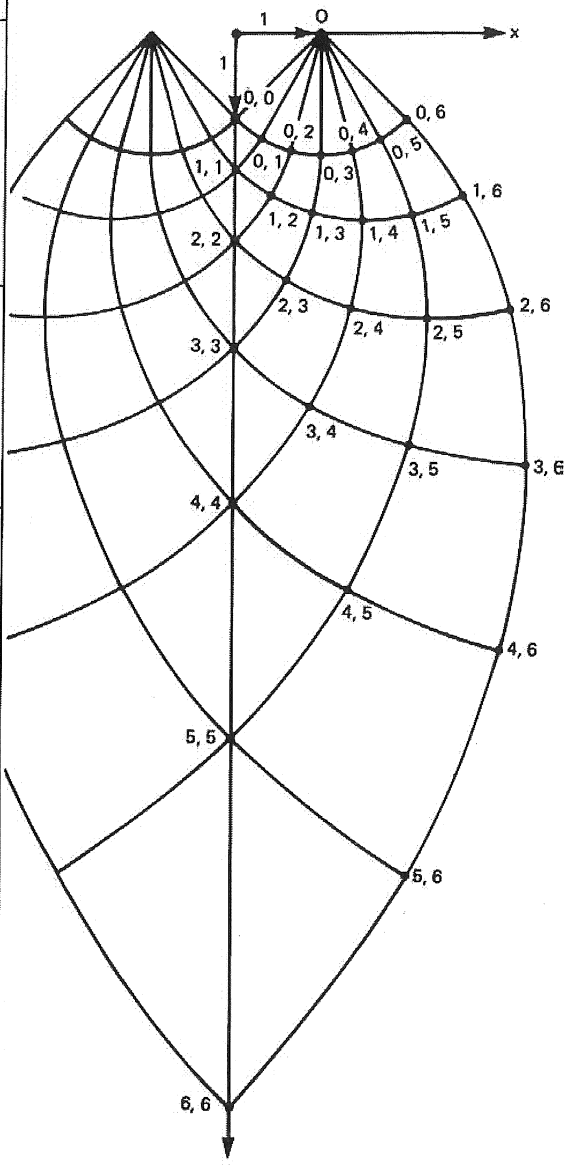

Fig. 5.7. Slipline field for plane strain frictionless indentation. From Hill [46] p. 156.

The slipline field, seen in Fig. 5.7, has a deformation zone geometry parameter $\Delta = 12.37$. In reality, this field has a too large Δ value to have physical meaning. This is seen in Fig. 5.6, where the slipline field changes for $\Delta > 8.75$. However, the slipline field is still illustrative for some basic problems, which are encountered when Δ increases.

By using the slipline field, it is possible to calculate stresses and mean pressures in the deformation zone. This is done by first calculating the mean stress σ_m, which is also the second principal stress σ_2. The mean stress is calculated using the right angle triangle $\Delta OO'(0,0)$, see Fig. 5.8, which originates from the top of the slipline field. The triangle is located just underneath of the indenter in Fig. 5.7.

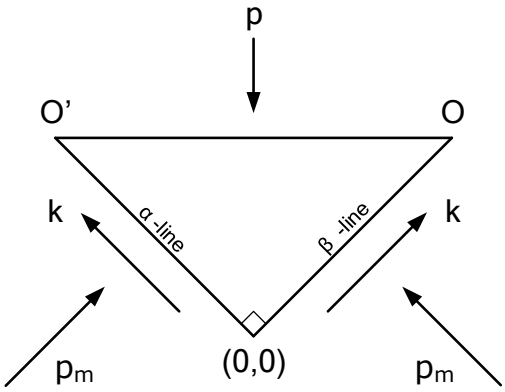

Fig. 5.8. Triangle from slipline field.

The hypotenuse of the triangle is loaded by the indentation pressure p. The two cathers are loaded by the shear flow stress k and normal stress p_m, which is the mean pressure. The indentation pressure p is the most compressive of the stresses. It therefore follows that the left cather is an α-line and the right catheter is a β-line. The mean pressure p_m in point (0,0) can be expressed using p and k by vertical force equilibrium of the triangle:

$$\begin{array}{rcll} 2p & = & 2\left(p_m + k\right) 2\dfrac{\sqrt{2}}{2}\dfrac{\sqrt{2}}{2} & \Leftrightarrow \\ p & = & p_m + k & \Leftrightarrow \\ p_m & = & p - k & \end{array} \tag{5.2}$$

The change in mean pressure along an α-line can be calculated by:

$$\Delta p_m = -2k\Delta\phi \tag{5.3}$$

where k is the shear flow stress and $\Delta\phi$ is the angle of rotation along the slipline. In Fig. 5.7 there is used an angle of 15° $\left(\dfrac{\pi}{12}\right)$ between each set of α- and β-lines. As an example of calculating the mean pressure along an α-line, the hydrostatic stress in point (0,1) is found:

$$\begin{aligned} p_m\left(0,1\right) =& p_m\left(0,0\right) + \Delta p_m \\ =& p - k - 2k\Delta\phi \\ =& p - k - 2k\frac{\pi}{12} \\ =& p - k - \frac{\pi}{6}k \end{aligned} \tag{5.4}$$

In the same manner the other mean pressures along the first α-line are found, and they are listed in Table 5.1:

Table 5.1. Mean pressure p_m along the first α-line.

Point	$\Delta\phi$	p_m
$(0,0)$	0	$p-k$
$(0,1)$	$\frac{\pi}{12}$	$p-k-\frac{\pi}{6}k$
$(0,2)$	$\frac{\pi}{6}$	$p-k-\frac{\pi}{3}k$
$(0,3)$	$\frac{\pi}{4}$	$p-k-\frac{\pi}{2}k$
$(0,4)$	$\frac{\pi}{3}$	$p-k-\frac{2\pi}{3}k$
$(0,5)$	$\frac{5\pi}{12}$	$p-k-\frac{5\pi}{6}k$
$(0,6)$	$\frac{\pi}{2}$	$p-k-\pi k$

The found mean pressures along the first α-line can then be used to find the mean pressures along the center of the slipline field. This is done by calculating the pressure change when moving along the β-lines from the α-line towards the center of the slipline field. The change in mean pressure along a β-line is given by:

$$\Delta p_m = 2k\Delta\phi \tag{5.5}$$

where k is the shear flow stress and $\Delta\phi$ is the angle of rotation along the slipline. As an example of calculating the mean stress along a β-line, the mean pressure in point (1,1) is found:

$$\begin{aligned} p_m(1,1) &= p_m(0,1) + 2k\Delta\phi \\ &= p-k+\tfrac{\pi}{6}k - 2k\tfrac{\pi}{12} \\ &= p-k+\tfrac{\pi}{6}k - \tfrac{\pi}{6}k \\ &= p-k-\tfrac{\pi}{3}k \end{aligned} \tag{5.6}$$

The other mean pressures along the center of the slipline field are found by the same procedure, and they are listed in Table 5.2:

Table 5.2. Mean pressure p_m along the center of the slipline field.

Point	$\Delta\phi$	p_m
$(0,0)$	0	$p-k$
$(1,1)$	$\frac{\pi}{12}$	$p-k-\frac{\pi}{3}k$
$(2,2)$	$\frac{\pi}{6}$	$p-k-\frac{2\pi}{3}k$
$(3,3)$	$\frac{\pi}{4}$	$p-k-\pi k$
$(4,4)$	$\frac{\pi}{3}$	$p-k-\frac{4\pi}{3}k$
$(5,5)$	$\frac{5\pi}{12}$	$p-k-\frac{5\pi}{3}k$
$(6,6)$	$\frac{\pi}{2}$	$p-k-2\pi k$

The indentation pressure p is given by:

$$p = 2k + \frac{4k}{H}\int_0^{H/2} 2\Delta\phi dy \tag{5.7}$$

where k is the shear flow stress, H is the thickness of the workpiece, $\Delta\phi$ is the angle of rotation along the slipline and dy is the incremental change of depth along the centerline of the slipline field. $y = 0$ at the top of the slipline field and $y = H/2$ at the centerline of the workpiece.

Eq. 5.7 is evaluated numerically using the trapezoidal rule, see Eldén et al. [29] p. 166:

$$\begin{aligned} p =& 2k + \frac{4k}{H}\int_0^{H/2} 2\Delta\phi dy \\ =& 2k + \frac{4k}{H}\frac{1}{2}\sum_{i=1}^{N} 2\left(\Delta\phi_{i+1} + \Delta\phi_i\right)\left(y_{i+1} - y_i\right) + R_T \\ =& 2k + \frac{4k}{H}\sum_{i=1}^{N}\left(\Delta\phi_{i+1} + \Delta\phi_i\right)\left(y_{i+1} - y_i\right) + R_T \end{aligned} \tag{5.8}$$

where N takes the value 7 for this particular field. R_T is the truncation error. As an example, the indentation pressure is calculated for the slipline field seen in Fig. 5.7:

$$\begin{aligned} p \;\approx\; & 2k + \frac{4k}{2 \cdot 12.37}[\left(\frac{\pi}{12} + 0\right)(1.605 - 1.0) \\ & + \left(\frac{\pi}{6} + \frac{\pi}{12}\right)(2.440 - 1.605) \\ & + \left(\frac{\pi}{4} + \frac{\pi}{6}\right)(3.640 - 2.440) \\ & + \left(\frac{\pi}{3} + \frac{\pi}{4}\right)(5.43 - 3.640) \\ & + \left(\frac{5\pi}{12} + \frac{\pi}{3}\right)(8.16 - 5.43) \\ & + \left(\frac{\pi}{2} + \frac{5\pi}{12}\right)(12.37 - 8.16)] \Leftrightarrow \\ p \;\approx\; & 5.92k \end{aligned} \tag{5.9}$$

By inserting the calculated indentation pressure into Table 5.2, it is possible to plot the mean stress $\sigma_2 = -\sigma_m$ along the centerline of the slipline system as can be seen in Fig. 5.9.

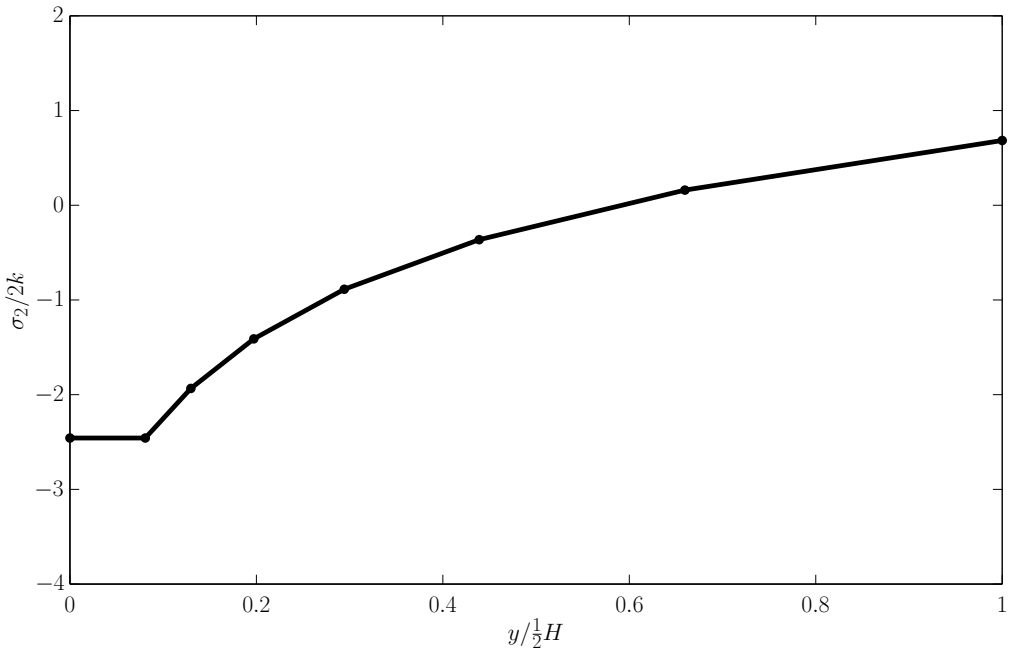

Fig. 5.9. Mean pressure along the centerline of the slipline system.

In Fig. 5.9 it should be noticed that both axes are normalized. The horizontal axis is used for the vertical distance y. It is normalized with the half workpiece thickness H/2. It takes the value 0 at the top of the slipline field, where there is contact between the die and the workpiece. It takes the value 1 at the center of the workpiece (point (6,6) in Fig. 5.7). The vertical axis is normalized with 2k, which is the flow stress according to Tresca's yield criterion.

When having calculated the mean stress $\sigma_2 = -\sigma_m$, it is possible to calculate the other two principal stresses σ_1 and σ_3 by Eq. 5.10 and Eq. 5.11:

$$\sigma_1 = \sigma_2 + k \tag{5.10}$$

$$\sigma_3 = \sigma_2 - k \tag{5.11}$$

Since the centerline of the slipline field is a symmetry line, it follows that the α- and β-lines intersect the centerline at 45° angles to the symmetry line. Since the α- and β-lines are lines of maximum shear stress, the principal stresses are therefore oriented with 45° degree angles to the sliplines. It therefore follows that at the centerline of the slipline field, σ_1 is parallel with the x-axis and σ_3 is parallel with the y-axis.

The two principal stresses can be seen in Fig. 5.10 and Fig. 5.11.

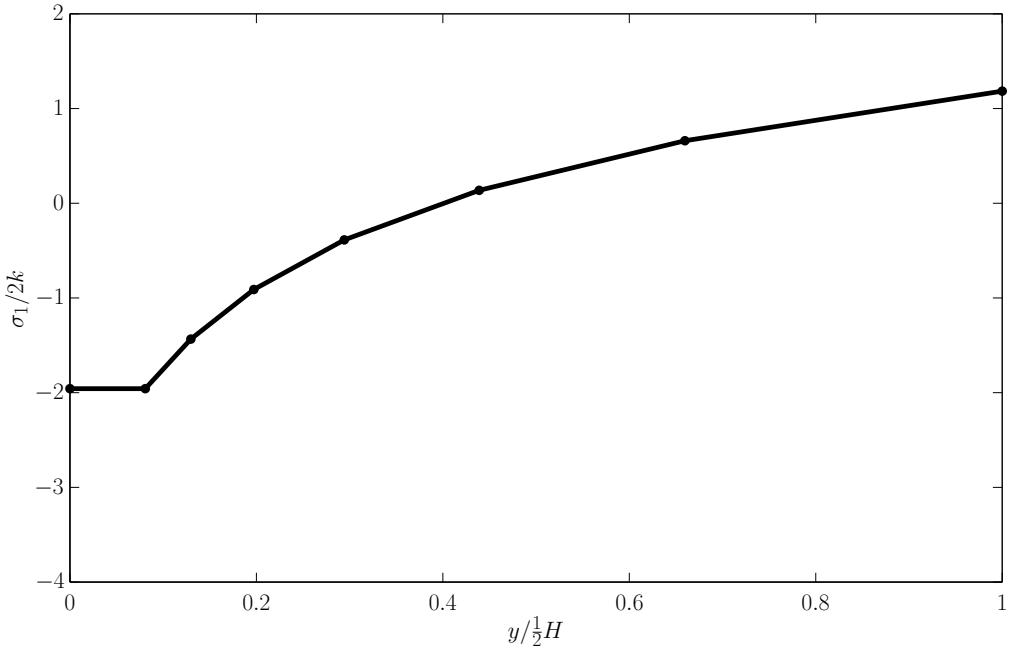

Fig. 5.10. Principal stress σ_1.

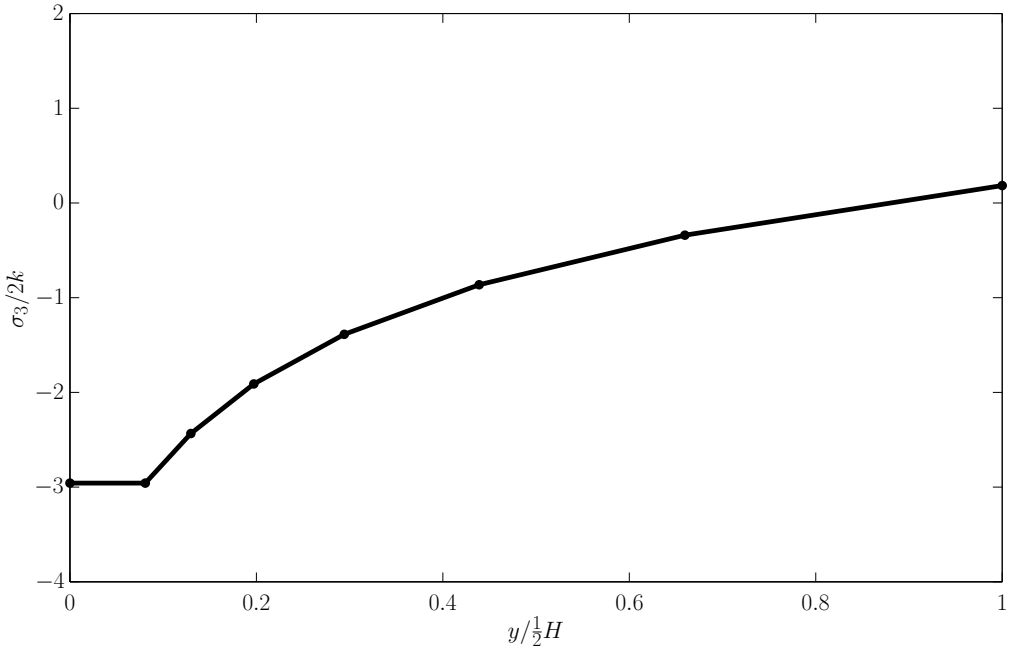

Fig. 5.11. Principal stress σ_3

Some interesting information can be deducted from Fig. 5.9, Fig. 5.10 and Fig. 5.11. The mean stress is mainly compressive, but at a distance approximately $0.6\dfrac{y}{H/2}$ to the centerline of the workpiece, it becomes tensile. The principal stress σ_1 is compressive close to the indentation die, but becomes tensile at a distance of approximately $0.4\dfrac{y}{H/2}$ into the workpiece. The principal stress σ_3 is mainly compressive, however it too becomes

tensile close to the centerline of the workpiece. With relation to defects it is especially unwanted to have tensile stresses in the center of the ingot since the center is the natural location for a number of defects, see Chapter 2 The stress situation therefore makes it likely that the defects could evolve and become more severe due to the stresses being tensile.

A control of the calculations can be conducted by integrating the principal stress σ_1 along the y-direction. Due to force equilibrium, the net force should be zero. The integration was conducted using the trapezoidal method an yielded $F_x = -5.33E - 15$, where F_x is the net horizontal force. Therefore the calculations seem to be correct.

5.6 Conclusion

The slipline analysis qualitatively explains the importance of die geometry when performing open die forging of ingots. It is seen that wide dies compared to the ingot are advantageous for ensuring compressive stresses and thereby preventing centreline porosities from expanding.

6 Ingot forging - Defects minimization by hot forging

6.1 Introduction

A number of defects occurring during casting were presented in Chapter 2. In this chapter it is described how hot forging may be able to reduce the effect of the defects and thereby ensuring a sound final part. Recommendations from both practical and theoretical experience are included.

6.2 Porosity closure by ingot forging

6.2.1 Experimental findings regarding porosity closure

Experimental work available in the literature regarding cast ingots being cut open (sectioned) for actual verification of defects sizes and distributions are rare. This is due to the high costs of producing an ingot. The steel plants always forge the cast ingots and producing a large number of full size ingots for research purposes is beyond the research budget for most steel plants. Occasionally an ingot is sectioned and the results made available for publication. One such is found in Wang et al. [101]. A 100-ton steel ingot made of 30Cr2Ni4MoV was cast and then sectioned. The ingot can be seen in Fig. 6.1.

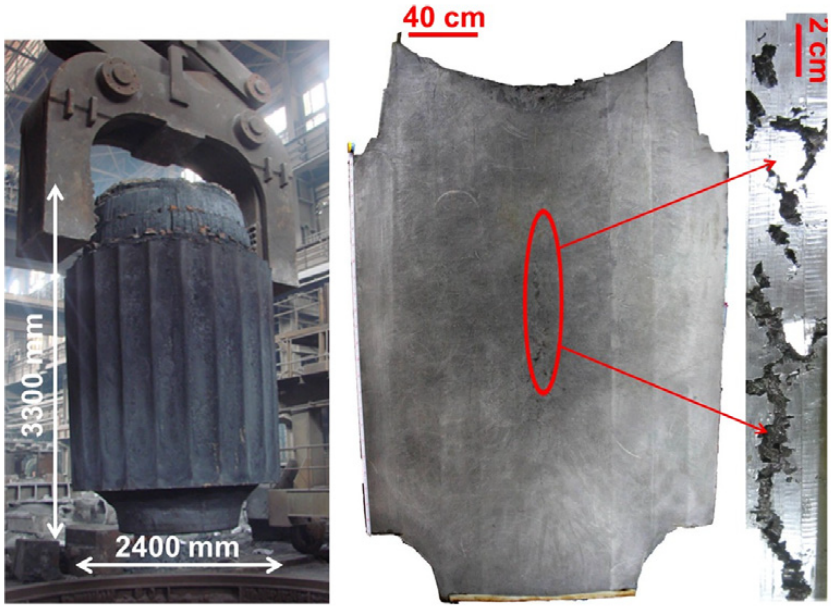

Fig. 6.1. Cast ingot and cross-section with centreline porosities. From Wang et al. [101].

The ingot is used for producing a low pressure rotor for a nuclear power plant. The casting was performed by usual procedure and is therefore known to be able to be subsequently forged to acceptable quality. It therefore follows that a centreline porosity region having a size of approximately $4mm/41mm \approx 10\%$ of the ingot diameter can be hot forged to an acceptable quality. The measures originate by measuring the porous zone using a ruler on the picture showing the sectioned ingot. It is also seen that the real porosity size is in the order of centimeters.

6.2.2 Upper bound analysis of porosity closure

Since cast ingots contain porosities, a natural advance from normal upper bound analysis was to introduce upper bound analysis for forging porous solids. Such a study is found in Melander & Ståhlberg [71] and in Ståhlberg et al. [94] where compression of a block containing either regularly or randomly distributed square or circular porosities is analyzed using upper bound analysis. The analysis was compared with compression of plasticine blocks with cut out porosities. Reasonable agreement between theory and measurements was found. By applying the analysis, it was possible to derive the degree of reduction necessary for closure of a given initial porosity fraction. The findings are seen in Fig. 6.2.

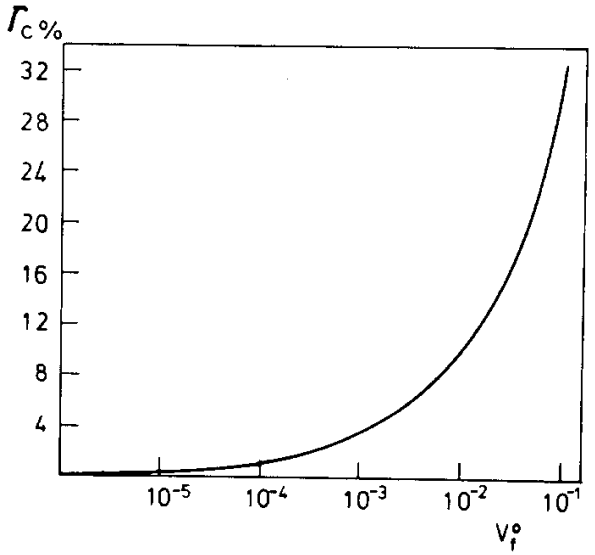

Fig. 6.2. Reduction necessary for closure of a given initial porosity fraction. From Melander & Ståhlberg [71].

From Fig. 6.2 it is seen that a substantial increase in the predicted reduction needed for porosity closure occurs when increasing the initial porosity density. The model predicts closure of even severely porous ingots by applying a reduction of approximately 30%.

Although giving valuable new insight into the prediction of porosity closure in ingot forging, the upper bound analysis suffers from assuming plane strain deformation and by only being able to apply simple die geometries.

6.2.3 FEM-analysis of porosity closure in ingot forging

With the emergence of more powerful computers, numerical analysis was used for supplementing upper bound and slipline analysis.

A study applying several different porous plasticity models (see 7.2.1) is found in Zhang et al. [110]. Here a unit volume cell is compressed. Using different porous plasticity models and also a representative volume element model, they try to estimate the effective strain necessary to close initial porosities. The applied models are the Gurson model (Gurson [42]), the Gurson-Tvergaard-Needleman model (Tvergaard [98]), the Budiansky-Hutschinson-Slutsky model (Budiansky et al. [14]), the Lee-Mear model (Lee & Mear [65]), a FE-model of deforming a representative volume element and finally the authors of the article's (Zhang et al. [110]) own model. The FE-model consists of a cube 20mm by 20mm by 20mm containing a spherical porosity in the center of the cube having radius 1mm, thus giving an initial porosity density of 0.017%, hence a very dilute porosity concentration.

Some of their findings can be seen in Fig. 6.3.

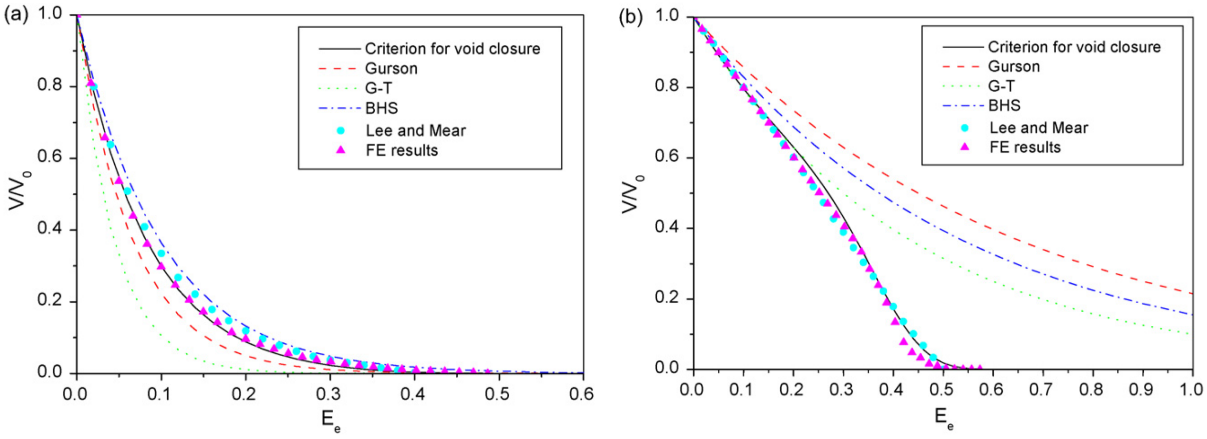

(a) $\frac{\sigma_m}{\bar{\sigma}} = -2.0$ **(b)** $\frac{\sigma_m}{\bar{\sigma}} = -0.6$

Fig. 6.3. Porosity closure as a function of effective strain for different porous plasticity models and two different values of mean stress. From Zhang et al. [110].

In Fig. 6.3 the evolution in porosity content of a solid is evaluated for increasing effective strain under different mean stress levels ($\frac{\sigma_m}{\bar{\sigma}}$) predicted by different porous plasticity models. It is seen that all models predict some closure of porosities for hydrostatic compression and that the closure increases with increasing straining. For large compressive stress states, there are small differences in the predicted closure. However for more moderatly compressive stress states, larger differences in predicted porosity closure between the applied models are seen. It can be seen that an effective strain of approximately 0.5 can be viewed as a minimum requirement for full closure of the initial porosities.

6.3 Minimization of segregations

As mentioned in Section 2.6, segregations are differences in chemical composition through the casting. The only way to even out the differences in chemical composition is through a homogenization heat treatment. Hereby the differences in chemical composition is leveled out through diffusion of alloying elements from volumes of high concentration to volumes of low concentration. This is feasible for the microsegregation, since the diffusion path is fairly small. However for a full homogenization of a large casting containing macrosegregations, a very long heat treatment time would be needed. Therefore this solution is not

feasible even when the casting is heated substantially in hot forging as described in Chapter 1. A rough estimate for the homogenization time is given in ASM Handbook Vol. 4 [7] p. 1847:

$$x^2 \approx Dt \tag{6.1}$$

where x is the distance between regions of high and low alloying content, t is time and D is the diffusion coefficient. For a plain carbon steel, the diffusion coefficient D can, in the high temperature range according to Tibbetts [97], be approximated by the empirical expression:

$$D \approx 0.47 cm^2/s \cdot exp\left(-1.6 \cdot C - \frac{37000\frac{cal}{mol} - 6600\frac{cal}{mol} \cdot C}{RT}\right) \tag{6.2}$$

where D is the diffusion coefficient with unit$[cm^2/s]$, C is the weight percent of carbon, R is the gas constant with unit $[\frac{cal}{mol \cdot K}]$ and T is the temperature in Kelvin. For a steel containing 0.42% carbon at a temperature of 1473K (1200°C) one obtains the following diffusion coefficient:

$$D \approx 0.47 cm^2/s \cdot exp\left(-1.6 \cdot 0.42 - \frac{37000\frac{cal}{mol} - 6600\frac{cal}{mol} \cdot 0.42}{1.986\frac{cal}{mol \cdot K} \cdot 1473K}\right) \approx 2.0 \cdot 10^{-6} cm^2/s \tag{6.3}$$

Inserting the diffusion coefficient in Eq. 6.1 one can draw a graph showing the homogenization time as function of distance between regions of low and high alloying content, see Fig. 6.4.

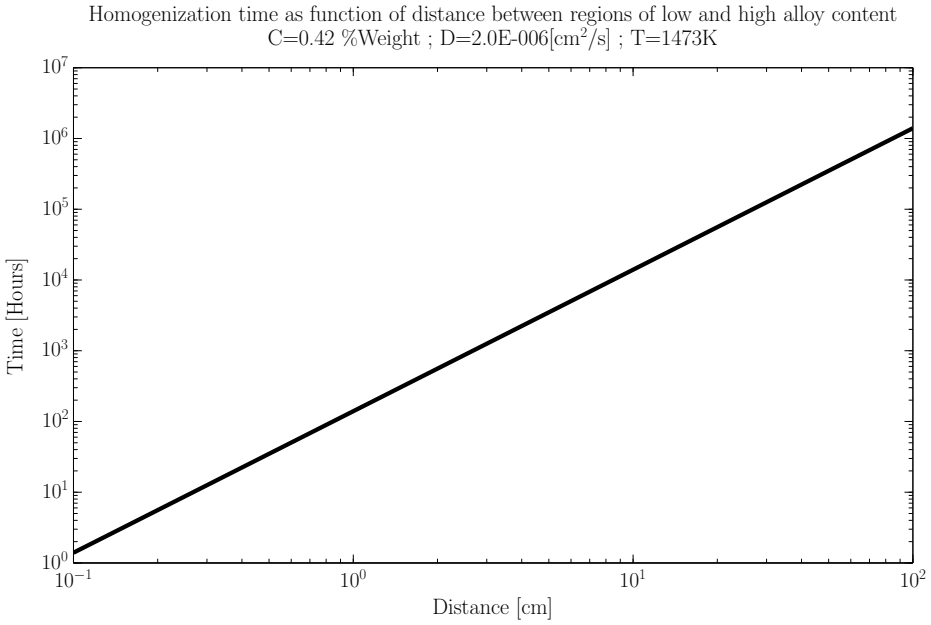

Fig. 6.4. Homogenization time as a function of distance between regions of low and high alloy content.

From Fig. 6.4 it is clear that full homogenization for large cast parts are not feasible within an acceptable process time. However a forging or rolling operation, which reduces the size of the casting, can substantially reduce the time for homogenization. This can be explained using Fig. 6.5. The figure shows a macrosegregated casting. It is subjected to some plastic deformation whereby its dimension in the direction of the segregation pattern (y-direction) is reduced to half height, and at the same time the casting is also elongated, see Fig. 6.5.

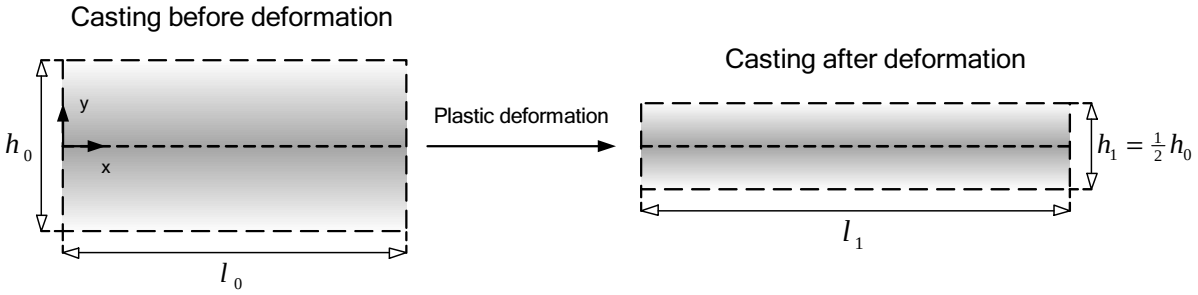

Fig. 6.5. Reducing homogenization time of macrosegregations due to deformation.

From Eq. 6.1 it is seen that the homogenization time in this case is reduced by 75%. The induced plastic deformation can thereby directly be used to reduce macrosegregations by reducing the homogenization time. However it requires that the casting is reduced in the direction of the segregation pattern (y-direction in Fig. 6.5). If the reduction is applied in the x-direction of the casting seen in Fig. 6.5, it increases the distance between the regions of minimum and maximum alloying content, and hereby the homogenization time is increased according to Eq. 6.1. Generally, as recommended in ASM Handbook Vol. 14 [5] p. 103-105, the only feasible way of minimizing macrosegregations in cast parts is by substantial hot forging. However if heavy cross sections of the final part are needed, macrosegregation can not be minimized by this method.

6.4 Slag inclusions

Like segregations, slag inclusions are also formed during the casting process. However they can not be dissolved by a heat treatment, but some slag inclusions may be positively affected by plastic deformation. Fredriksson & Åkerlind [34] list three different cases depending on the properties of the slag:

1. The slag particles are harder and stronger than the surrounding matrix material.

The slag particles will not be affected by plastic deformation since they can just deform the surrounding material when subjected to external forces. The principle can be seen in Fig. 6.6.

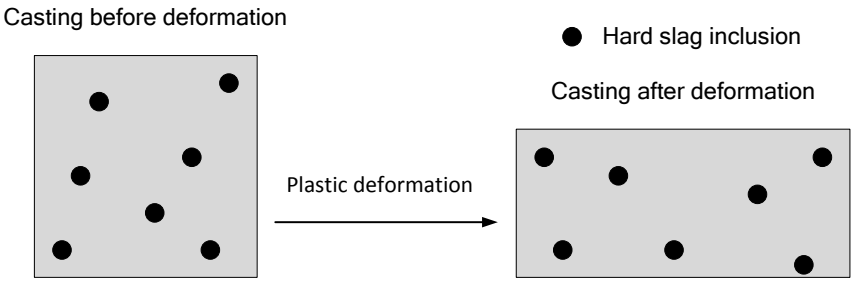

Fig. 6.6. Casting with hard slag inclusions subjected to plastic deformation.

2. The slag particles are softer than the surrounding matrix material. When subjecting the casting to plastic deformation, the slag particles will be compressed in the direction of the applied deformation and become elongated due to the applied deformation. This deformation pattern is seen in Fig. 6.7.

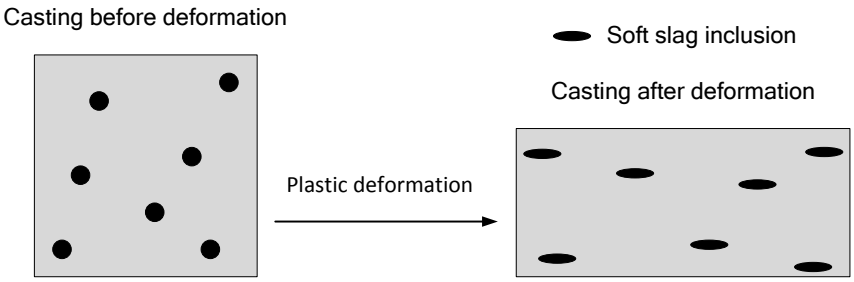

Fig. 6.7. Casting with soft slag inclusions subjected to plastic deformation.

3. The slag particles are brittle. When brittle slag particles are deformed plastically, they break into smaller pieces and the smaller pieces are distributed in the elongation direction parallel to the deformation direction. The situation can be seen in Fig. 6.8.

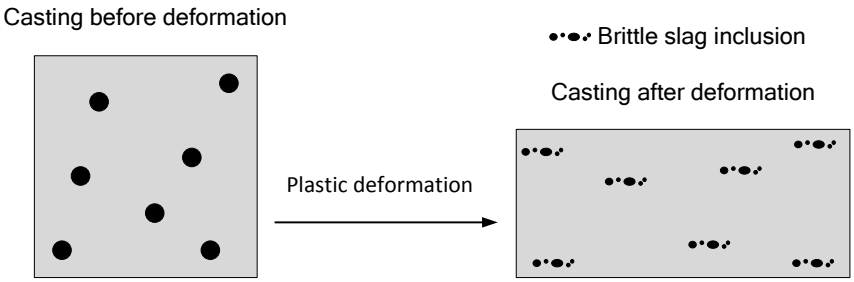

Fig. 6.8. Casting with brittle slag inclusions subjected to plastic deformation.

As it is seen, whether or not defects due to slag inclusions are suppressed or not, depends to a large extent on the properties of the slag itself. The slag particle properties are mainly influenced by the casting process and the slag forming elements added to the melt before casting.

6.5 Coarse grain structure

As mentioned in Section 2.5, large cast parts usually contain relatively coarse grain structure. The coarse grain structure, originating from the casting process, can be converted to a finer structure by hot deformation of the part. This was found experimentally in Campbell et al. [15], who did hot deformation of stainless steel AISI 304 with varying temperature, strain and strain rate. Here it was found that recrystallization was affected both by temperature, strain and strain rate. Examples of the findings are seen in Fig. 6.9.

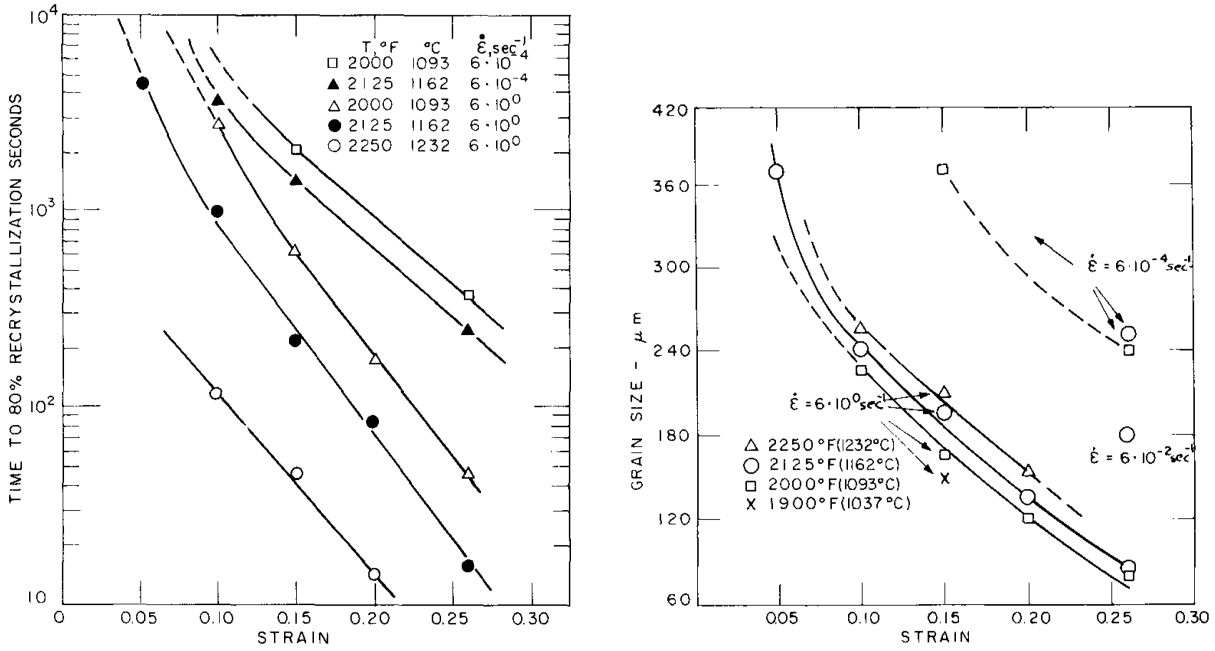

(a) Recrystallization time as function of strain for different temperatures.

(b) Grain size as function of strain for different temperatures.

Fig. 6.9. Grain structure refinement by deformation. From Campbell et al. [15].

It is seen from Fig. 6.9 that straining generally reduces recrystallization time. The recrystallization time is also reduced by temperature. The grain size however does not have a minimum for the highest temperature. This is probably due to rapid grain growth.

The governing principle responsible for the more rapid microstructure change is the fact that deformed metals recrystallize faster than undeformed metals. Also a larger reduction ratio gives rise to a finer grain structure than does lower reduction ratios. Therefore hot forging combines the elevated temperature needed for recrystallization and induces the deformation, which decreases the time for recrystallization, and gives rise to a finer grain structure. This finer grain structure gives better properties regarding fatigue, mechanical strength and toughness.

6.6 Guidelines from practical experience

Some simple guidelines in open die forging can be found in Semiatin [88] p. 102-103 and will be listed here. It is recommended that the deformation zone geometry parameter Δ, see Section 5.4, should be smaller than 1.6. Also a large die indentation depth into the casting should be performed in each indentation step. This is to ensure that the

deformation field reaches the center of the casting, hereby promoting conversion of the cast structure all the way through the casting. It is also recommended to deform the casting as much as possible to induce sufficient deformation. The purpose of the forging operation should therefore not only concern obtaining the final shape, but should also ensure sufficient deformation everywhere in the casting. It can also be beneficial to cool off the surface of the hot casting. This increases the flow stress at the surface of the casting according to equation Eq. 3.8. Thereby most of the plastic straining occurs in the middle of the ingot for a given compression.

Also of importance is the feed during the ingot forging operation. The feed is the distance the dies and the workpiece are moved compared to each other per forging indentation, and is labeled S_V, see Fig. 6.10.

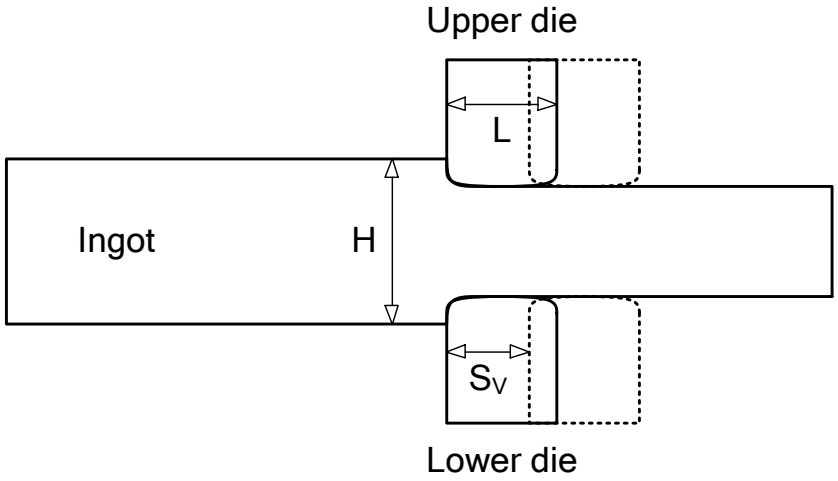

Fig. 6.10. Feed in ingot forging operation.

According to Lange [64] there are limitations on how large the feed should be per forging operation in order to ensure sound forgings. Ideally one would use a feed equal to the width L of the dies, since this would imply the fewest forging operations to achieve the desired workpiece shape. However this has an unfavorable influence on the plastic deformation pattern internally in the ingot. This can be seen in Fig. 6.11.

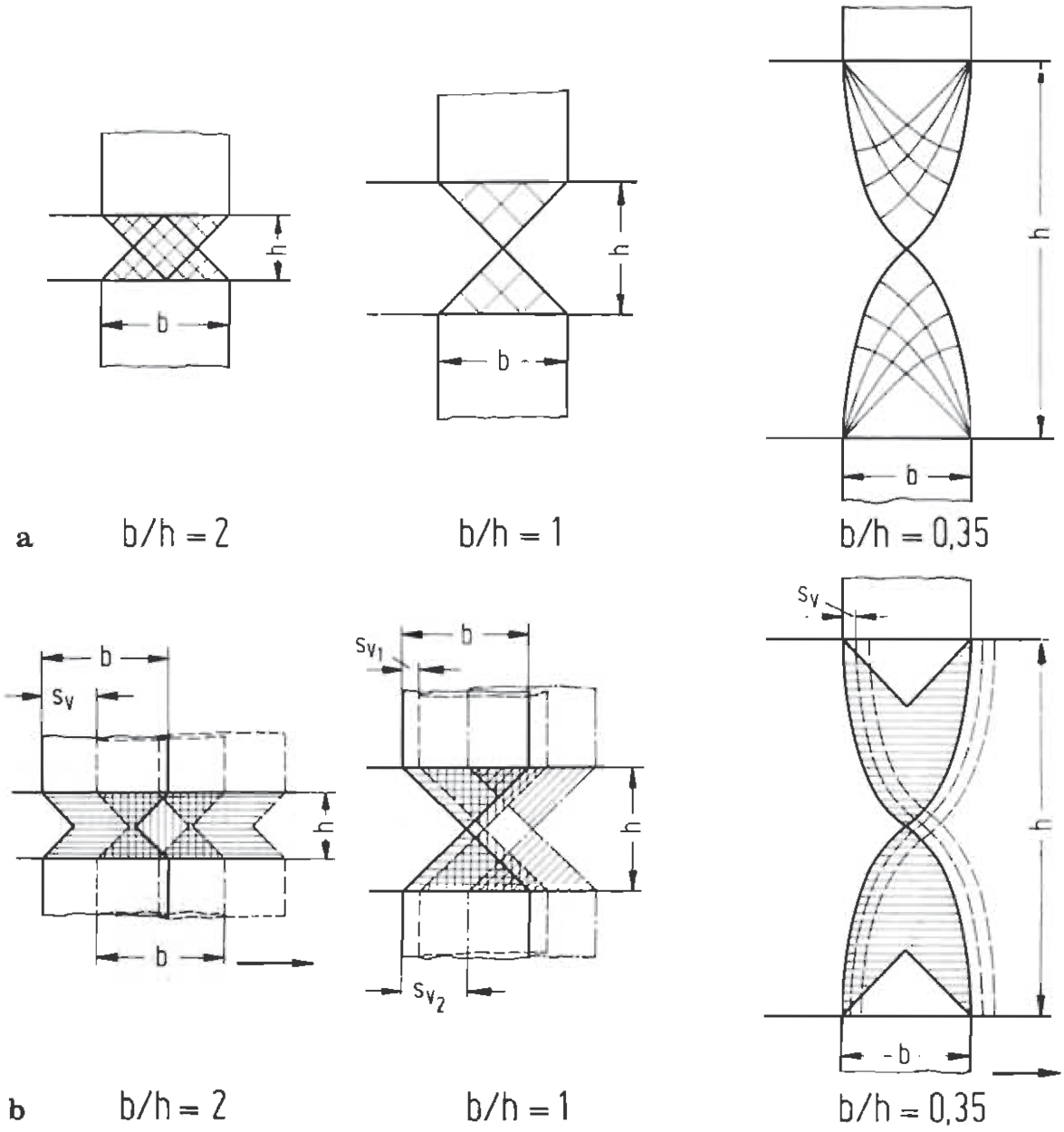

Fig. 6.11. Deformation field depending on deformation zone geometry and feed size. From Lange [64] p. 56.

From Fig. 6.11 the same deformation field is indicated as in Fig. 5.6. However now the deformation field is combined with the next deformation field, after movement of the workpiece after the first indentation and performing a new indentation, resulting in the three lower figures. They show the plastic deformation pattern depending on the feed S_V. It can be seen that if a large feed size is used for b/h=1, an undeformed dead zone is formed at the centerline. This implies that neither recrystallization nor porosity closure is enhanced by plastic deformation in this region. Therefore Lange [64] proposes to use a feed size of ½L or less when performing the ingot forging operation in order to ensure porosity closure and promote recrystallization.

6.7 Influence of die geometry on closure of centreline porosities

When forging a shaft from an ingot, two dies are applied for the ingot forging operation. In industry it is well known that it is beneficial to use a V-shaped lower die, see Fig. 6.12.

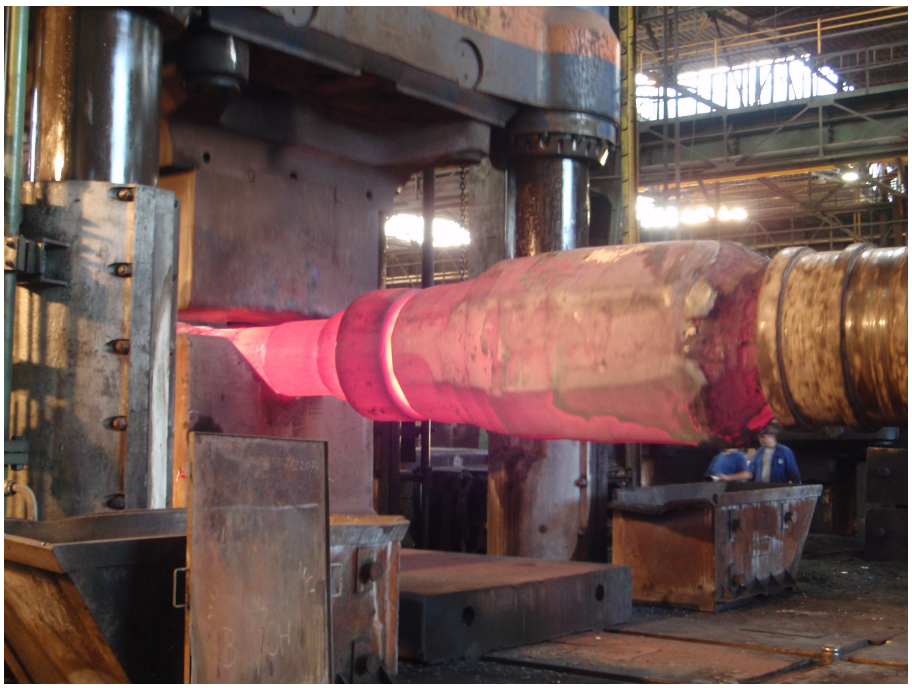

Fig. 6.12. Forging of shaft using V-shaped lower die. Courtesy to Vitkovice Heavy Machinery A/S.

The principle of forging using a V-shaped lower die may be seen in Fig. 6.13.

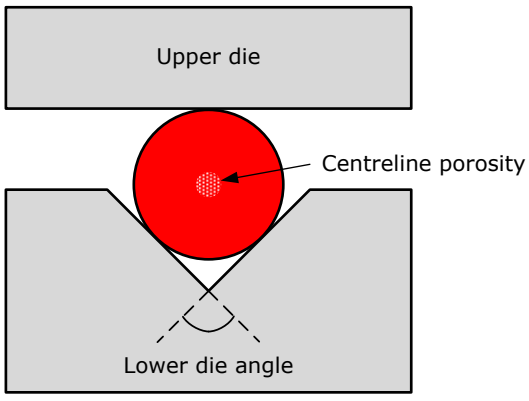

Fig. 6.13. V-shaped lower die applied in ingot forging.

The forging die layout consists of a lower die having inclined faces forming an angle, denoted here as the lower die angle. The upper die has a flat face.

Already Nasmyth [74] noticed that centreline porosity closure was influenced by the choice of lower die angle. Based on trial and error in the workshop, he estimated the

optimum lower die angle to be 80°.

The work of Johnson [51] introduced both slipline and upper-bound solutions for ingot forging and allowed for a better theoretical understanding of why a V-shaped lower die is beneficial for ingot forging. It was shown in Section 5.5 that an improper choice of die size compared to ingot size may give rise to tensile stresses in the center of the ingot when forging with flat parallel dies. Also it was shown (Section 5.3) that a very inclined lower die can result in dead zone formation in the center of the ingot whereby porosities are not closed during forging.

The choice of lower die angle in ingot forging is the main parameter investigated in latter chapters in the thesis.

6.8 Conclusion

A number of benefits of hot forging an ingot after casting have been listed. It is clear that a proper choice of forging procedure and die layout has potential to improve the quality of the part manufactured from a steel ingot.

7 Modelling of ductile damage in metal forming

7.1 Introduction

The purpose of a metal forming operation is to deform a workpiece into a different shape than the original one. However it is well known that at some point, it may not be possible to deform the material further because it fractures. Hence many metal forming operations are ultimately limited by fracture of the material due to the plastic deformation. It is therefore of interest to be able to predict when the metal starts to fracture. "When" is here understood as the combination of initial material properties, stress, strain and strain rate history, temperature, lubrication etc. which give rise to fracture of the material. Fracture in metal forming is influenced by all process parameters and a full description should therefore ideally take all of them into account. This may however be computational cumbersome so models ranging from very simple to more complex have been suggested through time. A review of some different strategies and models regarding modelling of ductile fracture is presented in the current chapter. Experimental forming fracture limit diagrams (FFLD) are presented as well as computational models for prediction of ductile fracture in metal forming.

7.1.1 Physical mechanism causing ductile fracture

The basic mechanism for ductile fracture is the formation of small porosities in the solid. These porosities may grow due to plastic forming of the solid and finally coalesce to form larger porosities, which can finally evolve to cracks. The principle can be seen in Fig. 7.1.

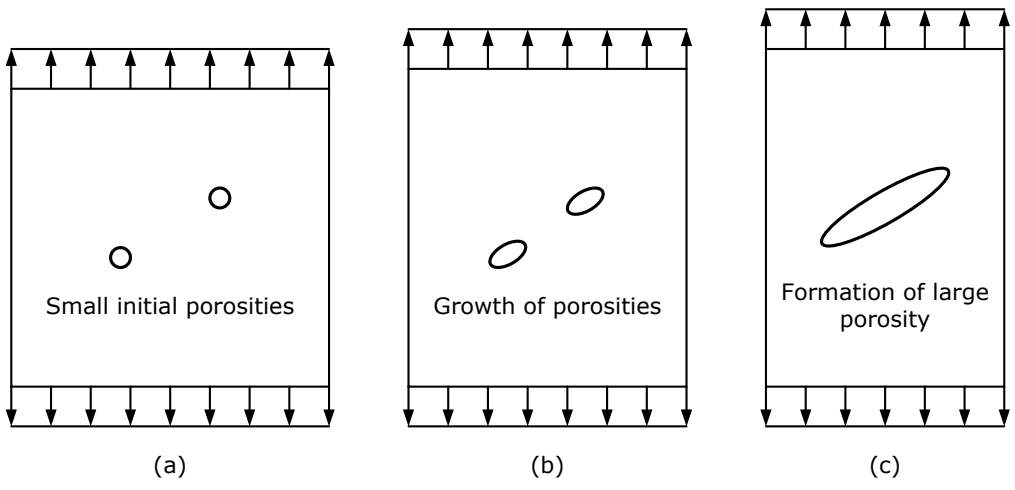

Fig. 7.1. Growth and coalescence of porosities due to plastic deformation.

The origin of the initial porosities can be small gas porosities from casting the metal. The origin of porosities can also be from debonding between the matrix material and intermetallic particles. It is argued in Atkins [8] that the debonding strength can vary quite substantially between different metal alloys. The principle is seen in Fig. 7.2.

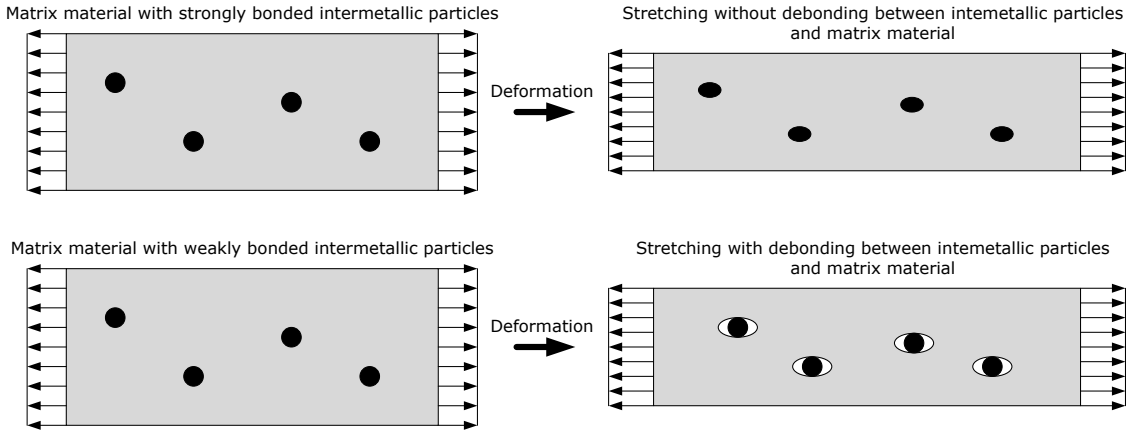

Fig. 7.2. Debonding between intermetallic particles and matrix material due to metal forming.

Fig. 7.2 explains why some metals can undergo substantial deformation with nucleation of new porosities before fracture, while others fracture almost immediately after nucleation of porosities. If the bonding strength between metal matrix material and the intermetallic particles is weak, nucleation of porosities starts almost immediately when deformation begins, resulting in the possibility of substantial straining with nucleation of porosities. If the bonding strength between the intermetallic particles and the metal matrix material is strong, nucleation only starts when the material is heavily stretched and fracture occurs shortly after the beginning of nucleation of porosities. A microstructural description of ductile damage should therefore ideally include both a nucleation and a growth model for porosities.

7.1.2 Influence of the hydrostatic stress on forming limit

From the nature of the process, porosity growth and linking to form a crack, it can qualitatively be understood that tensile stresses are promoting porosity growth while compressive stresses minimize porosity growth. This was experimentally found to be correct by Bridgman [12] who performed tensile tests of different steels under high hydrostatic pressures. He found that it was possible to increase the effective strain at fracture by a factor of four compared to tensile tests at atmospheric pressure when increasing the hydrostatic pressure to 30.000kg/cm^2 ($\approx$3000MPa) . The formability limit before fracture of a material is therefore dependent on the stress situation causing the deformation.

An early attempt to quantitatively describe the influence of the hydrostatic stress on the forming limit was given by Vujovic & Shabaik [100]. They introduced the quantity stress triaxiality β, which they defined as $\beta = \dfrac{I_1}{\sqrt{3J_2}} = \dfrac{3\sigma_m}{\sigma_e} = \dfrac{\sigma_{kk}}{\sigma_e}$, where I_1 is the first invariant of the stress tensor, J_2 is the second invariant of the deviatoric stress tensor

and σ_e is the effective von Mises stress. Often a different definition of stress triaxiality is used:

$$\beta = \frac{\sigma_m}{\bar{\sigma}} = \frac{\sigma_{kk}}{3\bar{\sigma}} \tag{7.1}$$

where $\bar{\sigma}$ is the effective stress. The main principal difference between the definition of stress triaxiality according to Eq. 7.1 and the one defined by Vujovic & Shabaik [100] is that the definition in Eq. 7.1 allows for the use of other yield criterion than the von Mises. For instance one could use a porous or an anisotropic yield criteria. Unless explicitly stated otherwise in the thesis, the definition in Eq. 7.1 is used in the thesis. A sketch of the principle of formability being dependent on stress triaxiality can be seen in Fig. 7.3. $\bar{\varepsilon}^C$ is the effective plastic strain at fracture. A plot of $\left(\beta, \bar{\varepsilon}^C\right)$ is here denoted as a formability diagram.

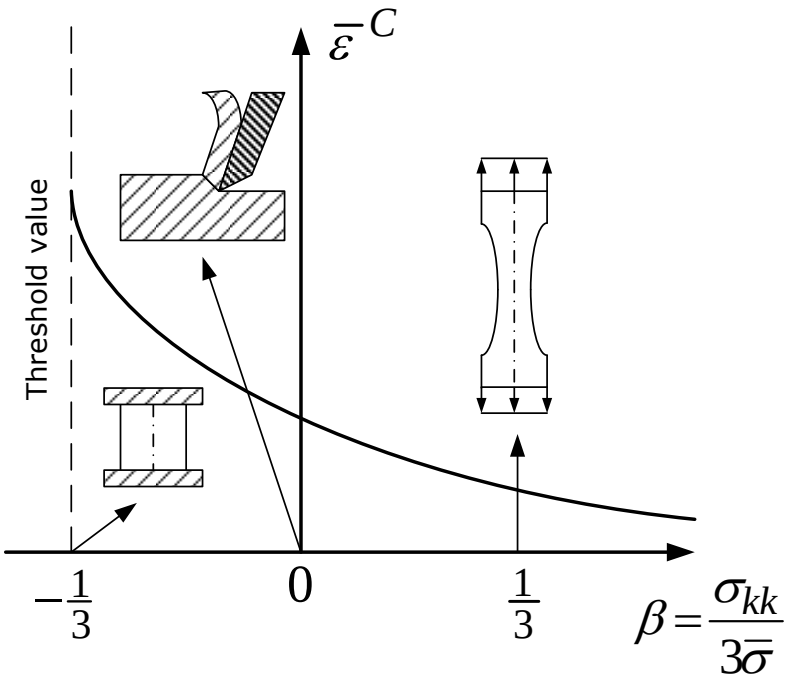

Fig. 7.3. Principal sketch of formability as a function of stress triaxiality. After Vujovic & Shabaik [100].

Fig. 7.3 should be interpreted qualitatively as the attainable deformation, measured as effective plastic strain at fracture $\bar{\varepsilon}^C$, increases with decreasing stress triaxiality. Three different metal forming operations are listed as examples of processes with different stress triaxiality. It should be noticed that in the original work of Vujovic & Shabaik [100], their proposed formability line continued further into the compressive range and did not include the assymptotic behaviour for $\beta = -\frac{1}{3}$. In the opinion of the author this is a mistake because the local stresses causing cracks to occur may be quite different than the overall stress situation. Therefore the author have included the assymptotic behaviour predicting infinite formability for $\beta < -\frac{1}{3}$. Regarding the shape of the formability line,

Johnson & Cook [50] reports an exponential diminishing of the effective strain at fracture for increasing stress triaxiality.

7.1.3 Forming fracture limit diagrams in principal strain space

Instead of plotting formability as a function of stress triaxiality, one can also plot the formability in a principal strain diagram. These types of diagrams were introduced by Keeler & Backofen [56] for stretching of metal sheets. Goodwin [36] expanded the diagram to drawing of metal sheets. Limit diagrams for bulk forming were presented in Kuhn et al. [62]. The formability is plotted in an $\left(\varepsilon^{pl}_{min}, \varepsilon^{pl}_{max}\right)$ diagram, here denoted as a forming fracture limit diagram, where ε^{pl}_{min} and ε^{pl}_{max} are the minimum and maximum in-plane principal plastic strains. In-plane refers to the experimental way the minimum and maximum plastic strains are determined. Usually a sample is deformed until cracks are observed on the surface of the specimen. The strains at the surface are then calculated from a grid, which has for instance been etched on top of the surface before deformation. It is often assumed in the forming limit diagram that the stress normal to the free surface is zero. Hence plane stress can be assumed for the forming limit diagram. An example of such a forming limit diagram can be seen in Fig. 7.4. Fig. 7.4a shows an experimentally obtained forming fracture limit diagram from Kuhn et al. [62]. Fig. 7.4b shows a principal forming fracture limit diagram.

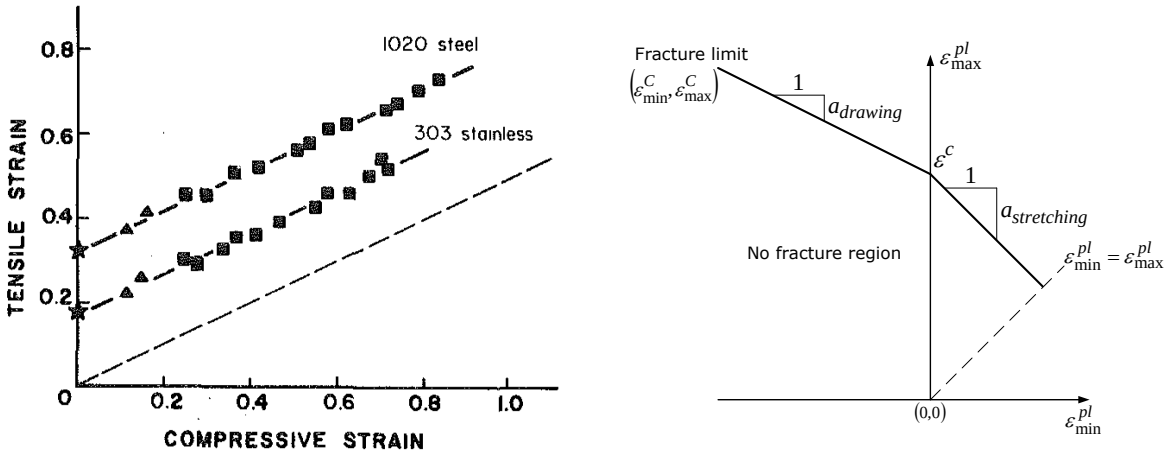

(a) Forming fracture limit diagram from Kuhn et al. [62].

(b) Principle of the forming fracture limit diagram.

Fig. 7.4. Forming fracture limit diagrams.

In Fig. 7.4b, ε^{C} is the maximum principal plastic strain at fracture in plane strain tension loading, the line $\left(\varepsilon^{C}_{min}, \varepsilon^{C}_{max}\right)$ is the fracture limit, $a_{drawing}$ and $a_{stretching}$ refer to the fact that the fracture line may have different slopes in the drawing and stretching region respectively. Examples of different forming fracture limit diagrams can be found in Embury & Duncan [30].

Erman et al. [31] also present experimental data indicating that the forming fracture line may even have different slopes in the drawing region depending on process conditions. Some examples can be seen in Fig. 7.5.

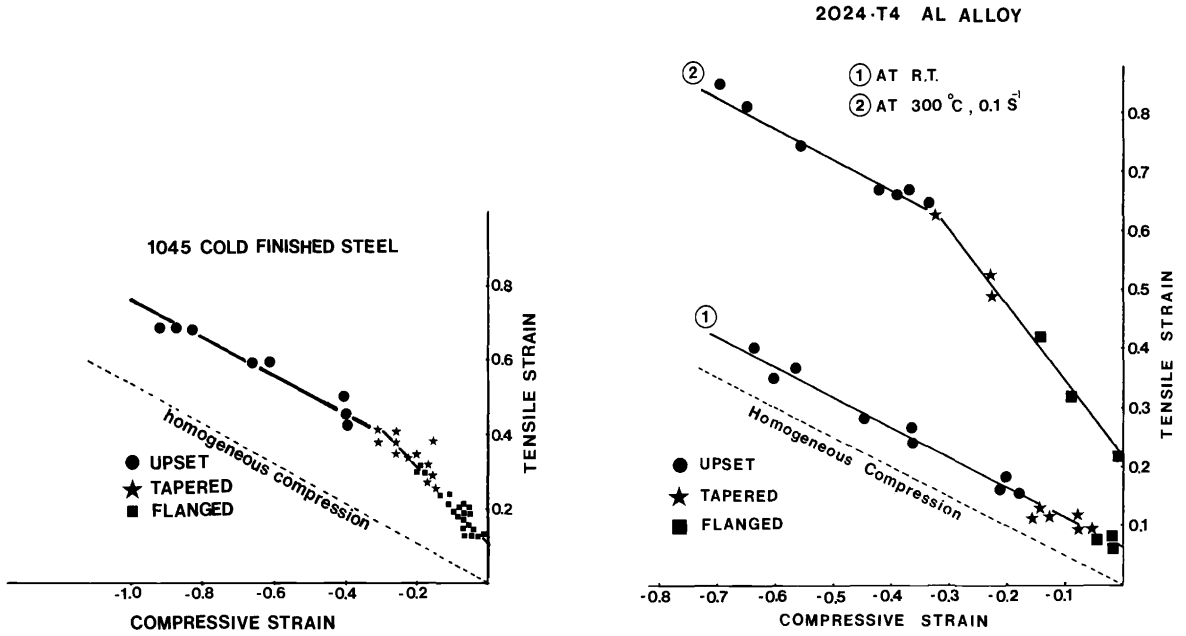

(a) Forming fracture limit diagram with different slopes in drawing region.

(b) Forming fracture limit diagram with different slopes due to temperature difference.

Fig. 7.5. Forming fracture limit diagrams. From Erman et al. [31].

From Fig. 7.5 it is seen that the point of shift from a fracture line with one slope to a fracture line with another slope may happen at other locations than along the maximum principle strain axis. The shift can be triggered by elevated temperature. It should also be noticed that the lowest fracture line is so close to origo that a shift in slope may be difficult to determine experimentally due to the low formability. In the experiments, the fracture lines have slopes of either approximately $-\frac{1}{2}$ or -1.

Some common linear plane stress loading paths are drawn in the forming fracture limit diagram and can be seen in Fig. 7.6. The slopes of the linear strain paths are also depicted. It is noticed that the line corresponding to uniaxial compression is parallel with one of the formability lines. Since the lines do not cross, there is infinite formability in case of pure compression.

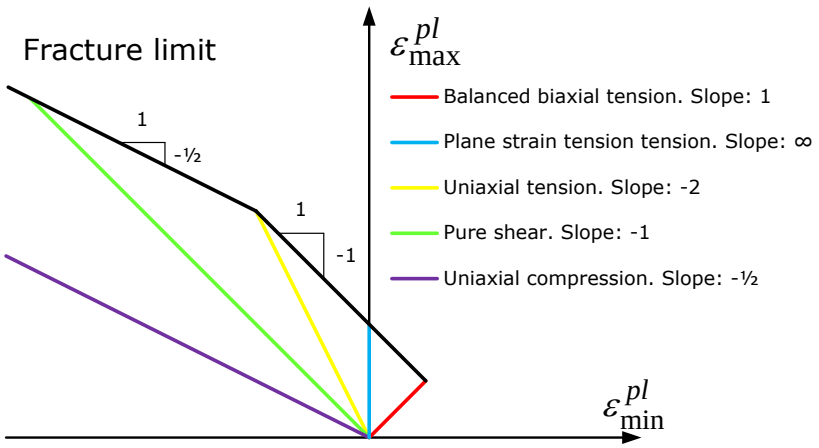

Fig. 7.6. Common loading paths in the forming fracture limit diagram.

A third forming fracture limit line is presented in Marciniak [69]. The line is seen in Fig. 7.7 and goes from B to D in the diagram.

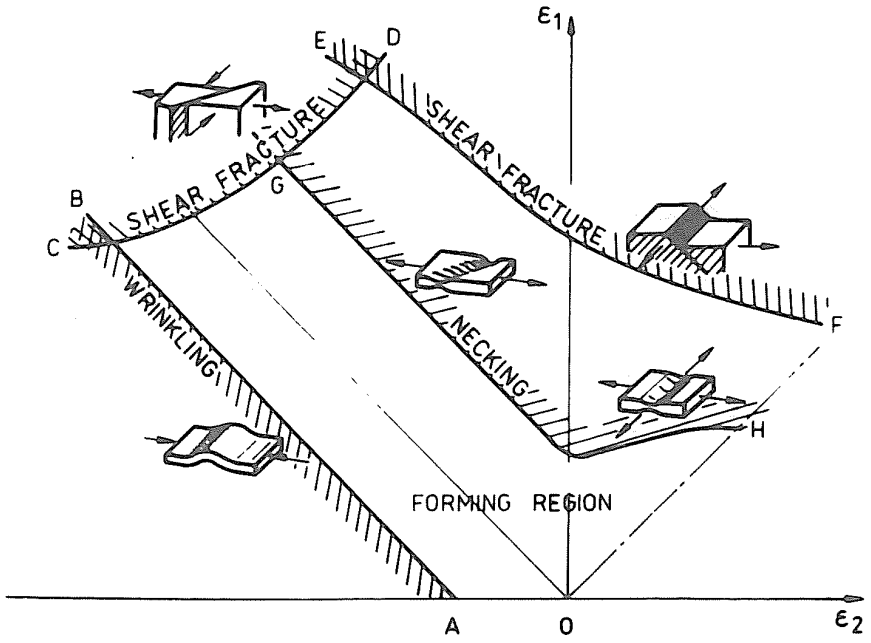

Fig. 7.7. Shear fracture forming limit line.

The author has not encountered this line in other works within ductile fracture and it is therefore not considered in the present analysis.

Forming fracture limit diagrams should not be confused with more traditional forming limit diagrams, mainly developed for sheet metal forming, where diffuse or local necking limits the formability.

The advantage of forming fracture limit diagrams, either presented as $\left(\beta, \bar{\varepsilon}^C\right)$ or $\left(\varepsilon^C_{min}, \varepsilon^C_{max}\right)$ diagrams, are that they reflect measured fracture of real specimens. The disadvantages are that they require sufficient experimental facilities to obtain the diagrams for a wide combination of stress and strain situations and are limited to plane stress.

7.2 Coupled ductile damage mechanics

A coupled ductile damage model is one where the flow stress of the material is affected by the evolution of some variable being representative for the accumulated damage of the material. This dependency may be fully coupled or semi-coupled. Fully coupled implying that the flow stress is modified during the iterations for force equilibrium, see Chapter 8. One may also use a semi-coupled approach where the yield surface is only modified at the beginning of a step. Thereby iterations for the damage variable are not needed. Computational time is thereby reduced. On the other hand force equilibrium in terms of current damage is not fulfilled.

Two major categories of coupled ductile damage exist: Porous metal plasticity and continuum damage mechanics.

7.2.1 Porous metal plasticity

Porous metal plasticity consists of having a metal containing some porosities. Usually the amount of porosity is modelled as some porosity density f, where $f = 0$ implies a porous-free metal and $f = 1$ corresponds to having no metal at all. The porous plasticity model consists of a yield surface being dependent on typically both deviatoric stresses S_{ij}, the mean stress σ_m and porosity density f, combined with an evolution algorithm for the change in porosity density $\dot{f}$ due to deformation. One such model is the Gurson-Tvergaard-Needleman model. Another model, utilized in the commercial FEM-simulation software DEFORM®, is presented in Section 8.6.

7.2.1.1 Gurson-Tvergaard-Needleman model

Gurson [42] derived both a yield criterion and a flow rule for a porous metal by an upper bound solution for a representative volume element containing either a spherical or a cylindrical porosity. The analysis was further developed by Tvergaard [98] and is known as the Gurson-Tvergaard-Needleman (GTN) model. The yield criterion is:

$$\frac{\sigma_e^2}{\sigma_M^2} + 2fq_1 cosh\left(\frac{q_2}{2}\frac{\sigma_{kk}}{\sigma_M}\right) - (1 + q_3 f) = 0 \tag{7.2}$$

where $\sigma_e = \sqrt{3J_2}$ is the Mises stress, σ_M is the flow stress of the fully dense material, q_1, q_2 and q_3 are constants. The yield criterion is supplemented by an evolution algorithm of the porosity density depending both on volumetric plastic strain rate $\dot{\varepsilon}_v^{pl} = \dot{\varepsilon}_{kk}^{pl}$ and nucleation of new porosities, which is described by a statistical distribution multiplied by the equivalent plastic strain rate of the matrix material. The basic idea being that the change in porosity density can be decomposed into two parts, one due to growth of existing porosities and one due to nucleation of new porosities:

$$\dot{f} = \dot{f}_{growth} + \dot{f}_{nucleation} \tag{7.3}$$

where

$$\dot{f}_{growth} = (1 - f)\,\dot{\varepsilon}_{kk} \tag{7.4}$$

and

$$\dot{f}_{nucleation} = \frac{f_N}{S_N\sqrt{2\pi}} exp\left[-\frac{1}{2}\left(\frac{\varepsilon_m - \varepsilon_N}{S_N}\right)^2\right] \tag{7.5}$$

where f_N is the fraction of porosity nucleating particles, ε_N is the mean strain for nucleation and S_N is the standard deviation of nucleation. The expression for nucleation of porosities is from Chu & Needleman [21]. If it is assumed that the material does not nucleate new porosities, the Gurson-Tvergaard-Needleman model does not predict accumulation of damage for a pure shear stress state.

A correction to take into account damage due to pure shear was introduced in Nahshon & Hutchinson [73]. It was proposed to modify the growth of nucleation by introducing:

$$\dot{f}_{growth} = (1 - f)\,\dot{\varepsilon}_{kk} + k_\omega f \omega(\sigma)\,\frac{S_{ij}\dot{\varepsilon}_{ij}^{pl}}{\sigma_e} \tag{7.6}$$

with

$$\omega(\sigma) = 1 - \left(\frac{27 J_3}{2\sigma_e^3}\right)^2 \tag{7.7}$$

and

$$J_3 = \frac{1}{3} S_{ij} S_{ik} S_{jk} \tag{7.8}$$

is the third invariant of the deviatoric stress tensor and k_ω sets the magnitude of porosity growth rate due to pure shear and is to be determined experimentally. It is by this modification theoretically possible for the Gurson-Tvergaard-Needleman model to predict porosity growth when loaded by pure shear. However, as the authors of the article mention, the damage parameter f can then no longer be interpreted directly as porosity. It should be viewed as either an effective porosity density or as a damage parameter.

7.2.2 Continuum damage mechanics

The concept of continuum damage mechanics was introduced by Kachanov [53]. The basic principle is that some damage parameter D expresses the accumulated damage of the material and gradually reduces the apparent flow stress $\tilde{\sigma}_o$ of the material compared to the flow stress σ_o of the undamaged material. The relation was introduced in Rabotnov [82] and is:

$$\tilde{\sigma}_o = (1 - D)\,\sigma_o \tag{7.9}$$

If $D = 0$ the material is undamaged and has full strength. For $D = 1$ the material is fractured and has zero strength. When $0 < D < 1$ the material is damaged to a smaller or larger degree. On the contrary to the aforementioned porous plasticity formulations, the damage variable D does not have a direct physical interpretation.

The model is mainly dependent on the evolution algorithm describing how the damage parameter D changes with deformation. For a description of some frequently used models, the reader is referred to Lemaitre [66] for a model of isotropic damage or Xue [107] for a model of anisotropic damage.

7.3 Uncoupled ductile damage models

In contrast to the coupled models mentioned in Section 7.2 the mechanical properties of the material are not affected by the accumulated damage when modelling uncoupled ductile damage. The prediction of damage becomes a postprocessing operation, where the calculated stresses and strains are used to quantitatively describe the damage experienced by the material. The general form of an uncoupled ductile damage criterion is:

$$C = \int f(\sigma_{ij})\, g\left(d\varepsilon_{ij}^{pl}\right) \tag{7.10}$$

where $f(\sigma_{ij})$ is a function of the stress tensor and $g\left(d\varepsilon_{ij}^{pl}\right)$ is a function of the infinitesimal plastic strain tensor. C is then the accumulated damage value. The basic idea is that if C becomes larger than some critical value, the material is considered to start

fracturing. It is therefore preferable if the critical value of C is constant and not process dependent. This may however be difficult to achieve in practice.

In the following, a number of different uncoupled ductile damage criteria are presented and some of their properties are discussed.

7.3.1 Freudenthal criterion

The Freudenthal criterion was introduced in Freudenthal [35] and has the form:

$$C = \int \bar{\sigma} d\bar{\varepsilon}^{pl} \tag{7.11}$$

where $\bar{\sigma}$ is the effective stress and $d\bar{\varepsilon}^{pl}$ is the effective plastic strain increment. The Freudenthal criterion may be interpreted as a plastic work criterion. The main drawback of the Freudenthal criterion is that it does not take into account the increased ductility for increasingly negative stress triaxialities. Whether the stresses are compressive or tensile are not reflected in the accumulated damage value. Since both $\bar{\sigma}$ and $d\bar{\varepsilon}^{pl}$ are non-negative, the Freudenthal criterion can only predict non-negative damage values.

7.3.2 Cockcroft & Latham criterion and normalized version

Cockcroft & Latham [22] introduced a damage criterion dependent on the largest principal stress σ_1 and the effective plastic strain increment $d\bar{\varepsilon}^{pl}$:

$$C = \int \sigma_1 d\bar{\varepsilon}^{pl} \tag{7.12}$$

A version of Eq. 7.12, normalized by the effective stress $\bar{\sigma}$, was presented in Oh et al. [77] and is:

$$C = \int \frac{\sigma_1}{\bar{\sigma}} d\bar{\varepsilon}^{pl} \tag{7.13}$$

Although lacking a theoretical basis, the normalized version have been found in studies like Gouveia et al. [38] and Landre et al. [63] to give reasonable constant damage values C for a number of different strain paths in bulk forming. It is also the default suggested damage criterion in DEFORM®. Due to these factors, the normalized Cockcroft & Latham criterion is applied extensively in this thesis.

7.3.3 Brozzo damage criterion

To make a damage criterion dependent on mean stress, Brozzo et al. [13] proposed a modified version of Eq. 7.12:

$$C = \int \frac{2\sigma_1}{3\left(\sigma_1 - \sigma_m\right)} d\bar{\varepsilon}^{pl} \tag{7.14}$$

7.3.4 McClintock damage criterion

A criterion based on growth of elliptic porosities was introduced in McClintock [70] and is expressed as:

$$C = \int \left(\frac{\sqrt{3}}{2\left(1-n\right)} sinh\left[\frac{\sqrt{3}\left(1-n\right)}{2} \frac{\sigma_a + \sigma_b}{\bar{\sigma}} \right] + \frac{3}{4} \frac{\sigma_a - \sigma_b}{\bar{\sigma}} \right) d\bar{\varepsilon}^{pl} \tag{7.15}$$

where σ_a and σ_b are the principal stresses in the directions of the major and minor axes of the elliptic porosity. σ_a and σ_b are at the same time also the largest and smallest principal stresses in the material. n is the strain hardening exponent in the Hollomon hardening law $\sigma_0 = C\left(\bar{\varepsilon}^{pl}\right)^n$. Generalized plane strain was assumed and it was also assumed that the ratio between stresses σ_a and σ_b was kept constant during deformation. It was also assumed that no rotation between the material and the directions of the applied stresses occurred during loading. More advanced computational procedures for varying stress ratios where also presented in the paper.

An interesting interpretation of Eq. 7.15 was presented in Oh et al. [77]. First it is noticed that a Taylor series expansion of $\sinh(x)$ is given by:

$$\sinh\left(x\right) = \sum_{n=0}^{\infty} \frac{x^{2n+1}}{(2n+1)!} = x + \frac{x^3}{3!} + \frac{x^5}{5!} + \frac{x^7}{7!} + ... \tag{7.16}$$

hence if $x \to 0$ then $\sinh\left(x\right) \to x$. Performing a Taylor series expansion of Eq. 7.15 when ignoring higher order terms yields:

$$\begin{aligned} C &= \int \left(\frac{\sqrt{3}}{2\left(1-n\right)} sinh\left[\frac{\sqrt{3}\left(1-n\right)}{2} \frac{\sigma_a + \sigma_b}{\bar{\sigma}} \right] + \frac{3}{4} \frac{\sigma_a - \sigma_b}{\bar{\sigma}} \right) d\bar{\varepsilon}^{pl} \\ &\approx \int \left(\frac{\sqrt{3}}{2\left(1-n\right)} \frac{\sqrt{3}\left(1-n\right)}{2} \frac{\sigma_a + \sigma_b}{\bar{\sigma}} + \frac{3}{4} \frac{\sigma_a - \sigma_b}{\bar{\sigma}} \right) d\bar{\varepsilon}^{pl} \\ &= \int \left(\frac{3}{4} \frac{\sigma_a + \sigma_b}{\bar{\sigma}} + \frac{3}{4} \frac{\sigma_a - \sigma_b}{\bar{\sigma}} \right) d\bar{\varepsilon}^{pl} \\ &= \frac{3}{2} \int \frac{\sigma_a}{\bar{\sigma}} d\bar{\varepsilon}^{pl} \end{aligned} \tag{7.17}$$

The Taylor series expansion with no higher order terms is reasonable if for instance the strain hardening exponent n is large or if the ratio $\frac{\sigma_a + \sigma_b}{\bar{\sigma}}$ is small. In Section 5.5 it was noticed that in the center of an ingot being forged by plane dies, a stress situation may arise where one principal stress is tensile and one is compressive, hence for such a deformation process, the Taylor series expansion could be a reasonable approximation and consistency between the McClintock criterion and the normalized Cockcroft & Latham criterion exists.

The author has noticed some inconsistencies in the formulation of the McClintock criterion in literature. Eq. 7.15 is consistent with the model presented in the original paper (McClintock [70]) and may also be found in Sowerby et al. [92] and Landre et al. [63]. A different version is presented in Oh et al. [77]:

$$K = \int \left(\frac{2}{\sqrt{3}\left(1-n\right)} sinh\left[\frac{\sqrt{3}\left(1-n\right)}{2} \frac{\sigma_a + \sigma_b}{\bar{\sigma}} \right] + \frac{\sigma_b - \sigma_a}{\bar{\sigma}} \right) d\bar{\varepsilon}^{pl} \tag{7.18}$$

with $K = \frac{4}{3} \ln\left(\frac{l_a^0}{2a_0} \right)$, where l_a^0 is the initial distance between two elliptic porosities and a_0 is the size of the initial major axis of the elliptic porosity. It is seen in Eq. 7.18 that the last term in the bracket has changed sign from $\sigma_a - \sigma_b$ to $\sigma_b - \sigma_a$. The same formula is also written in the DEFORM® manual (SFTC [89]). By a Taylor series expansion of

Eq. 7.18 (again neglecting higher order terms) one obtains:

$$K = 2 \int \frac{\sigma_b}{\bar{\sigma}} d\bar{\varepsilon}^{pl} \tag{7.19}$$

It is seen that this linearized criterion is dependent on σ_b and not σ_a. This seems strange to the author. If one thinks of a uniaxial tensile test of a very strain hardening material so that the linearization is still feasible, $\sigma_a = \bar{\sigma}$ and $\sigma_b = 0$, hence Eq. 7.19 predicts no damage when performing uniaxial tension of a very strain hardening material. To the author this indicates a printing error in the article of Oh et al. [77]. This is also underlined by the authors of the article themselves because they perform some calculations based on Eq. 7.18 where they insert the principal stresses σ_a and σ_b according to Eq. 7.15. However it is a little unlucky if Eq. 7.18, with the printing error, has been implemented in DEFORM®. To test this, a simulation of uniaxial tension of a cube of size 10mm x 10mm x 10mm was loaded in tension and elongated to a final length of 20mm in the z-direction. An artificial material with flow stress $\sigma_0 = 1\left(\bar{\varepsilon}^{pl}\right)^{0.99}$ was used to make the Taylor expansion of the hyperbolic sine function reasonable. Both damage based on the McClintock model and the normalized Cockcroft & Latham model was simulated using the default implementation. The result can be seen in Fig. 7.8.

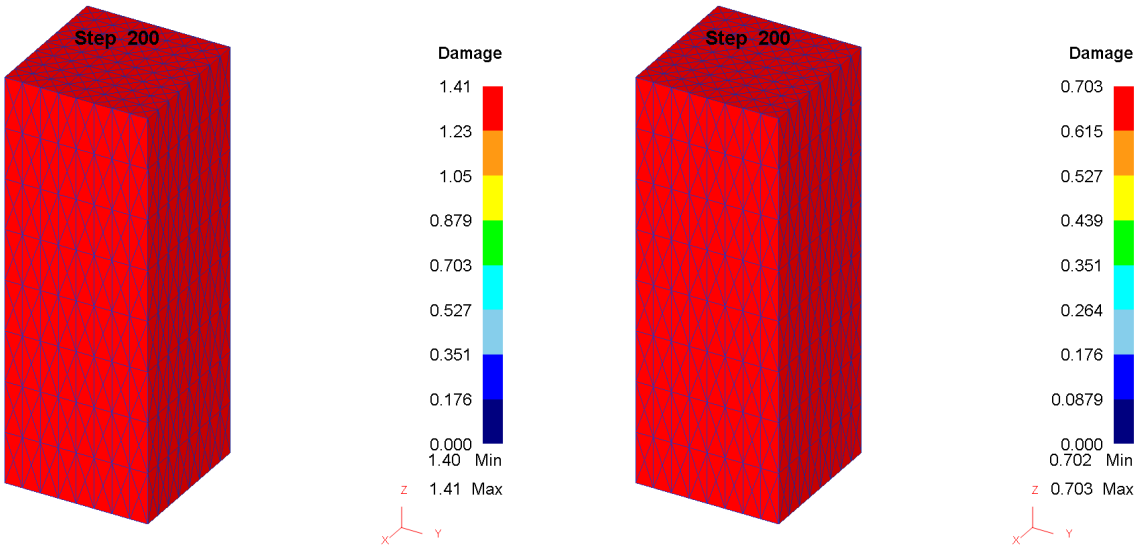

(a) McClintock. **(b)** Normalized Cockcroft & Latham.

Fig. 7.8. Comparison of predicted ductile damage for two different criteria.

It is seen from Fig. 7.8 that the predicted ductile damage for the McClintock criterion is approximately two times the normalized Cockcroft & Latham damage. This is also obtained when using the correct version of Eq. 7.18:

$$\begin{aligned} K &= \int \left(\frac{2}{\sqrt{3}\,(1-n)} sinh\left[\frac{\sqrt{3}\,(1-n)}{2} \frac{\sigma_a + \sigma_b}{\bar{\sigma}} \right] + \frac{\sigma_a - \sigma_b}{\bar{\sigma}} \right) d\bar{\varepsilon}^{pl} \\ &\approx \int \left(\frac{\sigma_a + \sigma_b}{\bar{\sigma}} + \frac{\sigma_a - \sigma_b}{\bar{\sigma}} \right) d\bar{\varepsilon}^{pl} \\ &= 2 \int \frac{\sigma_a}{\bar{\sigma}} d\bar{\varepsilon}^{pl} \end{aligned} \tag{7.20}$$

As it can be seen from Fig. 7.8 and Eq. 7.20 the implementation of the McClintock criterion is correct in DEFORM®, so the error is only in the manual and in the article of Oh et al. [77].

7.3.5 Rice & Tracey damage criterion

A model based on growth of spherical porosities in a representative volume element was derived by Rice & Tracey [83]:

$$\frac{\dot{R}}{R} = \frac{3}{2} exp\left(-\frac{5}{3}\right) exp\left(\frac{3}{2}\frac{\sigma_m}{\bar{\sigma}}\right) \dot{\bar{\varepsilon}}^{pl} \approx 0.283 exp\left(\frac{3}{2}\frac{\sigma_m}{\bar{\sigma}}\right) \dot{\bar{\varepsilon}}^{pl} \tag{7.21}$$

where $\dot{R}$ is the growth rate of the radius and R is the radius of a spherical porosity. An integral form of Eq. 7.21 is then used as damage criterion:

$$C = \int exp\left(\frac{3}{2}\frac{\sigma_m}{\bar{\sigma}}\right) d\bar{\varepsilon}^{pl} \tag{7.22}$$

It is seen from 7.22 that positive damage is predicted even for highly negative stress triaxialities. However since $exp(x) \to 0$ for $x \to -\infty$ the accumulated damage for highly compressive stress states becomes very small.

The author thinks it is interesting that there is a principal contradiction between the Rice & Tracey criterion and porous metal plasticity since the latter predicts an improvement in mechanical properties at compressive stress triaxialities due to densification of the material. On the contrary the Rice & Tracey criterion predicts a decline of mechanical properties at negative stress triaxialities.

7.3.6 Ayada damage criterion

A criterion dependent purely on the stress triaxiality level was proposed by Ayada et al. [9]:

$$C = \int \frac{\sigma_m}{\bar{\sigma}} d\bar{\varepsilon}^{pl} \tag{7.23}$$

The Ayada criterion is based on porosity nucleation and growth due to positive stress triaxiality while predicting closure for negative stress triaxialities.

7.3.7 Oyane damage criterion

A criterion based on porous metal plasticity was derived by Oyane [79]:

$$C = \int \left(1 + \frac{1}{a_o}\frac{\sigma_m}{\bar{\sigma}}\right) d\bar{\varepsilon}^{pl} \tag{7.24}$$

where a_o is a fitting constant.

In the same article Oyane also suggested a modified version non-linearly dependent on the accumulated effective plastic strain:

$$C = \int \left(1 + \frac{1}{a_o}\frac{\sigma_m}{\bar{\sigma}}\right) \left(\bar{\varepsilon}^{pl}\right)^n d\bar{\varepsilon}^{pl} \tag{7.25}$$

In the article it is noticed that Eq. 7.25 is in best agreement with experiments. Eq. 7.24 is however most cited in literature and is implemented in software systems. It is noticed that a power series expansion of $exp\left(\frac{3}{2}\frac{\sigma_m}{\bar{\sigma}}\right) \approx 1 + \frac{3}{2}\frac{\sigma_m}{\bar{\sigma}}$ for $|\ \frac{\sigma_m}{\bar{\sigma}}\ | < 1$, hence if $a_0 = \frac{2}{3}$ and $|\ \frac{\sigma_m}{\bar{\sigma}}\ | < 1$ the Oyane criterion would predict approximately the same damage as the Rice & Tracey criterion.

7.4 Conclusion

A number of models for the prediction of damage in metal forming operations have been presented and discussed in various detail level. The main focus has been on uncoupled ductile damage models. Here it is found that the normalized Cockcroft & Latham criterion is best suited for modelling uncoupled ductile damage in bulk metal forming, which is typically dominated by large, compressive stresses with some smaller, tensile stresses.

8 Finite Element Flow Formulation

8.1 Introduction

Metal forming operations can be analyzed using a number of analysis methods. The oldest method and the one closest to reality is to directly manufacture the part to evaluate whether the part has the desired properties and quality required. However it may be both time consuming and expensive to base product development on a trial-and-error basis. Therefore other methods of analysis are needed.

Siebel [91] introduced slab analysis of compression of cylindrical specimens. This analysis was later utilized for analyzing rolling by von Kármán [59]. Friction can be included in the analysis. Both plane strain and axisymmetric deformation can be calculated using the slab method, the main advantage being that closed form solutions to problems can be found, thereby making it fairly easy for the practicing engineer to calculate process forces.

The mathematical foundation of the slipline method was presented in Hencky [44]. The slipline method made it possible to calculate process forces and stress distributions in a metal forming operation. However the analysis is limited to plane strain deformation and ideal-plastic materials but does incorporate friction. A series of practical examples of metal forming operations analyzed using sliplines can be found in Hill [46], Prager & Hodge [81] and Johnson & Mellor [52].

Upper bound methods based on the upper bound theorem presented in Hill [46] have also been applied extensively for the calculation of both tool loads and material flow. The method is limited to simple deformation cases such as plane strain (Green [39]) or axisymmetric (Kudo [60]) deformation and ideal-plastic materials but can also include friction. One advantage of the upper bound method is that the calculated process forces are larger than or equal to the real process forces required for the metal forming operation. Thereby dimensioning of tools and machines are on the safe side regarding being able to perform the metal forming operation in contradiction to the lower bound, slab method of analysis.

The three listed methods slab analysis, slipline analysis and upper bound analysis were the main sources of theoretical analysis of metal forming operations until the emergence of sufficiently powerful computers. The main disadvantages of the methods are their restrictions to simple metal forming operations and lack of capabilities of taking into account more advanced nonlinear phenomena such as strain hardening. These problems were however solved by the emergence of cheaper and more powerful computers making finite element analysis available for a broader range of engineers and not only research groups at universities.

8.2 Basic concepts of FEA-analysis in relation to the finite element flow formulation

The ideal simulation of a metal forming operation would comprise complete tracking of both position, velocities and temperatures of all atoms constituting the solid to be analyzed. This is however not possible with the current state of development of computer power. Therefore Finite Element Analysis (FEA) constitutes of subdividing the solid into a number of elements of finite size and then fulfill the governing differential equation in an average sense over the element. An example of a tensile test bar subdivided into a number of finite elements can be seen in Fig. 8.1.

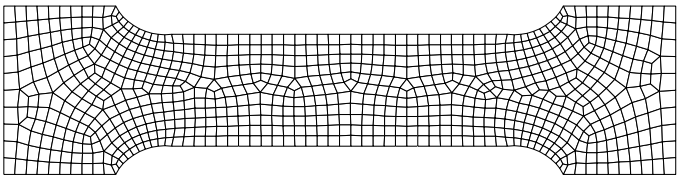

Fig. 8.1. Example of a finite element mesh.

A close inspection of Fig. 8.1 yields that each element is a quadrilateral. The four corners of each element are known as nodes. Each node has some variables associated with it, for instance position, velocity or temperature. It is these fundamental node variables which are used to express and fulfill the governing differential equation over the entire element. A solid consisting of only two elements and six nodes can be seen in Fig. 8.2.

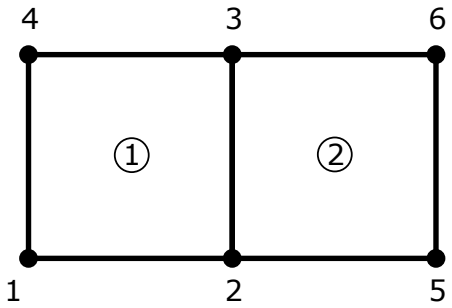

Fig. 8.2. Two finite elements.

It can be seen from Fig. 8.2 that element 1 consists of the nodes (1,2,3,4) and element 2 consists of the nodes (2,5,6,3). The numbering follows the tradition of being counter-clockwise in the element. It is seen that the nodes 2 and 3 are shared between the two elements. Since the idea of expressing the governing differential equation in an average sense for each element by some node variables, it follows that the solution for each element is connected to the neighbouring element with whom it shares some nodes. Hence finding an approximate solution fulfilling the governing differential equation in an average sense over and element is not independent for each element but connected to one another through shared nodes. Therefore the solution to the finite element equations for an entire solid consists of forming a global equation system for the solid, which expresses the equilibrium equations through some node variables and then solve the entire equilibrium

equation system to obtain the best solution for the node variables. How to generate the governing differential equations, fulfilled in an average sense over an element expressed by node variables, will be explained later in the chapter.

8.3 Strain and strain rate measures

As it is seen from the Levy-Mises flow rule (Eq. 8.82) as well as from the chapter regarding metal hardening (Chapter 3) and from the chapter regarding ductile damage (Chapter 7), strain and strain rates are frequently encountered in the description of the material behaviour in a given metal forming operation. Therefore a derivation of the strain and strain rate measure applied in the finite element flow formulation is presented with some examples for facilitating the understanding. The derivations can be found in for instance Dunne & Petrinic [28], Saanouni [86] or Bathe [10]. There is some difference between the labeling of the different terms in the three books. The author has tried either to use the term with most consensus between them or the ones which seemed most sensible.

8.3.1 Deformation of a body

A body may deform in a number of different ways. Here three principally different modes of deformation are considered: rigid body translation, rigid body rotation and stretching. The different modes of deformation are seen in Fig. 8.3.

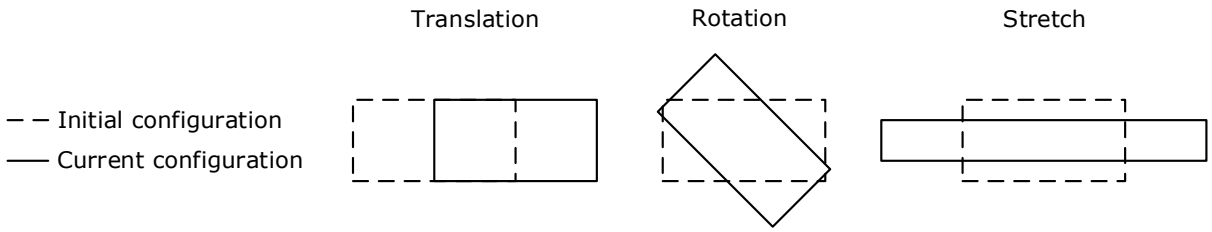

Fig. 8.3. Different modes of deformation.

Only stretch gives rise to physical straining of the body.
For deriving appropriate strain measures, Fig. 8.4 is useful.

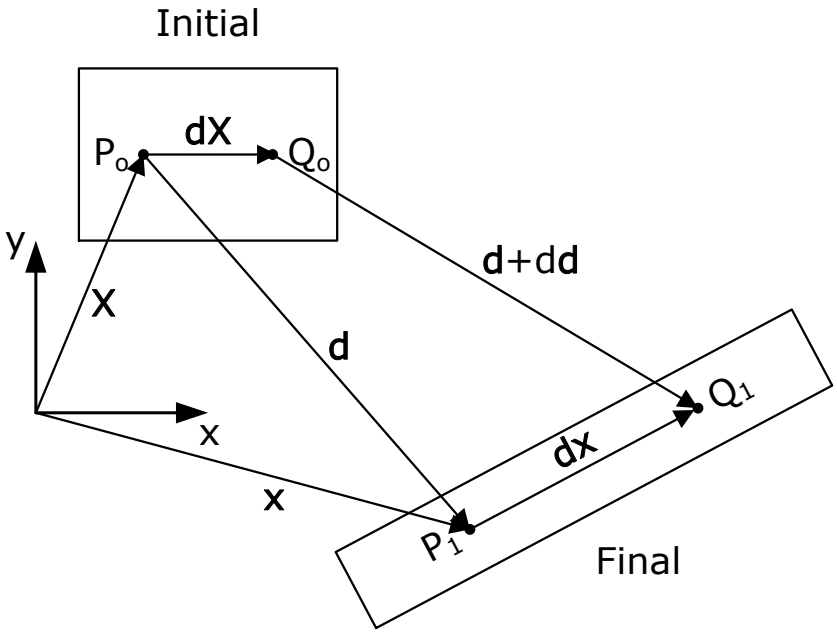

Fig. 8.4. Deformation of a body.

In Fig. 8.4 a body containing the two initial points $\mathbf{P}_o$ and $\mathbf{Q}_o$, connected by the infinitesimal vector $d\mathbf{X}$, is deformed into a final configuration with the same material points now labeled $\mathbf{P}_1$ and $\mathbf{Q}_1$, which are now being connected by the infinitesimal vector $d\mathbf{x}$. $\mathbf{X}$ is a vector from origo to $\mathbf{P}_o$ and $\mathbf{x}$ is a vector from origo to $\mathbf{P}_1$. $\mathbf{d}$ is a displacement vector from $\mathbf{P}_o$ to $\mathbf{P}_1$ and $(\mathbf{d} + d\mathbf{d})$ is a displacement vector from $\mathbf{Q}_o$ to $\mathbf{Q}_1$.

It follows from Fig. 8.4 that:

$$\mathbf{x} = \mathbf{X} + \mathbf{d} \tag{8.1}$$

or in tensor notation:

$$x_i = X_i + d_i \tag{8.2}$$

and:

$$\mathbf{x} + d\mathbf{x} = \mathbf{X} + d\mathbf{X} + \mathbf{d} + d\mathbf{d} \tag{8.3}$$

or in tensor notation:

$$x_i + dx_i = X_i + dX_i + d_i + dd_i \tag{8.4}$$

Inserting Eq. 8.1 into Eq. 8.3 yields:

$$\begin{array}{rcll} \mathbf{X} + \mathbf{d} + d\mathbf{x} & = & \mathbf{X} + d\mathbf{X} + \mathbf{d} + d\mathbf{d} & \Leftrightarrow \\ d\mathbf{x} & = & d\mathbf{X} + d\mathbf{d} & \Leftrightarrow \\ d\mathbf{x} & = & \left(\mathbf{I} + \dfrac{\partial \mathbf{d}}{\partial \mathbf{X}}\right) d\mathbf{X} & \end{array} \tag{8.5}$$

where $\mathbf{I}$ is the identity matrix. The quantity $\left(\mathbf{I} + \dfrac{\partial \mathbf{d}}{\partial \mathbf{X}}\right)$ is known as the deformation gradient $\mathbf{F}$ hence:

$$d\mathbf{x} = \left(\mathbf{I} + \frac{\partial \mathbf{d}}{\partial \mathbf{X}}\right) d\mathbf{X} = \mathbf{F} d\mathbf{X} \tag{8.6}$$

which can also be written in component form as:

$$\begin{bmatrix} dx \\ dy \\ dz \end{bmatrix} = \begin{bmatrix} 1 + \frac{\partial d_x}{\partial X} & \frac{\partial d_x}{\partial Y} & \frac{\partial d_x}{\partial Z} \\ \frac{\partial d_y}{\partial X} & 1 + \frac{\partial d_y}{\partial Y} & \frac{\partial d_y}{\partial Z} \\ \frac{\partial d_z}{\partial X} & \frac{\partial d_z}{\partial Y} & 1 + \frac{\partial d_z}{\partial Z} \end{bmatrix} \begin{bmatrix} dX \\ dY \\ dZ \end{bmatrix} \tag{8.7}$$

In tensor notation it becomes:

$$F_{ij} = \frac{\partial x_i}{\partial X_j} = \delta_{ij} + \frac{\partial d_i}{\partial X_j} \tag{8.8}$$

where δ_{ij} is Kronecker's delta.

By the definition of the deformation gradient in Eq. 8.6 it follows that the inverse deformation gradient $\mathbf{F}^{-1}$ is given by:

$$d\mathbf{X} = \mathbf{F}^{-1} d\mathbf{x} \Leftrightarrow \mathbf{F}^{-1} = \frac{d\mathbf{X}}{d\mathbf{x}} \tag{8.9}$$

In tensor notation the inverse deformation gradient becomes:

$$F^{-1}_{ij} = \frac{\partial X_i}{\partial x_j} \tag{8.10}$$

An intuitive idea of what the deformation gradient is may be obtained from Fig. 8.5. The initial parallelepiped depicted may be thought of as being spanned by the three vectors $\mathbf{X}1$, $\mathbf{X}2$ and $\mathbf{X}3$. Then by the deformation the initial parallelepiped is deformed into a differently shaped parallelepiped, which is spanned by the three vectors $\mathbf{x}1$, $\mathbf{x}2$ and $\mathbf{x}3$. Eq. 8.6 then yields:

$$\underbrace{\begin{bmatrix} x_1 & x_2 & x_3 \\ y_1 & y_2 & y_3 \\ z_1 & z_2 & z_3 \end{bmatrix}}_{\mathbf{x}} = \underbrace{\begin{bmatrix} F_{x1} & F_{x2} & F_{x3} \\ F_{y1} & F_{y2} & F_{y3} \\ F_{z1} & F_{z2} & F_{z3} \end{bmatrix}}_{\mathbf{F}} \underbrace{\begin{bmatrix} X_1 & X_2 & X_3 \\ Y_1 & Y_2 & Y_3 \\ Z_1 & Z_2 & Z_3 \end{bmatrix}}_{\mathbf{X}} \tag{8.11}$$

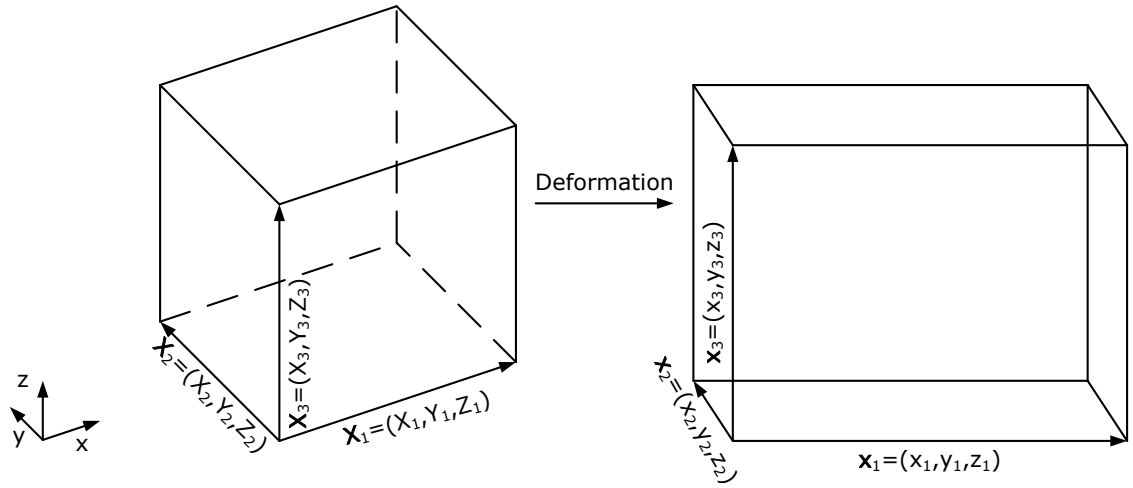

Fig. 8.5. Deformation gradient vector interpretation.

The deformation gradient acts as a scaling factor for the initial vectors spanning the initial parallelepiped, which is then transformed into the final parallelepiped shape by multiplication.

The volume of the initial (V_0) and final (V_1) body is given by:

$$V_0 = \det(d\mathbf{X}) \tag{8.12}$$

$$V_1 = \det(d\mathbf{x}) \tag{8.13}$$

it thereby follows:

$$\begin{array}{rcll} \det(d\mathbf{x}) & = & \det(\mathbf{F}\mathrm{d}\mathbf{X}) & \Leftrightarrow \\ \det(d\mathbf{x}) & = & \det(\mathbf{F})\det(\mathrm{d}\mathbf{X}) & \Leftrightarrow \\ \det(\mathbf{F}) & = & \dfrac{\det(d\mathbf{x})}{\det(\mathrm{d}\mathbf{X})} & \Leftrightarrow \\ \det(\mathbf{F}) & = & \dfrac{V_1}{V_0} & \end{array} \tag{8.14}$$

hence in case of volume constancy $\det(\mathbf{F}) = 1$.

Four different 2-dimensional examples of deformation are analyzed to facilitate the understanding of the deformation gradient $\mathbf{F}$. Out-of plane deformation is zero and volume constancy of the deforming body is maintained.

- Rigid body translation

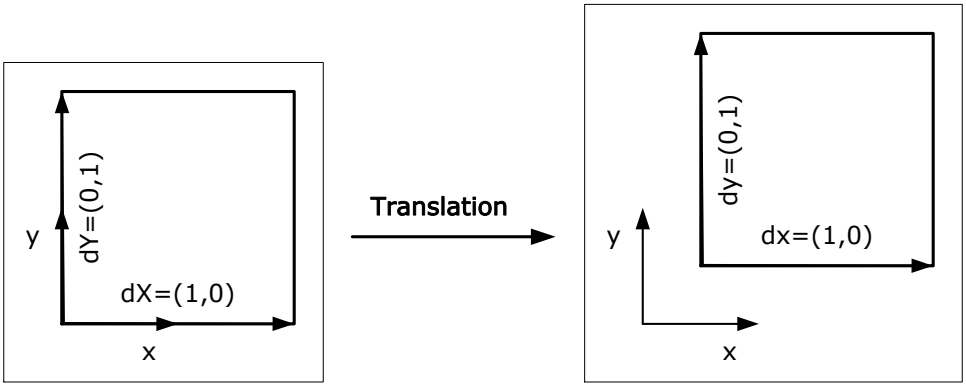

Fig. 8.6. Rigid body translation.

For the rigid body translation seen in Fig. 8.6 one obtains:

$$\begin{aligned} \begin{bmatrix} 1 & 0 \\ 0 & 1 \end{bmatrix} &= \mathbf{F} \begin{bmatrix} 1 & 0 \\ 0 & 1 \end{bmatrix} \quad \Leftrightarrow \\ \mathbf{F} &= \begin{bmatrix} 1 & 0 \\ 0 & 1 \end{bmatrix} \end{aligned} \tag{8.15}$$

- Rigid body rotation

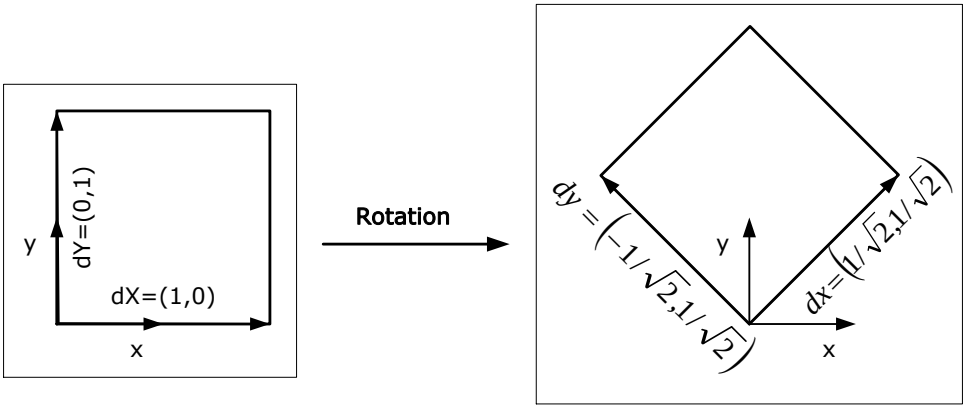

Fig. 8.7. Rigid body rotation.

For the rigid body rotation seen in Fig. 8.7 one obtains:

$$\begin{aligned} \begin{bmatrix} \frac{1}{\sqrt{2}} & -\frac{1}{\sqrt{2}} \\ \frac{1}{\sqrt{2}} & \frac{1}{\sqrt{2}} \end{bmatrix} &= \mathbf{F} \begin{bmatrix} 1 & 0 \\ 0 & 1 \end{bmatrix} \quad \Leftrightarrow \\ \mathbf{F} &= \begin{bmatrix} \frac{1}{\sqrt{2}} & -\frac{1}{\sqrt{2}} \\ \frac{1}{\sqrt{2}} & \frac{1}{\sqrt{2}} \end{bmatrix} \end{aligned} \tag{8.16}$$

- Stretching of body

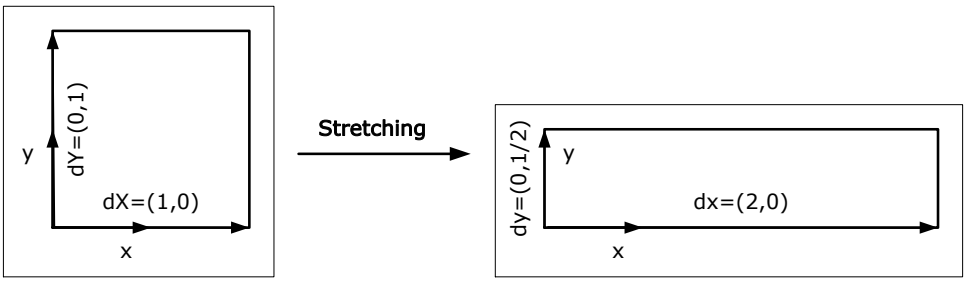

Fig. 8.8. Stretching of body.

For stretching of the body seen in Fig. 8.8 one obtains:

$$\begin{aligned} \begin{bmatrix} 2 & 0 \\ 0 & \frac{1}{2} \end{bmatrix} &= \mathbf{F} \begin{bmatrix} 1 & 0 \\ 0 & 1 \end{bmatrix} \quad \Leftrightarrow \\ \mathbf{F} &= \begin{bmatrix} 2 & 0 \\ 0 & \frac{1}{2} \end{bmatrix} \end{aligned} \tag{8.17}$$

- Deformation of body

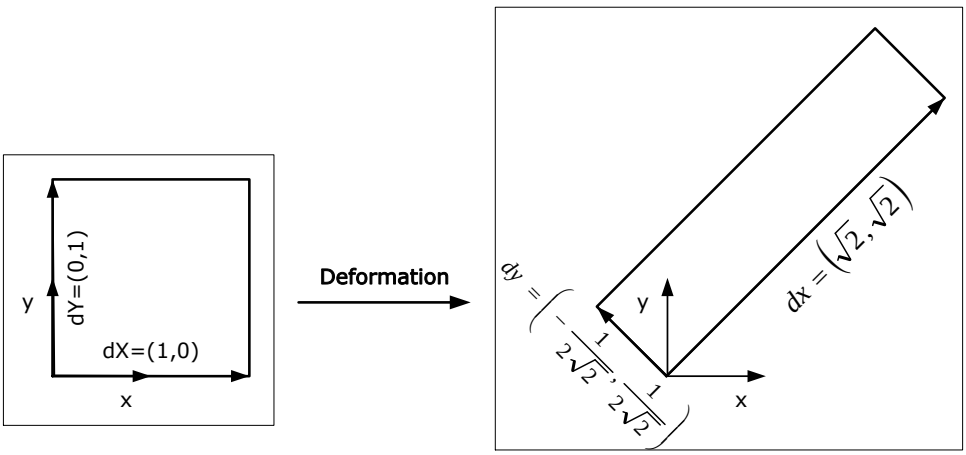

Fig. 8.9. Deformation of body.

For the deformation seen in Fig. 8.9 one obtains:

$$\begin{aligned} \begin{bmatrix} \sqrt{2} & -\frac{1}{2\sqrt{2}} \\ \sqrt{2} & \frac{1}{2\sqrt{2}} \end{bmatrix} &= \mathbf{F} \begin{bmatrix} 1 & 0 \\ 0 & 1 \end{bmatrix} \quad \Leftrightarrow \\ \mathbf{F} &= \begin{bmatrix} \sqrt{2} & -\frac{1}{2\sqrt{2}} \\ \sqrt{2} & \frac{1}{2\sqrt{2}} \end{bmatrix} \end{aligned} \tag{8.18}$$

For the four different examples it is seen that the deformation gradient $\mathbf{F}$ is in general unsymmetric and nonzero for both rigid body translation, rigid body rotation and stretch. It is therefore not a good measure of stretch alone.

8.3.2 Strain measures

Several different strain measures have been proposed based on the deformation gradient $\mathbf{F}$. Some of them are presented here and analyzed in relation to the four different deformations mentioned in 8.3.1.

8.3.2.1 Right Cauchy-Green deformation tensor and Green-Lagrange strain tensor

The right Cauchy-Green deformation tensor is defined as:

$$C_{ij} = \frac{\partial x_i}{\partial X_k} \frac{\partial x_j}{\partial X_k} \tag{8.19}$$

or in matrix form:

$$\mathbf{C} = \mathbf{F}^T \mathbf{F} \tag{8.20}$$

The right Cauchy-Green deformation matrix is calculated for the four different modes of deformation and listed in Table 8.1.

Table 8.1. Right Cauchy-Green deformation matrix for different modes of deformation.

Rigid body translation	$\mathbf{C} = \begin{bmatrix} 1 & 0 \\ 0 & 1 \end{bmatrix} \begin{bmatrix} 1 & 0 \\ 0 & 1 \end{bmatrix}$ $= \begin{bmatrix} 1 & 0 \\ 0 & 1 \end{bmatrix}$
Rigid body rotation	$\mathbf{C} = \begin{bmatrix} \frac{1}{\sqrt{2}} & \frac{1}{\sqrt{2}} \\ -\frac{1}{\sqrt{2}} & \frac{1}{\sqrt{2}} \end{bmatrix} \begin{bmatrix} \frac{1}{\sqrt{2}} & -\frac{1}{\sqrt{2}} \\ \frac{1}{\sqrt{2}} & \frac{1}{\sqrt{2}} \end{bmatrix}$ $= \begin{bmatrix} 1 & 0 \\ 0 & 1 \end{bmatrix}$
Stretching	$\mathbf{C} = \begin{bmatrix} 2 & 0 \\ 0 & \frac{1}{2} \end{bmatrix} \begin{bmatrix} 2 & 0 \\ 0 & \frac{1}{2} \end{bmatrix}$ $= \begin{bmatrix} 4 & 0 \\ 0 & \frac{1}{4} \end{bmatrix}$
Deformation	$\mathbf{C} = \begin{bmatrix} \sqrt{2} & \sqrt{2} \\ -\frac{1}{2\sqrt{2}} & \frac{1}{2\sqrt{2}} \end{bmatrix} \begin{bmatrix} \sqrt{2} & -\frac{1}{2\sqrt{2}} \\ \sqrt{2} & \frac{1}{2\sqrt{2}} \end{bmatrix}$ $= \begin{bmatrix} 4 & 0 \\ 0 & \frac{1}{4} \end{bmatrix}$

The right Cauchy-Green deformation matrix $\mathbf{C}$ is symmetric but is non-zero for both rigid body displacement, rotation and stretching. It is therefore not appropriate for measuring stretch alone. However it is utilized in the Green-Lagrange strain tensor as:

$$E_{ij} = \frac{1}{2}\left(\frac{\partial x_k}{\partial X_i}\frac{\partial x_k}{\partial X_j} - \delta_{ij}\right) \tag{8.21}$$

or in matrix form:

$$\mathbf{E} = \frac{1}{2}\left(\mathbf{C} - \mathbf{I}\right) \tag{8.22}$$

The Green-Lagrange strains corresponding to the four different deformation modes are

calculated in Table 8.2.

Table 8.2. Green-Lagrange strain matrix for different modes of deformation.

Rigid body translation	$\mathbf{E} = \frac{1}{2}\left(\begin{bmatrix} 1 & 0 \\ 0 & 1 \end{bmatrix} - \begin{bmatrix} 1 & 0 \\ 0 & 1 \end{bmatrix}\right) = \begin{bmatrix} 0 & 0 \\ 0 & 0 \end{bmatrix}$
Rigid body rotation	$\mathbf{E} = \frac{1}{2}\left(\begin{bmatrix} 1 & 0 \\ 0 & 1 \end{bmatrix} - \begin{bmatrix} 1 & 0 \\ 0 & 1 \end{bmatrix}\right) = \begin{bmatrix} 0 & 0 \\ 0 & 0 \end{bmatrix}$
Stretching	$\mathbf{E} = \frac{1}{2}\left(\begin{bmatrix} 4 & 0 \\ 0 & \frac{1}{4} \end{bmatrix} - \begin{bmatrix} 1 & 0 \\ 0 & 1 \end{bmatrix}\right) = \begin{bmatrix} \frac{3}{2} & 0 \\ 0 & -\frac{3}{8} \end{bmatrix}$
Deformation	$\mathbf{E} = \frac{1}{2}\left(\begin{bmatrix} 4 & 0 \\ 0 & \frac{1}{4} \end{bmatrix} - \begin{bmatrix} 1 & 0 \\ 0 & 1 \end{bmatrix}\right) = \begin{bmatrix} \frac{3}{2} & 0 \\ 0 & -\frac{3}{8} \end{bmatrix}$

It is seen that the Green-Lagrange strain tensor is zero for both the rigid body translation and the rigid body rotation. For the stretching and the deformation case, similar strains are obtained, hence the strain measure is rotation free. This is because both strains reefer to the initial configuration. It is also seen that the volumetric strain ($\varepsilon_{vol} = \varepsilon_{11} + \varepsilon_{22}$) is non-zero for the stretching and deformation cases even though the physical volume change of the body is zero.

8.3.3 Left Cauchy-Green deformation tensor and logarithmic strain tensor

The left Cauchy-Green deformation tensor is defined as:

$$B_{ij} = \frac{\partial x_i}{\partial X_k}\frac{\partial x_j}{\partial X_k} \tag{8.23}$$

or in matrix notation

$$\mathbf{B} = \mathbf{F}\mathbf{F}^T \tag{8.24}$$

The left Cauchy-Green deformation matrix is calculated for the four different modes of deformation and listed in Table 8.3.

Table 8.3. Left Cauchy-Green deformation matrix for different modes of deformation.

Rigid body translation	$\mathbf{B} = \begin{bmatrix} 1 & 0 \\ 0 & 1 \end{bmatrix}\begin{bmatrix} 1 & 0 \\ 0 & 1 \end{bmatrix} = \begin{bmatrix} 1 & 0 \\ 0 & 1 \end{bmatrix}$
Rigid body rotation	$\mathbf{B} = \begin{bmatrix} \frac{1}{\sqrt{2}} & -\frac{1}{\sqrt{2}} \\ \frac{1}{\sqrt{2}} & \frac{1}{\sqrt{2}} \end{bmatrix}\begin{bmatrix} \frac{1}{\sqrt{2}} & \frac{1}{\sqrt{2}} \\ -\frac{1}{\sqrt{2}} & \frac{1}{\sqrt{2}} \end{bmatrix} = \begin{bmatrix} 1 & 0 \\ 0 & 1 \end{bmatrix}$
Stretching	$\mathbf{B} = \begin{bmatrix} 2 & 0 \\ 0 & \frac{1}{2} \end{bmatrix}\begin{bmatrix} 2 & 0 \\ 0 & \frac{1}{2} \end{bmatrix} = \begin{bmatrix} 4 & 0 \\ 0 & \frac{1}{4} \end{bmatrix}$
Deformation	$\mathbf{B} = \begin{bmatrix} \sqrt{2} & -\frac{1}{2\sqrt{2}} \\ \sqrt{2} & \frac{1}{2\sqrt{2}} \end{bmatrix}\begin{bmatrix} \sqrt{2} & \sqrt{2} \\ -\frac{1}{2\sqrt{2}} & \frac{1}{2\sqrt{2}} \end{bmatrix} = \begin{bmatrix} \frac{17}{8} & \frac{15}{8} \\ \frac{15}{8} & \frac{17}{8} \end{bmatrix}$

The left Cauchy-Green deformation matrix $\mathbf{B}$ is symmetric but is non-zero for both rigid

body translation, rotation and stretching. It is therefore not appropriate for measuring stretch alone. However it is utilized in the logarithmic strain tensor as:

$$\varepsilon_{ij} = -\frac{1}{2}\ln\left(B_{ij}^{-1}\right) \tag{8.25}$$

The logarithmic strains corresponding to the four different deformation modes are calculated in Table 8.4. When taking the natural logarithm of matrices containing some zeroes, the strains are calculated by the matrix rule from Culver [25].

Table 8.4. Logarithmic strain matrix for different modes of deformation.

Rigid body translation	$\boldsymbol{\varepsilon} = -\frac{1}{2}\ln\left(\begin{bmatrix} 1 & 0 \\ 0 & 1 \end{bmatrix}^{-1}\right) = \begin{bmatrix} 0 & 0 \\ 0 & 0 \end{bmatrix}$
Rigid body rotation	$\boldsymbol{\varepsilon} = -\frac{1}{2}\ln\left(\begin{bmatrix} 1 & 0 \\ 0 & 1 \end{bmatrix}^{-1}\right) = \begin{bmatrix} 0 & 0 \\ 0 & 0 \end{bmatrix}$
Stretching	$\boldsymbol{\varepsilon} = -\frac{1}{2}\ln\left(\begin{bmatrix} 4 & 0 \\ 0 & \frac{1}{4} \end{bmatrix}^{-1}\right) = \begin{bmatrix} \ln(2) & 0 \\ 0 & \ln\left(\frac{1}{2}\right) \end{bmatrix}$
Deformation	$\boldsymbol{\varepsilon} = -\frac{1}{2}\ln\left(\begin{bmatrix} \frac{17}{8} & \frac{15}{8} \\ \frac{15}{8} & \frac{17}{8} \end{bmatrix}^{-1}\right) = \begin{bmatrix} 0 & \ln(2) \\ \ln(2) & 0 \end{bmatrix}$

It can be seen from Table 8.4 that the logarithmic strain is zero for both rigid body translation and rigid body rotation. The volumetric strain is zero for the stretching and also zero for the deformation. It is interesting to see how the logarithmic strain predicts different values of strain for the stretching and deformation. This is because the

logarithmic strain refers to the final geometry.

8.3.3.1 Polar decomposition

Often the deformation gradient is divided into an orthogonal rotation matrix $\mathbf{R}$ and a symmetric stretch matrix $\mathbf{U}$ or $\mathbf{V}$:

$$\mathbf{F} = \mathbf{RU} = \mathbf{VR} \tag{8.26}$$

$\mathbf{U}$ is known as the right and $\mathbf{V}$ as the left stretch matrix.
The principle is seen in Fig. 8.10.

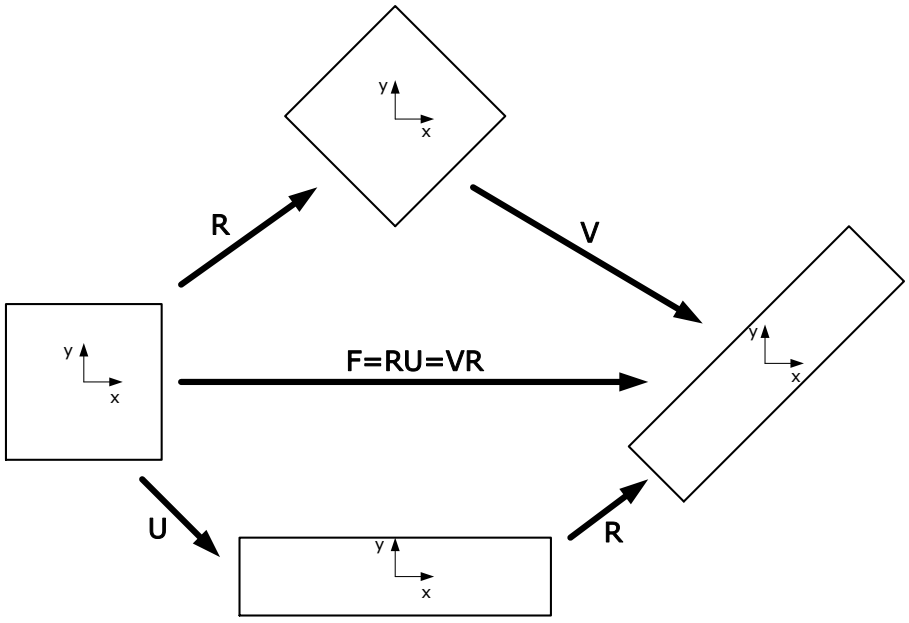

Fig. 8.10. Polar decomposition of deformation gradient.

From Fig. 8.10 it is seen that the decomposition $\mathbf{F} = \mathbf{RU}$ implies first stretching and then rotation of the body being deformed. The decomposition $\mathbf{F} = \mathbf{VR}$ implies first rotation and then stretching. The first decomposition is suitable for for instance anisotropic metals where material and coordinate axes do not necessary have the same orientation. The disadvantage is that one must keep track of the local material axes of each finite element and that accumulated strains must be rotated before adding further strain. The second decomposition allows for adding further straining directly to the already accumulated strains without rotation. However this decomposition is only suitable for isotropic materials.

The Cauchy right matrix becomes:

$$\begin{aligned} \mathbf{C} &= \mathbf{F}^{\mathrm{T}}\mathbf{F} \\ &= (\mathbf{RU})^{T}\,\mathbf{RU} \\ &= \mathbf{U}^{\mathrm{T}}\mathbf{R}^{\mathrm{T}}\mathbf{RU} \\ &= \mathbf{U}^{\mathrm{T}}\mathbf{U} \\ &= \mathbf{U}^{2} \end{aligned} \tag{8.27}$$

It is seen from Eq. 8.27 that the Cauchy right matrix is only dependent on the stretch $\mathbf{U}$.

The Cauchy left matrix becomes:

$$\begin{aligned} \mathbf{B} &= \mathbf{F}\mathbf{F}^T \\ &= \mathbf{V}\mathbf{R}\left(\mathbf{V}\mathbf{R}\right)^T \\ &= \mathbf{V}\mathbf{R}\mathbf{R}^{\mathrm{T}}\mathbf{V}^{\mathrm{T}} \\ &= \mathbf{V}\mathbf{V}^{\mathrm{T}} \\ &= \mathbf{V}^2 \end{aligned} \tag{8.28}$$

It is seen from Eq. 8.28 that the Cauchy left matrix is only dependent on the stretch $\mathbf{V}$.

For a 2-dimensional deformation, the rotation matrix $\mathbf{R}$ can be expressed using Fig. 8.11.

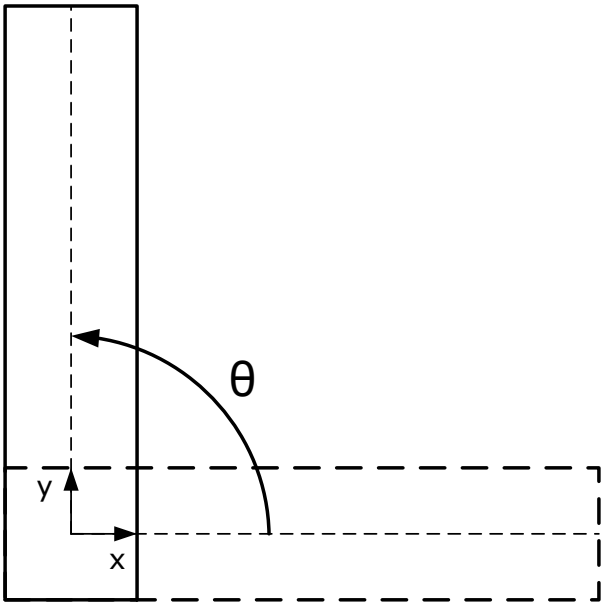

Fig. 8.11. Rotation of body.

According to Fig. 8.11 the rotation matrix becomes:

$$\mathbf{R} = \begin{bmatrix} \cos\left(\theta\right) & -\sin\left(\theta\right) \\ \sin\left(\theta\right) & \cos\left(\theta\right) \end{bmatrix} \tag{8.29}$$

From Eq. 8.29 it follows:

$$\mathbf{R}^{-1} = \frac{1}{\left(\cos\left(\theta\right)\right)^2 + \left(\sin\left(\theta\right)\right)^2} \begin{bmatrix} \cos\left(\theta\right) & \sin\left(\theta\right) \\ -\sin\left(\theta\right) & \cos\left(\theta\right) \end{bmatrix} = \begin{bmatrix} \cos\left(\theta\right) & \sin\left(\theta\right) \\ -\sin\left(\theta\right) & \cos\left(\theta\right) \end{bmatrix} = \mathbf{R}^T \tag{8.30}$$

hence the matrix $\mathbf{R}$ is orthogonal for this choice of rotation matrix.
The time derivative of the rotation matrix is given by:

$$\dot{\mathbf{R}} = \dot{\theta} \begin{bmatrix} -\sin\left(\theta\right) & -\cos\left(\theta\right) \\ \cos\left(\theta\right) & -\sin\left(\theta\right) \end{bmatrix} \tag{8.31}$$

where $\dot{\theta}$ is the rotation rate.

8.3.3.2 Deformation rate

Since constitutive laws, such as the Levy-Mises flow rule, may be expressed using strain rates rather than strains, it is necessary to express the deformation of a body in terms of rates. One such measure is the time derivative of the deformation gradient:

$$\dot{\mathbf{F}} = \frac{\partial}{\partial t}\left(\frac{\partial \mathbf{x}}{\partial \mathbf{X}}\right) = \frac{\partial \mathbf{u}}{\partial \mathbf{X}} = \frac{\partial \mathbf{u}}{\partial \mathbf{x}}\frac{\partial \mathbf{x}}{\partial \mathbf{X}} = \mathbf{L}\mathbf{F} = \dot{\mathbf{V}}\mathbf{R} + \mathbf{V}\dot{\mathbf{R}} \tag{8.32}$$

The quantity $\mathbf{L} = \dfrac{\partial \mathbf{u}}{\partial \mathbf{x}}$ is known as the velocity gradient. By inversion it follows:

$$\mathbf{L} = \dot{\mathbf{F}}\mathbf{F}^{-1} \tag{8.33}$$

The velocity gradient may be be decomposed into a symmetric[1] and an antisymmetric[2] part as:

$$\mathbf{L} = sym\left(\mathbf{L}\right) + asym\left(\mathbf{L}\right) \tag{8.34}$$

The symmetric part is known as the rate of deformation and is related to stretching of the body:

$$\mathbf{D} = sym\left(\mathbf{L}\right) = \frac{1}{2}\left(\mathbf{L} + \mathbf{L}^T\right) \tag{8.35}$$

The antisymmetric part is known as the continuum spin and is related to the rotation of the body:

$$\mathbf{W} = asym\left(\mathbf{L}\right) = \frac{1}{2}\left(\mathbf{L} - \mathbf{L}^T\right) \tag{8.36}$$

It is seen that:

$$\mathbf{L} = \mathbf{D} + \mathbf{W} \tag{8.37}$$

Some useful relations when performing calculations are:

$$\mathbf{V} = \mathbf{R}\mathbf{U}\mathbf{R}^T \tag{8.38}$$

$$\dot{\mathbf{V}} = \left(\dot{\mathbf{R}}\mathbf{U} + \mathbf{R}\dot{\mathbf{U}} - \mathbf{V}\dot{\mathbf{R}}\right)\mathbf{R}^T \tag{8.39}$$

$$\mathbf{D} = \mathbf{R}sym\left(\dot{\mathbf{U}}\mathbf{U}^{-1}\right)\mathbf{R}^T \tag{8.40}$$

$$\mathbf{W} = \dot{\mathbf{R}}\mathbf{R}^T + \mathbf{R}asym\left(\dot{\mathbf{U}}\mathbf{U}^{-1}\right)\mathbf{R}^T \tag{8.41}$$

For an illustration of the different measures, both $\dot{\mathbf{F}}$, $\mathbf{L}$, $\mathbf{D}$ and $\mathbf{W}$ are calculated for the four different deformations listed in 8.3.1. It is noticed that for pure rotation $\mathbf{U} = \mathbf{I}$ and $\dot{\mathbf{U}} = \mathbf{0}$ and for pure stretching $\mathbf{R} = \mathbf{I}$ and $\dot{\mathbf{R}} = \mathbf{0}$. It is assumed that the deformation occurs with constant strain rate and rotation rate. The results are seen in Table 8.5.

[1] A_{ij} is symmetric if $A_{ij} = A_{ji}$
[2] A_{ij} is antisymmetric if $A_{ij} = -A_{ji}$

Table 8.5. Different deformations of a body.

	Rigid body translation	Rigid body rotation	Stretching	Deformation
$\mathbf{U}$	$\begin{bmatrix} 1 & 0 \\ 0 & 1 \end{bmatrix}$	$\begin{bmatrix} 1 & 0 \\ 0 & 1 \end{bmatrix}$	$\begin{bmatrix} 2 & 0 \\ 0 & \frac{1}{2} \end{bmatrix}$	$\begin{bmatrix} 2 & 0 \\ 0 & \frac{1}{2} \end{bmatrix}$
$\dot{\mathbf{U}}$	$\begin{bmatrix} 0 & 0 \\ 0 & 0 \end{bmatrix}$	$\begin{bmatrix} 0 & 0 \\ 0 & 0 \end{bmatrix}$	$\begin{bmatrix} 2 & 0 \\ 0 & -\frac{1}{2} \end{bmatrix}$	$\begin{bmatrix} 2 & 0 \\ 0 & -\frac{1}{2} \end{bmatrix}$
$\mathbf{R}$	$\begin{bmatrix} 1 & 0 \\ 0 & 1 \end{bmatrix}$	$\begin{bmatrix} \frac{1}{\sqrt{2}} & -\frac{1}{\sqrt{2}} \\ \frac{1}{\sqrt{2}} & \frac{1}{\sqrt{2}} \end{bmatrix}$	$\begin{bmatrix} 1 & 0 \\ 0 & 1 \end{bmatrix}$	$\begin{bmatrix} \frac{1}{\sqrt{2}} & -\frac{1}{\sqrt{2}} \\ \frac{1}{\sqrt{2}} & \frac{1}{\sqrt{2}} \end{bmatrix}$
$\dot{\mathbf{R}}$	$\begin{bmatrix} 0 & 0 \\ 0 & 0 \end{bmatrix}$	$\begin{bmatrix} -\frac{1}{\sqrt{2}} & -\frac{1}{\sqrt{2}} \\ \frac{1}{\sqrt{2}} & -\frac{1}{\sqrt{2}} \end{bmatrix}$	$\begin{bmatrix} 0 & 0 \\ 0 & 0 \end{bmatrix}$	$\begin{bmatrix} -\frac{1}{\sqrt{2}} & -\frac{1}{\sqrt{2}} \\ \frac{1}{\sqrt{2}} & -\frac{1}{\sqrt{2}} \end{bmatrix}$
$\dot{\mathbf{F}}$	$\begin{bmatrix} 0 & 0 \\ 0 & 0 \end{bmatrix}$	$\begin{bmatrix} -\frac{1}{\sqrt{2}} & -\frac{1}{\sqrt{2}} \\ \frac{1}{\sqrt{2}} & -\frac{1}{\sqrt{2}} \end{bmatrix}$	$\begin{bmatrix} 2 & 0 \\ 0 & -\frac{1}{2} \end{bmatrix}$	$\begin{bmatrix} 0 & 0 \\ 2\sqrt{2} & -\frac{1}{\sqrt{2}} \end{bmatrix}$
$\mathbf{L}$	$\begin{bmatrix} 0 & 0 \\ 0 & 0 \end{bmatrix}$	$\begin{bmatrix} 0 & -1 \\ 1 & 0 \end{bmatrix}$	$\begin{bmatrix} 1 & 0 \\ 0 & -1 \end{bmatrix}$	$\begin{bmatrix} 0 & 0 \\ 2 & 0 \end{bmatrix}$
$\mathbf{D}$	$\begin{bmatrix} 0 & 0 \\ 0 & 0 \end{bmatrix}$	$\begin{bmatrix} 0 & 0 \\ 0 & 0 \end{bmatrix}$	$\begin{bmatrix} 1 & 0 \\ 0 & -1 \end{bmatrix}$	$\begin{bmatrix} 0 & 1 \\ 1 & 0 \end{bmatrix}$
$\mathbf{W}$	$\begin{bmatrix} 0 & 0 \\ 0 & 0 \end{bmatrix}$	$\begin{bmatrix} 0 & -1 \\ 1 & 0 \end{bmatrix}$	$\begin{bmatrix} 0 & 0 \\ 0 & 0 \end{bmatrix}$	$\begin{bmatrix} 0 & -1 \\ 1 & 0 \end{bmatrix}$

8.3.3.3 Multiplicative decomposition into elastic and plastic deformation

In the previous part, the deformation gradient and its associate measures have been expressed in total form, hence they consist of both an elastic and a plastic part, reflecting

that real life deformations also consist of both elastic and plastic deformation. It may be advantageous to separate elastic and plastic deformation from one another. This is achieved using Fig. 8.12.

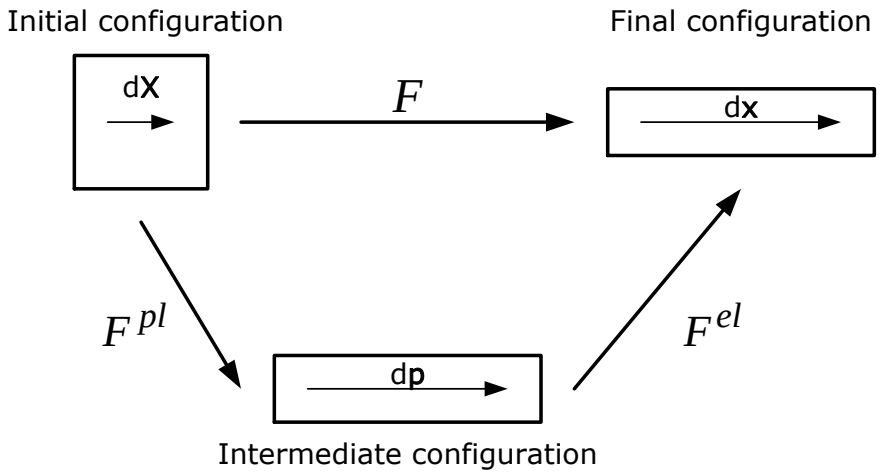

Fig. 8.12. Multiplicative decomposition of deformation gradient.

In Fig. 8.12 the deforming body first undergoes a pure plastic deformation from $d\mathbf{X}$ to $d\mathbf{p}$:

$$d\mathbf{p} = \mathbf{F}^{pl} d\mathbf{X} \tag{8.42}$$

where $\mathbf{F}^{pl}$ is the plastic deformation gradient and $d\mathbf{p}$ is an intermediate state of deformation of the body after having undergone pure plastic deformation.

Thereafter the plastically deformed body undergoes a pure elastic deformation:

$$d\mathbf{x} = \mathbf{F}^{el} d\mathbf{p} = \mathbf{F}^{el}\mathbf{F}^{pl} d\mathbf{X} \tag{8.43}$$

Since $d\mathbf{x} = \mathbf{F} d\mathbf{X}$ it follows:

$$\mathbf{F} = \mathbf{F}^{el}\mathbf{F}^{pl} \tag{8.44}$$

Eq. 8.44 is known as the multiplicative decomposition. The decomposition is not to be interpreted as having direct physical meaning. The body does not first deform plastically and then elastically. Both types of deformation occur simultaneously.

As mentioned in 8.3.3.1, the deformation gradient $\mathbf{F}$ generally consists of both stretch and rotation. If one assumes that all rotation occurs during the plastic deformation it follows:

$$\mathbf{F}^{el} = \mathbf{V}^{el} \tag{8.45}$$

and

$$\mathbf{F}^{pl} = \mathbf{V}^{pl}\mathbf{R} \tag{8.46}$$

where $\mathbf{V}^{el}$ is a symmetric, elastic stretch matrix, $\mathbf{V}^{pl}$ is a symmetric, plastic stretch matrix and $\mathbf{R}$ is the orthogonal rotation matrix.

Applying this decomposition to the velocity gradient (Eq. 8.33) yields:

$$
\begin{aligned}
\mathbf{L} &= \dot{\mathbf{F}}\mathbf{F}^{-1} \\
&= \frac{\partial}{\partial t}\left(\mathbf{F}^{el}\mathbf{F}^{pl}\right)\left(\mathbf{F}^{el}\mathbf{F}^{pl}\right)^{-1} \\
&= \left(\dot{\mathbf{F}}^{el}\mathbf{F}^{pl} + \mathbf{F}^{el}\dot{\mathbf{F}}^{pl}\right)\left(\mathbf{F}^{pl}\right)^{-1}\left(\mathbf{F}^{el}\right)^{-1} \\
&= \dot{\mathbf{F}}^{el}\left(\mathbf{F}^{el}\right)^{-1} + \mathbf{F}^{el}\dot{\mathbf{F}}^{pl}\left(\mathbf{F}^{pl}\right)^{-1}\left(\mathbf{F}^{el}\right)^{-1} \\
&= \dot{\mathbf{V}}^{el}\left(\mathbf{V}^{el}\right)^{-1} + \mathbf{V}^{el}\dot{\mathbf{F}}^{pl}\left(\mathbf{F}^{pl}\right)^{-1}\left(\mathbf{V}^{el}\right)^{-1}
\end{aligned}
\tag{8.47}
$$

The elastic velocity gradient is given by:

$$
\mathbf{L}^{el} = \dot{\mathbf{V}}^{el}\left(\mathbf{V}^{el}\right)^{-1} = \mathbf{D}^{el} + \mathbf{W}^{el} \tag{8.48}
$$

and the plastic velocity gradient:

$$
\mathbf{L}^{pl} = \dot{\mathbf{F}}^{pl}\left(\mathbf{F}^{pl}\right)^{-1} = \mathbf{D}^{pl} + \mathbf{W}^{pl} \tag{8.49}
$$

Inserting Eq. 8.48 and Eq. 8.49 into Eq. 8.47 yields:

$$
\begin{aligned}
\mathbf{L} &= \mathbf{L}^{el} + \mathbf{V}^{el}\mathbf{L}^{pl}\left(\mathbf{V}^{el}\right)^{-1} \qquad \Leftrightarrow \\
&= \mathbf{D}^{el} + \mathbf{W}^{el} + \mathbf{V}^{el}\left(\mathbf{D}^{pl} + \mathbf{W}^{pl}\right)\left(\mathbf{V}^{el}\right)^{-1}
\end{aligned}
\tag{8.50}
$$

Inserting Eq. 8.50 into Eq. 8.35 and Eq. 8.36 gives:

$$
\mathbf{D} = sym\left(\mathbf{L}\right) = \mathbf{D}^{el} + sym\left(\mathbf{V}^{el}\mathbf{D}^{pl}\left(\mathbf{V}^{el}\right)^{-1}\right) + sym\left(\mathbf{V}^{el}\mathbf{W}^{pl}\left(\mathbf{V}^{el}\right)^{-1}\right) \tag{8.51}
$$

and

$$
\mathbf{W} = asym\left(\mathbf{L}\right) = \mathbf{W}^{el} + asym\left(\mathbf{V}^{el}\mathbf{D}^{pl}\left(\mathbf{V}^{el}\right)^{-1}\right) + asym\left(\mathbf{V}^{el}\mathbf{W}^{pl}\left(\mathbf{V}^{el}\right)^{-1}\right) \tag{8.52}
$$

8.3.3.4 Pure plastic deformation

In case of pure plastic deformation $\mathbf{D}^{el} = \mathbf{0}$, $\mathbf{V}^{el} = \mathbf{I}$, $sym\left(\mathbf{D}^{pl}\right) = \mathbf{D}^{pl}$[3], $sym\left(\mathbf{W}^{pl}\right) = \mathbf{0}$[4], $\mathbf{W}^{el} = \mathbf{0}$, $asym\left(\mathbf{D}^{pl}\right) = \mathbf{0}$[5] and $asym\left(\mathbf{W}^{pl}\right) = \mathbf{W}^{pl}$[6].

Eq. 8.51 and Eq. 8.52 therefore reduces to:

$$
\mathbf{D} = \mathbf{D}^{pl} = \frac{1}{2}\left(\mathbf{L} + \mathbf{L}^{T}\right) \tag{8.53}
$$

and

$$
\mathbf{W} = \mathbf{W}^{pl} = \frac{1}{2}\left(\mathbf{L} - \mathbf{L}^{T}\right) \tag{8.54}
$$

The velocity gradient for a pure plastic deformation is[7]:

[3] $sym\left(A_{ij}\right) = A_{ij}$ if A_{ij} is symmetric
[4] $sym\left(A_{ij}\right) = \mathbf{0}$ if A_{ij} is antisymmetric
[5] $asym\left(A_{ij}\right) = \mathbf{0}$ if A_{ij} is symmetric
[6] $asym\left(A_{ij}\right) = A_{ij}$ if A_{ij} is antisymmetric
[7] Chain rule: $\dfrac{\partial u_i}{\partial x_j} = \dfrac{\partial u_i}{\partial X_k}\dfrac{\partial X_k}{\partial x_j}$

$$\mathbf{L} = \dot{\mathbf{F}}\mathbf{F}^{-1} = \frac{\partial \mathbf{u}}{\partial \mathbf{X}}\frac{\partial \mathbf{X}}{\partial \mathbf{x}} = \frac{\partial \mathbf{u}}{\partial \mathbf{x}} \tag{8.55}$$

or in tensor notation:

$$L_{ij} = \frac{\partial u_i}{\partial x_j} \tag{8.56}$$

The rate of deformation then becomes:

$$D_{ij} = \frac{1}{2}\left(L_{ij} + L_{ji}\right) = \frac{1}{2}\left(\frac{\partial u_i}{\partial x_j} + \frac{\partial u_j}{\partial x_i}\right) \tag{8.57}$$

The continuum spin becomes:

$$W_{ij} = \frac{1}{2}\left(L_{ij} - L_{ji}\right) = \frac{1}{2}\left(\frac{\partial u_i}{\partial x_j} - \frac{\partial u_j}{\partial x_i}\right) \tag{8.58}$$

In case of pure plastic deformation one therefore has:

$$\dot{\varepsilon}_{ij}^{pl} = D_{ij} = \frac{1}{2}\left(\frac{\partial u_i}{\partial x_j} + \frac{\partial u_j}{\partial x_i}\right) \tag{8.59}$$

It is interesting to notice that the derived strain rate measure for a pure plastic deformation does not depend on choosing a strain measure but only on the choice of decomposition of deformation gradient.

Eq. 8.59 should not be confused with the time derivative of the traditional small strain measure:

$$\dot{\varepsilon}_{ij} = \frac{\partial}{\partial t}\left(\frac{1}{2}\left(d_{i,j} + d_{j,i}\right)\right) = \frac{1}{2}\left(u_{i,j} + u_{j,i}\right) = \frac{1}{2}\left(\frac{\partial u_i}{\partial x_j} + \frac{\partial u_j}{\partial x_i}\right) \tag{8.60}$$

8.4 Equilibrium equations

8.4.1 Dynamic equilibrium equations

The basic governing differential equations for the finite element flow formulation is the volumetric equilibrium equations without gravitational forces.

The equations may be derived using the cube seen in Fig. 8.13.

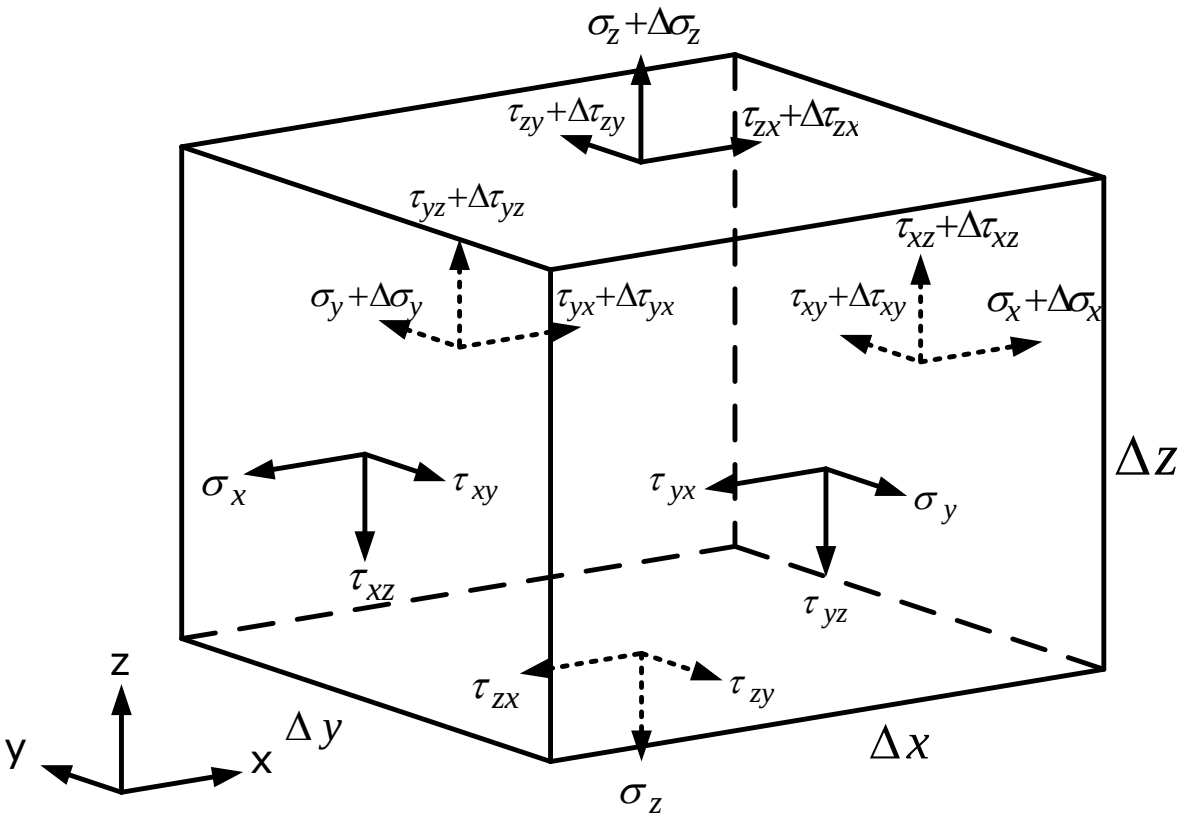

Fig. 8.13. Surface traction's on element.

Newtons second law in the three directions yields:

x-direction

$$\begin{aligned}(\sigma_x + \Delta\sigma_x - \sigma_x)\,\Delta y\Delta z + (\tau_{yx} + \Delta\tau_{yx} - \tau_{yx})\,\Delta x\Delta z + (\tau_{zx} + \Delta\tau_{zx} - \tau_{zx})\,\Delta x\Delta y &= \rho\Delta x\Delta y\Delta z\dot{u}_x \quad \Leftrightarrow \\ \frac{\Delta\sigma_x}{\Delta x} + \frac{\Delta\tau_{yx}}{\Delta y} + \frac{\Delta\tau_{zx}}{\Delta z} &= \rho\dot{u}_x \end{aligned} \tag{8.61}$$

y-direction

$$\begin{aligned}(\sigma_y + \Delta\sigma_y - \sigma_y)\,\Delta x\Delta z + (\tau_{xy} + \Delta\tau_{xy} - \tau_{xy})\,\Delta y\Delta z + (\tau_{zy} + \Delta\tau_{zy} - \tau_{zy})\,\Delta x\Delta y &= \rho\Delta x\Delta y\Delta z\dot{u}_y \quad \Leftrightarrow \\ \frac{\Delta\sigma_y}{\Delta y} + \frac{\Delta\tau_{xy}}{\Delta x} + \frac{\Delta\tau_{zy}}{\Delta z} &= \rho\dot{u}_y \end{aligned} \tag{8.62}$$

z-direction

$$\begin{aligned}(\sigma_z + \Delta\sigma_z - \sigma_z)\,\Delta x\Delta y + (\tau_{xz} + \Delta\tau_{xz} - \tau_{xz})\,\Delta y\Delta z + (\tau_{yz} + \Delta\tau_{yz} - \tau_{yz})\,\Delta x\Delta z &= \rho\Delta x\Delta y\Delta z\dot{u}_z \quad \Leftrightarrow \\ \frac{\Delta\sigma_z}{\Delta z} + \frac{\Delta\tau_{xz}}{\Delta x} + \frac{\Delta\tau_{yz}}{\Delta y} &= \rho\dot{u}_z \end{aligned} \tag{8.63}$$

Taking the limit of Eq. 8.61-Eq. 8.63 yields the force equilibrium equations:

$$\begin{aligned} \frac{\partial \sigma_x}{\partial x} + \frac{\partial \tau_{yx}}{\partial y} + \frac{\partial \tau_{zx}}{\partial z} &= \rho \dot{u}_x \\ \frac{\partial \sigma_y}{\partial y} + \frac{\partial \tau_{xy}}{\partial x} + \frac{\partial \tau_{zy}}{\partial z} &= \rho \dot{u}_y \\ \frac{\partial \sigma_z}{\partial z} + \frac{\partial \tau_{xz}}{\partial x} + \frac{\partial \tau_{yz}}{\partial y} &= \rho \dot{u}_z \end{aligned} \tag{8.64}$$

Eq. 8.64 may be expressed in tensor notation as:

$$\sigma_{ij,j} = \rho \dot{u}_i \tag{8.65}$$

where $\sigma_{ij,j}$ is the partial derivatives of the Cauchy stress tensor, ρ is the density and $\dot{u}_i$ is the acceleration (time derivative of velocities u_i).

8.4.2 Quasi-static equilibrium equations

In the case of negligible inertia forces ($\rho \dot{u}_i \approx 0$), Eq. 8.65 reduces to the quasi-static equilibrium equations:

$$\sigma_{ij,j} = 0 \tag{8.66}$$

Eq. 8.66 is known as the "strong form" and is the basis for the rest of the chapter.

8.5 Effective stress, yield function, criterion and surface - Von Mises plasticity

Often it is beneficial to be able to evaluate a complex 3-dimensional stress state σ_{ij} in terms of a scalar value $\bar{\sigma}$, which is known as the effective or equivalent stress. One such measure is the effective von Mises stress:

$$\bar{\sigma} = \sqrt{\frac{3}{2}\sigma_{ij}\sigma_{ij} - \frac{1}{2}\sigma_{ii}\sigma_{jj}} = \sqrt{\frac{3}{2}S_{ij}S_{ij}} = \sqrt{3J_2} \tag{8.67}$$

where $S_{ij} = \sigma_{ij} - \delta_{ij}\sigma_m = \sigma_{ij} - \delta_{ij}\sigma_{kk}/3$ are the deviatoric stresses, δ_{ij} is the Kronecker delta taking the value 1 when $i = j$ and 0 when $i \neq j$ and $J_2 = \frac{1}{2}S_{ij}S_{ij}$ is the second invariant of the deviatoric stress tensor.

The limit stress, when the material deforms plastically, is known as the flow stress σ_o. The criterion (also called condition) for yielding to occur is therefore $\bar{\sigma} = \sigma_0$.

The yield function $f(\sigma_{ij})$ is defined by:

$$f(\sigma_{ij}) = \bar{\sigma} - \sigma_o \tag{8.68}$$

It should be noticed in relation to Eq. 8.68 that $\bar{\sigma}$ is only dependent on the choice of effective stress function and on the stress state, whereas σ_0 is only dependent on material, temperature, strain, strain rate, density etc. hence it is only material related.

Often a different version of the yield function is used for mathematical convenience:

$$f(\sigma_{ij}) = \bar{\sigma}^2 - \sigma_o^2 = \frac{3}{2}S_{ij}S_{ij} - \sigma_o^2 \tag{8.69}$$

The criterion for yielding of the material was $\bar{\sigma} = \sigma_0$, hence $f(\sigma_{ij}) = 0$. All the different combinations of stresses fulfilling the yield criterion form a surface known as the yield surface:

$$f(\sigma_{ij}) = \bar{\sigma} - \sigma_o = 0 \tag{8.70}$$

If the stress state described by the effective stress $\bar{\sigma}$ is inside the yield surface, elastic deformation is occurring and if it is on the yield surface, elasto-plastic deformation is occurring. It is not possible for the effective stress $\bar{\sigma}$ to be outside the yield surface.

The possibility for creep is not considered in this presentation.

8.6 Effective stress, yield function, criterion and surface - Porous metal plasticity

An early porous plasticity model for compacting of metal powders was developed by Kuhn & Downey [61] and Green [41]:

$$\bar{\sigma}^2 = AJ_2 + BI_1^2 \tag{8.71}$$

where $\bar{\sigma}$ is the effective stress, $J_2 = \frac{1}{2}S_{ij}S_{ij}$ is the second invariant of the deviatoric stress tensor, $I_1 = \sigma_{kk} = \delta_{ij}\sigma_{ij}$ is the trace of the stress tensor and A and B are functions depending on the relative porosity density R.

The yield function is given by:

$$f(\sigma_{ij}) = AJ_2 + BI_1^2 - \sigma_f^2 \tag{8.72}$$

where σ_f is the flow stress in uniaxial compression of the porous material. It can then be shown that $B = 1 - \frac{A}{3}$. If the material is fully dense, $A = 3$ and the von Mises yield function (Eq. 8.69) is recovered.

The flow stress of the porous material σ_f is related to the flow stress of the fully dense material σ_o by:

$$\sigma_f^2 = \eta\sigma_o^2 \tag{8.73}$$

where η is a function of the relative density $R = \frac{\rho}{\rho_o}$, where ρ is the density of the porous material and ρ_o is the density of the fully dense material.

The relationship between relative density R, η and A should be obtained experimentally. Shima & Oyane [90] suggested the following relations including an extra variable f:

$$A = \frac{3}{1 + \frac{1}{9f^2}} \tag{8.74}$$

$$\eta = \frac{R^5}{1 + \frac{1}{9f^2}} \tag{8.75}$$

$$f = \frac{0.4}{\sqrt{1-R}} \tag{8.76}$$

It is noticed in Eq. 8.76 that if $R = 1$, $f = \infty$. Since $R = 1$ implies a fully dense material, it is common to change the material behaviour from that of a porous material to that of a fully dense material when R reaches a value sufficiently close to 1 in order to avoid dividing by zero.

The rate of change in relative density $\dot{R}$ is related to the volumetric plastic strain rate $\dot{\varepsilon}_v^{pl} = \dot{\varepsilon}_{kk}^{pl}$:

$$\dot{R} = -\dot{\varepsilon}_v^{pl} R \tag{8.77}$$

For a thorough description of flow rule and numerical implementation the reader is referred to Kobayashi et al. [58]. One remark should be made regarding the porous plasticity formulation. Damage of the material, modelled as a loss of density, requires positive volumetric dilatation. This implies that pure shear stress deformation, where the volumetric strain is zero, does not result in a loss in density and therefore damage is not accumulated.

8.7 Flow rules

Druckers normality hypothesis (Drucker [27]) states that for plastic deformation, the plastic strain increment $d\varepsilon_{ij}^{pl}$ is normal to the yield surface $f(\sigma_{ij})$:

$$d\varepsilon_{ij}^{pl} = d\lambda \frac{\partial f}{\partial \sigma_{ij}} \tag{8.78}$$

where $d\lambda$ is the plastic multiplier scaling the size of the plastic strain increment.

8.7.1 Levy-Mises flow rule

The normal $\dfrac{\partial f}{\partial \sigma_{ij}}$ may be determined by differentiation of the von Mises yield surface (Eq. 8.69):

$$\frac{\partial f}{\partial \sigma_{ij}} = 3S_{ij} \tag{8.79}$$

hence a normal to the von Mises yield surface is the deviatoric stress tensor S_{ij}. Noticing that $d\varepsilon_{ij}^{pl} = \dot{\varepsilon}_{ij}^{pl} dt$ and $d\lambda = \dot{\lambda} dt$, where $\dot{\varepsilon}_{ij}^{pl}$ are the plastic strain rates and $\dot{\lambda}$ is the time derivative of the plastic multiplier, Eq. 8.78 is written as:

$$\dot{\varepsilon}_{ij}^{pl} = \dot{\lambda} S_{ij} \tag{8.80}$$

The rate of the plastic multiplier may be determined by writing Eq. 8.80 in uniaxial tension:

$$\begin{aligned} \dot{\varepsilon}_{11}^{pl} &= \dot{\lambda}\frac{2}{3}\sigma_{11} \quad \Leftrightarrow \\ \dot{\lambda} &= \frac{3}{2}\frac{\dot{\varepsilon}_{11}^{pl}}{\sigma_{11}} \end{aligned} \tag{8.81}$$

knowing that in uniaxial tension $\dot{\bar{\varepsilon}}^{pl} = \sqrt{\frac{2}{3}\dot{\varepsilon}_{ij}^{pl}\dot{\varepsilon}_{ij}^{pl}} = \dot{\varepsilon}_{11}^{pl}$, where $\dot{\bar{\varepsilon}}^{pl}$ is the effective plastic strain rate, and $\sigma_{11} = \bar{\sigma}$, Eq. 8.81 becomes:

$$\begin{aligned} \dot{\varepsilon}_{ij}^{pl} &= \frac{3}{2}\frac{\dot{\bar{\varepsilon}}^{pl}}{\bar{\sigma}} S_{ij} \quad \Leftrightarrow \\ S_{ij} &= \frac{2}{3}\frac{\bar{\sigma}}{\dot{\bar{\varepsilon}}^{pl}}\dot{\varepsilon}_{ij}^{pl} \end{aligned} \tag{8.82}$$

hence the Levy-Mises flow rule relates deviatoric stresses to plastic strain rates.

8.7.2 Shima-Oyane flow rule

If the porous yield surface of Shima & Oyane (Eq. 8.72) is inserted into Eq. 8.78 and taking advantage of $B = 1 - \frac{A}{3}$ one obtains:

$$\frac{\partial f}{\partial \sigma_{ij}} = AS_{ij} + 2\left(3 - A\right)\delta_{ij}^2\sigma_{ij} \tag{8.83}$$

The normality hypothesis then yields:

$$\dot{\varepsilon}_{ij}^{pl} = \dot{\lambda}\left[AS_{ij} + 2\left(3 - A\right)\delta_{ij}^2\sigma_{ij}\right] \tag{8.84}$$

Again the time derivative of the plastic multiplier $\left(\dot{\lambda}\right)$ is determined from uniaxial tension:

$$\begin{aligned} \dot{\varepsilon}_{11}^{pl} &= \dot{\lambda}\left[A\frac{2}{3}\sigma_{11} + 2\left(3 - A\right)\frac{1}{3}\sigma_{11}\right] \quad \Leftrightarrow \\ \dot{\lambda} &= \frac{1}{2}\frac{\dot{\bar{\varepsilon}}^{pl}}{\bar{\sigma}} \end{aligned} \tag{8.85}$$

whereby the associated flow rule becomes:

$$\begin{aligned} \dot{\varepsilon}_{ij}^{pl} &= \frac{1}{2}\frac{\dot{\bar{\varepsilon}}^{pl}}{\bar{\sigma}}\left[AS_{ij} + 2\left(3 - A\right)\delta_{ij}^2\sigma_{ij}\right] \quad \Leftrightarrow \\ \dot{\varepsilon}_{ij}^{pl} &= \frac{\dot{\bar{\varepsilon}}^{pl}}{\bar{\sigma}}\left[\frac{A}{2}S_{ij} + \left(3 - A\right)\delta_{ij}^2\sigma_{ij}\right] \end{aligned} \tag{8.86}$$

By splitting the deviatoric stresses $S_{ij} = \sigma_{ij} - \frac{\delta_{ij}\sigma_{ij}}{3}$ one obtains:

$$\dot{\varepsilon}_{ij}^{pl} = \frac{\dot{\bar{\varepsilon}}^{pl}}{\bar{\sigma}}\left[\frac{A}{2} - \frac{A}{6}\delta_{ij} + \left(3 - A\right)\delta_{ij}^2\right]\sigma_{ij} \tag{8.87}$$

By inversion (Oh et al. [78]) the stresses are obtained as function of strain rates:

$$\sigma_{ij} = \frac{\bar{\sigma}}{\dot{\bar{\varepsilon}}^{pl}}\left[\frac{2}{A}\left(\dot{\varepsilon}_{ij}^{pl} - \frac{1}{3}\delta_{ij}\dot{\varepsilon}_{ij}^{pl}\right) + \frac{\delta_{ij}}{3\left(3 - A\right)}\delta_{ij}\dot{\varepsilon}_{ij}^{pl}\right] \tag{8.88}$$

hence the Shima-Oyane flow rule relates plastic strain rates and stresses.

It should be noticed that for the porous formulation, the effective plastic strain rate is given by:

$$\dot{\bar{\varepsilon}}^{pl} = \sqrt{\frac{2}{A} e_{ij}^{pl} e_{ij}^{pl} + \frac{1}{3\,(3-A)} \left(\delta_{ij} \dot{\varepsilon}_{ij}^{pl}\right)^2} \tag{8.89}$$

where $\dot{e}_{ij}^{pl} = \dot{\varepsilon}_{ij}^{pl} - \frac{1}{3}\delta_{ij}\dot{\varepsilon}_{ij}^{pl}$ is the deviatoric plastic strain rate tensor.

8.8 Derivation of finite element equations using the variational formulation

In textbooks such as Kobayashi et al. [58] the finite element equations for the flow formulation are derived using the variational method. This method consists of expressing a functional π, which should be stationary for arbitrary variations $\delta\dot{\bar{\varepsilon}}^{pl}$. The functional π is defined as:

$$\pi = \int_V \bar{\sigma}\dot{\bar{\varepsilon}}^{pl} dV - \int_S \tau_i u_i dS \tag{8.90}$$

where $\bar{\sigma}$ is the effective stress and $\dot{\bar{\varepsilon}}^{pl}$ is the effective plastic strain rate integrated over the volume V of the domain. τ_i are surface traction's and u_i are surface velocities integrated over the surface S of the domain. The integral over the volume is the internally dissipated power and the surface integral is the externally applied power. Stationarity of the functional yields:

$$\delta\pi = \int_V \bar{\sigma}\delta\dot{\bar{\varepsilon}}^{pl} dV - \int_S \tau_i \delta u_i dS = 0 \tag{8.91}$$

The variational functional (Eq. 8.91) expresses an energy balance since it demands that the externally applied power must equal the internally dissipated power.

Plastic incompressibility is typically enforced by Lagrangian multipliers λ or a penalty factor K, which is a large number.

8.8.1 Formulation using Lagrangian multipliers

Eq. 8.90 is modified by adding the term $\int_V \lambda\dot{\varepsilon}_V^{pl} dV$:

$$\pi = \int_V \bar{\sigma}\dot{\bar{\varepsilon}}^{pl} dV + \int_V \lambda\dot{\varepsilon}_V^{pl} - \int_S \tau_i u_i dS \tag{8.92}$$

where $\dot{\varepsilon}_{ii}^{pl} = \dot{\varepsilon}_V^{pl}$ is the volumetric plastic strain rate. Stationarity of Eq. 8.92 yields:

$$\delta\pi = \int_V \bar{\sigma}\delta\dot{\bar{\varepsilon}}^{pl} dV + \int_V \lambda\delta\dot{\varepsilon}_V^{pl} dV + \int_V \dot{\varepsilon}_V^{pl}\delta\lambda dV - \int_S \tau_i \delta u_i dS = 0 \tag{8.93}$$

Eq. 8.93 is split into two parts as follows:

$$\begin{aligned} \textstyle\int_V \bar{\sigma}\delta\dot{\bar{\varepsilon}}^{pl} dV + \int_V \lambda\delta\dot{\varepsilon}_V^{pl} dV - \int_S \tau_i \delta u_i dS &= 0 \\ \textstyle\int_V \dot{\varepsilon}_V^{pl}\delta\lambda dV &= 0 \end{aligned} \tag{8.94}$$

The splitting is motivated by ensuring a sufficient number of equations compared to the number of unknowns pr. element.

8.8.2 Formulation using penalty factor

Eq. 8.90 is modified by adding the term $\frac{K}{2}\int_V \left(\dot{\varepsilon}_V^{pl}\right)^2 dV$:

$$\pi = \int_V \bar{\sigma}\dot{\bar{\varepsilon}}^{pl} dV + \frac{K}{2}\int_V \left(\dot{\varepsilon}_V^{pl}\right)^2 dV - \int_S \tau_i u_i dS \tag{8.95}$$

Stationarity of the functional yields:

$$\delta\pi = \int_V \bar{\sigma}\delta\dot{\bar{\varepsilon}}^{pl} dV + K\int_V \dot{\varepsilon}_V^{pl}\delta\dot{\varepsilon}_V^{pl} dV - \int_S \tau_i \delta u_i dS \tag{8.96}$$

8.9 The author's derivation of the finite element equations using the Galerkin method

Although well established in textbooks on the subject of the finite element flow formulation, the author is not satisfied with the variational formulation of the finite element equations. In the author's opinion the variational formulation lacks physical interpretation and it is not intuitively clear how to generate the discretized equations from the variational formulation. Therefore the author has derived the finite element equations based on the Galerkin method, which is part of a family of methods known as weighted residual methods, see for instance Cook et al. [23] chapter 5.

The first step in deriving the finite element equations is to multiply the governing differential equations (Eq. 8.66) by some weight functions w_i and to enforce equilibrium in an average sense over a finite volume V:

$$\int_V w_i \sigma_{ij,j} dV = 0 \tag{8.97}$$

By applying partial integration to Eq. 8.97, the following is obtained:

$$\int_V w_i \sigma_{ij,j} dV = -\int_V w_{i,j}\sigma_{ij} dV + \int_V \left(w_i\sigma_{ij}\right)_{,j} dV \tag{8.98}$$

The right hand side in Eq. 8.98 is rewritten using the divergence theorem:

$$-\int_V w_{i,j}\sigma_{ij} dV + \int_V \left(w_i\sigma_{ij}\right)_{,j} dV = -\int_V w_{i,j}\sigma_{ij} dV + \int_S w_i\sigma_{ij}n_j dS = 0 \tag{8.99}$$

where n_j is the unit normal to the surface S of the finite element. Noticing that $\sigma_{ij}n_j = \tau_i$ implies:

$$\int_S w_i\sigma_{ij}n_j dS = \int_S w_i\tau_i dS \tag{8.100}$$

where τ_i are the surface tractions.

Splitting the stress tensor σ_{ij} into a deviatoric part S_{ij} and a mean (hydrostatic) part $\sigma_m = \sigma_{kk}/3$ gives:

$$\int_V w_{i,j}S_{ij} dV + \int_V w_{i,j}\delta_{ij}\sigma_m dV = \int_S w_i\tau_i dS \tag{8.101}$$

If the interpolating functions N_i are used as weight functions w_i Eq. 8.101 yields:

$$\int_V N_{i,j} S_{ij} dV + \int_V N_{i,j} \delta_{ij} \sigma_m dV = \int_S N_i \tau_i dS \tag{8.102}$$

8.9.1 Penalty based finite element equations

According to Zienkiewicz & Taylor [111] p. 5 the mean stress σ_m is related to the volumetric plastic strain rate $\dot{\varepsilon}_V^{pl} = \dot{\varepsilon}_{kk}^{pl}$ through:

$$\sigma_m = K \dot{\varepsilon}_V^{pl} \tag{8.103}$$

where K is the volumetric viscosity of the material. Inserting Eq. 8.103 into Eq. 8.102 gives:

$$\int_V N_{i,j} S_{ij} dV + K \int_V N_{i,j} \delta_{ij} \dot{\varepsilon}_V^{pl} dV = \int_S N_i \tau_i dS \tag{8.104}$$

which are the finite element equations, derived using the Galerkin method, on tensor form. It is noticed that if $K \to \infty$, $\dot{\varepsilon}_V^{pl} \to 0$ for a given mean stress σ_m. A large volumetric viscosity therefore implies approximate incompressibility of the material. This method of enforcing plastic incompressibility of the material is known as penalization. K may therefore be interpreted as a penalty factor penalizing volumetric shrinkage.

Inserting Levy-Mises flow rule $S_{ij} = \frac{2}{3} \frac{\bar{\sigma}}{\dot{\bar{\varepsilon}}^{pl}} \dot{\varepsilon}_{ij}^{pl}$ into Eq. 8.104 yields:

$$\int_V N_{i,j} \frac{2}{3} \frac{\bar{\sigma}}{\dot{\bar{\varepsilon}}^{pl}} \dot{\varepsilon}_{ij}^{pl} dV + K \int_V N_{i,j} \delta_{ij} \dot{\varepsilon}_V^{pl} dV = \int_S N_i \tau_i dS \tag{8.105}$$

Eq. 8.105 is known as the irreducible finite element flow formulation.

8.9.2 Velocity-Pressure based finite element equations

The mean stress σ_m in Eq. 8.102 may also be treated as an unknown instead of being substituted by Eq. 8.103. It is then necessary to introduce an extra equation to have the same number of equations as the number of unknowns in order to obtain a unique solution. The extra equation comes from that the volumetric plastic strain rate must be zero in an element, hence:

$$\int_V \dot{\varepsilon}_V^{pl} dV = 0 \tag{8.106}$$

The equation system to be solved then becomes:

$$\begin{array}{rcl} \int_V N_{i,j} S_{ij} dV + \int_V N_{i,j} \delta_{ij} \sigma_m dV & = & \int_S N_i \tau_i dS \\ \int_V \dot{\varepsilon}_V^{pl} dV & = & 0 \end{array} \tag{8.107}$$

where the unknowns in each element are the nodal velocities and the mean stress in the element.

It is noticed when comparing Eq. 8.94 and Eq. 8.107 that the mean stress σ_m is equal to the Lagrangian multiplier λ. It is also noticed that the introduced method of deriving the finite element equations does not include splitting of an equation into two parts, but follows directly from combining an equation system with one more unknown, the mean

stress σ_m, than equations originating from the formulation, with an extra equation to form an equation system with as many equations as unknowns.

8.10 Finite element equations for computer implementation

The finite element equations on tensor form (Eq. 8.105) are expressed in a form involving both vectors and matrices to enhance the understanding of how to perform a practical computer implementation of the finite element flow formulation.

The interpolating functions are expressed as $N_i = \mathbf{N}^T$. The shape functions $\mathbf{N}^T$ depend on element type and order of the shape functions.

Velocities $\mathbf{u}$ inside an element may be interpolated using the shape functions $\mathbf{N}^T$ and a velocity vector $\mathbf{v}^e$ containing nodal values of velocities for the element:

$$\mathbf{u} = \mathbf{N}^T \mathbf{v}^{\mathrm{e}} \tag{8.108}$$

The partial derivatives of the shape functions are then expressed as $N_{i,j} = \mathbf{L}\mathbf{N}^T = \mathbf{B}$ where $\mathbf{B}$ is the strain-rate matrix and $\mathbf{L}$ is a differential operator matrix:

$$\mathbf{L} = \begin{bmatrix} \dfrac{\partial}{\partial x} & 0 & 0 \\ 0 & \dfrac{\partial}{\partial y} & 0 \\ 0 & 0 & \dfrac{\partial}{\partial z} \\ \dfrac{\partial}{\partial y} & \dfrac{\partial}{\partial x} & 0 \\ 0 & \dfrac{\partial}{\partial z} & \dfrac{\partial}{\partial y} \\ \dfrac{\partial}{\partial z} & 0 & \dfrac{\partial}{\partial x} \end{bmatrix} \tag{8.109}$$

From the interpolated element velocities $\mathbf{u}$ the strain rates $\dot{\boldsymbol{\varepsilon}}^{pl}$ can be written as:

$$\dot{\boldsymbol{\varepsilon}}^{pl} = \mathbf{L}\mathbf{u} = \mathbf{L}\mathbf{N}^{\mathrm{T}}\mathbf{v}^{\mathrm{e}} = \mathbf{B}\mathbf{v}^e \tag{8.110}$$

It should be noticed that the tensor $\dot{\varepsilon}_{ij}^{pl}$ has nine components but, due to symmetry of the tensor, there are only six components in $\dot{\boldsymbol{\varepsilon}}^{pl}$. Therefore $\frac{2}{3}\dot{\varepsilon}_{ij}^{pl}$ can be expressed by:

$$\frac{2}{3}\dot{\boldsymbol{\varepsilon}}^{pl} = \mathbf{D}\mathbf{B}\mathbf{v}^e \tag{8.111}$$

where $\mathbf{D} = diag\left\{\frac{2}{3}, \frac{2}{3}, \frac{2}{3}, \frac{1}{3}, \frac{1}{3}, \frac{1}{3}\right\}$.

The volumetric strain rate $\dot{\boldsymbol{\varepsilon}}_V^{pl}$ is written as:

$$\dot{\boldsymbol{\varepsilon}}_V^{pl} = \mathbf{C}^T\mathbf{B}\mathbf{v}^e \tag{8.112}$$

where $\mathbf{C}^T = \{1, 1, 1, 0, 0, 0\}^T$ is the Kronecker delta (δ_{ij}) on vectorized form.

8.10.1 Finite element equations based on penalty formulation

Eq. 8.105 was integrated over the entire domain V. However since the domain is supposed to be subdivided into a number of smaller finite elements, the integral is expressed accordingly:

$$\begin{aligned} \int_V N_{i,j} \frac{2}{3} \frac{\bar{\sigma}}{\dot{\bar{\varepsilon}}^{pl}} \dot{\varepsilon}_{ij}^{pl} dV + K \int_V N_{i,j} \delta_{ij} \dot{\varepsilon}_V^{pl} dV &= \int_S N_i \tau_i dS \quad \Leftrightarrow \\ \sum_{N=1}^{N^e} \left(\int_{V^e} N_{i,j} \frac{2}{3} \frac{\bar{\sigma}}{\dot{\bar{\varepsilon}}^{pl}} \dot{\varepsilon}_{ij}^{pl} dV^e + K \int_{V^e} N_{i,j} \delta_{ij} \dot{\varepsilon}_V^{pl} dV^e - \int_{S^e} N_i \tau_i dS^e \right) &= 0 \end{aligned} \tag{8.113}$$

where N^e is the number of finite elements and V^e and S^e are respectively the volume and surface area of the finite element.

Eq. 8.113 is then expressed using matrices and vectors:

$$\begin{aligned} \sum_{N=1}^{N^e} \left(\int_{V^e} N_{i,j} \frac{2}{3} \frac{\bar{\sigma}}{\dot{\bar{\varepsilon}}^{pl}} \dot{\varepsilon}_{ij}^{pl} dV^e + K \int_{V^e} N_{i,j} \delta_{ij} \dot{\varepsilon}_V^{pl} dV^e - \int_{S^e} N_i \tau_i dS^e \right) &= 0 \quad \Leftrightarrow \\ \sum_{N=1}^{N^e} \left(\int_{V^e} \frac{\bar{\sigma}}{\dot{\bar{\varepsilon}}^{pl}} \mathbf{B}^{\mathrm{T}} \mathbf{D} \mathbf{B} \mathbf{v}^e dV^e + K \int_{V^e} \mathbf{B}^{\mathrm{T}} \mathbf{C} \mathbf{C}^{\mathrm{T}} \mathbf{B} \mathbf{v}^e dV^e - \int_{S^e} \mathbf{N} \boldsymbol{\tau} dS^e \right) &= \mathbf{0} \end{aligned} \tag{8.114}$$

where $\boldsymbol{\tau}$ is the surface traction vector.

8.10.2 Finite element equations based on velocity-pressure formulation

Again the integral Eq. 8.107 over the entire domain V is subdivided into integration over a number of finite elements.

$$\begin{aligned} \int_V N_{i,j} S_{ij} dV + \int_V N_{i,j} \delta_{ij} \sigma_m dV - \int_S N_i \tau_i dS &= 0 \quad \Leftrightarrow \\ \sum_{N=1}^{N^e} \left(\int_{V^e} N_{i,j} S_{ij} dV^e + \int_{V^e} N_{i,j} \delta_{ij} \sigma_m dV^e - \int_{S^e} N_i \tau_i dS^e \right) &= 0 \end{aligned} \tag{8.115}$$

Eq. 8.115 is then expressed using matrices and vectors:

$$\begin{aligned} \sum_{N=1}^{N^e} \left(\int_{V^e} N_{i,j} S_{ij} dV^e + \int_{V^e} N_{i,j} \delta_{ij} \sigma_m dV^e - \int_{S^e} N_i \tau_i dS^e \right) &= 0 \quad \Leftrightarrow \\ \sum_{N=1}^{N^e} \left(\int_{V^e} \frac{\bar{\sigma}}{\dot{\bar{\varepsilon}}^{pl}} \mathbf{B}^{\mathrm{T}} \mathbf{D} \mathbf{B} \mathbf{v}^e dV^e + \int_{V^e} \mathbf{B}^{\mathrm{T}} \mathbf{C} \sigma_m dV^e - \int_{S^e} \mathbf{N} \boldsymbol{\tau} dS^e \right) &= \mathbf{0} \end{aligned} \tag{8.116}$$

The volumetric strain Eq. 8.106 becomes:

$$\begin{aligned} \int_V \dot{\varepsilon}_V^{pl} dV &= 0 \quad \Leftrightarrow \\ \sum_{N=1}^{N^e} \int_{V^e} \dot{\varepsilon}_V^{pl} dV^e &= 0 \quad \Leftrightarrow \\ \sum_{N=1}^{N^e} \int_{V^e} \mathbf{C}^{\mathrm{T}} \mathbf{B} \mathbf{v}^e dV^e &= \mathbf{0} \end{aligned} \tag{8.117}$$

The equations Eq. 8.116 and Eq. 8.117 are then combined to form an equation system:

$$\sum_{N=1}^{N^e}\left(\begin{bmatrix} \int_{V^e}\frac{\bar{\sigma}}{\dot{\bar{\varepsilon}}^{pl}}\mathbf{B}^{\mathrm{T}}\mathbf{D}\mathbf{B}dV^e & \int_{V^e}\mathbf{B}^{\mathrm{T}}\mathbf{C}dV^e \\ \int_{V^e}\mathbf{C}^{\mathrm{T}}\mathbf{B}dV^e & 0 \end{bmatrix}\begin{bmatrix} \mathbf{v}^e \\ \sigma_m \end{bmatrix}\right) = \sum_{N=1}^{N^e}\left(\begin{bmatrix} \int_{S^e}\mathbf{N}\boldsymbol{\tau}dS^e \\ 0 \end{bmatrix}\right) \quad (8.118)$$

8.10.3 Numerical integration of finite element equations

It can be seen from Eq. 8.114 and Eq. 8.118 that numerical integration needs to be performed in order to obtain the finite element equations. For the penalized finite element equations, a problem may occur. This is seen from the following. First it is beneficial to divide Eq. 8.114 into three integrals:

$$\begin{array}{ccccc} \underbrace{\sum_{N=1}^{N^e}\int_{V^e}\frac{\bar{\sigma}}{\dot{\bar{\varepsilon}}^{pl}}\mathbf{B}^{\mathrm{T}}\mathbf{D}\mathbf{B}\mathbf{v}^e dV^e}_{\mathbf{K}^D\mathbf{v}} & + & \underbrace{\sum_{N=1}^{N^e}K\int_{V^e}\mathbf{B}^{\mathrm{T}}\mathbf{C}\mathbf{C}^{\mathrm{T}}\mathbf{B}\mathbf{v}^e dV^e}_{\mathbf{K}^H\mathbf{v}} & = & \underbrace{\sum_{N=1}^{N^e}\int_{S^e}\mathbf{N}\boldsymbol{\tau}dS^e}_{\mathbf{f}} \\ & + & \mathbf{K}^H\mathbf{v} & = & \mathbf{f} \\ & & \left(\mathbf{K}^D+\mathbf{K}^H\right)\mathbf{v} & = & \mathbf{f} \end{array} \iff \quad (8.119)$$

where $\mathbf{K}^D$ is the deviatoric part of the finite element equations and $\mathbf{K}^H$ is the hydrostatic part. $\mathbf{v}$ is the nodal point velocity vector containing velocities of all nodes in the entire volume and $\mathbf{f}$ is the right hand side.

It can then be seen from Eq. 8.119 that using a large penalty factor K leads to locking because $\mathbf{K}^H \to \infty$ and the velocities obtained are the trivial solution $\mathbf{v} = \mathbf{0}$, hence if too large a value of the penalty factor is utilized, the finite element mesh locks. To circumvent this problem, different numerical integration schemes are utilized. The finite element equations of $\mathbf{K}^H$ are under integrated, hence the matrix is singular (rank-deficient). The finite element equations of $\mathbf{K}^D$ are fully integrated so the entire matrix system $\left(\mathbf{K}^D+\mathbf{K}^H\right)$ is non-singular.

The problems of the penalized finite element equations are avoided by the velocity-pressure formulation (Eq. 8.118), but at the expense of introducing an extra variable σ_m for each element and thereby increasing the size of the equation system to be solved.

The numerical integration is performed using Gauss quadrature. The basic idea is to evaluate the integrand at some points in the finite element and then to sum the different values to give the total value of the integral for the particular element. The sampling points are so-called Gauss points. The number and location of Gauss points are both dependent on integration order and element type. The general form of converting the analytical form of an integral to a numerical one in three dimensions is the following:

$$I = \int_{-1}^{1}\int_{-1}^{1}\int_{-1}^{1}\phi\left(\xi,\eta,\zeta\right)d\xi d\eta d\zeta \approx \sum_{i}^{l}\sum_{j}^{m}\sum_{k}^{n}W_i W_j W_k \phi\left(\xi,\eta,\zeta\right) \quad (8.120)$$

where $\phi\left(\xi,\eta,\zeta\right)$ is the function to be integrated expressed by the natural coordinates (ξ,η,ζ) and W_i, W_j and W_k are weight factors. How many Gauss points that are needed is determined by the polynomial order of the function ϕ. If the polynomial order is $2n-1$ then an n order integration scheme will be sufficient for full integration. From Eq. 8.119 it can be seen that the polynomial order is determined by the order of the derivative of the interpolating functions, hence the order of the product of the two $\mathbf{B}$ matrices. If linear

interpolating functions $\mathbf{N}$ are utilized, the $\mathbf{B}$ matrices will be linear functions of (ξ, η, ζ) and therefore their product will be a polynomial of maximum order 2. Hence a 2. order Gauss quadrature scheme will be sufficient for full integration. If a 1. order integration scheme is applied, only reduced integration will be achieved. For a 4 node quadrilateral element that will imply four integration points for full integration and 1 point for reduced integration. The principle can be seen in Fig. 8.14

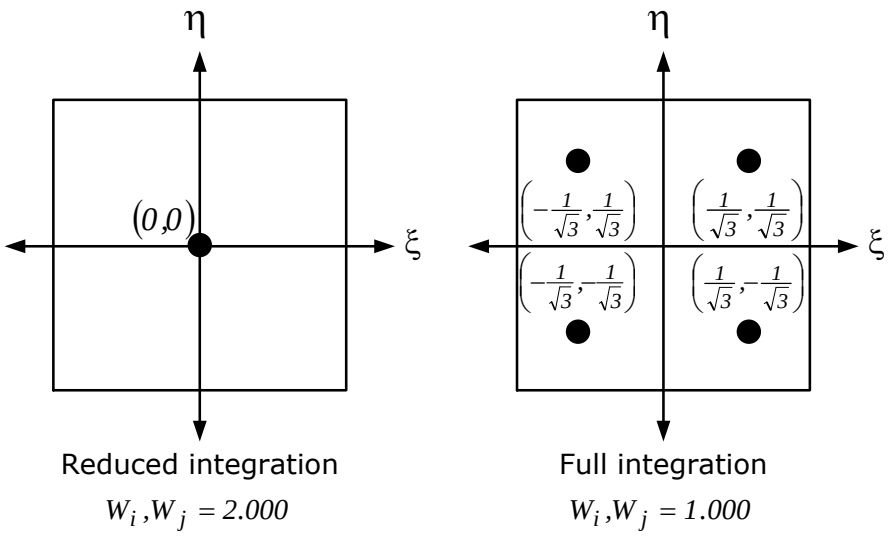

Fig. 8.14. Gauss quadrature for 4 node quadrilateral element.

For further information regarding numerical integration of finite element equations the reader is referred to the books of Kobayashi et al. [58] and Cook et al. [23].

8.10.4 Solution of the finite element equations

Once the finite element equations (Eq. 8.119) have been integrated and assembled into one large matrix $\mathbf{K} = \left(\mathbf{K}^D + \mathbf{K}^H\right)$ and boundary conditions imposed, the equation system $\mathbf{Kv} = \mathbf{f}$ needs to be solved. It is seen from the expression for $\mathbf{K}^D$ that the finite element equations have a direct dependence on the found velocities $\mathbf{v}$, at least through the effective plastic strain rate $\dot{\bar{\varepsilon}}^{pl}$ but possibly also through friction, and the effective stress $\bar{\sigma}$ may also be strain rate dependent. Therefore it is necessary to iterate for the velocities $\mathbf{v}$. The simplest iterative scheme is the direct substitution method, where the stiffness matrix $\mathbf{K}$ is repeatedly updated based on the most recently found velocities $\mathbf{v}$. This is continued until the change in the found velocities from one iteration to the next is sufficiently small. To measure "small", two different criteria are used, velocity norms and force norms:

$$\frac{\| \triangle \mathbf{v} \|_2}{\|^i \mathbf{v} \|_2} \leq \epsilon_V \tag{8.121}$$

$$\frac{\| \triangle \mathbf{f} \|_2}{\|^i \mathbf{f} \|_2} \leq \epsilon_f \tag{8.122}$$

where $\| \triangle \mathbf{v} \|_2 = \| {}^{i+1}\mathbf{v} - {}^{i}\mathbf{v} \|_2$ is the Euclidean norm of the change in velocity from iteration i to iteration $i+1$ and $\| \triangle \mathbf{f} \|_2 = \|^{i+1} \mathbf{f} - {}^{i}\mathbf{f} \|_2$ is the eucledian norm of the change in nodal forces from iteration i to iteration $i+1$. ϵ_V and ϵ_f are the convergence tolerance of respectively the velocities and forces.

For information regarding more advanced iteration procedures like the Newton-Raphson method, the reader is referred to the books of Nielsen et al. [75] and Kobayashi et al. [58].

8.11 Conclusion

An introduction to the finite element flow formulation has been given. The purpose was to give the reader a schematic introduction. The main point of interest is the derivation of the finite element equations by direct use of the static equilibrium equations. Thereby it was shown that the penalized version of the finite element flow formulation follows as a natural consequence of static force equilibrium.

9 Physical modelling of ingot forging

9.1 Introduction

Since the manufacturing of a full-size ingot weighing maybe several hundred tons is very expensive and also beyond what most metal forming laboratories can practically handle, one way of obtaining knowledge regarding ingot forging is by the utilization of downscaled models.

The use of laboratory substitutes for real parts is very common. Metal may for instance be replaced by wax (Wanheim et al. [105]). The laboratory substitute materials may also be used for experimental verification of a calculation model. In Danckert & Wanheim [26] wax is used to verify slipline analysis for various processes. Lead (Pb) has also been applied as model material, especially to model hot forging processes (Altan et al. [2], Kim et al. [57]).

The purpose of the experiments described in this chapter is to verify the influence of die geometry on the closure of centreline porosities and to verify the FEM calculations.

The 2D FEM simulations presented in this chapter was performed using an in-house FEM code developed by the author. The 3D simulations are performed using DEFORM-3D®.

The results from the experiments and subsequent FEM analysis was published in Christiansen et al. [17] and Christiansen et al. [20].

9.2 Manufacturing of parts

Before the experiments could be conducted, it was necessary to manufacture a number of downscaled lead model ingots, known as billets. A tool enabling forging using different lower die angles was also manufactured. The process of manufacturing the billets is described next.

9.2.1 Manufacturing of lead billets

Commercially pure lead is molten in an oven an thereafter poured into a mould and left to solidify. The cast lead billet after opening the mould is seen in Fig. 9.1a.

(a) Cast lead billet.

(b) Lead billet after machining and centreline hole drilling.

Fig. 9.1. Lead billet manufacturing.

The cast lead billets where subsequently machined to a length of 100mm and a diameter of 30mm, thus giving semi-plane strain conditions if being compressed radially along its entire length (see Fig. 9.3b). Inspired by the literature containing a large number of plane strain analyses, the author was aiming at reaching similar experimental conditions.

In order to mimic a centreline porosity, 5mm holes where drilled through some of the billets in order to simulate a porous ingot being forged, see Fig. 9.1b. It should be noticed that a 5mm hole corresponding to $5mm/30mm \approx 17\%$ of the billet diameter must be viewed as a severe porosity. However as mentioned in 6.2.1 not vastly disproportional. Due to the length of the billets, it was not possible to drill holes with smaller diameter when demanding the hole to be drilled from one side only. Smaller holes could have been manufactured by drilling from both ends of the billet. That possibility was disregarded in order to ensure concentricity of the hole.

9.2.2 Manufacturing of die tool

In order to investigate the influence of the lower die angle (Fig. 6.13), a die tool was manufactured. Initially two different lower die angles (90^o and 120^o) where milled in a block of Aluminium AA6061-T6 (see Fig. 9.2a). Since the aluminium block consists of precipitation hardened aluminium, it has a yield strength much larger than commercially pure lead. According to Kalpakjian & Schmid [54] p. 171 Aluminium AA6061-T6 has a yield strength of approximately 275MPa.

Later both a 60^o and a 150^o lower die angle were also milled in the same aluminium block, thereby increasing the number of possible lower die angles for experiments. The die tool, with all lower die angles, can be seen in Fig. 9.2b.

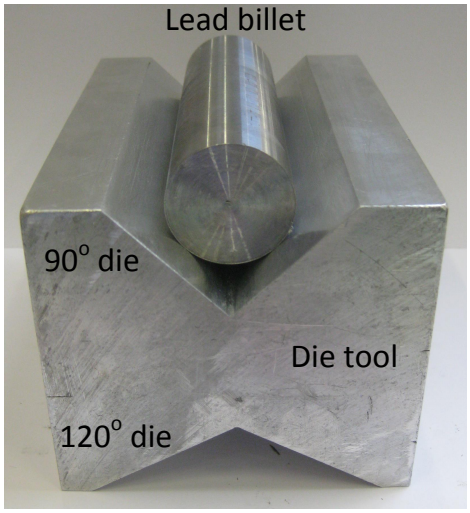

(a) Die tool and lead billet.

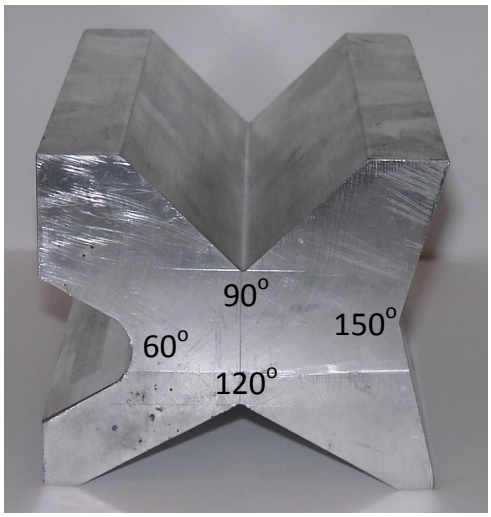

(b) Die tool with 60°, 90°, 120°, and 150° lower die angles.

Fig. 9.2. Die tool for simulation of forging with different lower die angles.

9.3 Experimental procedure

After having manufactured billets and die tool, they are placed in a hydraulic Instron Satec 1200kN press with data acquisition of load-stroke curves, see Fig. 9.3a. The die tool is placed on the lower die of the press. Thereafter the upper die of the press is displaced downwards in order to compress the billet. The upper die of the press is placed close to the billet before compression is started, hence deformation starts almost immediately when starting the recording of load-stroke data. Any slight threshold before deformation is removed manually during subsequent data processing. The measurements are also corrected for elastic deflection of the press.

(a) Hydraulic press and data acquisition.

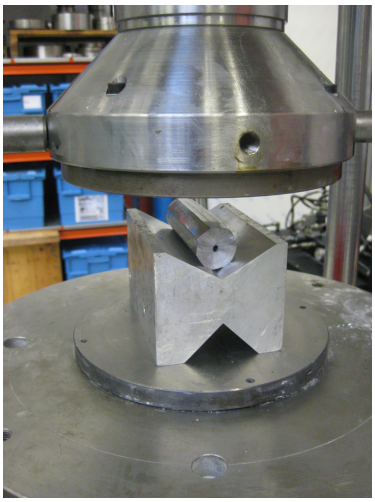

(b) Billet and die tool in press.

Fig. 9.3. Experimental setup.

A detailed view of a billet, which has been compressed multiple times, can be seen in Fig. 9.3b.

Utilization of a flat (180°) lower die is realized by placing the billet directly in between the dies of the press without using the die tool. By the described method, it is possible to forge downscaled model ingots using different lower die angles.

9.4 Stress-strain curve of lead

For the numerical simulation it is necessary to obtain the stress-strain curve of the commercially pure lead. Two cylinders where manufactured having a diameter to height ratio of approximately 1. The height and diameter of each cylinder was measured 3 times using a vernier caliper and an average value was calculated. The results are seen in Table 9.1. The cylinders are then used for upsetting tests in order to determine the stress-strain curve.

Table 9.1. Geometry of cylinders for upsetting tests.

Cylinder 1		Cylinder 2	
Diameter [mm]	Height [mm]	Diameter [mm]	Height [mm]
17.98	18.09	22.00	22.01

The experimental setup for upsetting tests are seen in Fig. 9.4. The upsetting was performed with Teflon sheets placed in between the contacting surfaces of the cylinder and the press in order to reduce friction.

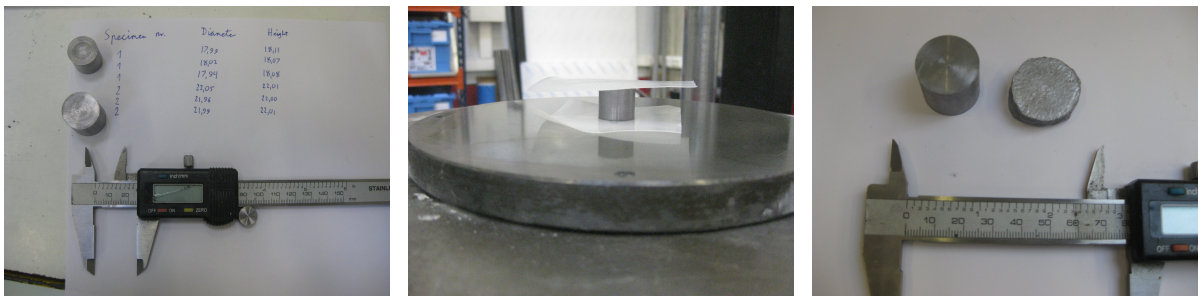

(a) Measuring cylinders. **(b)** Cylinder in press. **(c)** Cylinder after upsetting.

Fig. 9.4. Experimental determination of work hardening behaviour.

Corresponding values of load and stroke were recorded during upsetting. The measurements were subsequently corrected for elastic deflection of the press. Assuming homogeneous deformation, the data was then converted to stress-strain curves, seen in Fig. 9.5 with a fitted Hollomon curve.

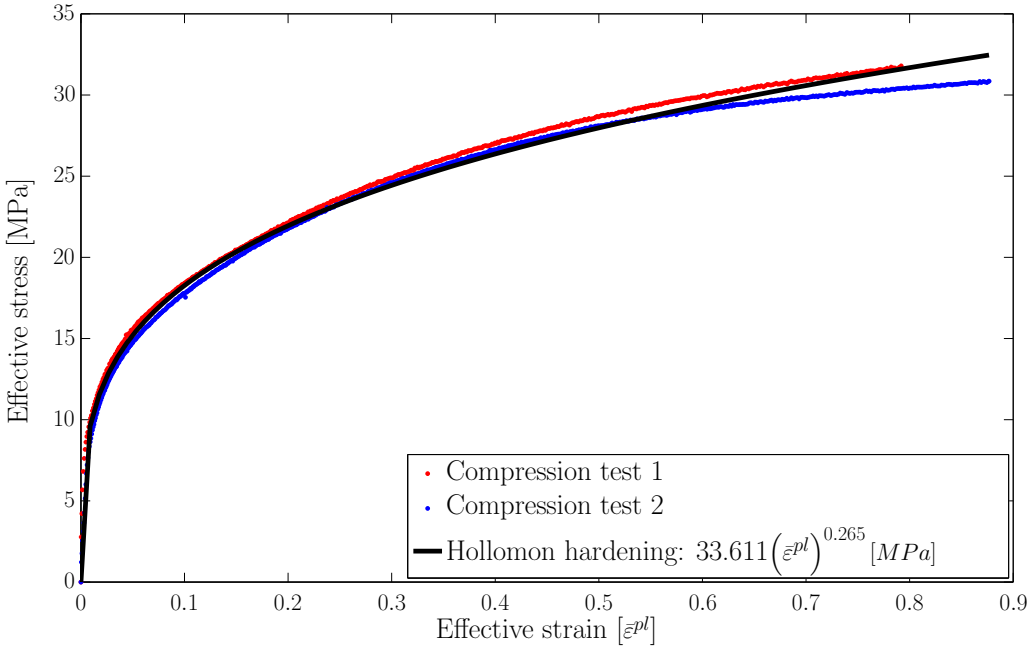

Fig. 9.5. Stress-strain curve for lead.

From Fig. 9.5 it is seen that the flow stress of the lead is substantially lower than the yield strength of the aluminium die tool, hence plastic deformation of the die tool is unlikely to occur.

9.5 Compression tests

9.5.1 Initial tests for verification of FEM simulation

For initial testing, compression tests were performed. The tests consisted of compressing billets for verifying the agreement between measured and FEM calculated load-stroke curves and the prediction of morphology of the deformed billets. An overview of the experiments and billet geometries can be seen in Table 9.2.

Table 9.2. Single step compression experiments.

Billet geometry	Billet length [mm]	Billet diameter [mm]	Hole diameter [mm]	Lower die angle [°]	Press stroke [mm]
Solid	105.96	30.24	-	180 (Flat)	14.5
Hollow	98.70	30.20	5.06	180 (Flat)	5.59
Hollow	105.03	30.27	5.21	90	7.57
Hollow	99.45	30.18	5.07	120	7.46

Pictures, showing the specimens before and after deformation, can be seen in Fig. 9.6.

(a) 180° lower die. **(b)** 90° lower die. **(c)** 120° lower die.

Fig. 9.6. Billet before and after being forged using different lower dies.

The process was also modelled using FEM. Two different programs where utilized. A 2D program developed by the author and the commercial program DEFORM-3D®. The 2D program assumes either plane strain or plane stress loading. It has the benefit of being fast calculating (less than 5min for the simulations performed in this chapter) and is therefore well suited for for instance optimization calculations. It is therefore of interest to investigate how well 2D simulations can model the physical experiments.

Since the deformation process in reality is 3 dimensional, and because 3 dimensional computations are applied in subsequent chapters, it is also of interest to verify that the author is capable of performing simulations using DEFORM-3D® with reasonable accuracy.

9.5.2 2D simulations

2D simulations using 4-node quadrilateral elements with linear interpolating functions are applied. An example of a simulation layout is seen in Fig. 9.7-Fig. 9.8. Vertical symmetry along the centerline of the ingot is utilized.

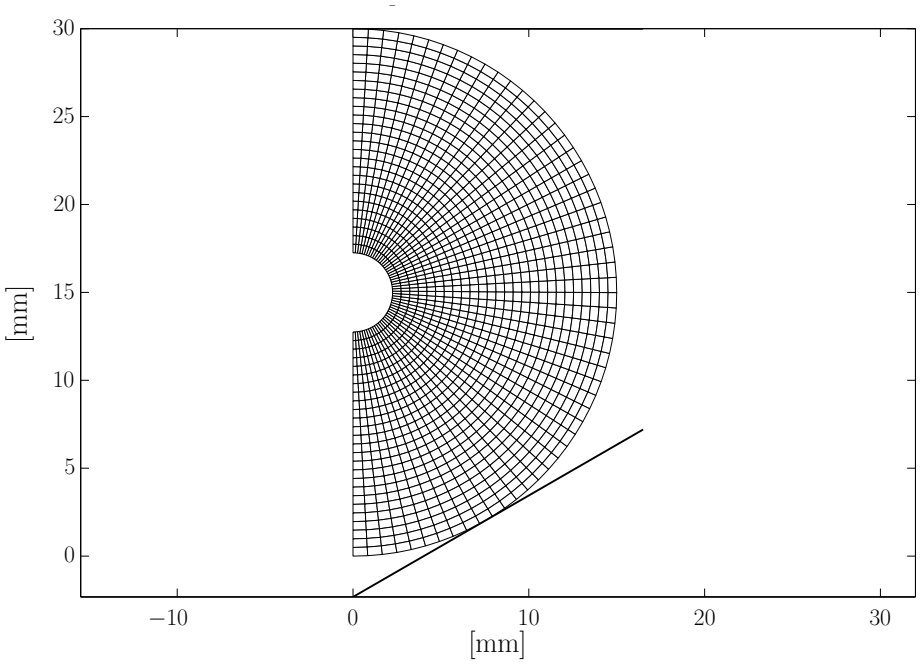

Fig. 9.7. Mesh before deformation.

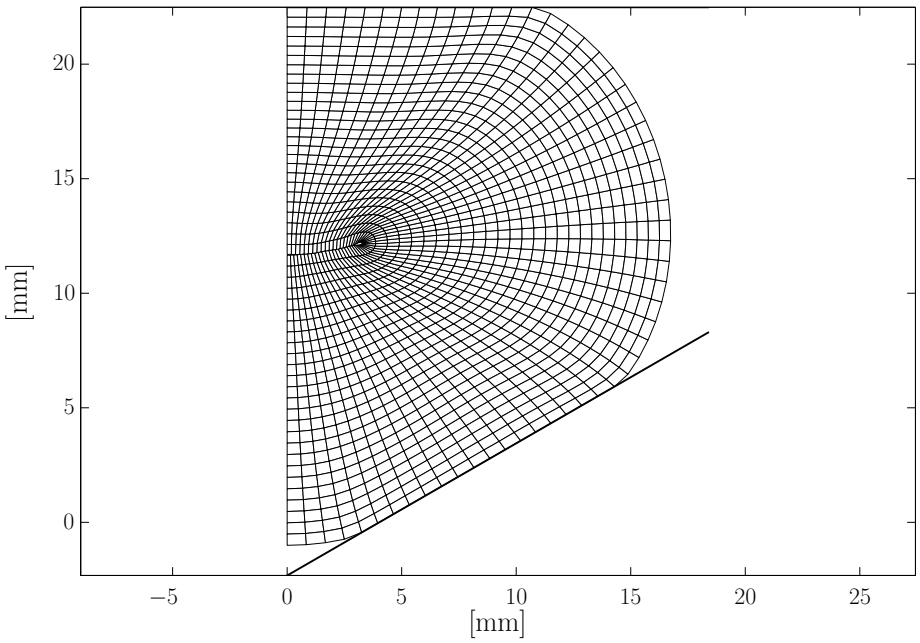

Fig. 9.8. Mesh after deformation.

1920 elements (1998 nodes) are used for the solid ingot and 1430 elements (1512 nodes) for the hollow ones. A penalty factor of 10^7 is used and the convergence criterion of the velocities is 0.01. The is no force convergence criterion. The upper die is displaced downwards while the lower die remains stationary. Plane strain and plane stress models are used to model the forging load in order to evaluate the difference. Plane stress models are applied when evaluating the hole morphology because the end surface of the billet is loaded in plane stress. The tools are modelled as rigid and the contact to be frictionless. A summary of FEM settings may be seen in Table 9.3.

Table 9.3. FEM simulation settings.

Mesh	
Solid billet	1920 elements (1998 nodes, 4-node quadrilateral)
Hollow billet	1430 elements (1512 nodes, 4-node quadrilateral)
Penalty factor	$K = 10^7$
Convergence criterion	$\frac{\|\triangle \mathbf{v}\|}{\|\mathbf{v}\|} = 0.01$
Number of time steps	200
Ingot material	Pure lead, $\sigma_o = 33.611 \left(\bar{\varepsilon}^{pl}\right)^{0.265} MPa$
Friction	Frictionless
Dies	Rigid-contact surface elements

After forging the billets, optical scans where taken of the deformed workpiece ends. This allows for a qualitative comparison between predicted and physical morphology of the forged billets. Such a comparison of the ends of the billets can be seen in Fig. 9.9.

Plane stress is assumed in the FEM simulations when comparing morphology of the billet ends.

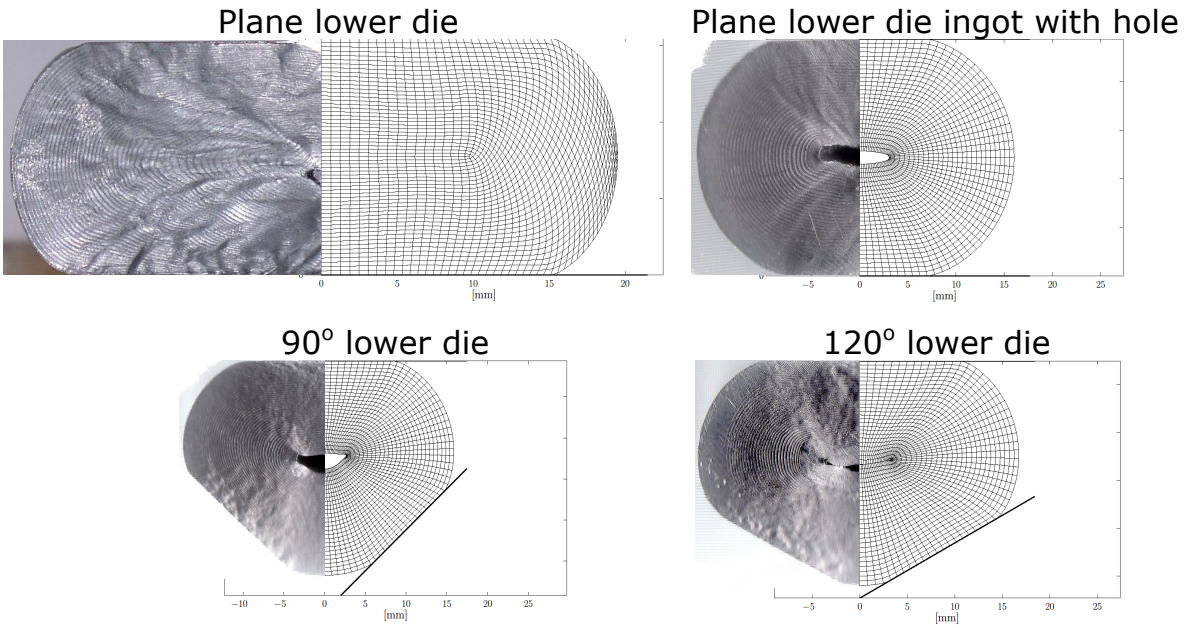

Fig. 9.9. Comparison of billet morphology with FEM simulations. [Author's own code].

From Fig. 9.9 reasonable agreement is seen between the numerically simulated and experimentally found hole morphology after compression for the 180° and the 90° lower die angles. When forging using the 120° lower die, some deviation in predicted and scanned hole morphology is observed.

The press load and stroke length was also recorded during the experiments. It is therefore possible to compare measured and computed loads during the forging operation. Both 2D plane strain and plane stress as well as 3D simulations are shown in Fig. 9.10-Fig. 9.13. The 3D simulations are discussed in 9.5.3. It should be noticed that the stroke length has been corrected for elastic deflection of the press.

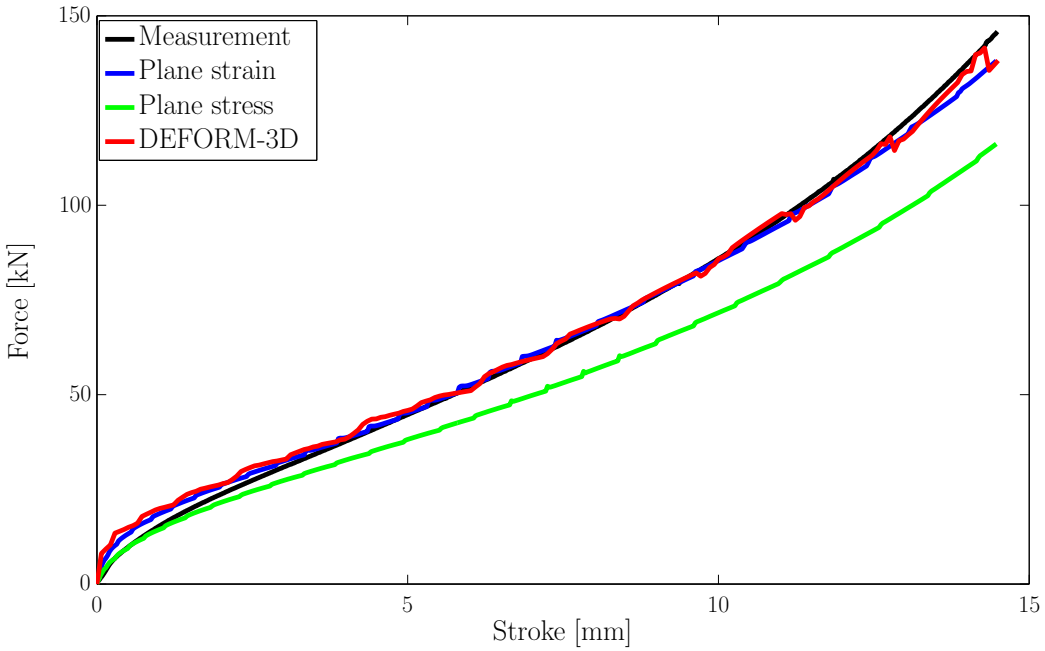

Fig. 9.10. Comparison of load-stroke curves between measurements and simulations. Plane lower die solid billet.

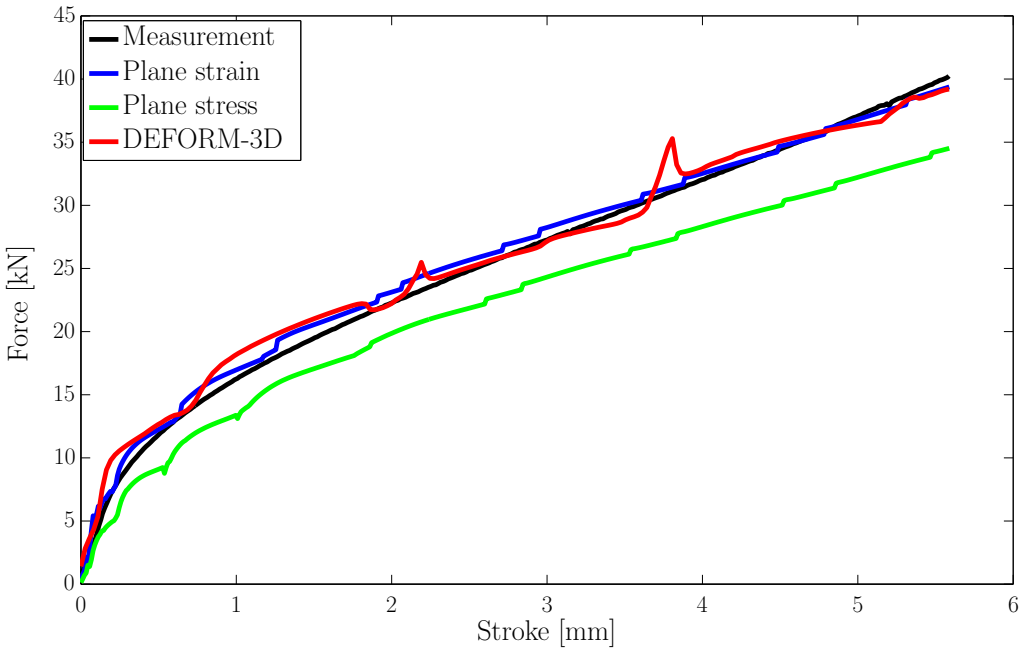

Fig. 9.11. Comparison of load-stroke curves between measurements and simulations. Plane lower die hollow billet.

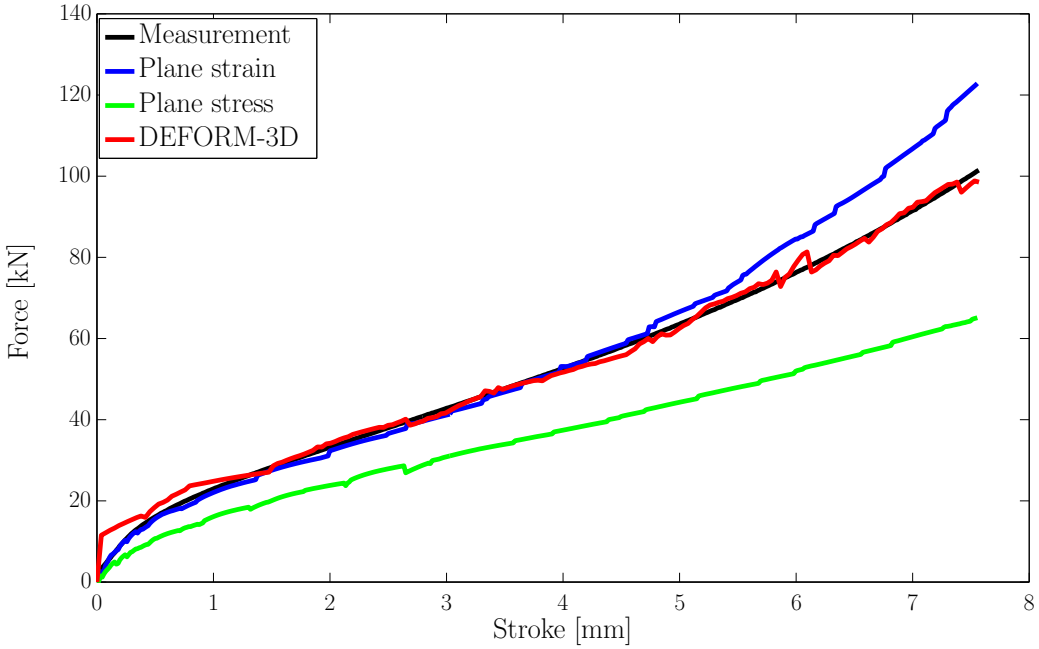

Fig. 9.12. Comparison of load-stroke curves between measurements and simulations. 90° lower die.

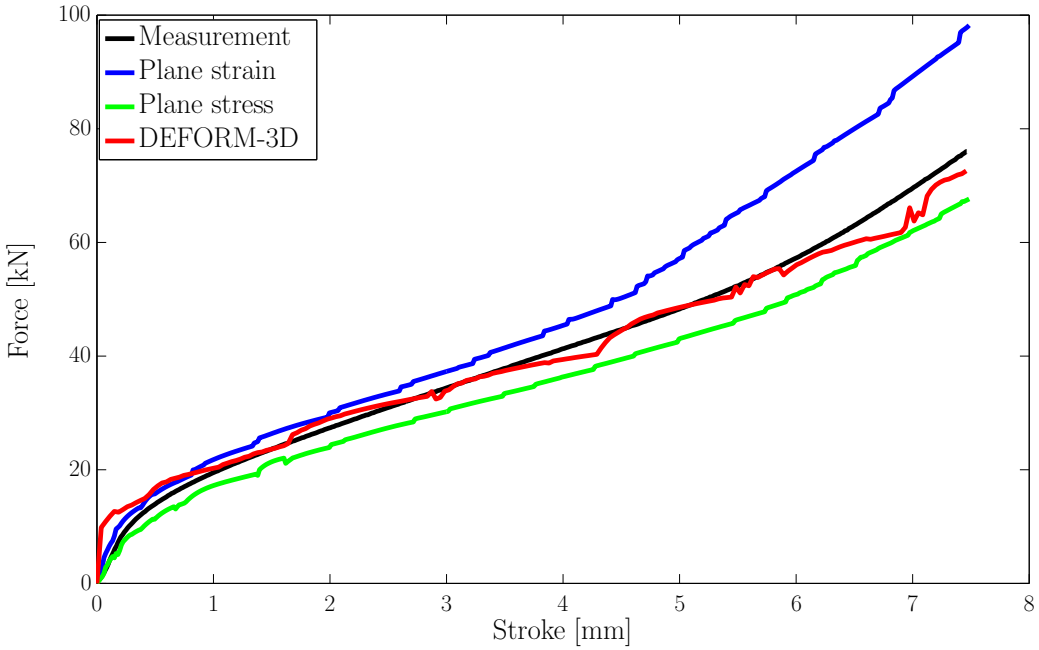

Fig. 9.13. Comparison of load-stroke curves between measurements and simulations. 120° lower die.

From Fig. 9.10-Fig. 9.13 it is seen that the plane stress assumption gives rise to the predicted loads being smaller than the measured loads. Plane strain assumption results in reasonable load prediction for both the solid and hollow billet being compressed by a plane lower die. For the 90° and 120° lower dies, plane strain gives reasonable load predictions

until approximately 4mm compression (13% of initial billet diameter). Thereafter the predicted load starts to deviate substantially from the measured load. The reason for this is that the inclined lower dies impedes horizontal material flow and the material therefore has a larger tendency to flow in the out-of-plane direction. For the plane lower die, resistance against horizontal material flow is less and therefore plane strain is a more reasonable assumption for these loading situations.

The "bumps" on the FEM-calculated force-stroke curves occur when a new node (line of nodes in 3D) are comming into contact with the upper die.

9.5.3 3D simulations

The 3D simulations are performed using DEFORM-3D®. 8-node brick elements with linear interpolation functions are utilized. The solid billet is discretized using 4680 elements (5709 nodes). The hollow billets are discretized using 5700 elements (7200 nodes). The simulations where performed using Coulomb friction with a friction coefficient ranging between 0.05 and 0.1 in order to obtain reasonable agreement between measured and predicted load-stroke curves. A summary of the FEM simulation settings may be found in Table 9.4.

Table 9.4. FEM simulation settings.

Mesh	
Solid billet	4680 elements (5709 nodes, 8-node brick)
Hollow billet	5700 elements (7200 nodes, 8-node brick)
Penalty factor	$K = 10^7$
Convergence criteria	$\frac{\|\triangle \mathbf{v}\|}{\|\mathbf{v}\|} \leq 0.01$ and $\frac{\|\triangle \mathbf{f}\|}{\|\mathbf{f}\|} \leq 0.1$
Number of time steps	200
Ingot material	Pure lead, $\sigma_o = 33.611 \left(\bar{\varepsilon}^{pl}\right)^{0.265} MPa$
Friction	$\tau = \mu p$, μ ranging between 0.05 and 0.1
Dies	Rigid-contact surface elements

A comparison between scans of the ends of the billets and DEFORM® simulations are seen in Fig. 9.14.

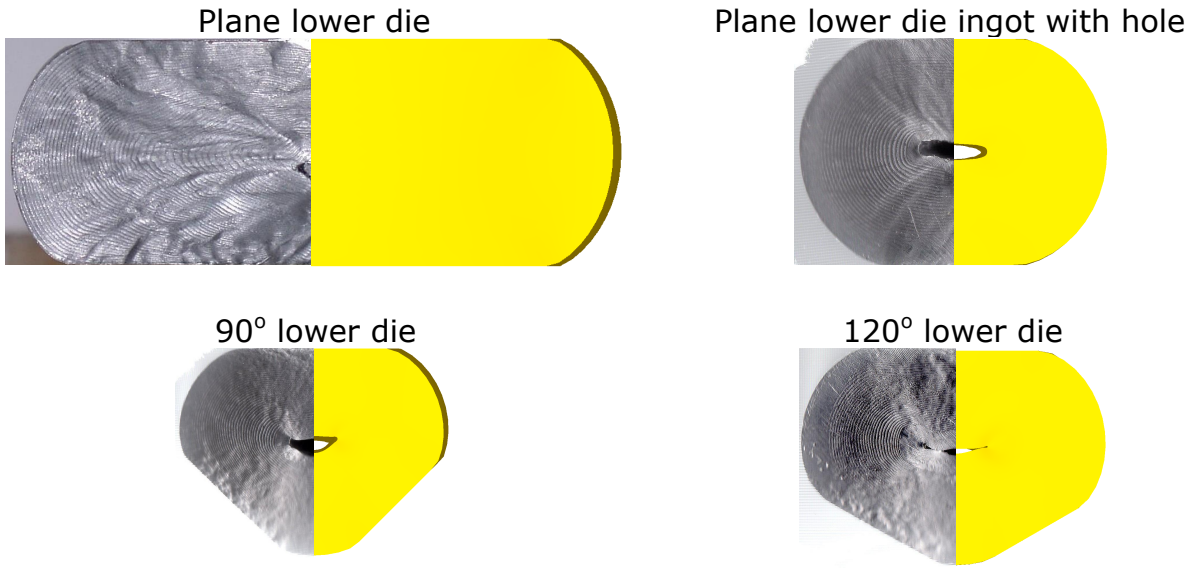

Fig. 9.14. Comparison of billet morphology with FEM simulations.

Reasonable agreement between predicted and scanned end morphologies are seen in Fig. 9.14. There is some deviation for the 90° lower die but overall the different billet end morphologies are well represented by the DEFORM® simulations. The computation time for a simulation was approximately 25min.

The computed press loads are seen in Fig. 9.10-Fig. 9.13, where they can be compared with the measured loads and the loads predicted using 2D simulations. For the 3D simulations, the friction coefficient was varied between 0.05 and 0.1 in order to obtain reasonable fits for the different simulations. Friction is therefore fairly small. This is in some contrast to the experimental findings in Gouveia et al. [38], where pure lead was also utilized for forging experiments. Here a friction factor of m=0.35 was found to model friction correctly and thereby indicating fairly large friction. It must here be remembered that a Hollomon material predicts small values of flow stress at the beginning of deformation. Therefore one needs a large friction factor in order to have some friction stress. The author tried also to model the compression of the billets using the constant friction model and found m=0.4-0.5 as a friction factor giving reasonable fit between measured and predicted loads. Therefore the author concludes that the frictional stress is fairly small and the experiments are best modelled using the Coulomb friction law. This can however not be transferred to the real hot forging process of full size ingots.

9.5.4 Quantitative validation of internal hole reduction

Further experiments were conducted after the initial tests. Two further lower die angles (60° and 150°) were milled into the aluminium block to allow for further experiments. A one-stroke compression of billets by different lower die angles of 60°, 90°, 120°, 150° and 180° were then performed. The stroke length was approximately 3mm (10% of billet diameter) for each compression. An overview of the experiments is found in Table 9.5.

Table 9.5. Hole reduction experiments.

Lower die angle [°]	Billet length [mm]	Billet diameter [mm]	Press stroke [mm]
60	98.05	29.99	2.84
90	101.10	30.08	2.71
120	98.74	30.01	2.81
150	99.66	30.05	2.80
180	100.23	30.10	2.76

An initial billet and the compressed billets are seen Fig. 9.15.

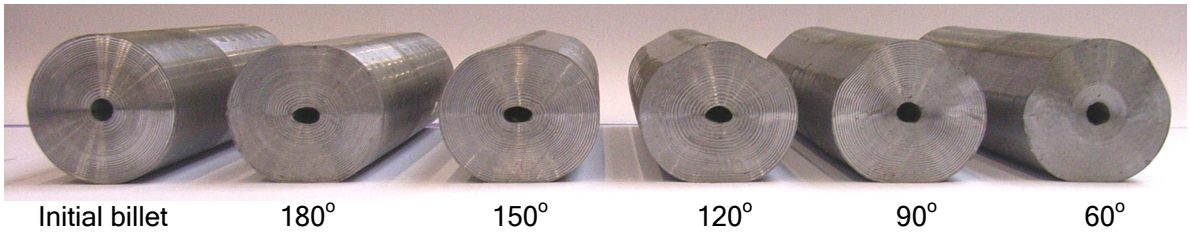

Fig. 9.15. Billets used for test.

After compression, optical scans of the ends of the billets were performed. Developing a customized MATLAB® program, it was possible to extract the cross-sectional area of the drilled holes after compression, from the optical scans. The program consists of recognizing black pixels, which are part of a larger group of black pixels, hence gray pixels or individual black pixels are filtered out. A principal sketch of a scan, divided into pixels, can be seen in Fig. 9.16a. Fig. 9.16b then shows the recognized hole based on the scan after filtering. The black grid indicating pixels is only for illustrative purposes. The pixel resolution of the scans was 1200 by 1200 dpi, hence a fine resolution was used.

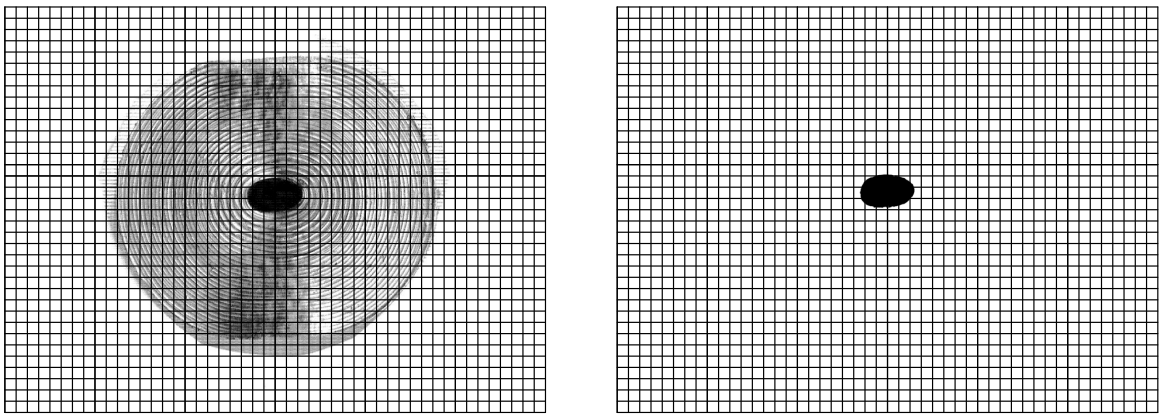

(a) Scan of billet end with drilled hole.

(b) Recognized hole morphology.

Fig. 9.16. Hole morphology recognition.

The recognized black areas can then be compared with the areas predicted from the FEM simulations. As a measure of hole closure, the area ratio $A_{final}/A_{initial}$, where

$A_{initial}$ is the initial and A_{final} is the final cross-sectional area of the drilled hole, was used as a measure for quantification of the FEM simulations. Unfortunately the initial area $A_{initial}$ was not measured on the entire series of manufactured billets. The ones measured had an average value of Ø4.82mm, which was smaller than found in 9.5.1. To test for sensitivity of hole closure depending on initial hole size, 2D FEM simulations were conducted using initial hole sizes of Ø4.5mm and Ø5.0mm. Using these limits as initial values of the 2D FEM simulations, both plane strain and plane stress models were performed and compared to the experiments. The results can be seen in Fig. 9.17.

3D simulations were also performed using DEFORM®. Here the initial hole size of the billets were set to Ø4.82mm. The predicted area ratios for these simulations are also found in Fig. 9.17.

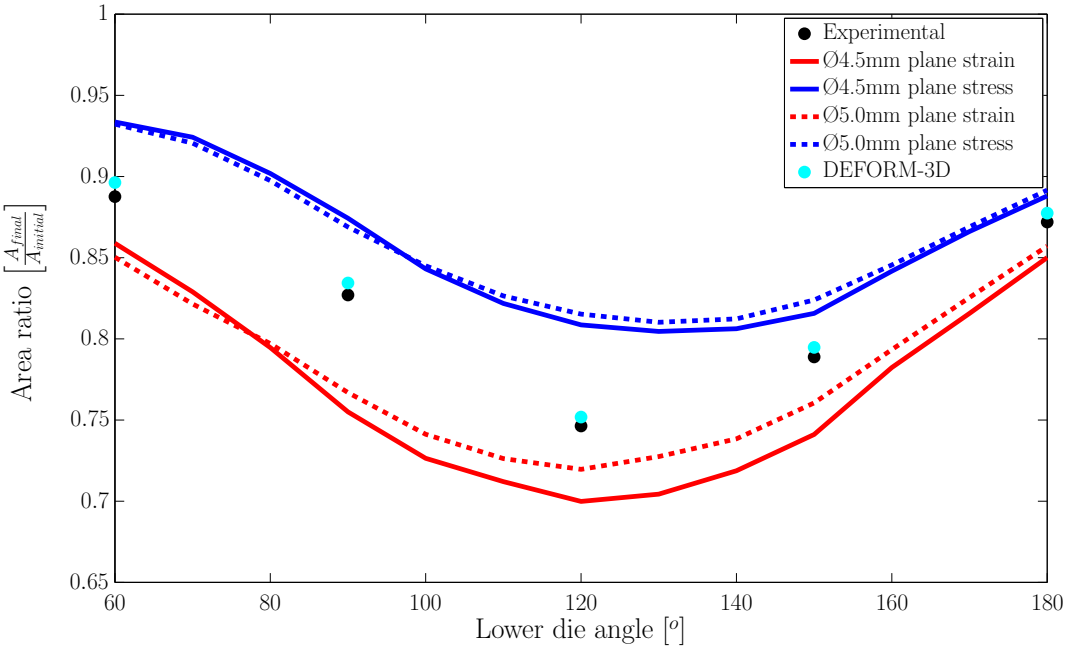

Fig. 9.17. Comparison of experimental hole closure with FEM-simulations.

It can be seen from Fig. 9.17 that different lower die angles result in different degrees of centreline hole closure for the same press stroke length. A maximum closure appear to occur for a lower die angle of 120°. It can also be seen that there is little change in the predicted closure regardless whether the initial diameter is 4.5mm or 5.0mm in the 2D FEM simulations. The assumption of plane stress or plane strain changes the predicted closure significantly with plane strain resulting in a larger degree of centreline porosity closure. The experimentally observed centreline hole closure appears to fall in-between plane stress and plane strain. There is good agreement between the DEFORM-3D® simulations and the measured area ratio. It can be noticed that all the DEFORM-3D® simulations lie above the measured area ratios. Some reasons for this could be that the stroke length utilized in the simulations were determined from the force-stroke measurements and are therefore somewhat influenced by personal estimation of when the forging began to take place. The correction for elastic deflection of the press may, however, also not be fully correct. It shall, furthermore, be noticed that the stress-strain curves were not fully identical for the two compression tests, thus indicating some

variation from billet to billet. The author tried to use an interpolated stress-strain curve based on the two upsetting tests but did not achieve much different results in predicted area ratio. The assumption of rigid tools should only increase the closure of the drilled holes and is therefore not considered to be the source of lacking of closure.

9.6 Discussion of experiments

When performing experimental work, as with any other kind of work, one increases (hopefully) ones knowledge. The author will here discuss the experiments and give some recommendations for future experiments in the same area/approach.

At the time when it was decided to make the billets long compared to the diameter, in order to obtain plane strain deformation, the author was somewhat inspired by especially the analytical solutions such as upper bound methods. Since the upper bound method is based on plane strain, it was therefore natural to aim at such a geometry. Also the author was somewhat eager to test his newly written FEM program which, at that time, could not simulate plane stress but only plane strain. From a visit to a forging company, the author also remembered that the forging dies where 1m wide, and such a tool size often implies plane strain, especially when friction is large, as it is in hot forging. The author had not thought about the fact that the ingot being forged is 2m in diameter, hence giving a diameter (D_{ingot}) to width (L_{die}) ratio of $L_{die}/D_{ingot} = 1/2$. As a rule of thumb, the ratio L_{die}/D_{ingot} should be larger than 5 to have plane strain conditions. Therefore the actual industrial process is expected to be closer to plane stress. That was however not realized by the author at the time when the experiments were conducted.

Based on the aforementioned, the author will therefore recommend to manufacture billets with smaller length to diameter ratio. This will also facilitate experimentation with smaller hole sizes since shorter billets give the possibility of drilling smaller diameter holes.

9.7 Conclusion

The dependence of internal porosity closure on the lower die angle has been verified by means of physical simulation using downscaled model ingots. At the same time, 2D FEM simulation has been shown to be able to model centreline hole closure reasonably correct for reductions up to approximately 13%. Of the experimental lower die angles of 60°, 90°, 120°, 150°, 180°, the maximum centreline hole closure, for approximately same press stroke length, was found to occur when applying a lower die angle of 120°.

Based on the knowledge gained through experimentation, it is recommended by the author to use billets with smaller length/diameter ratio for modelling ingot forging. This also makes it possible to drill holes with smaller diameter, thus reducing the porosity size modelled in the experiment to more realistic simulations of real forgings.

10 Optimization of lower die angle in single stroke compression of ingots with centreline hole

10.1 Introduction

Based on the experiments described in Chapter 9, a numerical optimization process is performed. It was found in Chapter 9 that different lower die angles result in different centreline hole reductions, described by the area ratio $A_{final}/A_{initial}$. It could therefore be of interest to numerically investigate how the optimum lower die angle, defined by giving the maximum closure, is influenced by factors like work-hardening properties of the ingot and friction between dies and ingot. This question is analyzed further by means of 2D FEM simulations. 2D simulations are applied mainly to reduce computational time but also because they can describe the material flow in ingot forging reasonably well. The simulations are performed using the in-house, FEM program developed by the author. The results of this chapter was published in Christiansen et al. [19].

10.2 Numerical simulation layout

The ingot modelled is 2000mm in diameter and has a centreline hole of 100mm ($100mm/2000mm = 5\%$ of diameter). 1687 quadrilateral elements are used (1763 nodes). Vertical symmetry is utilized. The dies are assumed to be rigid. The constant friction model $\tau = m_f k$ is applied. Two values of friction are investigated: $m_f = 0.0$ and $m_f = 0.5$. The stroke length of the upper die is 200mm ($200mm/2000mm = 10\%$ if ingot diameter) and the press speed is 50mm/s, which is also what is approximately utilized for forging an ingot of this size. In some cases, stroke lengths of 100mm and 300mm are also applied for investigating the influence of the stroke length. The lower die is stationary. An example of initial and final mesh can be seen in Fig. 10.1. It is noticed that a biased mesh is utilized for having good resolution around the centreline hole and the contact areas between dies and ingot.

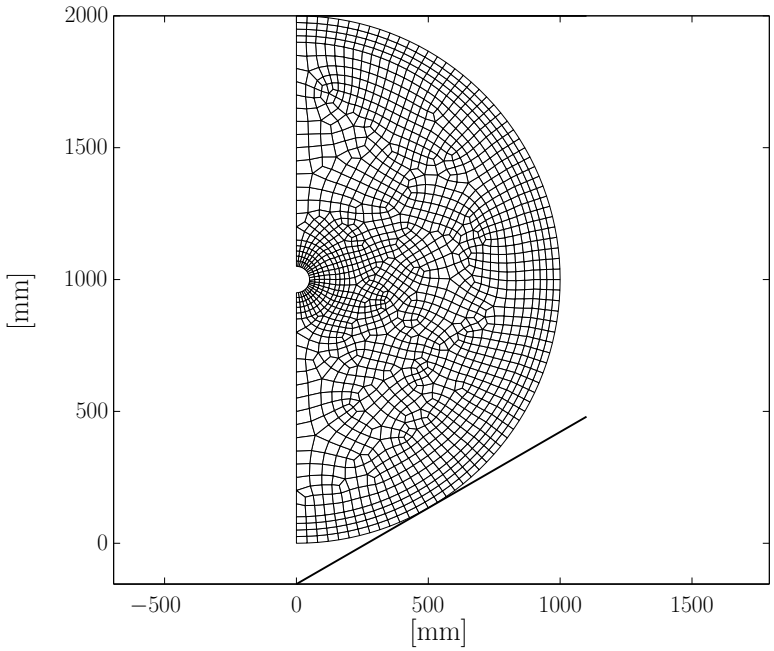

(a) Initial mesh.

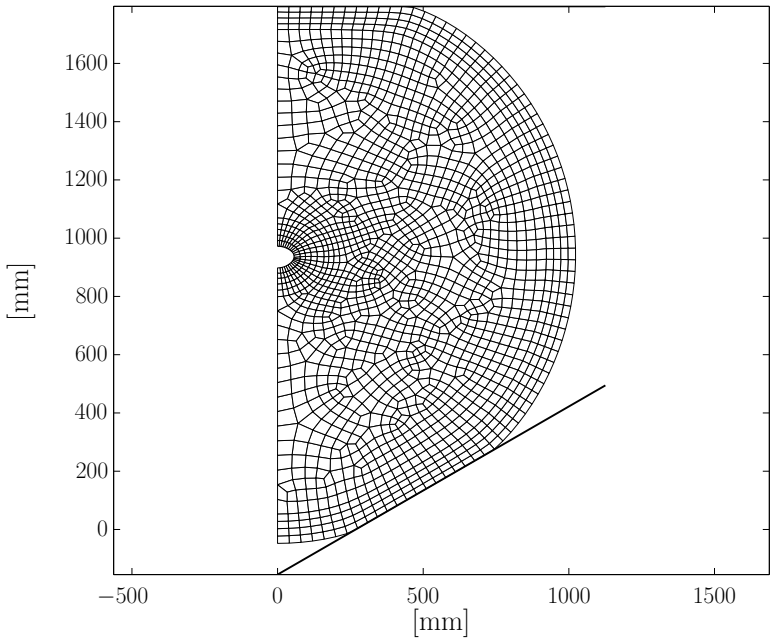

(b) Final mesh.

Fig. 10.1. Mesh utilized for simulation. [Author's own code].

A summary of simulation settings are found in Table 10.1.

Table 10.1. FEM simulation settings.

Ingot outer diameter	2000mm
Centreline hole	100mm
Mesh	1687 quadrilateral elements (1763 nodes)
Penalty factor	$K = 10^7$
Convergence criterion	$\frac{\|\triangle \mathbf{v}\|}{\|\mathbf{v}\|} \leq 0.01$
Number of time steps	200
Friction	Two values: $m_f = [0, 0.5]$
Press speed	50mm/s
Dies	Rigid-contact surface elements

In order to investigate the influence of work-hardening behaviour, a number of different variations of the Fields-Backofen hardening model $\left(\sigma_o = C\left(\bar{\varepsilon}^{pl}\right)^n\left(\dot{\bar{\varepsilon}}^{pl}\right)^m\right)$ are applied. The different applied hardening parameters are seen in Table 10.2.

Table 10.2. Hardening parameters.

C [MPa]	n	m
100	0.0	0.0
100	0.2	0.0
100	0.4	0.0
100	0.0	0.2
100	0.0	0.4
100	0.2	0.2

10.3 Examples of simulations

10.3.1 Frictionless compression of ideal-plastic material

Some examples of predicted effective plastic strain are seen in Fig. 10.2 for an ideal plastic material ($\sigma_o = 100MPa$) to give some indication of the material flow depending on the lower die angle. The 200mm compression is performed frictionless.

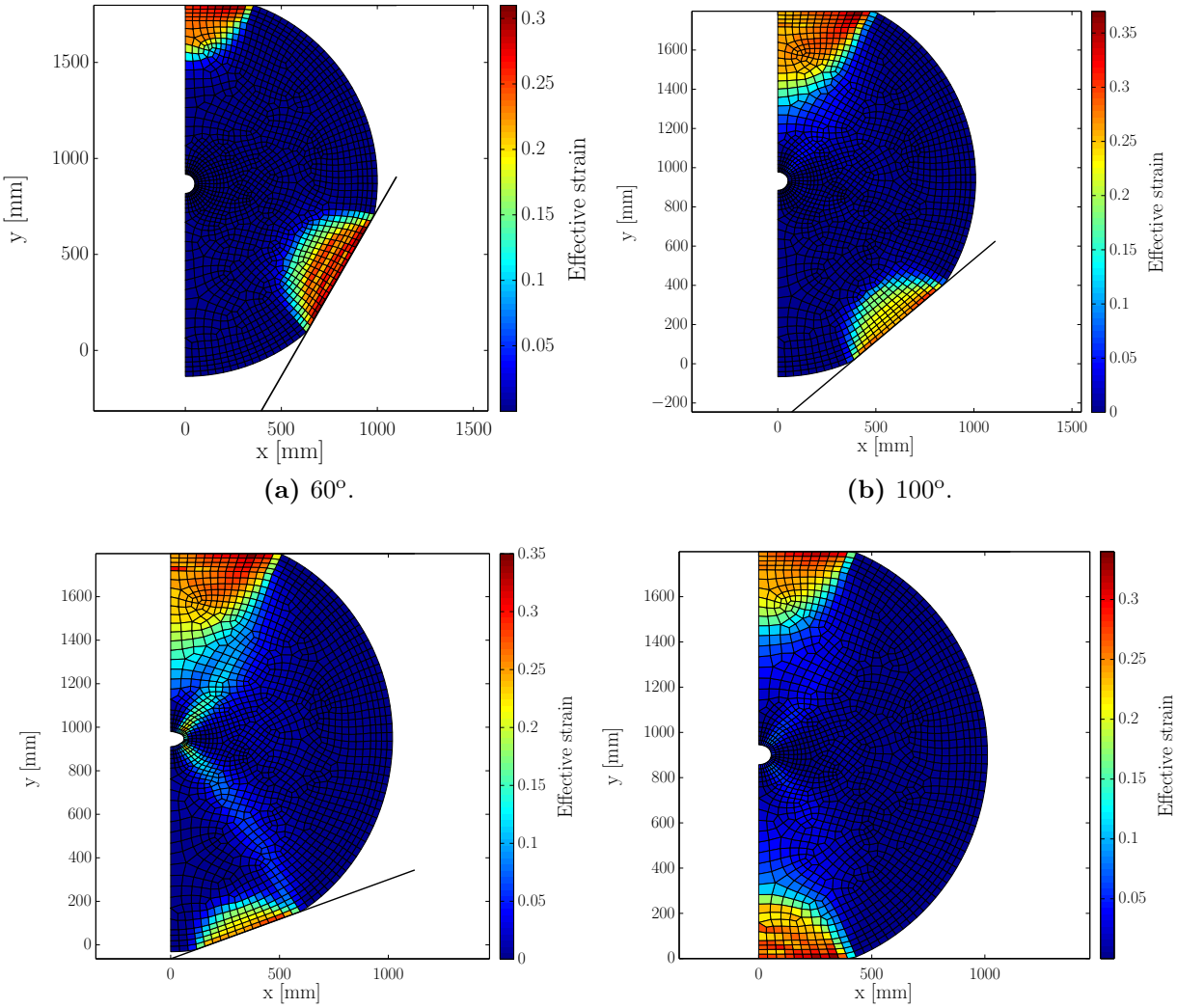

(a) 60°. **(b)** 100°.

(c) 140°. **(d)** 180°.

Fig. 10.2. Effective plastic strain for different lower die angles. [Author's own code]. ($\sigma_o = 100MPa$, $m_f = 0.0$).

In Fig. 10.2 clear differences are seen regarding predicted plastic flow. It is seen that the majority of plastic straining generally occurs close to the dies in contact with the ingot. For the 140° lower die, a forging cross of plastic straining is seen reaching the center hole in the ingot. Since closure of a centreline defect must require plastic straining to occur in the region surrounding it, this figure indicates that differences in closure are to be expected when forging with different lower die angles. However whether the centreline hole opens or closes is not easily determinable from the plot by pure visual inspection.

10.3.2 Compression of ideal-plastic material with friction

The same simulation as in 10.3.1 is performed except that a friction factor $m_f = 0.5$ is applied in the simulation. Plots of the effective plastic strains are seen in Fig. 10.3.

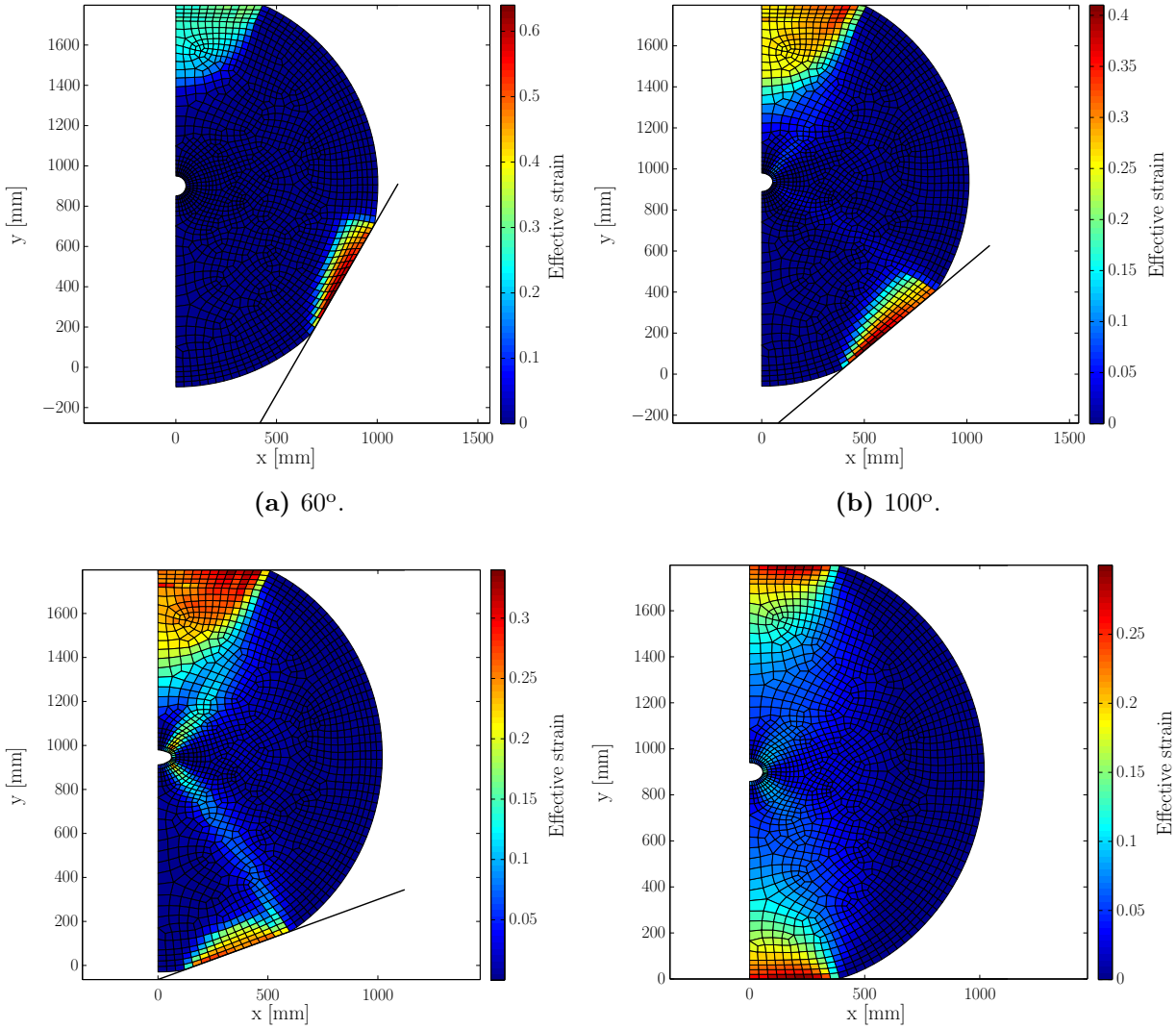

(a) 60°. **(b)** 100°.

(c) 140°. **(d)** 180°.

Fig. 10.3. Effective plastic strain for different lower die angles.($\sigma_o = 100MPa$, $m_f = 0.5$). [Author's own code].

It can be seen from Fig. 10.3 that the increased friction increases the effective plastic strain for the more inclined dies such as the 60°. Here the maximum effective plastic strain increases from approximately 0.3 to 0.6. When applying lower dies less inclined, the strains become quite similar. The overall deformation pattern seems not to be much changed by friction, but larger straining appears to occur at the die-ingot interface.

10.3.3 Frictionless compression of Hollomon hardening ingot

Setting the ingot material to be Hollomon hardening $\left(\sigma_o = 100\left(\bar{\varepsilon}^{pl}\right)^{0.4} MPa\right)$ and performing a frictionless compression of 200mm, the resulting effective plastic strain can be seen in Fig. 10.4.

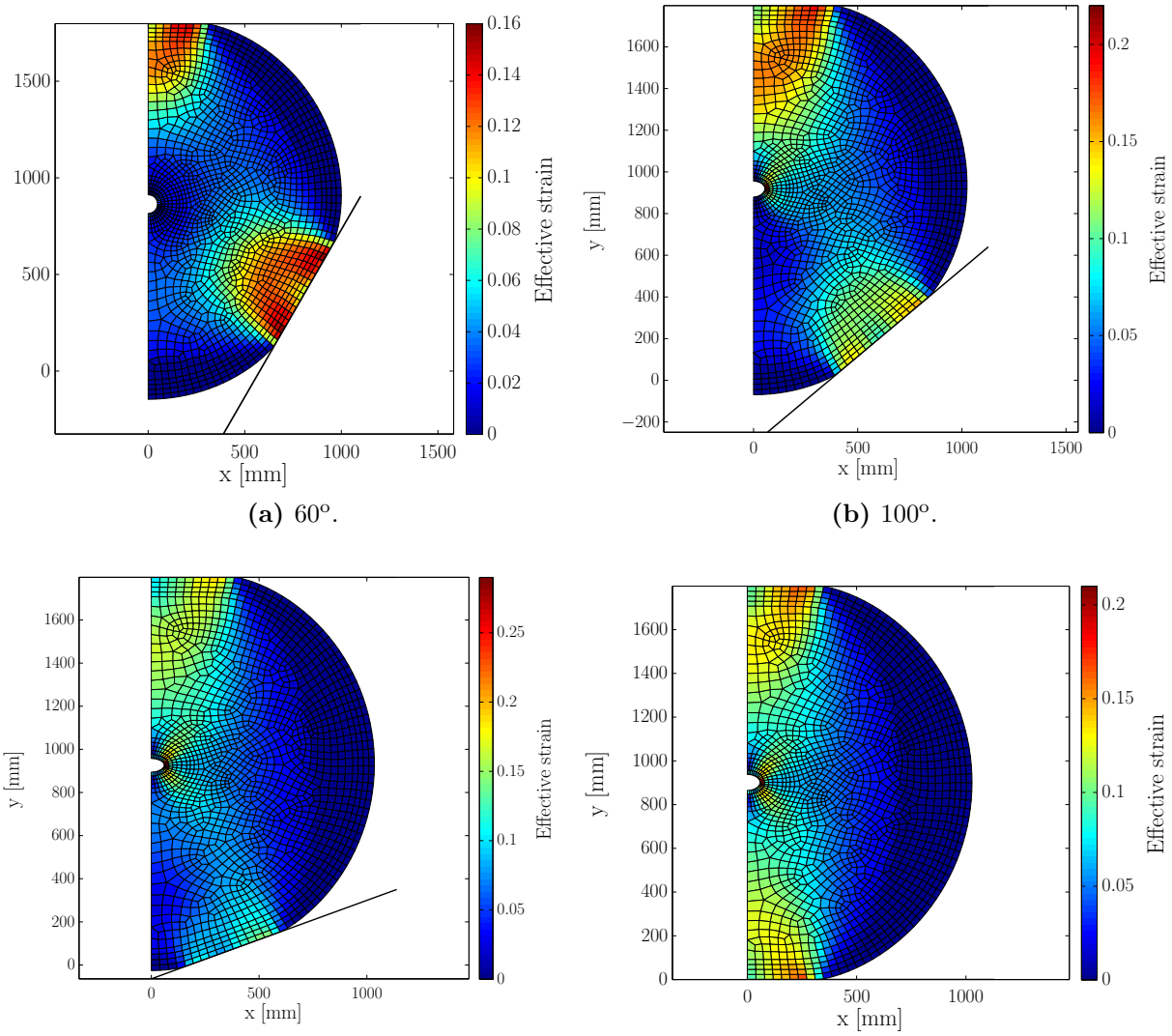

(a) 60°. **(b)** 100°.

(c) 140°. **(d)** 180°.

Fig. 10.4. Effective plastic strain for different lower die angles. $\left(\sigma_o = 100\left(\bar{\varepsilon}^{pl}\right)^{0.4},\ m_f = 0.0\right)$. [Author's own code].

It can be seen from Fig. 10.4 that the strain hardening material distributes the plastic strain to a larger part of the ingot. A larger part of the ingot should therefore experience the beneficial metallurgical effects of the ingot forging process. It is more difficult to quantify from the figures whether that also manifests itself in a larger closure of the centreline hole.

10.3.4 Frictionless compression of Norton-hardening ingot

If one assumes a strain rate hardening material model such as Norton hardening $\left(\sigma_o = 100\left(\dot{\bar{\varepsilon}}^{pl}\right)^{0.4} MPa\right)$ and frictionless compression, the following figure indicates the effective plastic strain.

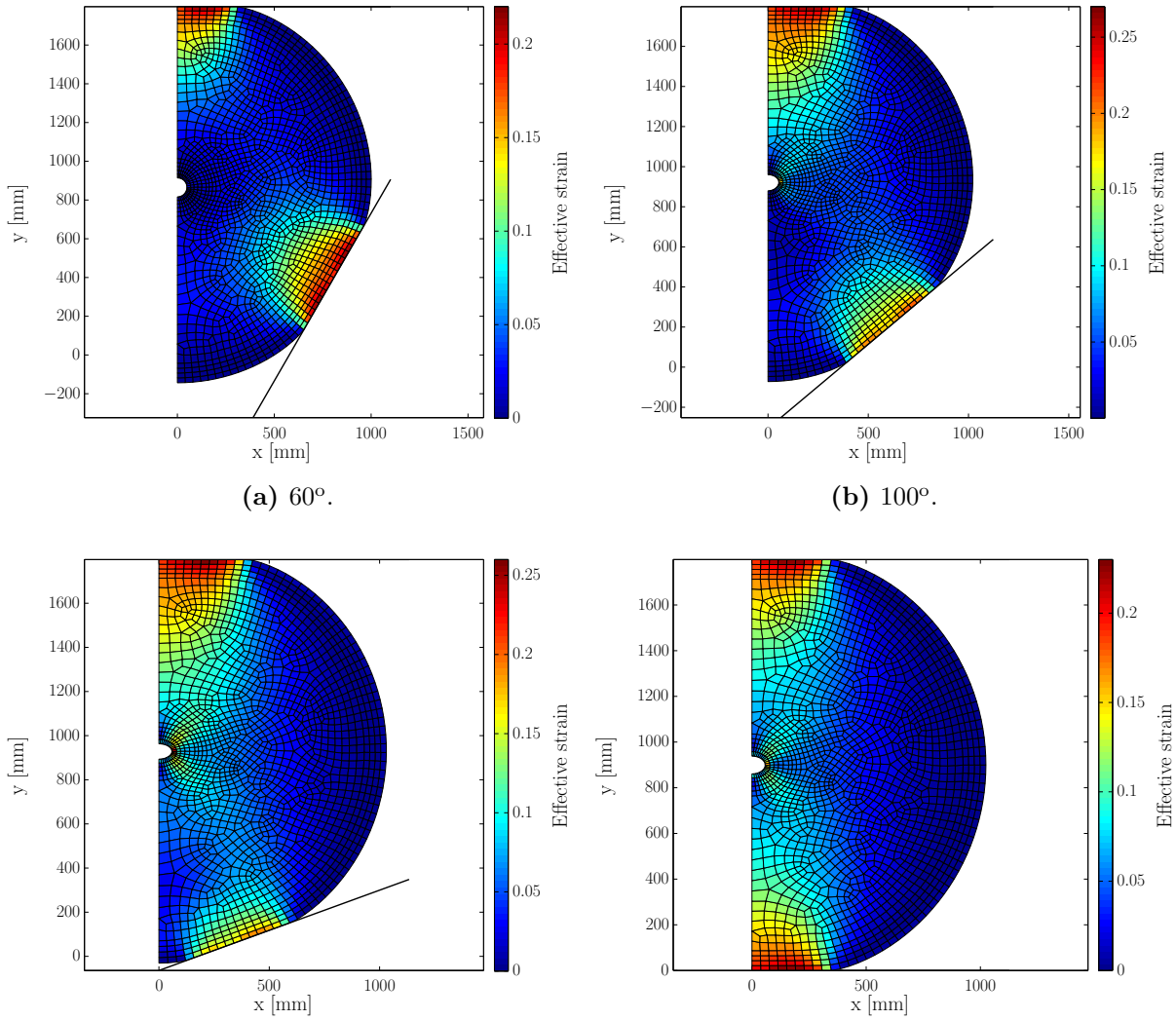

(a) 60°. **(b)** 100°.

(c) 140°. **(d)** 180°.

Fig. 10.5. Effective plastic strain for different lower die angles. $\left(\sigma_o = 100\left(\dot{\bar{\varepsilon}}^{pl}\right)^{0.4},\ m_f = 0.0\right)$. [Author's own code].

Fig. 10.5 indicates approximately the same strain pattern as in Fig. 10.4. From a material flow perspective it therefore seems less important whether the material is considered to strain or strain rate harden. The important parameter is how much the material hardening is influencing the centreline hole closure.

10.4 Optimum lower die angle depending on material and friction

By conducting single stroke, 200mm compressions for the materials listed in Table 10.2 with and without friction, it is possible to draw curves displaying the area ratio $A_{final}/A_{initial}$ as a function of the lower die angle, which ranges from 60° to 180° (flat). Such curves are presented in the following.

10.4.1 Strain hardening

The area ratio, as a function of lower die angle, is plotted for varying strain hardening exponents and friction factor in Fig. 10.6.

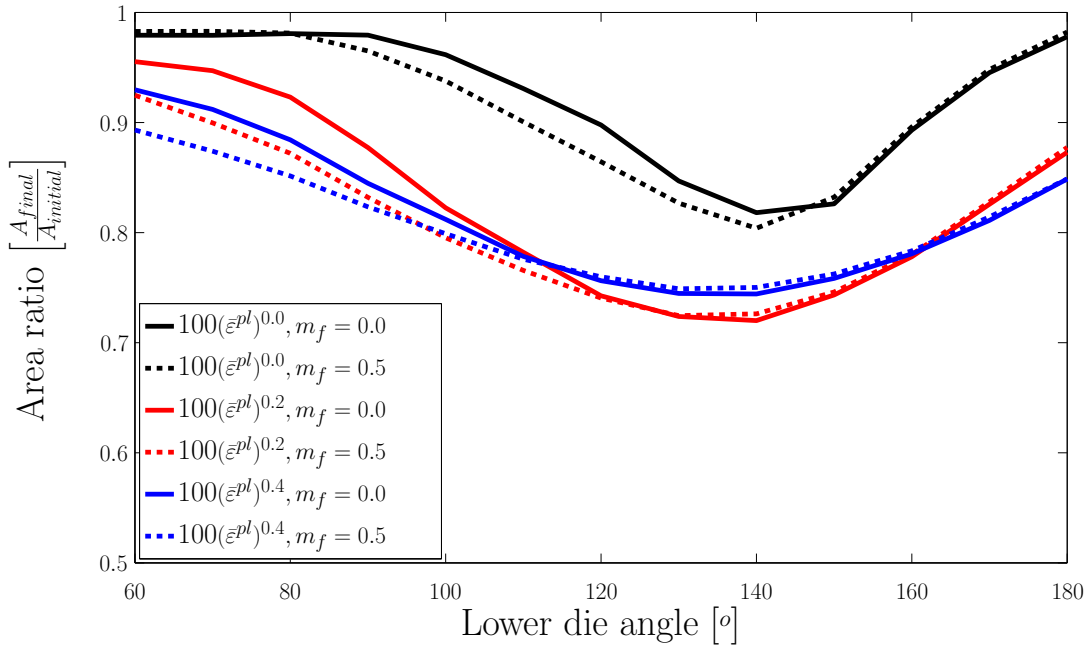

Fig. 10.6. Area ratio as function of lower die angle for different strain hardening behaviours. [Author's own code].

From Fig. 10.6 it is seen that an optimum appears to exist for a lower die angle of approximately 130°-150°. It can be seen that the location of the optimum is quite independent of both friction and strain hardening exponent. The degree of centreline hole closure is however affected by the strain hardening with the ideal-plastic material closing least and the material with strain hardening exponent of n=0.2 closing a bit more than the one with n=0.4. Friction has only minor influence on the location of the optimum.

10.4.2 Strain rate hardening

A plot of the area ratio, as a function of the lower die angle, is seen for different strain rate hardening exponents in Fig. 10.7.

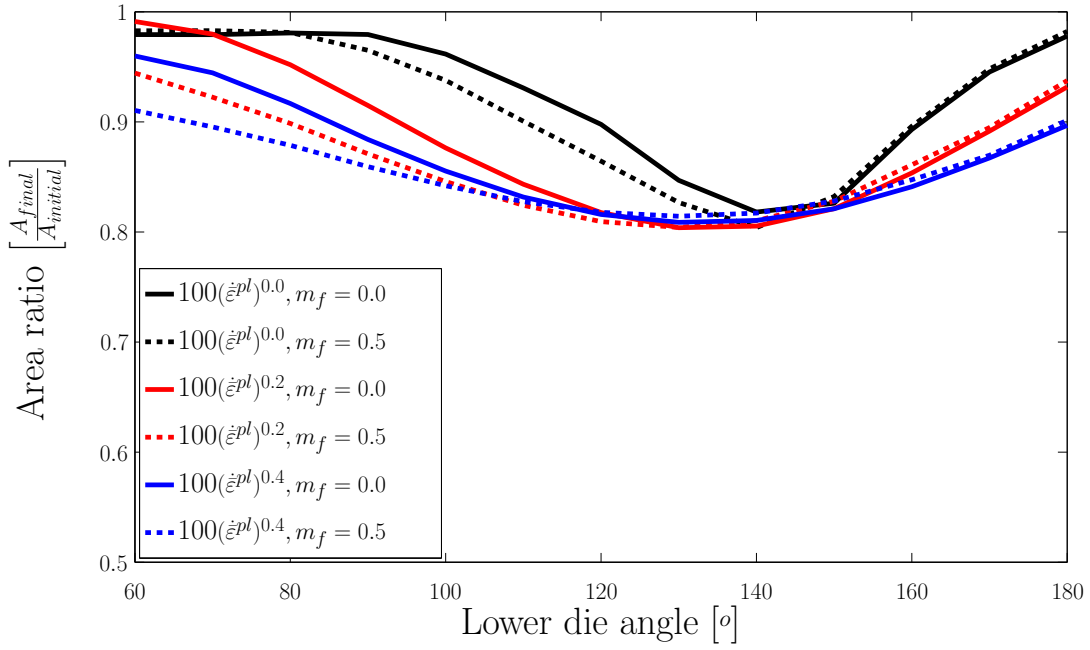

Fig. 10.7. Area ratio as function of lower die angle for different strain rate hardening behaviours. [Author's own code].

It is seen from that maximum closure occurs for a lower die angle of approximately 130°-150°. It is also noticed that the optimum is more distinct for the ideal-plastic material than for the strain rate hardening materials, where a broader range of lower die angles results in fairly the same degree of centreline hole closure. Friction has only a minor influence on the location of the optimum.

10.4.3 Combined hardening

The area ratio for a combined hardening material, with a strain and a strain rate hardening material behaviour, as a function of the lower die angle, can be seen in Fig. 10.8.

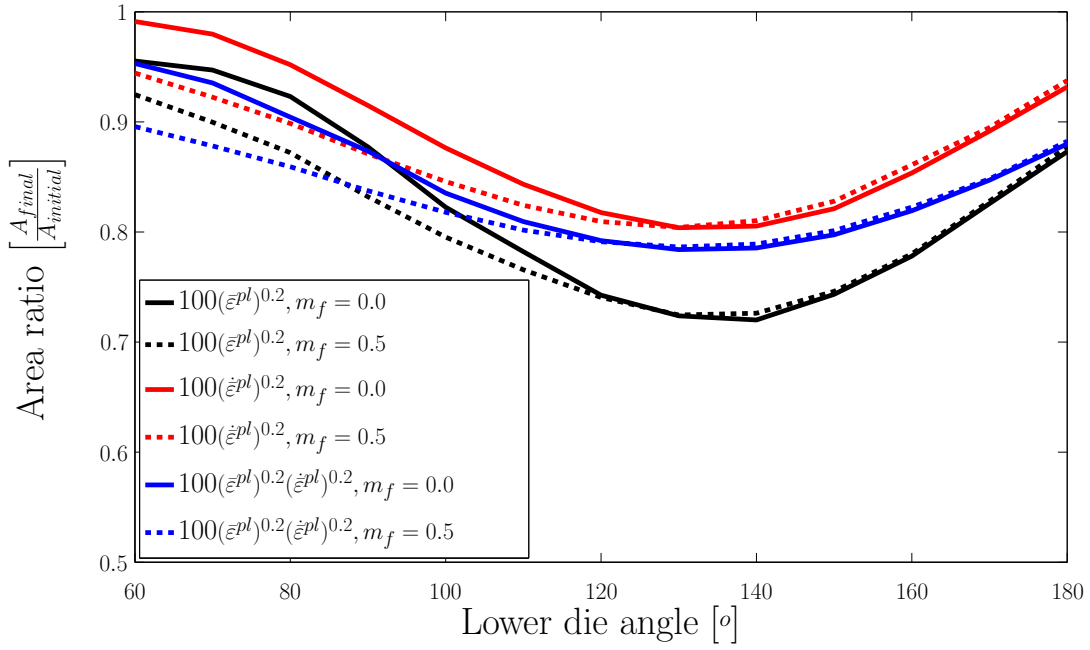

Fig. 10.8. Area ratio as a function of lower die angle for different hardening behaviours. [Author's own code].

Applying a combined hardening material does not result in significant differences from a pure strain hardening or a pure strain rate hardening material as seen in Fig. 10.8. The maximum predicted closure occurs for a lower die angle of approximately 130°-140° and friction has only a minor influence on the location of the optimum.

10.4.4 Maximum forging force as function of material properties

The maximum forging force is also calculated for the different material hardening models. For simplicity only simulations with friction are plotted in Fig. 10.9. The die width is 1000mm.

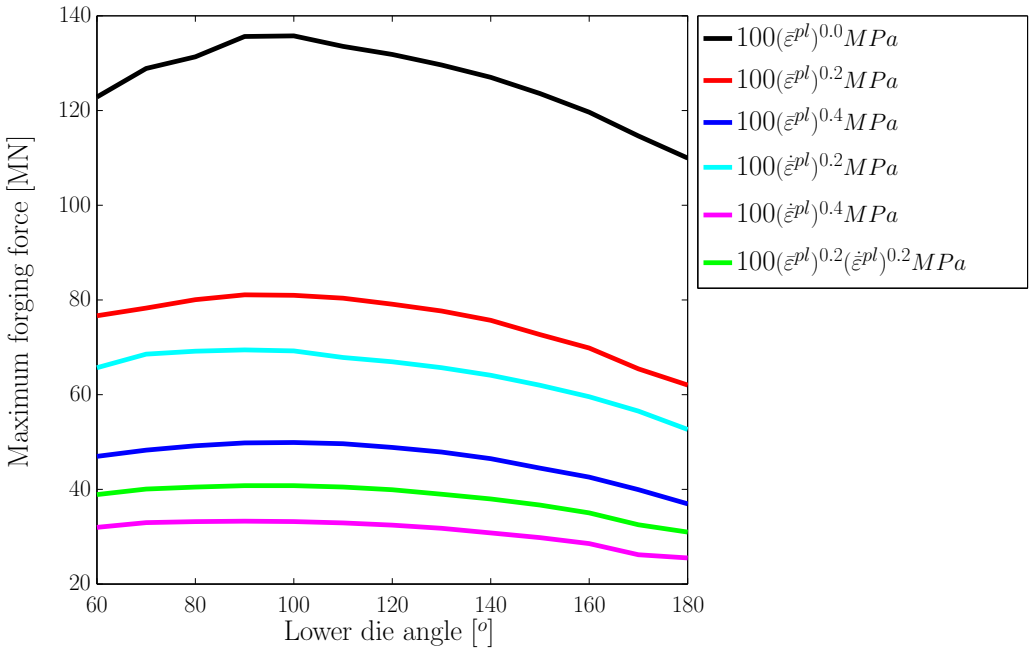

Fig. 10.9. Maximum forging force for different material hardening behaviours. [Author's own code].

As it can be seen from Fig. 10.9 the maximum forging force is quite different for different materials. From a practical point of view one should therefore be careful when forging ingots of different materials using the same press. When the press can deliver sufficient force for forging one type of ingot, it is not necessarily sufficient for forging an ingot of a different material although ingot dimensions may be the same.

10.5 The influence of the stroke length on centreline hole closure

In order to investigate whether the optimum lower die angle for a single stroke compression is influenced by the stroke length of the moving upper die, three different stroke lengths are compared: 100mm, 200mm and 300mm. An ingot with hardening behaviour described by $\sigma_o = 100\left(\dot{\bar{\varepsilon}}^{pl}\right)^{0.2}$ is compressed. This material is chosen to model steel 42CrMo4 at 1200°C. An analysis of the slope of the experimental stress-strain-rate curve seen in Fig. 3.1b yields $m \approx 0.19$. A plot of the predicted centreline hole closure may be seen in Fig. 10.10.

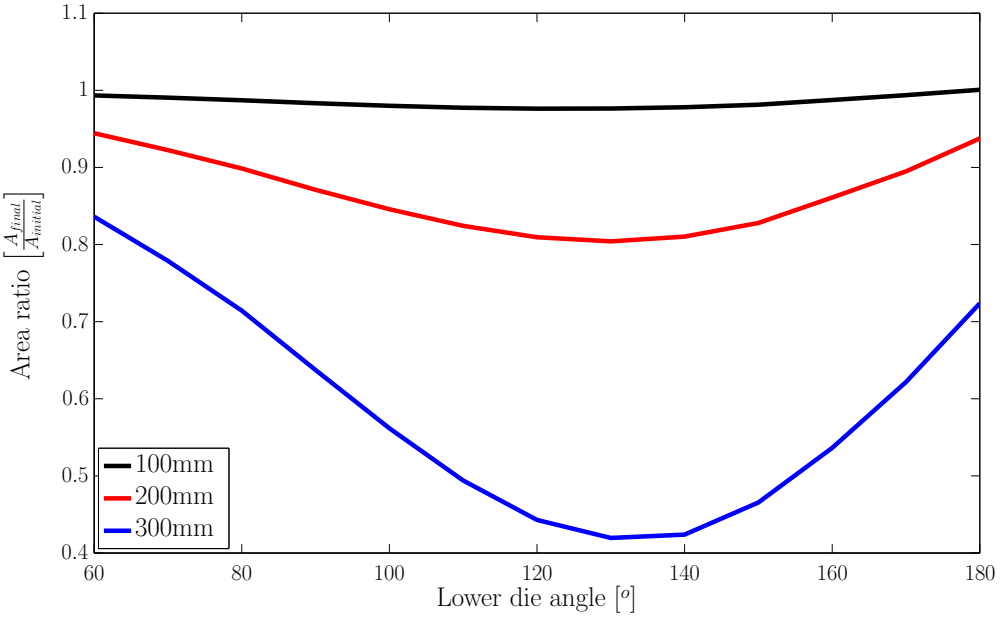

Fig. 10.10. Centreline hole closure for different lower die angles and press stroke lengths. [Author's own code].

From Fig. 10.10 a clear increase in the centreline hole closure is observed when increasing the press stroke length, which is in accordance with the practical findings that the press stroke should be as large as possible. It is also seen that the location of the optimum lower die angle becomes more distinct but does not change. The predicted optimum lower die angle is approximately 130°.

The maximum forging force needed for the compression can be seen in Fig. 10.11.

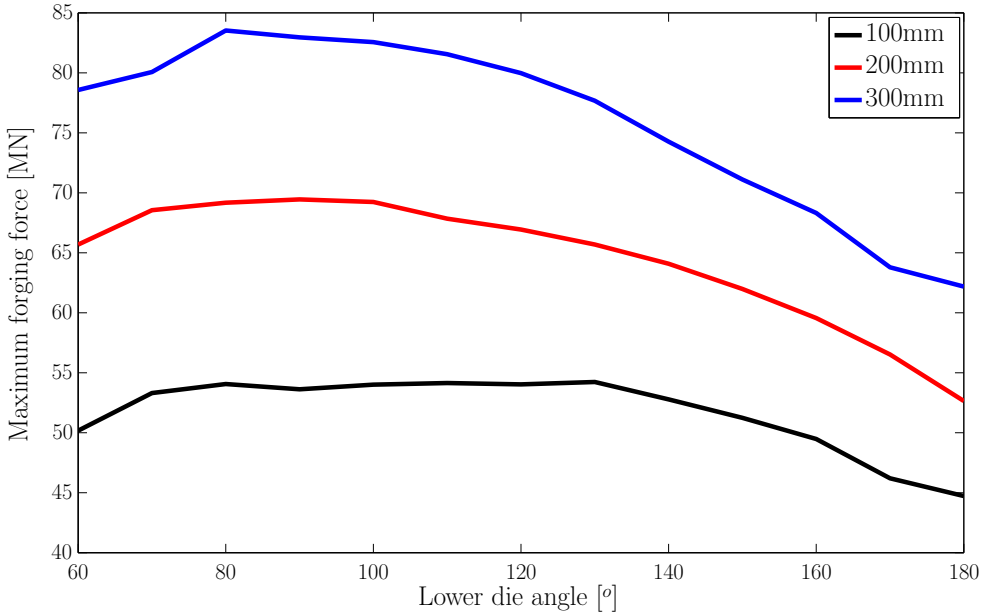

Fig. 10.11. Maximum forging force for different lower die angles and press stroke lengths. [Author's own code].

Fig. 10.11 shows an increase in maximum forging force with increasing stroke length. The increase in forging force is not linear with stroke length increase and seems to increase less as the stroke length increases. It is interesting to notice that the maximum forging force occurs for a lower die angle of approximately 90° whereas the maximum centreline hole closure occurs for a lower die angle of approximately 130°-140° in a single stroke compression operation.

10.6 Conclusion

The die geometry in ingot forging operations has been optimized regarding closure of centreline porosities, here modelled as a hollow centreline defect. The optimization has been performed using a one-stroke approach with variables being ingot material, friction, lower die angle and press stroke length. It has been found that an optimum angle, for all the different material hardening behaviours tested, was approximately 130°-140°. Friction seems only to have a minor influence on the process and only for quite inclined lower dies. The location of the optimum becomes more pronounced as the stroke length is increased. This however does also increase the forging force, hence for larger reductions in a single stroke, a large press is needed. This may in practice limit the maximum applicable stroke. Different materials also affect the maximum press force, hence forging ingots of same dimensions but of different materials may not necessarily be possible using the same press. It is interesting to notice that maximum closure appears for a different lower die angle than the one giving rise to the maximum press force. One should however be careful about making conclusions based on a single stroke compression since the actual ingot forging operation comprises a number of forging operations with intermediate rotations of the ingot. This is therefore investigated further in the next chapters.

11 Optimization of lower die angle in multi stroke forging operations - Damage mechanics approach

11.1 Introduction

Since the ingot forging process consists of several compressions, with intermediate rotations of the ingot, this should be considered, when searching for the optimum lower die angle by performing simulations. Due to the increased computational work necessary to perform multi stroke forging operations, the author decided not to include material and stroke length as design variables. The variable investigated in this chapter is therefore only the lower die angle. As mentioned in Chapter 7, the induced damage during forging can be modelled by for instance uncoupled ductile damage criteria or by porous plasticity. In this chapter, damage is modelled by the uncoupled normalized Cockcroft & Latham criterion (see 7.3.2). In order to evaluate the best lower die angle, optimization criteria are needed. In this chapter a combination of damage and strain are used. The best lower die angle is defined as the one which reduces ductile damage while allowing for plastic straining to occur in order to have the beneficial metallurgical effects from the plastic straining (see Chapter 2 and Chapter 6).

The geometrical shape of the final component, i.e. how circular the cross-section of the ingot is after forging, is not considered as a primary criterion for the forging operation. The main purpose is to ensure mechanical soundness of the part rather than geometric shape.

11.2 Numerical simulation layout

The simulation is performed using the commercial FEM program DEFORM-2D®. A 2D plane stress model is utilized. The ingot is assumed to have a diameter of 2000mm. 2067 quadrilateral elements with 2119 nodes are used. The ingot is compressed 200mm (10% of the initial diameter) in each stroke. 17 strokes are applied with 45° rotation between each stroke, as is also done in industrial practice. Five different lower die angles are applied (60°, 90°, 120°, 150°, 180°). The initial temperature of the ingot is 1200°C. The heat transfer coefficient between dies and ingot is set to 5kW/(m^{2}K). Heat transfer into air is not taken into account in the simulation because the heat loss into the air is much dependent on how fast the ingot can be manipulated during the forging procedure, hence it is much dependent on equipment and the skill of the personnel. Therefore only heat loss to the dies are investigated, concerning whether this heat loss is significant or not.

A problem was encountered by the author when bringing the ingot in contact with the lower die after rotation. Often the ingot was only in contact with one of the inclined parts of the lower die. Therefore a large part of the press stroke would be used on rigid

body movement of the ingot until it started touching both the inclined parts of the lower die. To circumvent this problem, the author had to manually adjust the ingot after rotation to bring it into contact with both of the inclined parts of the lower die before each forging operation. This was a rather time consuming procedure since it could not be automatized, and therefore limited the number of performed simulations. An illustration of the simulation layout can be seen in Fig. 11.1.

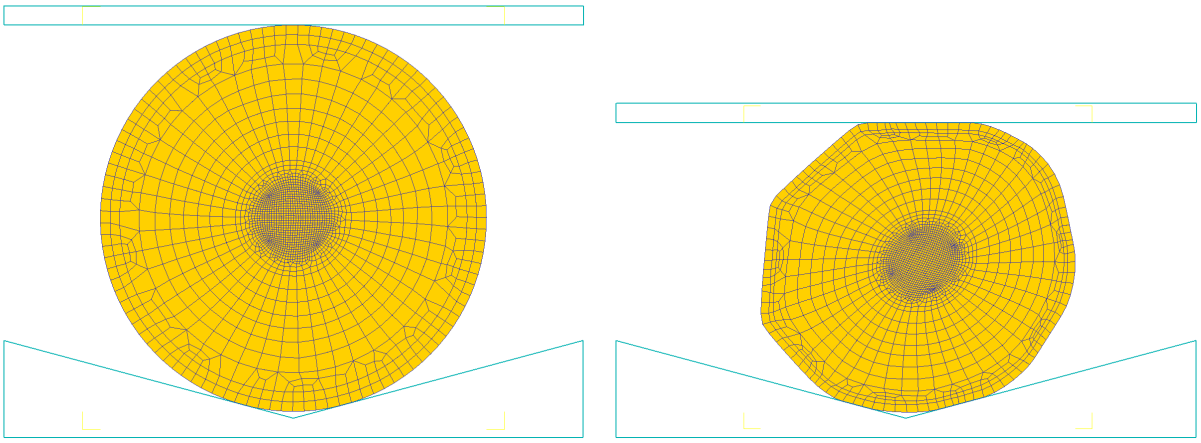

(a) Initial. **(b)** Final.

Fig. 11.1. Simulation layout before and after forging.

It can be seen from Fig. 11.1 that an unstructured mesh is used with more elements at the circumference for good description of the contact between ingot and dies, and a refined mesh in the center region in order to carry out a detailed investigation here to determine the evolution of centreline defects.

A summary of the simulation settings are found in Table 11.1.

Table 11.1. FEM simulation settings.

Ingot diameter	2000mm
Penalty factor	$K = 10^6$
Mesh	2067 4-node quadrilateral elements (2119 nodes)
Number of time steps	200
Convergence criteria	$\frac{\|\triangle \mathbf{v}\|}{\|\mathbf{v}\|} \leq 0.01$ and $\frac{\|\triangle \mathbf{f}\|}{\|\mathbf{f}\|} \leq 0.1$
Press speed	50mm/s
Friction	$m_f = 0.5$
Ingot material	42CrMo4 (Flow stress data from DEFORM® database)
Damage modelling	Uncoupled normalized Cockcroft & Latham
Dies	Rigid-contact surface elements
Heat transfer coefficient ingot-dies	5kW/(m^{2}K)
Forging procedure	17 strokes, 200mm comp., 45^o rotation in between

11.3 Examples of simulation results

As an illustration of the simulations, some examples of effective plastic strain and ductile damage, predicted by the normalized Cockcroft & Latham criterion, are presented. All

figures represend the end of the entire deformation process.

11.3.1 Effective plastic strain

The effective plastic strain after 17 strokes can be seen in Fig. 11.2-Fig. 11.6.

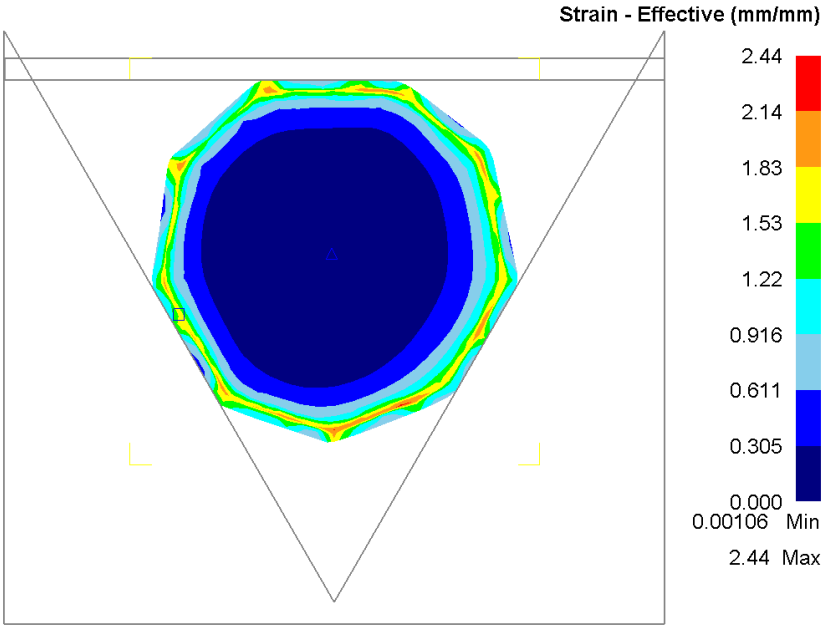

Fig. 11.2. Effective plastic strain. 60º lower die.

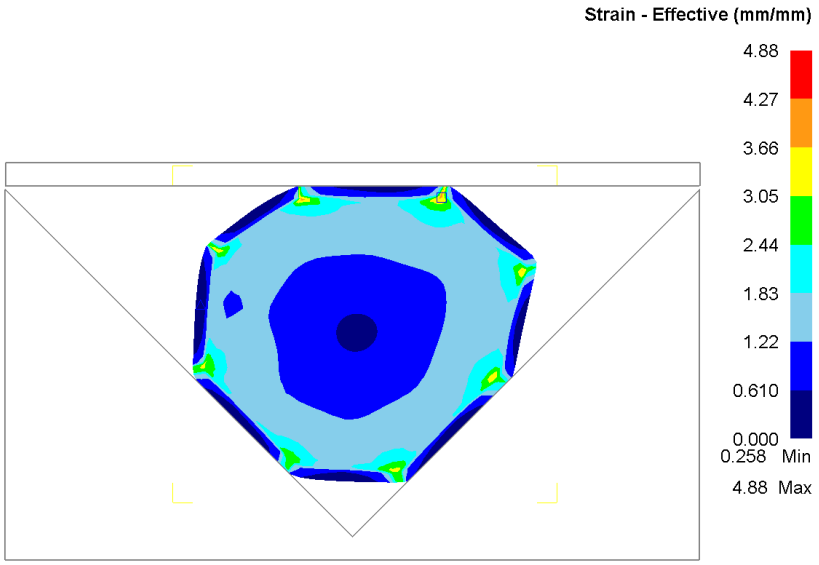

Fig. 11.3. Effective plastic strain. 90º lower die.

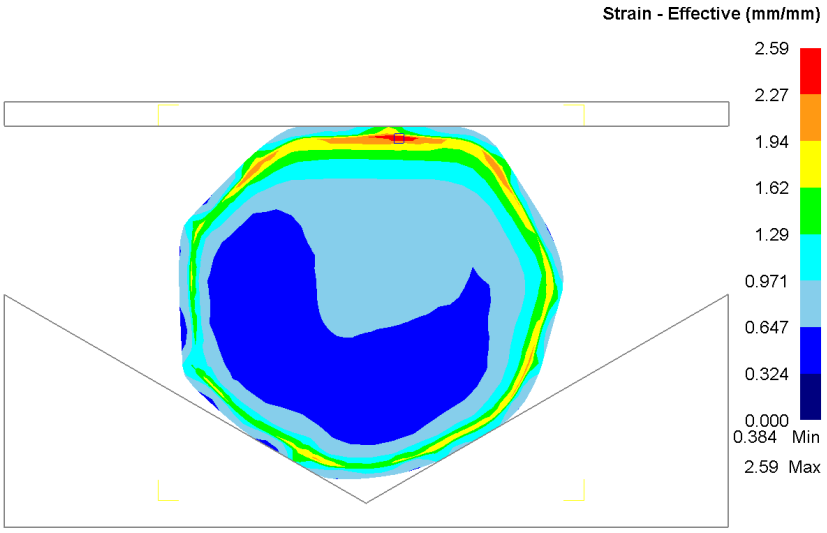

Fig. 11.4. Effective plastic strain. 120º lower die.

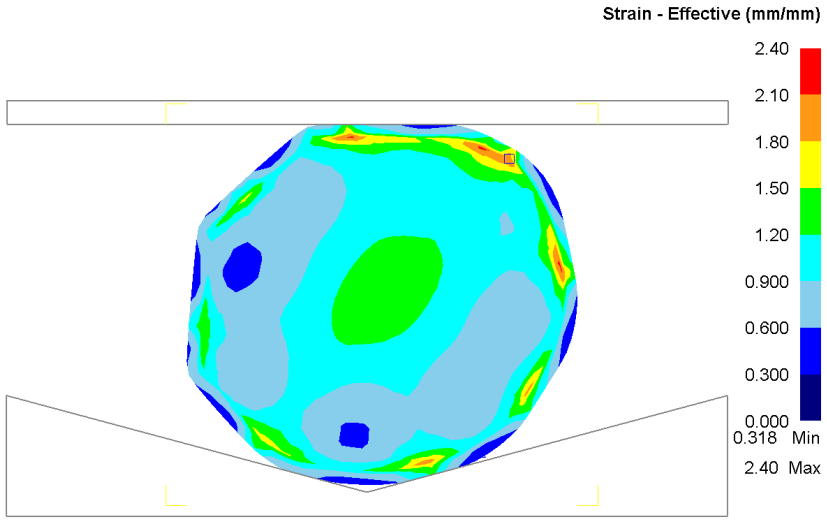

Fig. 11.5. Effective plastic strain. 150º lower die.

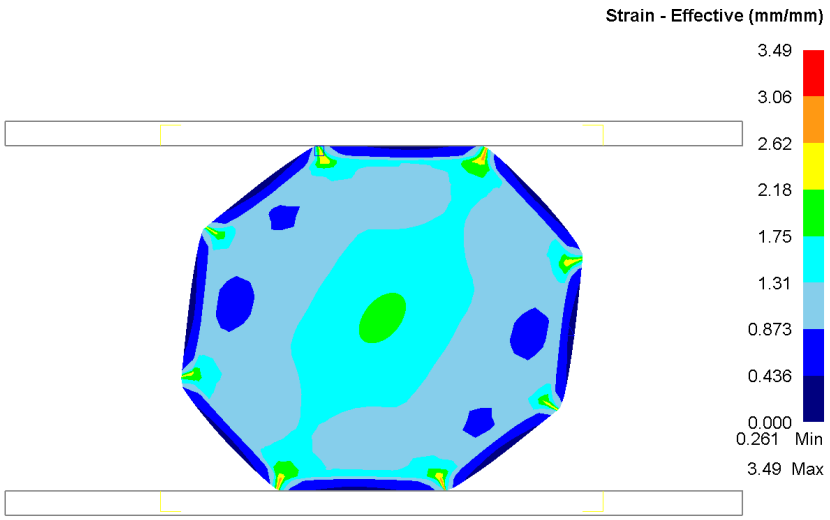

Fig. 11.6. Damage. 180° lower die.

Quite different strain patterns are observed in Fig. 11.2-Fig. 11.6. It is noticed that a large dead zone appears in Fig. 11.2. This is in qualitative agreement with the upper bound analysis in Section 5.3. For the other lower die angles, the smallest effective plastic strain appearing in an element is approximately 0.25, hence some straining is appearing everywhere.

11.3.2 Examples of ductile damage

The predicted accumulated ductile damage can be seen in Fig. 11.7-Fig. 11.11.

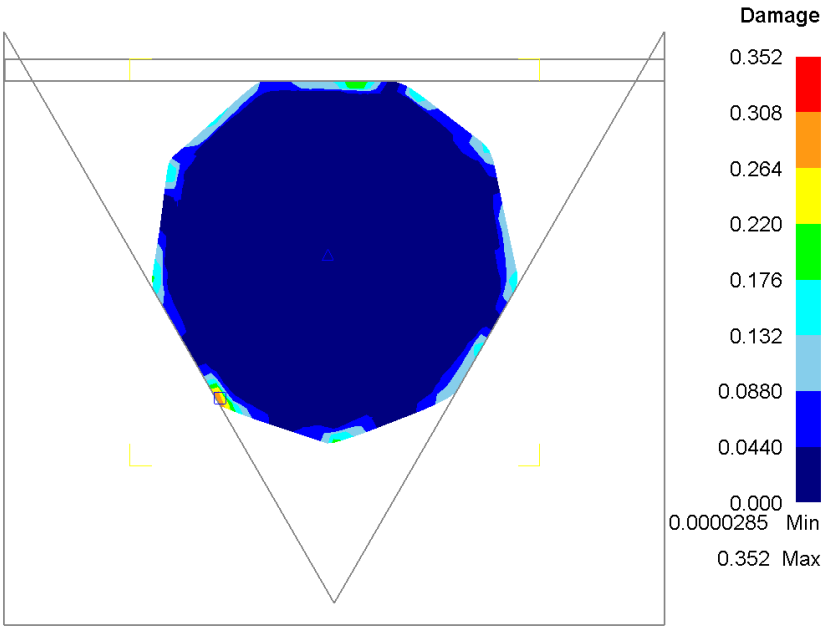

Fig. 11.7. Damage. 60° lower die.

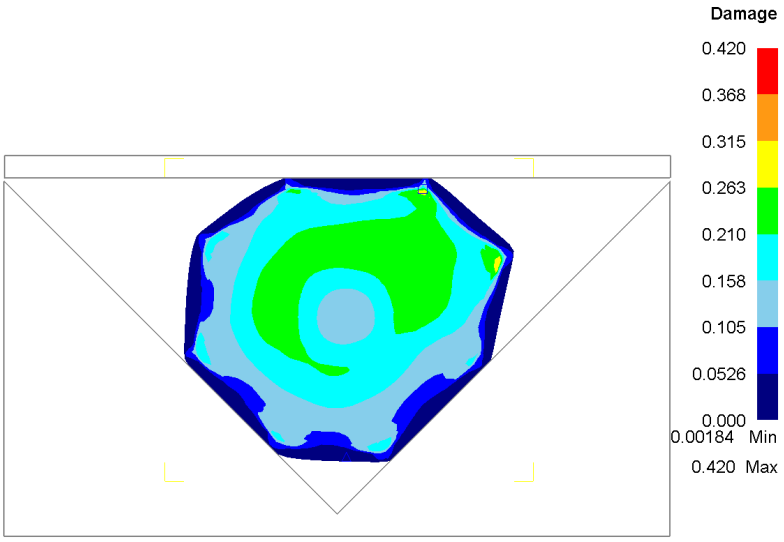

Fig. 11.8. Damage. 90º lower die.

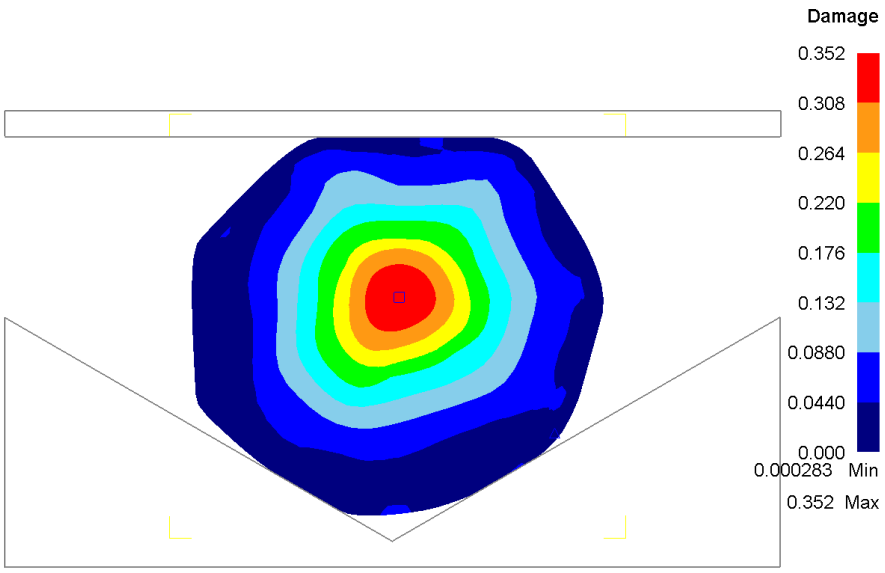

Fig. 11.9. Damage. 120º lower die.

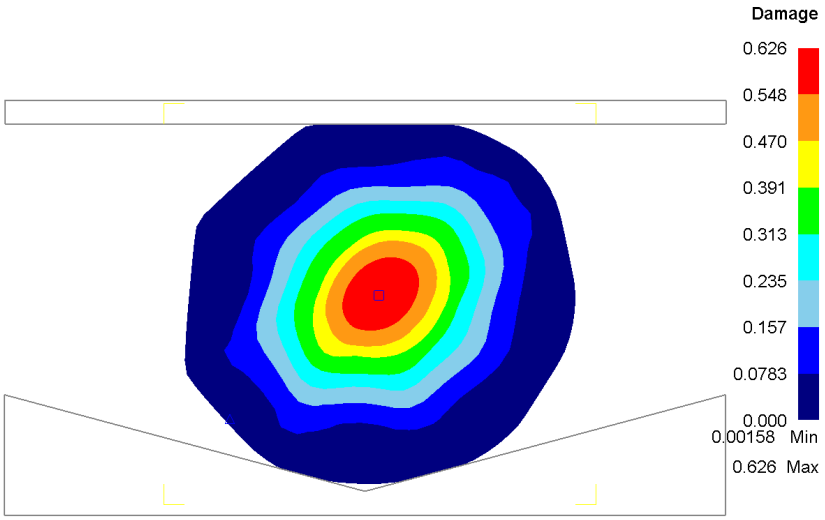

Fig. 11.10. Damage. 150° lower die.

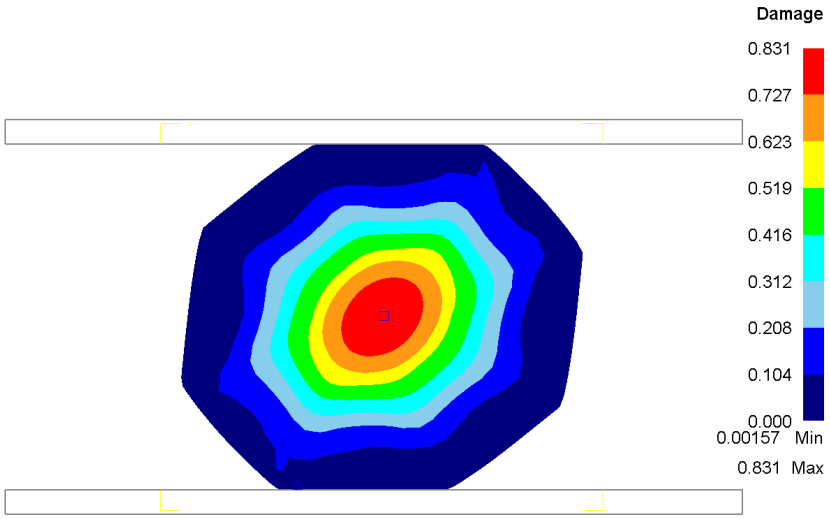

Fig. 11.11. Damage. 180° lower die.

In Fig. 11.7 damage is more or less predicted only to occur at the perimeter of the ingot. This fits with the predicted effective plastic strain (see Fig. 12.4), where a large dead zone is predicted in the center. The damage seems to be fairly evenly distributed when forging with a 90° lower die (Fig. 11.8). When forging with dies of 120°, 150° or 180°, the damage is predicted to have a maximum in the center of the ingot an decreases towards the periphery.

11.3.3 Examples of temperature

Two examples of computed temperatures in the ingot, after 17 compressions, are seen in Fig. 11.12-Fig. 11.13.

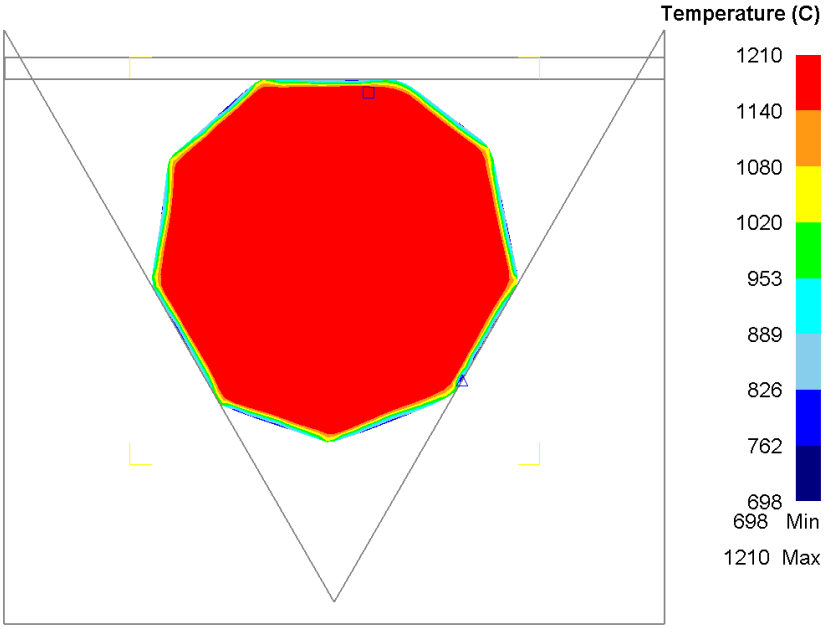

Fig. 11.12. Temperature. 60° lower die.

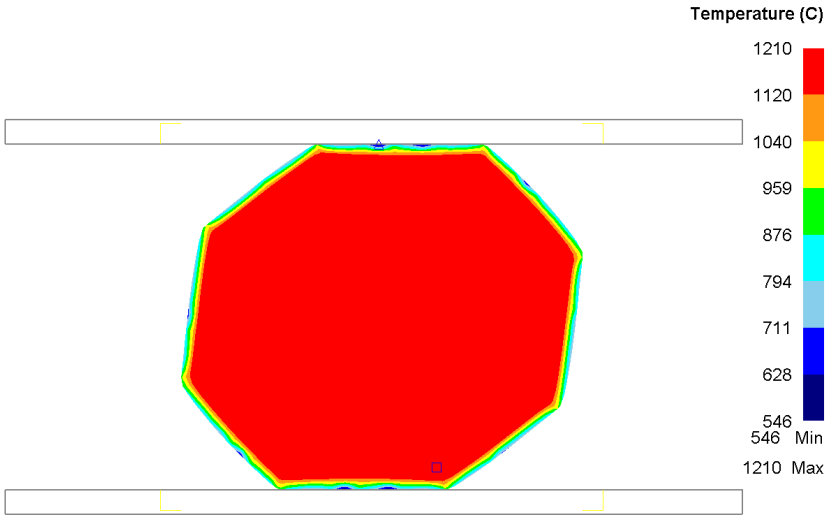

Fig. 11.13. Temperature. 180° lower die.

From Fig. 11.12-Fig. 11.13 it is seen that cooling at the die contacts only has an influence on a thin surface layer at the circumference of the ingots. The process is therefore considered not to be sensitive to this cooling effect. If cooling to the surroundings is neglected the process could be modelled as isothermal to save computational time. The total cooling time during the 17 strokes is 68s.

11.4 Evolution of the deformation

For an overview of the evolution of the different process parameters during the entire process, some different measures are applied. They are the following:

- Degree of reduction: $R = \dfrac{A_0 - A_i}{A_0}$, where A_0 is the initial cross-sectional area of the ingot and A_i is the cross-sectional area after forging stroke number i.
- Mean effective plastic strain of all the elements in the cross-section.
- Minimum effective plastic strain occurring in an element in the cross-section.
- Mean damage of all the elements in the cross-section.
- Maximum damage occurring in an element in the cross-section.

The degree of reduction gives an impression of how much the ingot has been forged. The mean effective plastic strain describes how much of the deformation that has resulted in hopefully beneficial deformation of the grains in the ingot. The minimum effective plastic strain should be high, thereby indicating that the entire ingot has been plastically deformed, so that dead zones are avoided. The mean damage should be kept low in order not to introduce unwanted defects in the ingot. The maximum damage occurring in an element should also be kept low for the same reasons as the mean damage.

It should be noticed that when calculating the mean values, a simple average of all the element values are taken. Element size is not taken into account, whereby the center and perimeter elements, which were of smaller size, have a larger influence on the average than the larger elements. In the opinion of the author this is not a disadvantage since more weight is assigned to the regions of interest. Especially the center region of the ingot, which is the primary zone of interest, gets an increased influence. It is still possible to compare between the simulations because same mesh is applied for all cases.

11.4.1 Reduction degree

The degree of reduction after each stroke can be seen in Fig. 11.14.

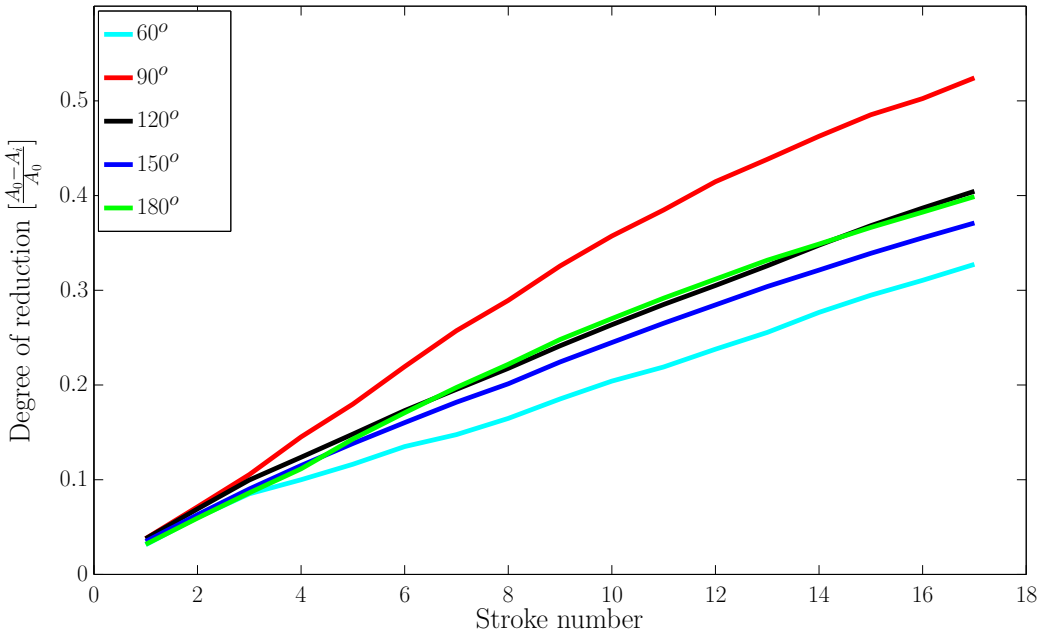

Fig. 11.14. Degree of reduction for different lower die angles.

For an overview, the final values of the degree of reduction are listed in descending order in Table 11.2.

Table 11.2. Degree of reduction after stroke No. 17.

Lower die angle	Reduction degree
90°	0.52
120°	0.40
180°	0.40
150°	0.37
60°	0.33

From Fig. 11.14 and Table 11.2 it is seen that the 90° lower die angle result in the largest degree of reduction. The ranking of which lower die angles results in the largest degree of reduction after each step is also fairly monotonic with operation number. Hence it does not shift from one step to another, which lower die angle that gives rise to the largest reduction degree.

11.4.2 Effective plastic strain

The mean and minimum effective plastic strain after each stroke can be seen in Fig. 11.15 and Fig. 11.16.

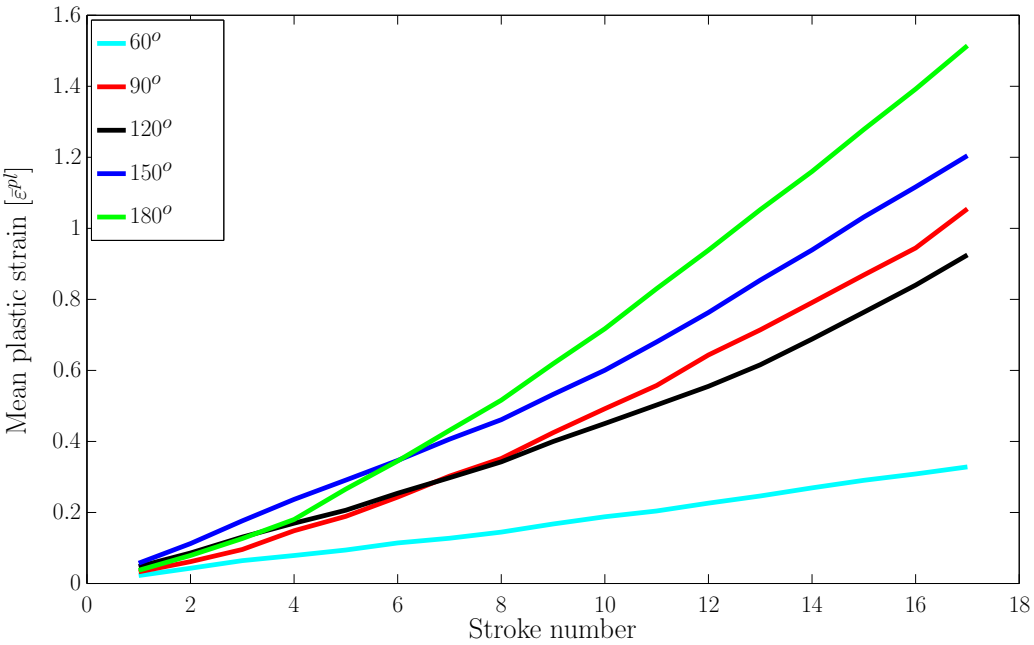

Fig. 11.15. Mean $\bar{\varepsilon}^{pl}$.

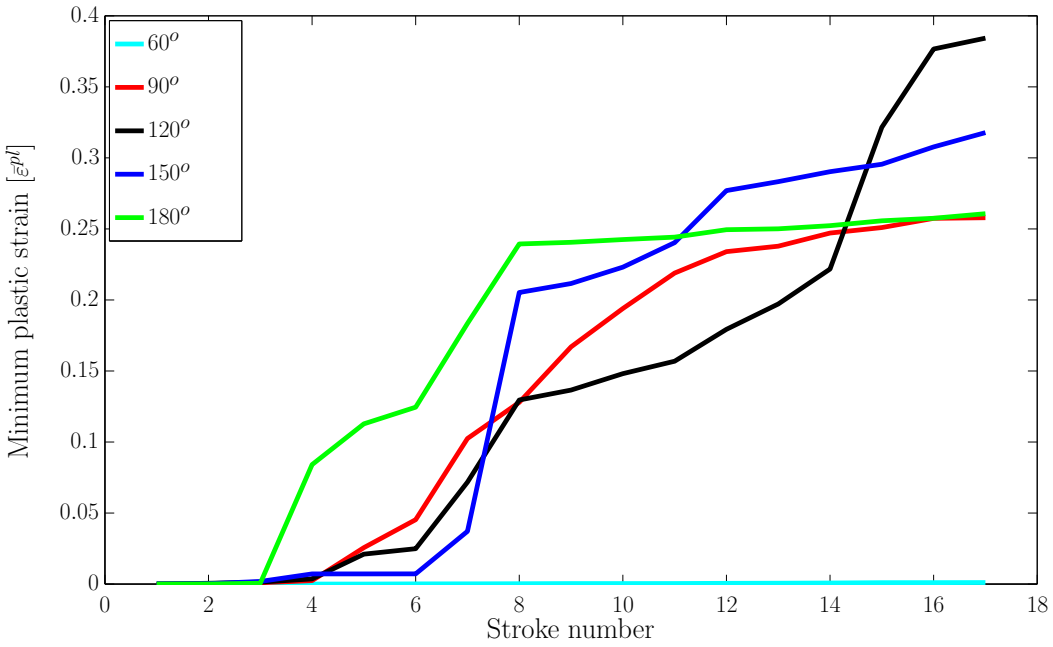

Fig. 11.16. Minimum $\bar{\varepsilon}^{pl}$.

For an overview, the approximate final values of mean and minimum effective plastic strain are listed in descending order in Table 11.3 and Table 11.4.

Table 11.3. Mean $\bar{\varepsilon}^{pl}$.

Lower die angle	Mean $\bar{\varepsilon}^{pl}$
180°	1.51
150°	1.20
90°	1.05
120°	0.93
60°	0.33

Table 11.4. Minimum $\bar{\varepsilon}^{pl}$.

Lower die angle	Minimum $\bar{\varepsilon}^{pl}$
120°	0.38
150°	0.32
180°	0.26
90°	0.26
60°	0.00

It is seen from Fig. 11.15 and Table 11.3 that forging using a 180° lower die gives rise to the largest mean effective plastic strain and 60° gives rise to the smallest one. The evolution of mean effective plastic strain is also fairly monotonically increasing with the number of strokes. The ranking of the different lower dies is constant after approximately 6 strokes.

Regarding the minimum effective plastic strain occurring in an element, see Fig. 11.16 and Table 11.4, the 120° lower die gives rise to the largest value whereas 60° results in the smallest value due to the larger dead zone in the center. Some fluctuations occur with number of strokes, as regarding which lower die angle results in the largest value of minimum plastic strain.

11.4.3 Ductile damage

The mean and maximum ductile damage after each stroke can be seen in Fig. 11.17 and Fig. 11.18.

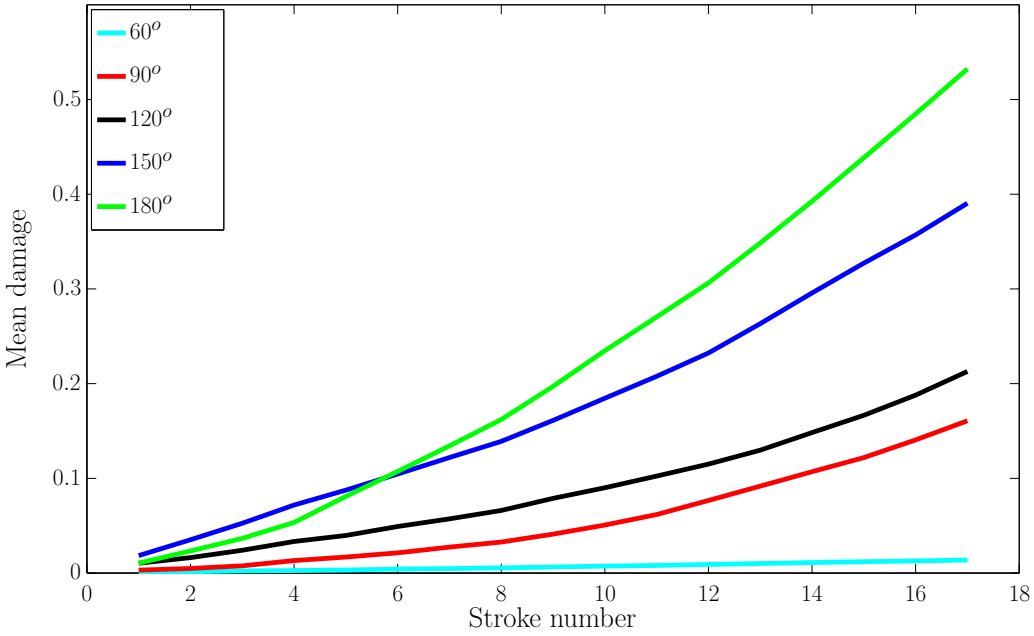

Fig. 11.17. Mean damage.

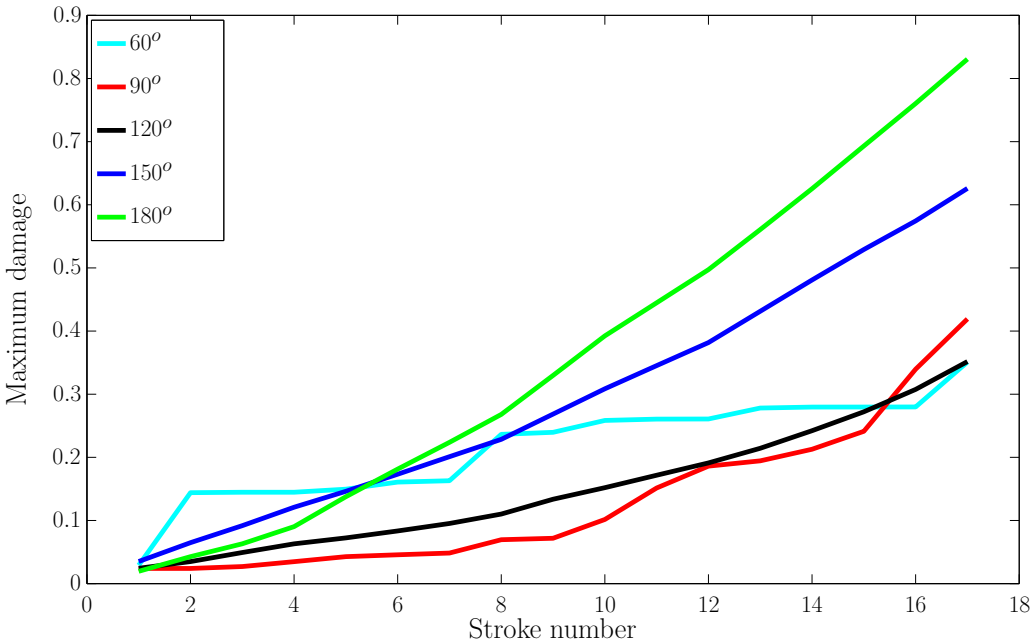

Fig. 11.18. Maximum damage.

An overview of the final values of mean and maximum damage can be seen in Table 11.5 and Table 11.6.

Table 11.5. Mean damage.

Lower die angle	Mean damage
180°	0.53
150°	0.39
120°	0.21
90°	0.16
60°	0.01

Table 11.6. Maximum damage.

Lower die angle	Maximum damage
180°	0.83
150°	0.63
90°	0.42
120°	0.35
60°	0.35

The mean damage, seen in Fig. 11.17 and Table 11.5 evolves fairly monotonic with 180° resulting in the largest mean damage and 60° resulting in the smallest mean damage. Again the ranking is constant after approximately 6 strokes. There is some more fluctuation in the ranking of the maximum damage, see Fig. 11.18. However forging with a 180° lower die gives rise to the worst final result. The 150° die is also unsuitable. The 60°, 90° and 120° dies give fairly similar results regarding maximum ductile damage with shifts during the forging sequence as to which one gives smallest damage.

11.5 Ranking of lower die angles

In order to make a ranking of the different lower die angles, the author uses a simple ranking system by assigning the value 1 to the "best" and ranking the other relative to the value of the best lower die angle. "Best" is defined for the effective plastic strain as the largest value. The motivation being that a large value implies recrystallization and is therefore beneficial. "Best" as regarding damage is defined as the lowest value. The motivation being that a small value implies small formation and growth of porosities in the ingot.

The ranking regarding effective plastic strain and ductile damage is seen in Fig. 11.19 and Fig. 11.20.

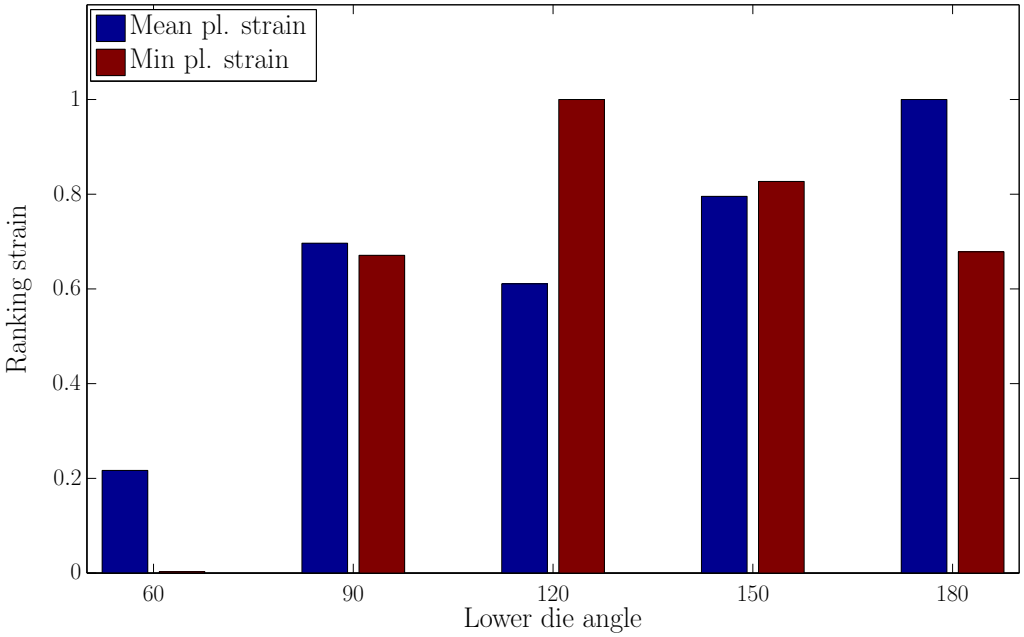

Fig. 11.19. Ranking regarding effective plastic strain.

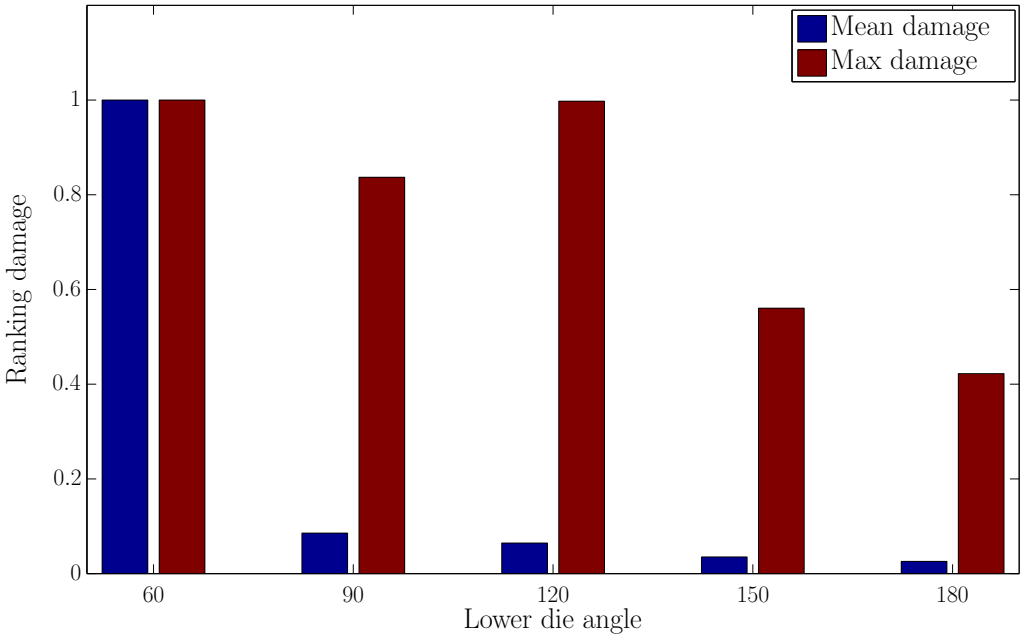

Fig. 11.20. Ranking regarding damage.

The net score is calculated by taking the average of the four different scores for each lower die angle. The final score is seen in Fig. 11.21.

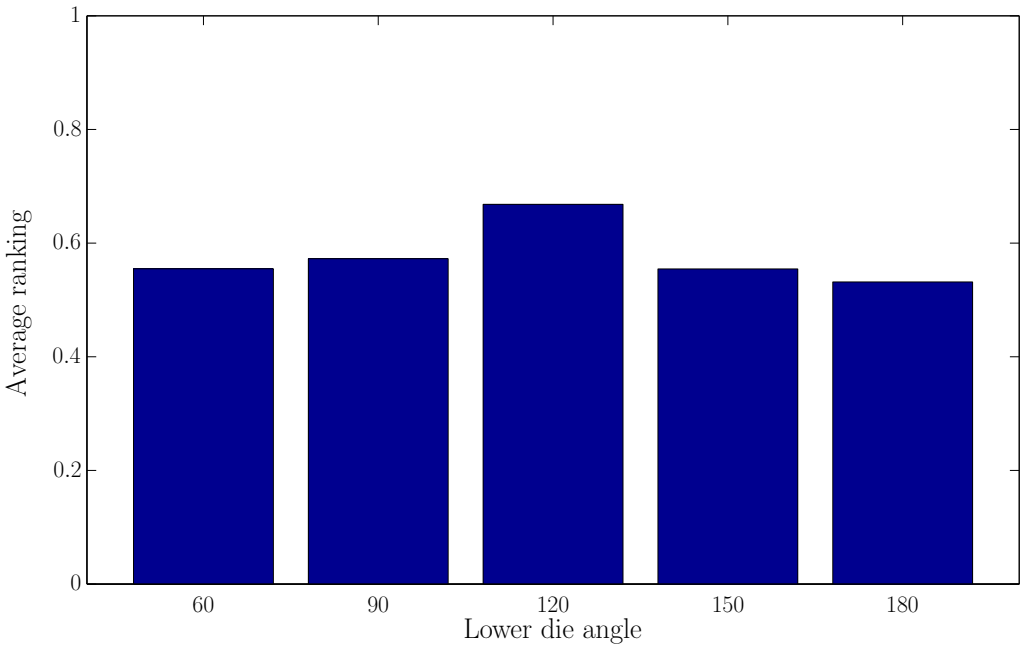

Fig. 11.21. Optimum lower die angle.

The score can also be seen, ranked in ascending order, in Table 11.7.

Table 11.7. Score for the different lower die angles.

Lower die angle	Average points
120°	0.67
90°	0.57
60°	0.55
150°	0.55
180°	0.53

From Fig. 11.21 and Table 11.7 the 120° die is the best. The other die angles are ranked fairly evenly.

It needs to be emphasized that this ranking is quite primitive and it may be beneficial in future work to use some more advanced statistical measures for describing the distribution of the element variables damage and effective plastic strain. The procedure for finding the optimum lower die angle, as described in this chapter, should only be viewed as a first suggestion.

11.6 Conclusion

Multi stroke forging of a real size cross-section of an ingot has been modelled using a plane stress model. Five different lower die angles have been utilized in a 17 stroke forging operation with 45° rotation between strokes. The process has been quantitatively described by the measures effective plastic strain and normalized Cockcroft & Latham damage. A primitive ranking scheme yielded that the 120° die is best when evaluated in terms of effective plastic strain and ductile damage.

12 Optimization of lower die angle in multi stroke forging operations - Porous plasticity approach

12.1 Introduction

In Chapter 11 an optimization of the lower die angle in ingot forging was performed by uncoupled ductile damage modelling. Another approach to model damage is to use a porous plasticity model, see 7.2.1, where accumulated damage is modelled as a loss in density, which changes the yield surface. This approach is also adopted to optimize the lower die angle.

The numerical procedure follows the one outlined in Chapter 10. Five lower die angles (60°,90°,120°,150°,180°) are used to forge an ingot in 17 consecutive strokes with a given fixed displacement. An initial porosity density is assigned in order to mimic a real porosity distribution in a cross-section of an ingot after casting. A combination of strain and density measures are then applied to rank the different lower die angles.

12.2 Numerical simulation layout

Numerical simulations are performed using the commercial software DEFORM-3D®. A simple 2D plane stress model would have been more suitable. However porous plasticity is not implemented in DEFORM-2D® for plane stress. Therefore an approximately plane stress model is set up in DEFORM-3D®. An ingot with 2000mm in diameter but only 10mm in thickness is utilized. The small thickess ensures approximately plane stress conditions. All nodes on one side of the plate are fixed in longitudinal direction. Thereby approximately plane stress is achieved, while the ingot cross-section is still free to deform in the other directions.

The forging process consists of 17 strokes with a stroke length of 200mm (10% of initial ingot diameter) each. The ingot is rotated between each stroke. Two different angles of rotation are applied: 45° and 75°. 45° is applied because this is used in industrial practice. However the author was also interested in applying a different angle of rotation, the motivation being that after 8 rotations using 45°, the ingot has been rotated a complete round and the same areas of the ingot are being compressed once more. By applying 75° rotation, new areas are brought into contact after reaching a complete round. It would be interesting to study whether this would make a difference in the predicted optimum lower die angle.

2067 8-node brick elements (4196 nodes) are used together with the same mesh layout as in Chapter 11. An example on the model can be seen in Fig. 12.1.

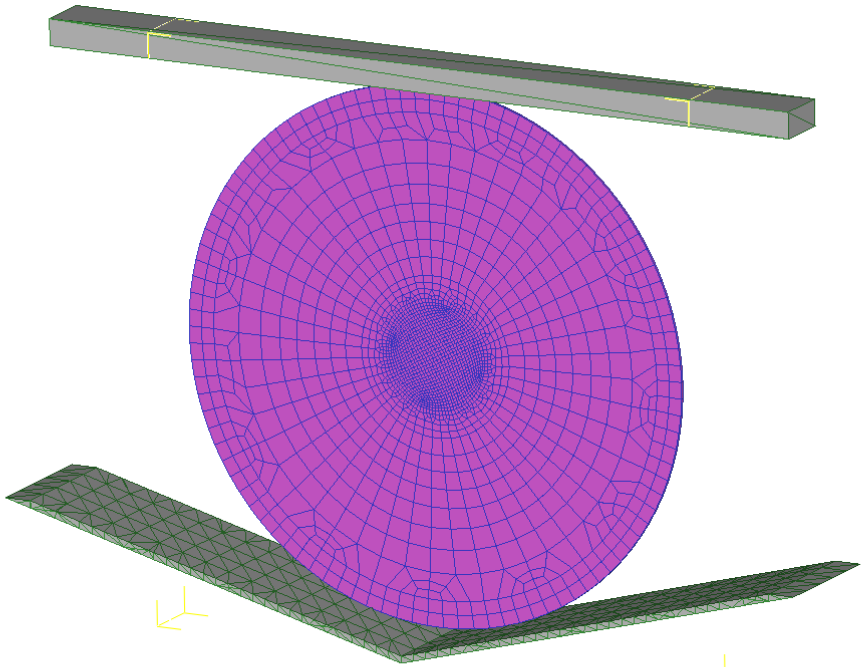

Fig. 12.1. Simulation layout.

A varying relative density $R = \frac{\rho}{\rho_o}$, where ρ is the actual density and ρ_o is the density of the fully dense material, is assigned. From the center to a radius of 100mm, a relative density of 0.25 is assigned. Then the relative density increases linearly from 0.25 at radius 100mm to 0.9 at radius 200mm. From radius 200mm to the outer edge at radius 1000mm, the relative density increases linearly to 0.99. This relative density is motivated by P. Kotas[1], who has simulated ingot casting using the commercial software Magmasoft. The simulation of Kotas and the implemented relative density in DEFORM® 3D can be seen in Fig. 12.2 and Fig. 12.3. The slightly non-symmetric prescribed relative density seen in Fig. 12.3 is attributed to the non-symmetric mesh.

[1]Former member of the Process Modelling Group at DTU. Now employee at Magma Gießereitechnologie GmbH.

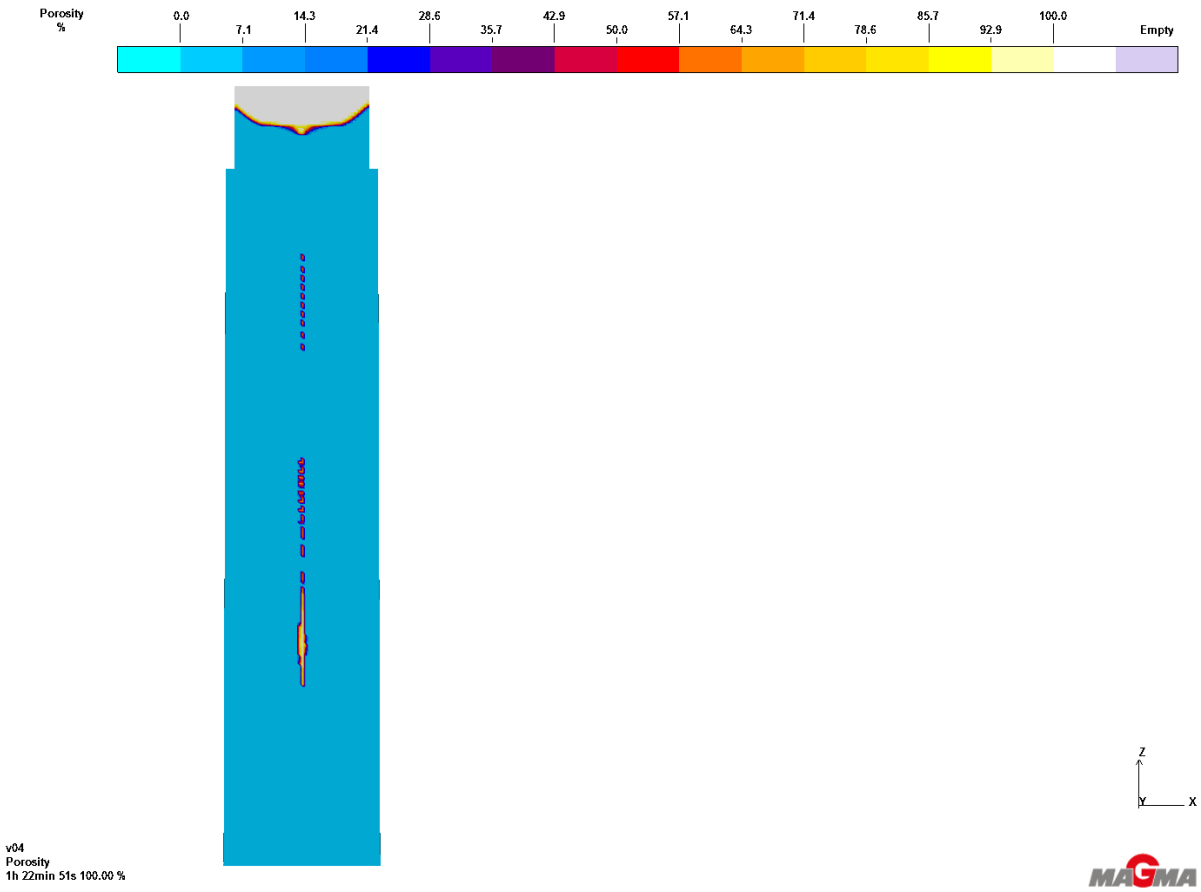

Fig. 12.2. Simulated porosities in a cast ingot. Courtesy to Dr. P. Kotas, Magma Gießereitechnologie GmbH.

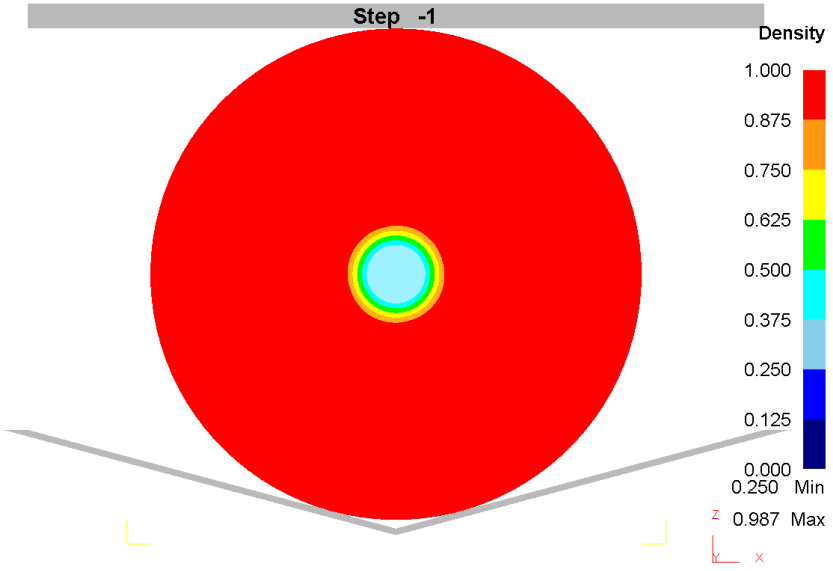

Fig. 12.3. Prescribed initial relative density utilized for simulation using DEFORM-3D®.

The simulated ingot in Magmasoft has a diameter of approximately 460mm and a length of approximately 2300mm. It is therefore somewhat smaller than the ingot investigated by the author, but at least it provides some clue regarding the porosity size and location. The very porous region constitutes approximately 6% of the ingot diameter. Since the size of the porous zone is likely to increase with ingot diameter, and given the porous zone of approximately 10% of the diameter mentioned in 6.2.1, it is found to be reasonable to assign a porous centreline zone with a size of approximately 10% of the ingot diameter. A summary of the simulation settings can be seen in Table 12.1.

Table 12.1. FEM simulation settings.

Ingot diameter	2000mm
Penalty factor	$K = 10^6$
Mesh	2067 8-node brick elements (4196 nodes)
Number of time steps	200
Convergence criteria	$\frac{\|\triangle \mathbf{v}\|}{\|\mathbf{v}\|} \leq 0.01$ and $\frac{\|\triangle \mathbf{f}\|}{\|\mathbf{f}\|} \leq 0.1$
Press speed	50mm/s
Friction	$m_f = 0.5$
Ingot material	42CrMo4 (Flow stress data from DEFORM® database)
Damage modelling	Relative density
Dies	Rigid-contact surface elements
Heat transfer coefficient ingot-dies	5kW/(m^{2}K)
Forging procedure	17 strokes, 200mm comp., 45° or 75° rotation

12.3 Examples of simulations

In order to facilitate the understanding of the forging process, figures are presented showing effective plastic strain and relative density after completion of the 17 forging strokes.

12.3.1 Effective plastic strain, 45° rotation

The effective plastic strain after 17 strokes with 45° intermediate rotations are seen in Fig. 12.4-Fig. 12.8.

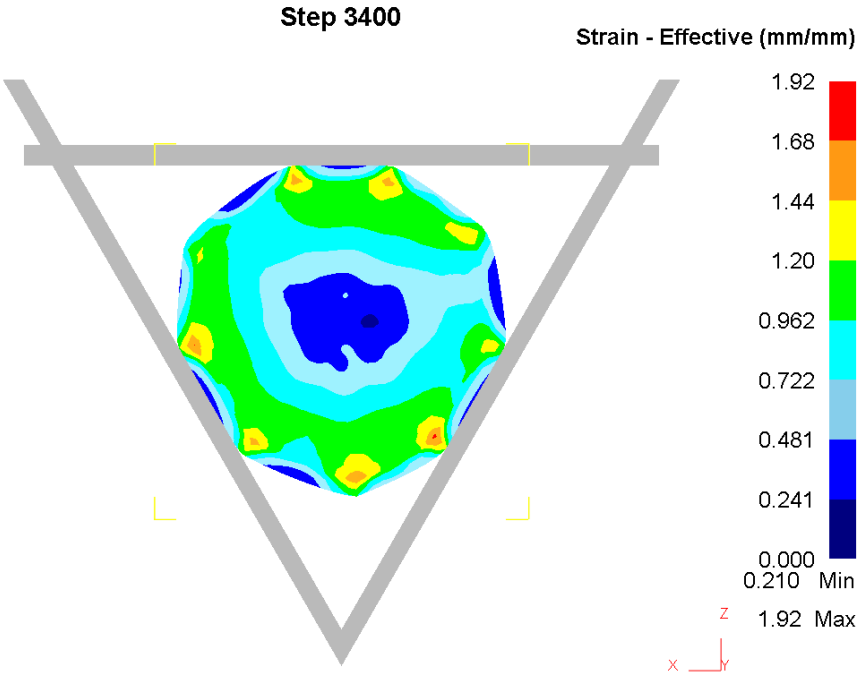

Fig. 12.4. Effective plastic strain. 60° lower die.

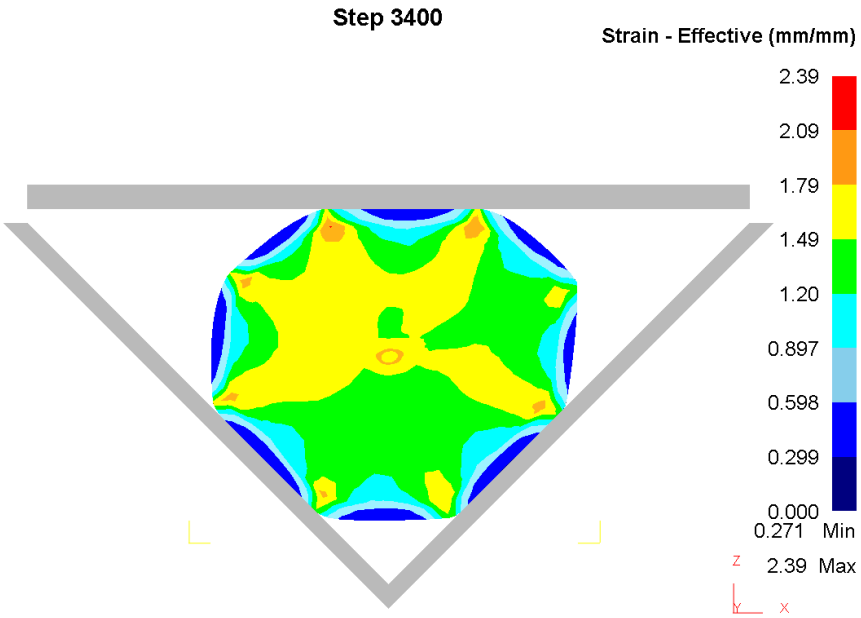

Fig. 12.5. Effective plastic strain. 90° lower die.

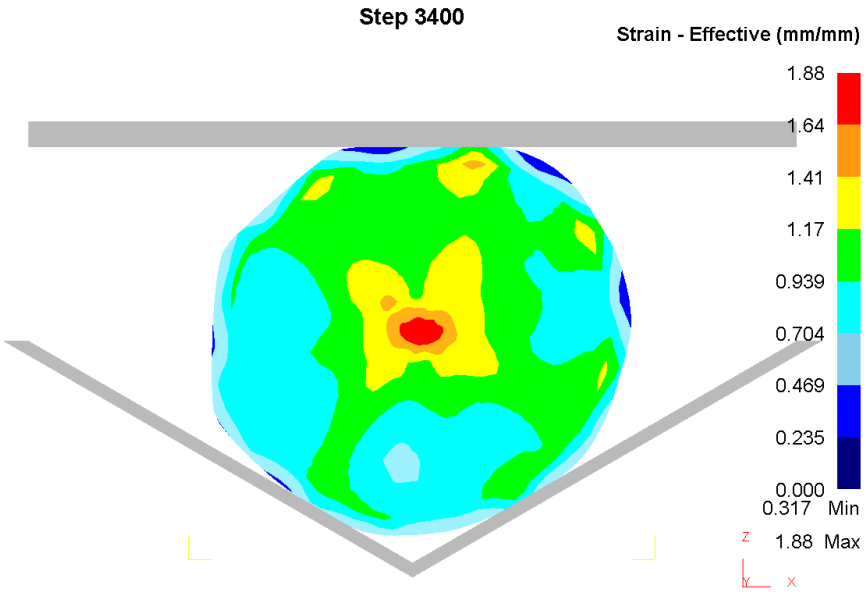

Fig. 12.6. Effective plastic strain. 120° lower die.

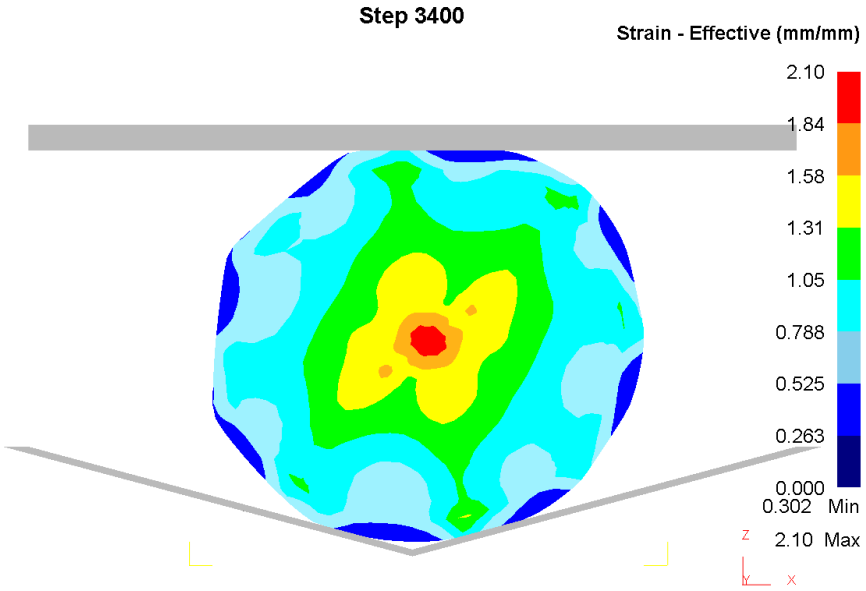

Fig. 12.7. Effective plastic strain. 150° lower die.

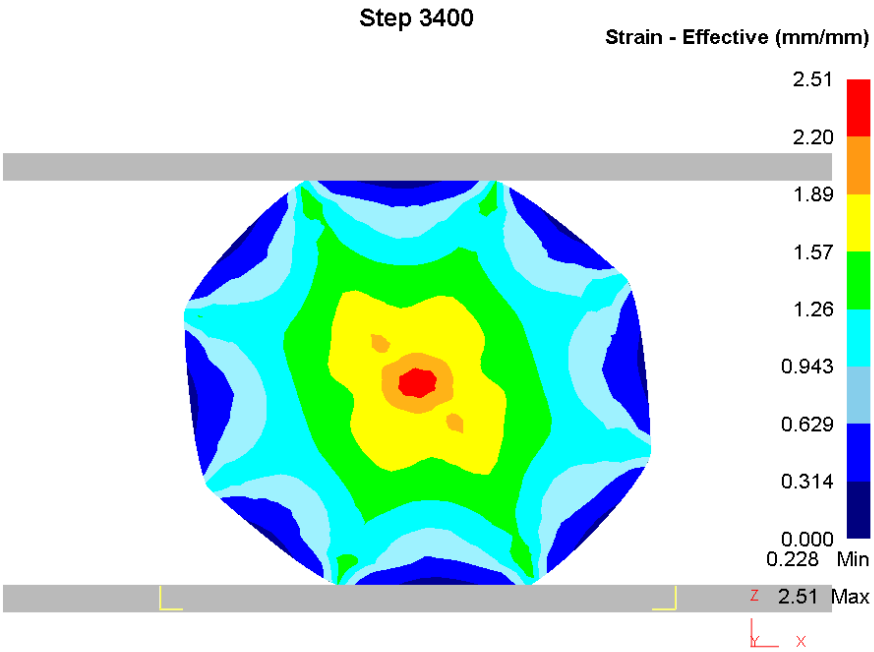

Fig. 12.8. Effective plastic strain. 180° lower die.

From Fig. 12.4-Fig. 12.8 it is seen that the dead zone occurring when forging with a 60° lower die has diminished in comparison to Fig. 11.2. Comparing Fig. 12.4-Fig. 12.8 it is noticed that increasing the lower die angle results in larger strain in the center as compared to other places in the ingot cross-section. This differs from forging a fully dense ingot as seen in Fig. 11.3-Fig. 11.6 where the largest strain appears along the perimeter of the ingot cross-section.

12.3.2 Effective plastic strain, 75° rotation

The effective plastic strain after 17 strokes with 75° intermediate rotations are seen in Fig. 12.9-Fig. 12.13. It is noticed that forging with die angles 90° and 120° results in a final cross-section far from circular.

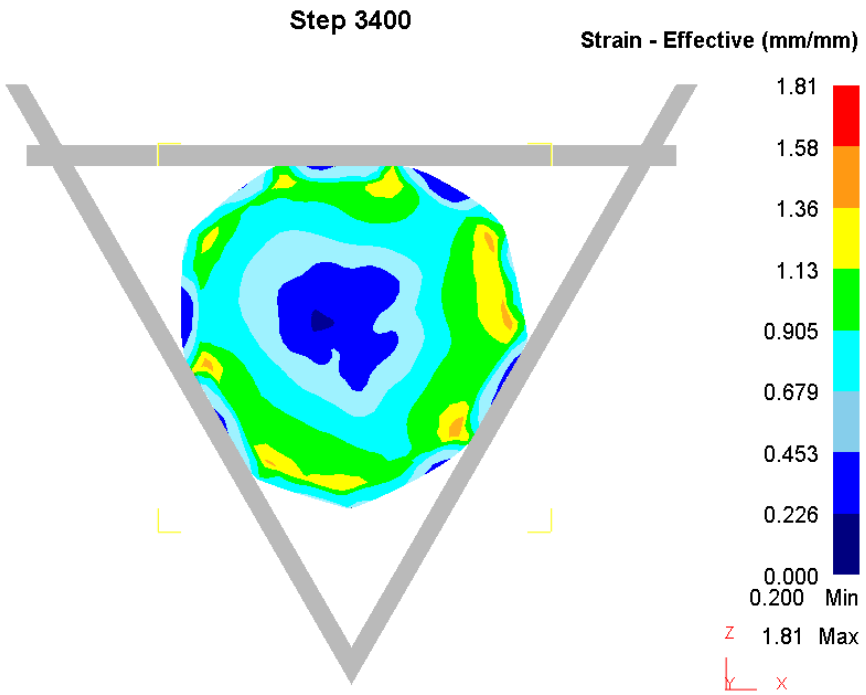

Fig. 12.9. Effective plastic strain. 60º lower die.

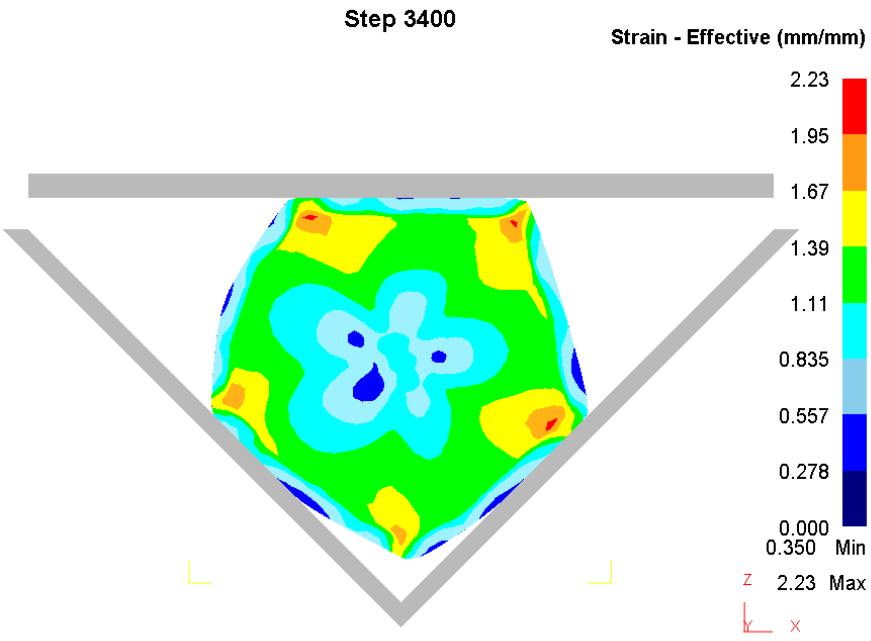

Fig. 12.10. Effective plastic strain. 90º lower die.

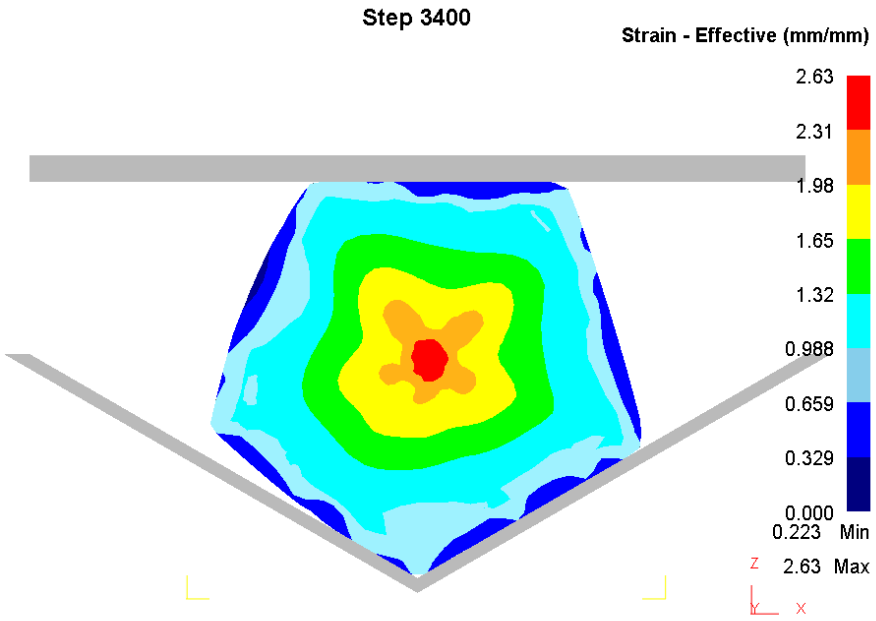

Fig. 12.11. Effective plastic strain. 120º lower die.

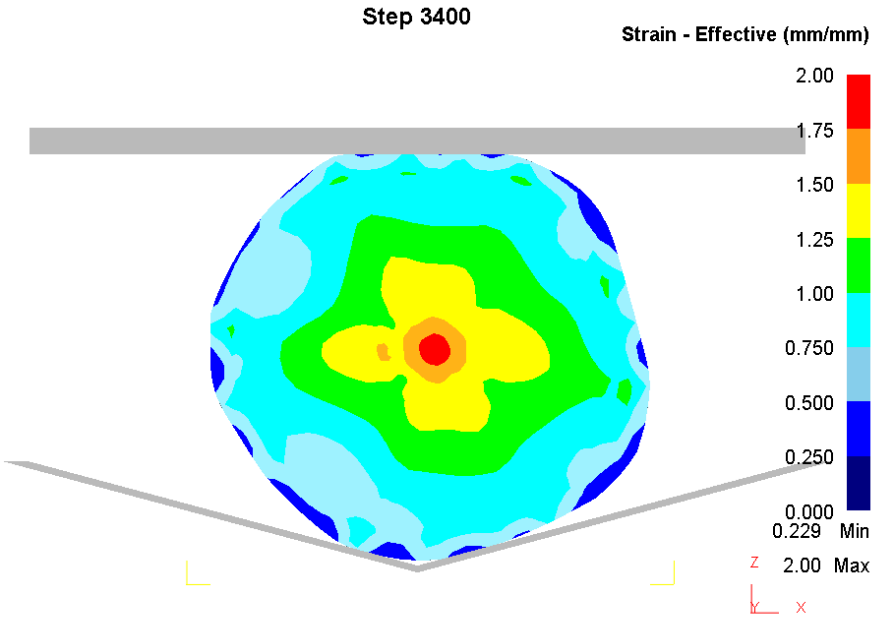

Fig. 12.12. Effective plastic strain. 150º lower die.

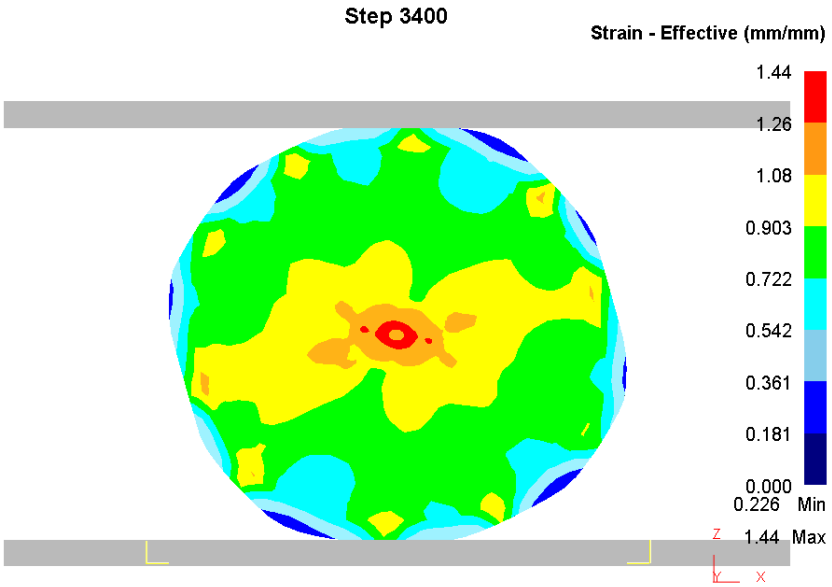

Fig. 12.13. Effective plastic strain. 180° lower die.

A more detailed comparison of strains when forging with 75° intermediate rotation angle versus 45° is found in 12.4.2.

12.3.3 Relative density, 45° rotation

The relative densities after 17 strokes with 45° intermediate rotations are seen in Fig. 12.14-Fig. 12.18.

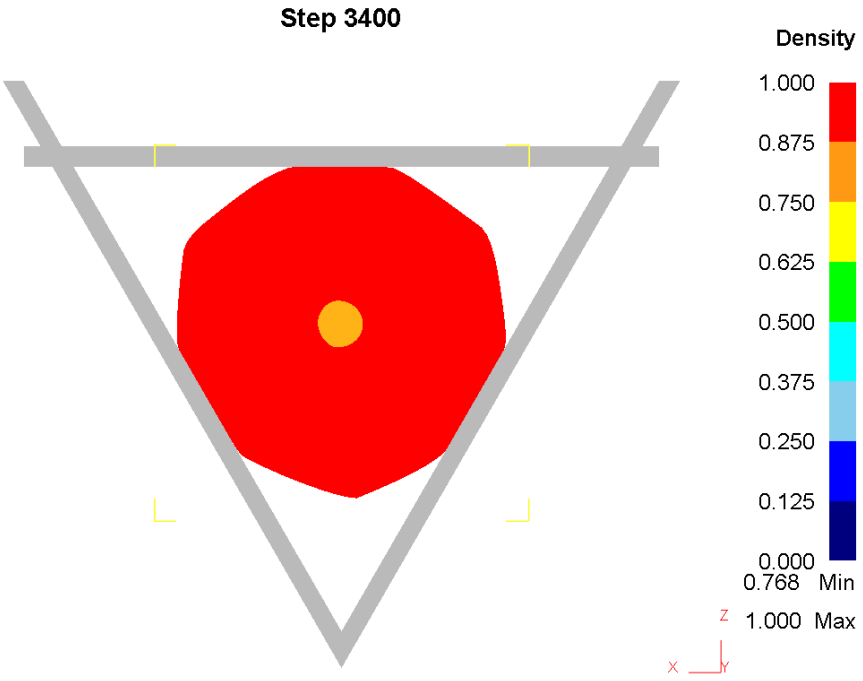

Fig. 12.14. Relative density. 60° lower die.

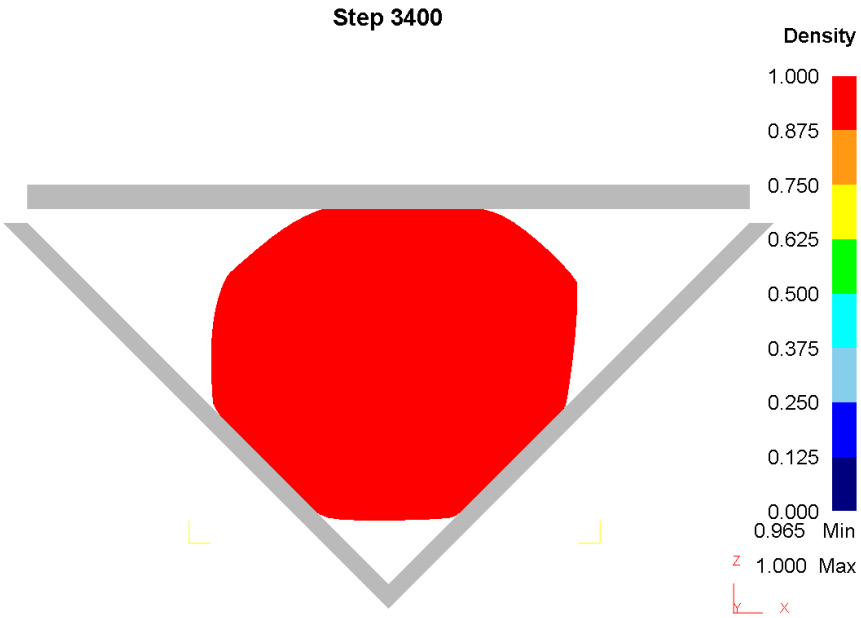

Fig. 12.15. Relative density. 90º lower die.

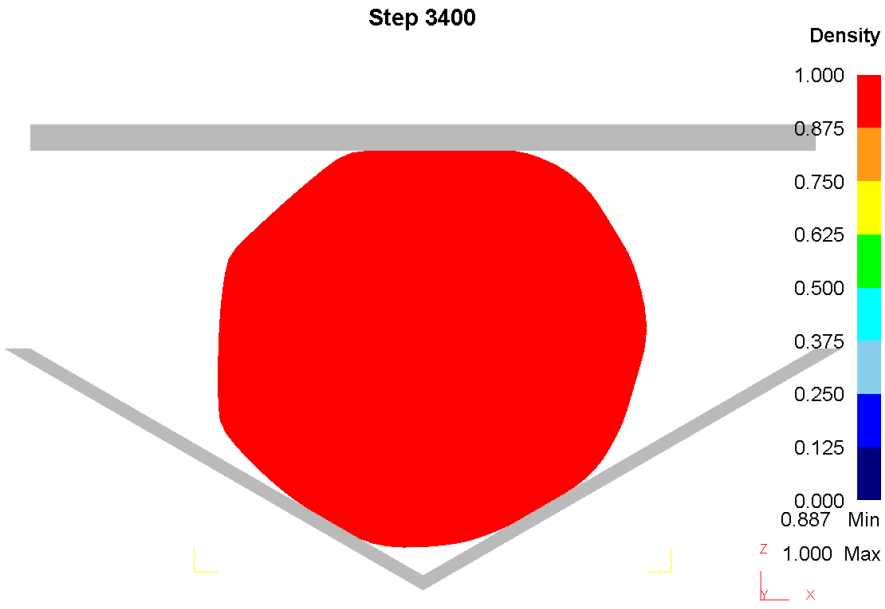

Fig. 12.16. Relative density. 120º lower die.

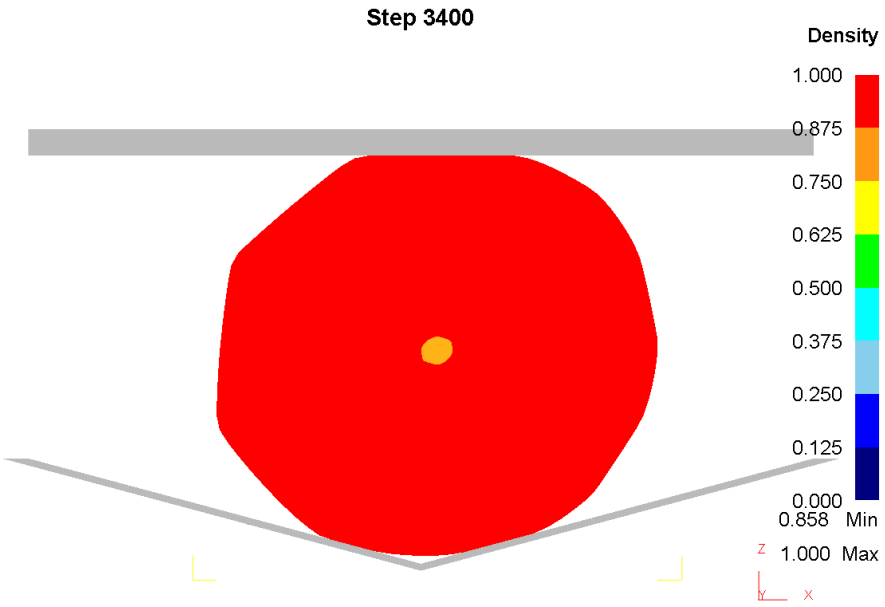

Fig. 12.17. Relative density. 150° lower die.

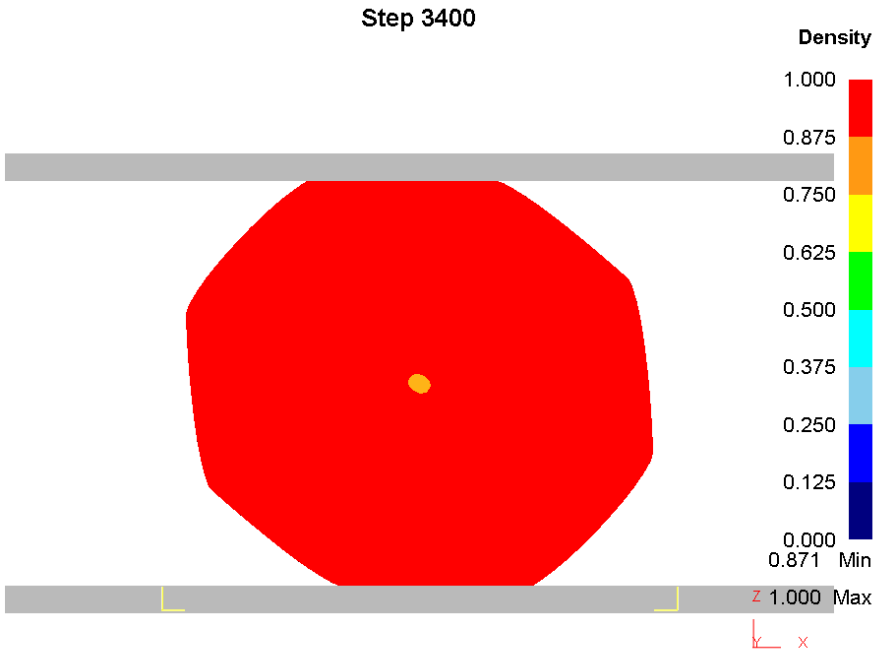

Fig. 12.18. Relative density. 180° lower die.

In general a substantial increase in the density of the ingot cross-section is seen in Fig. 12.14-Fig. 12.18. By visual inspection, 90° and 120° lower die angles appear to give rise to the largest relative density after forging.

12.3.4 Relative density, 75° rotation

The relative densities after 17 strokes with 75° intermediate rotations are seen in Fig. 12.19-Fig. 12.23.

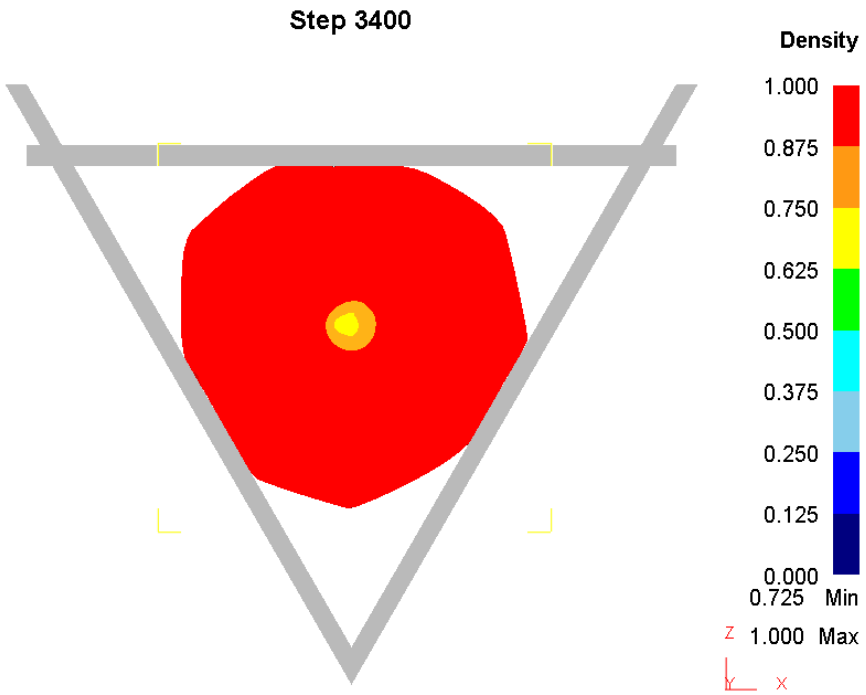

Fig. 12.19. Relative density. 60º lower die.

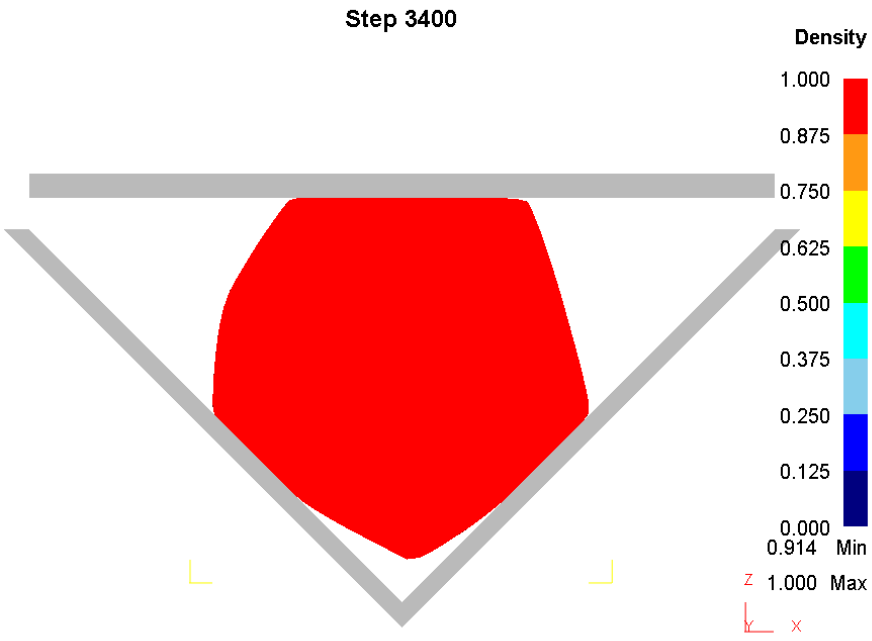

Fig. 12.20. Relative density. 90º lower die.

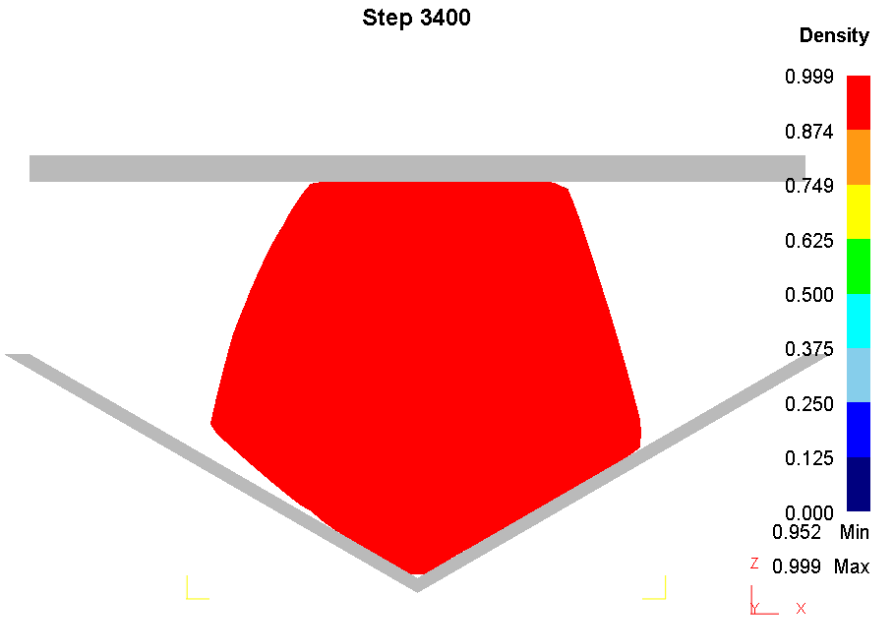

Fig. 12.21. Relative density. 120º lower die.

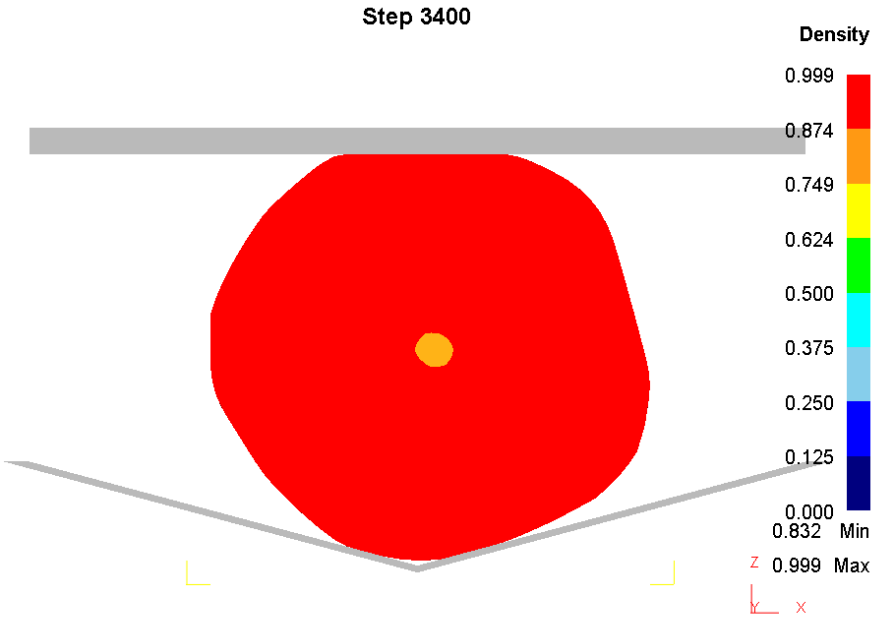

Fig. 12.22. Relative density. 150º lower die.

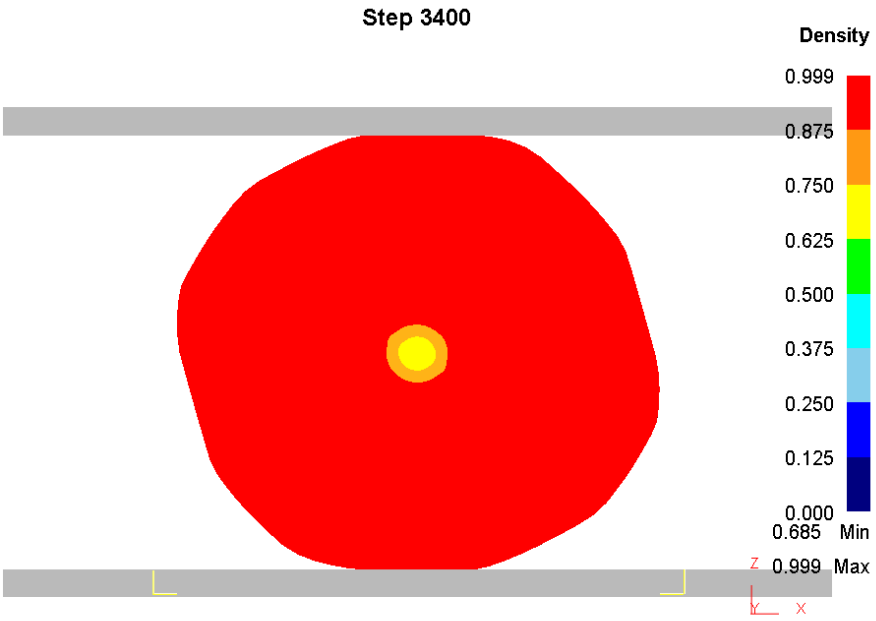

Fig. 12.23. Relative density. 180° lower die.

Similar large density increase is noticed with 75° rotation and best results are again obtained with 90° and 120° dies. A more detailed analysis of the predicted relative densities are given in 12.4.3.

12.4 Evolution of deformation

The evaluations of the different lower die angles and angles of rotation follows the procedure outlined in Section 11.4. Instead of damage, relative density is evaluated. The best forging is considered to be the one with the largest mean relative density and the largest minimum relative density in an element. The effective plastic strain is evaluated as in Section 11.4.

12.4.1 Degree of reduction

The evolution in degree of reduction for both 45° and 75° rotation are seen in Fig. 12.24 and Fig. 12.25.

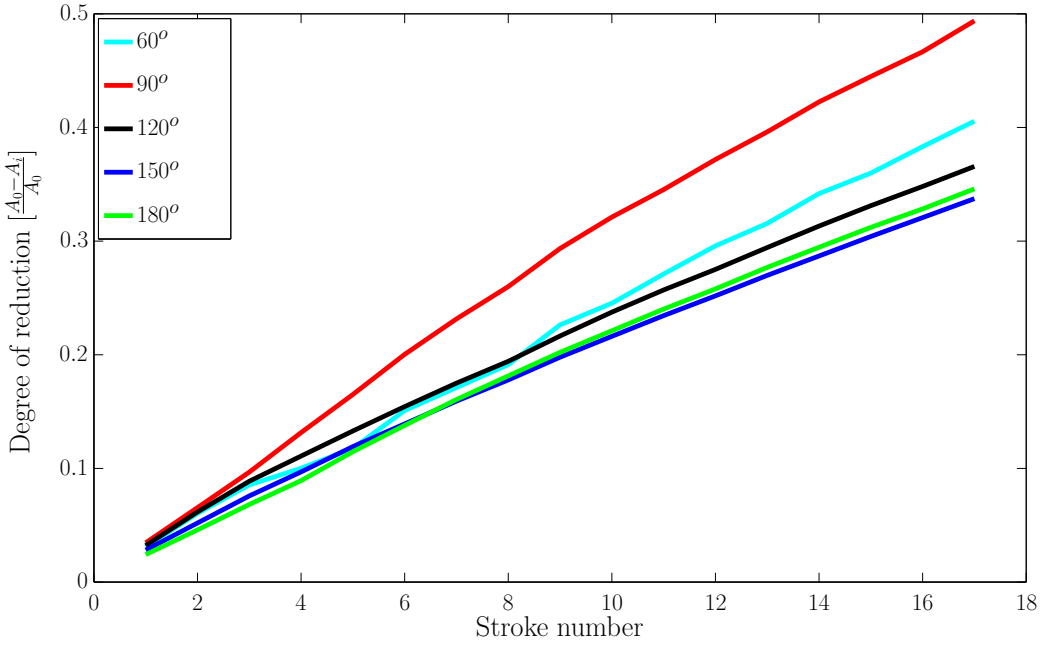

Fig. 12.24. Degree of reduction, 45° rotation.

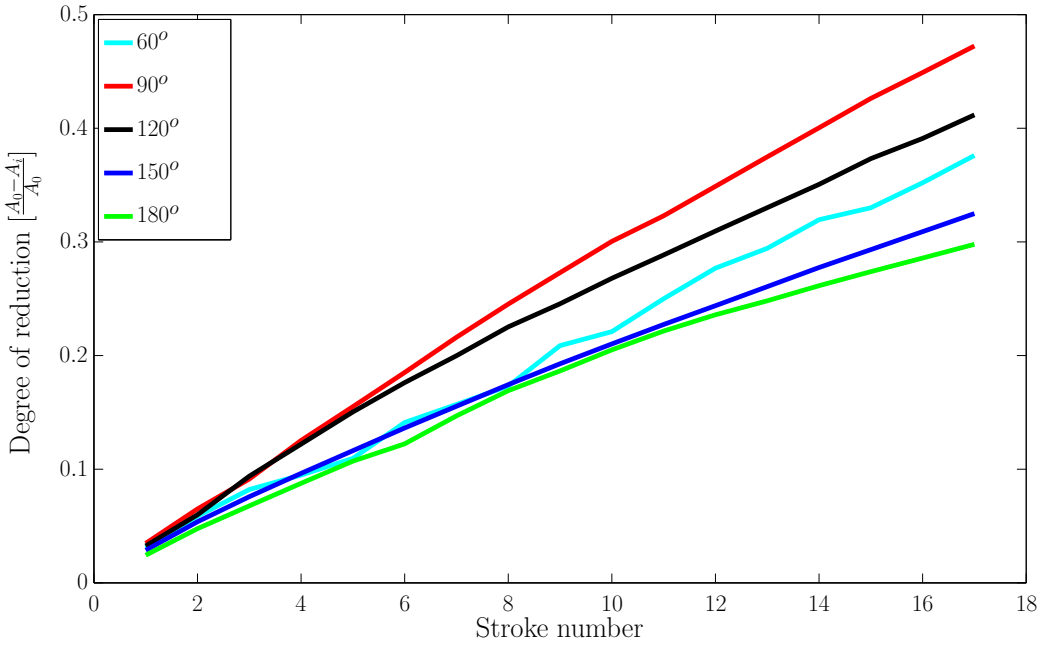

Fig. 12.25. Degree of reduction, 75° rotation.

The graphs in Fig. 12.24 andFig. 12.25 indicate a fairly monotonic increase in degree of reduction for all lower die angles and rotations. The optimum lower die angle and rotation angle which give rise to the largest degree of reduction, is therefore not significantly influenced by the number of compression strokes or rotation angle.

The degree of reduction after 17 strokes can be seen in descending order in Table 12.2-Table 12.3.

Table 12.2. 45° rotation.

Lower die angle	Degree of reduction
90°	0.49
60°	0.41
120°	0.37
180°	0.35
150°	0.34

Table 12.3. 75° rotation.

Lower die angle	Degree of reduction
90°	0.47
120°	0.41
60°	0.38
150°	0.32
180°	0.30

From Table 12.2-Table 12.3 it is seen that the ranking is somewhat changed with the angle of rotation. 90° is, however, the one which causes the largest degree of reduction for both angles of rotation.

12.4.2 Effective plastic strain

The evolution of mean plastic strain after each forging stroke is seen in Fig. 12.26 and Fig. 12.27.

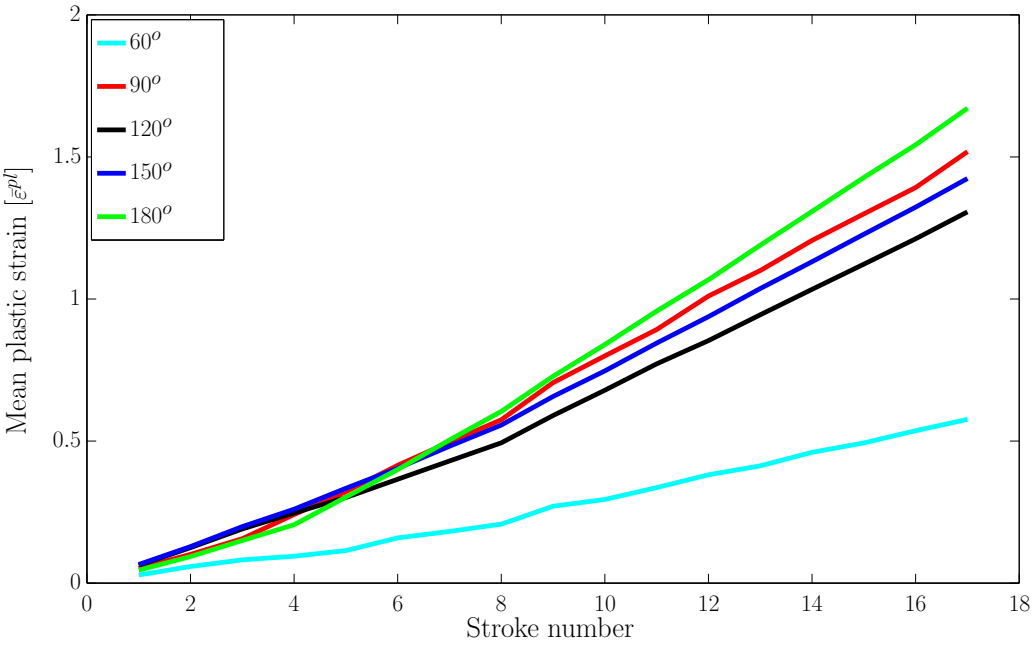

Fig. 12.26. Mean $\bar{\varepsilon}^{pl}$, 45° rotation.

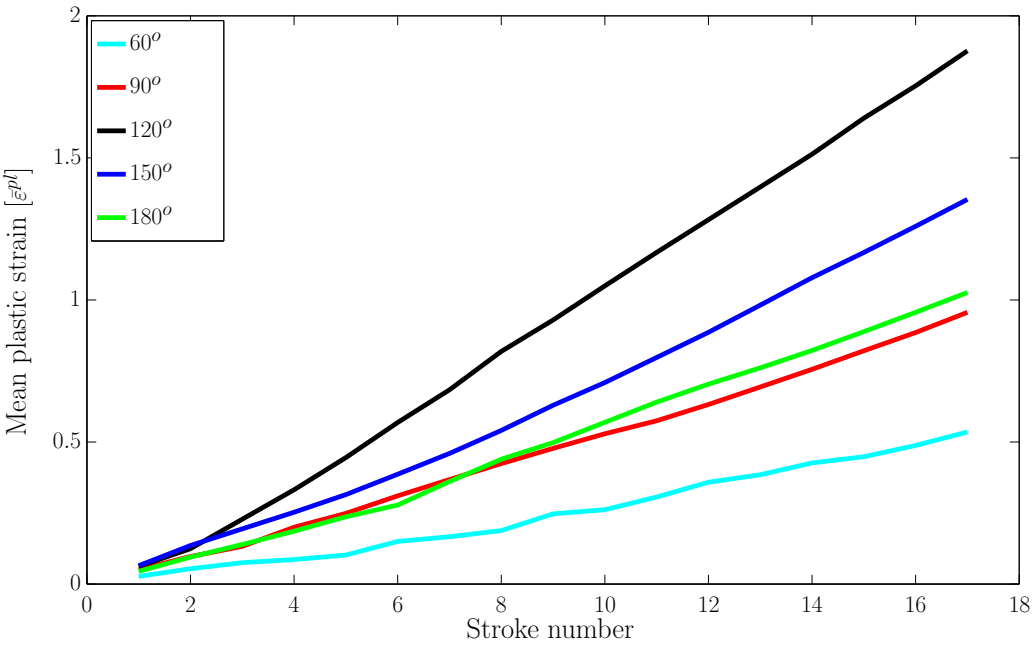

Fig. 12.27. Mean $\bar{\varepsilon}^{pl}$, 75° rotation.

Fig. 12.26 and Fig. 12.27 indicate a fairly steady increase of the mean effective plastic strain for all lower die angles and both rotation angles as the number of strokes increase. The ranking is stable after approximately 7 strokes for the 45° rotation and after 3 strokes for the 75° rotation.

A table showing the final values, sorted in descending order, is seen in Table 12.4 and Table 12.5.

Table 12.4. 45° rotation.

Lower die angle	Mean $\bar{\varepsilon}^{pl}$
180°	1.67
90°	1.52
150°	1.42
120°	1.31
60°	0.58

Table 12.5. 75° rotation.

Lower die angle	Mean $\bar{\varepsilon}^{pl}$
120°	1.88
150°	1.35
180°	1.03
90°	0.96
60°	0.54

From Table 12.4 and Table 12.5 it is seen that the order of which lower die angle gives rise to the largest mean effective strain is influenced by the choice of angle of rotation.

The minimum plastic strain appearing in an element is seen in Fig. 12.28 and Fig. 12.29 as a function of stroke number.

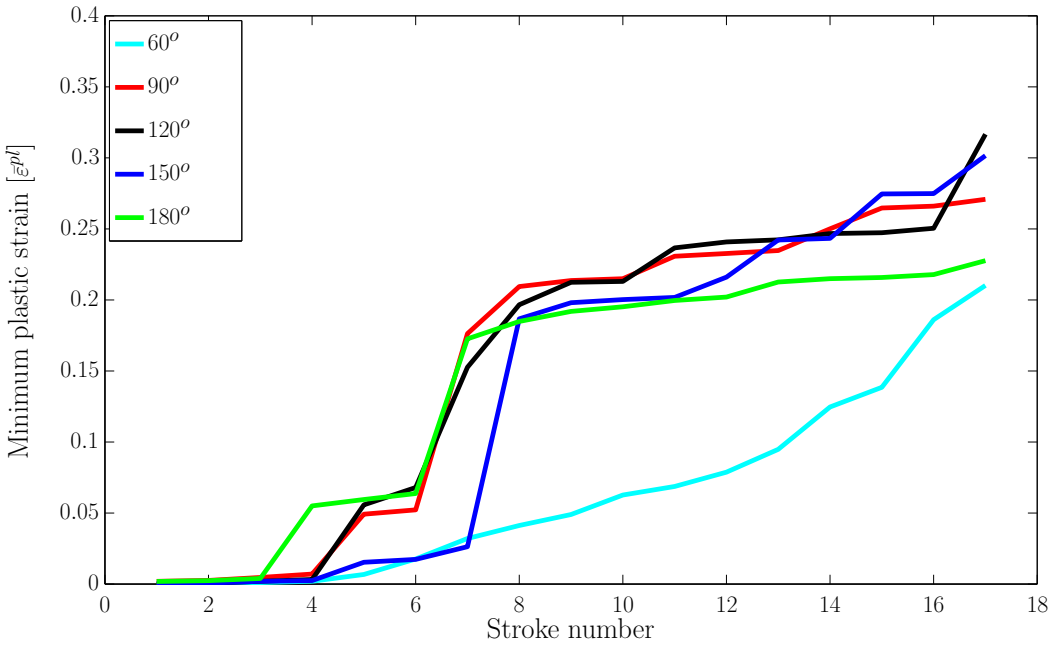

Fig. 12.28. Minimum $\bar{\varepsilon}^{pl}$, 45° rotation.

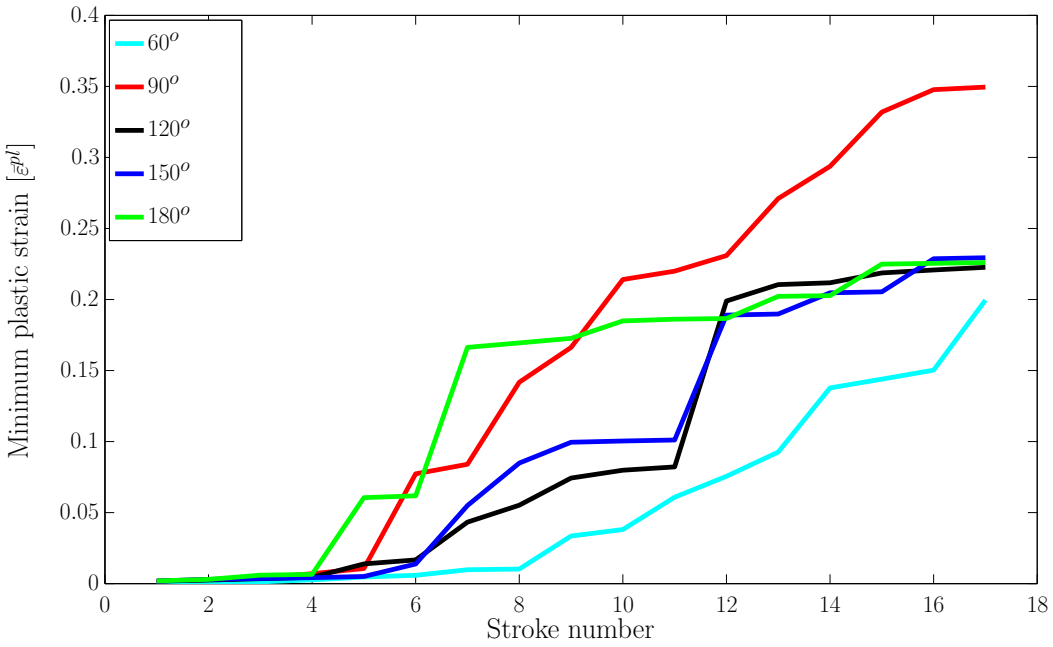

Fig. 12.29. Minimum $\bar{\varepsilon}^{pl}$, 75° rotation.

It is seen from Fig. 12.28 and Fig. 12.29 that the minimum effective plastic strain evolves in a more unsteady manner than the mean value. However it does appear that the best lower die angles tend to be best throughout the 17 forging steps. A table summarizing the final values, sorted in descending order, is seen in Table 12.6 and Table 12.7.

Table 12.6. 45° rotation.

Lower die angle	Min. $\bar{\varepsilon}^{pl}$
120°	0.32
150°	0.30
90°	0.27
180°	0.23
60°	0.21

Table 12.7. 75° rotation.

Lower die angle	Min. $\bar{\varepsilon}^{pl}$
90°	0.35
150°	0.23
180°	0.23
120°	0.22
60°	0.20

From Table 12.6 and Table 12.7 it is seen that changing the angle of rotation affects the ranking of the different lower die angles. When comparing with Table 12.4 and Table 12.5 it is also seen that the optimum lower die angle regarding mean effective plastic strain is not the same as the ones resulting in the maximum value of minimum effective plastic strain.

12.4.3 Relative density

The evolution in mean relative density R is seen in Fig. 12.30 and Fig. 12.31.

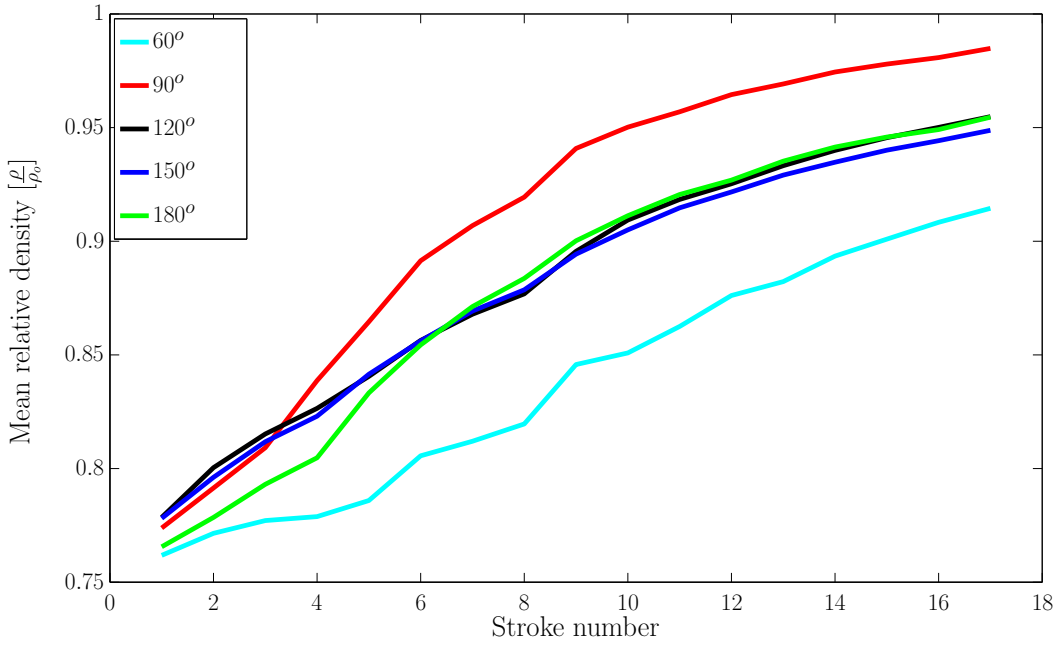

Fig. 12.30. Mean R, 45° rotation.

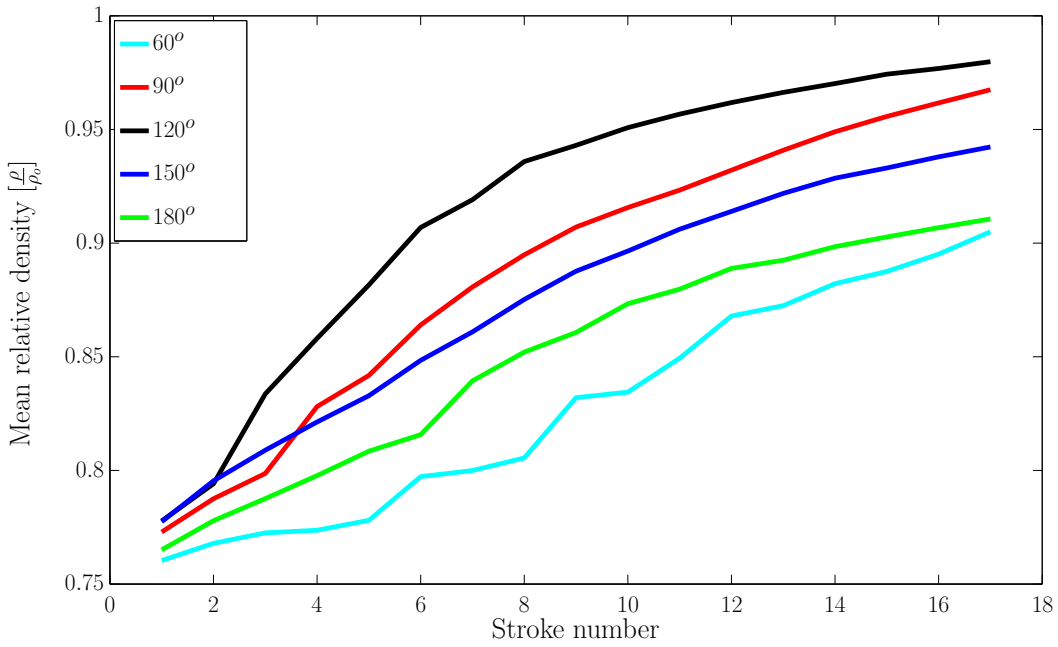

Fig. 12.31. Mean R, 75° rotation.

From Fig. 12.30 and Fig. 12.31 it can be deduced that the mean relative density increases fairly steady for all lower die angles as the forging procedure evolves. The ranking is stable after approximately 4 strokes. A table showing the final mean densities can be seen in Table 12.8 and Table 12.9, sorted in descending order.

Table 12.8. 45° rotation.

Lower die angle	Mean relative density
90°	0.98
120°	0.96
180°	0.96
150°	0.95
60°	0.91

Table 12.9. 75° rotation.

Lower die angle	Mean relative density
120°	0.98
90°	0.97
150°	0.94
180°	0.91
60°	0.91

From Table 12.8 and Table 12.9 it is seen that several of the different lower die angles make it possible to forge the ingot cross-section to a large value of relative density. It seems that performing a 75° rotation lowers the obtained mean relative density in general.

The evolution in minimum relative density occurring in an element can be found in Fig. 12.32 and Fig. 12.33 for different lower die angles and rotation angles.

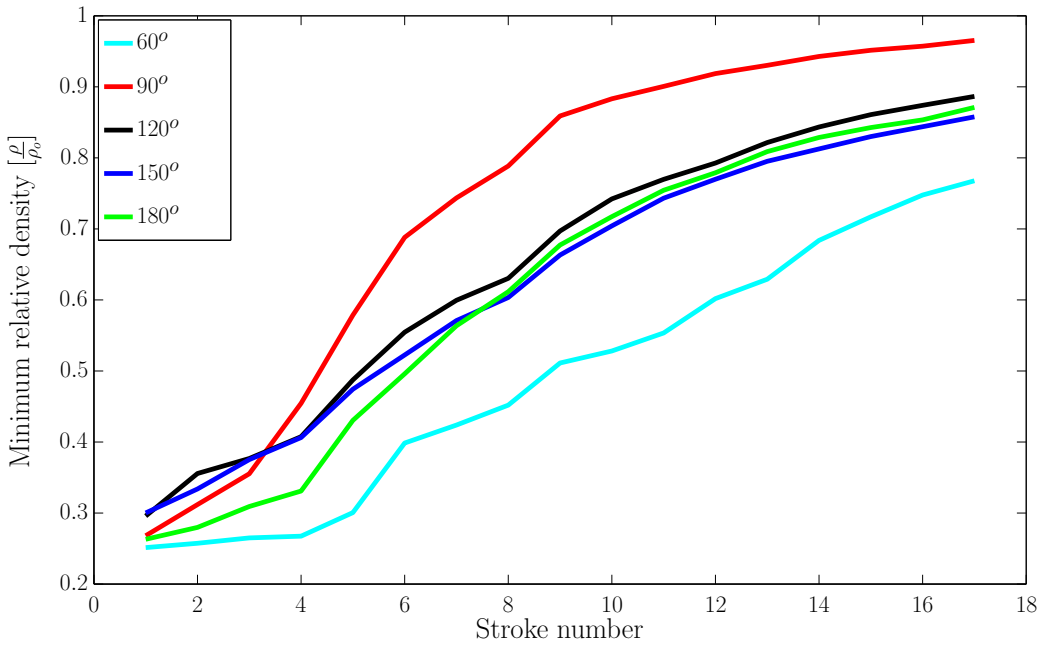

Fig. 12.32. Minimum relative density, 45° rotation.

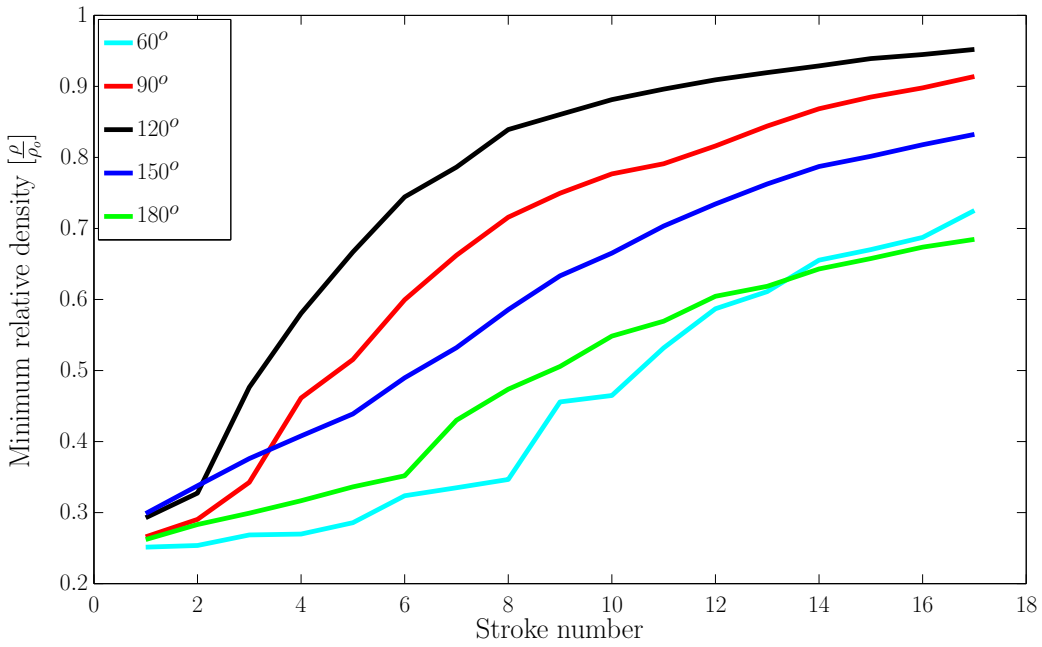

Fig. 12.33. Minimum relative density, 75° rotation.

In Fig. 12.32 and Fig. 12.33 a steady increase in minimum relative density is seen. A summary of the attained minimum relative densities after 17 strokes is seen in Table 12.10 and Table 12.11 in descending order.

Table 12.10. 45° rotation.

Lower die angle	Min. R
90°	0.97
120°	0.89
180°	0.87
150°	0.86
60°	0.77

Table 12.11. 75° rotation.

Lower die angle	Min. R
120°	0.95
90°	0.91
150°	0.83
60°	0.73
180°	0.68

It is seen from Table 12.10 and Table 12.11 that marked differences in minimum relative densities are obtained when forging with different lower die angles. It can also be found that the angle of rotation influences the results to a quite large degree. Notice for instance how the 180° lower die angle drops from a minimum relative density of 0.87 to 0.68 when changing the angle of rotation from 45° to 75°.

It should be noticed that the 90° lower die angle gives significantly better result than the other lower die angles, when performing 45° rotation, regarding minimum relative density.

12.4.4 Ranking of lower die angles

In order to compare the different lower die angles to one another, a ranking is performed. The basic idea follows the procedure outlined in Section 11.5. The evaluation of effective plastic strain is the same but instead of evaluating damage, relative density is evaluated. "Best" is then defined for relative density as having the largest value, hence being closest to a fully dense material.

Ranking as regards effective plastic strain is seen in Fig. 12.34 and as regards relative density in Fig. 12.35.

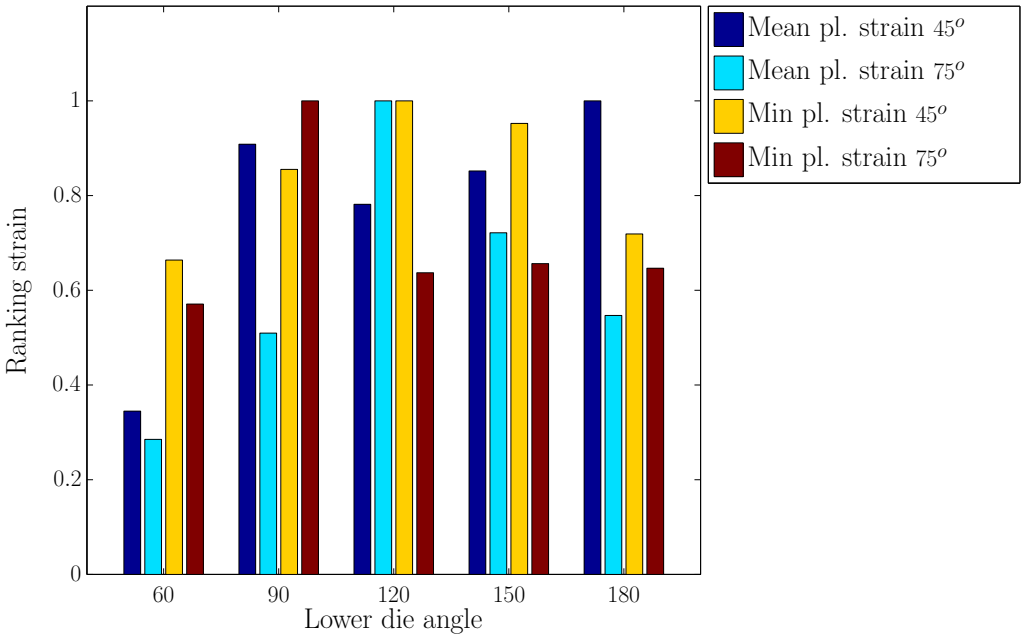

Fig. 12.34. Ranking as regards effective plastic strain.

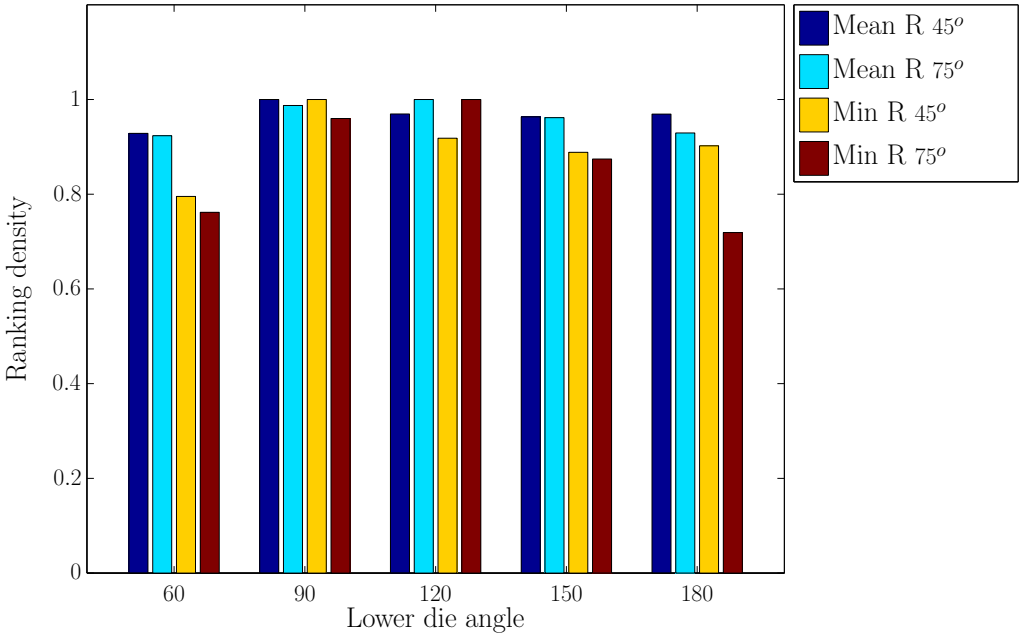

Fig. 12.35. Ranking as regards relative density.

The total average ranking for 45º and 75º are seen in Fig. 12.36.

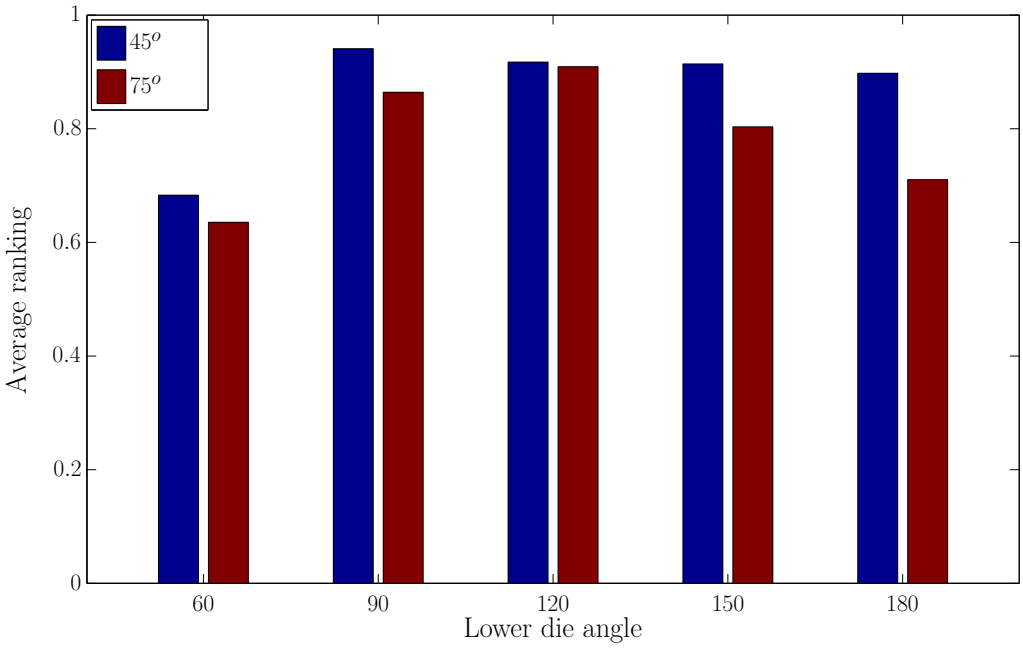

Fig. 12.36. Optimum lower die angle.

A table summarizing the optimum is seen in Table 12.12 and Table 12.13.

Table 12.12. Optimum, 45° rotation.

Lower die angle	Average points
90°	0.94
120°	0.92
150°	0.91
180°	0.90
60°	0.68

Table 12.13. Optimum, 75° rotation

Lower die angle	Average points
120°	0.91
90°	0.86
150°	0.80
180°	0.71
60°	0.64

As sefen from Table 12.12 and Table 12.13, the 45° rotation results generally in a better ranking with less variation in the points than using 75° rotation, hence applying 45° rotation makes the forging operation less sensitive to the applied lower die angle. Since forging with 45° rotation also gives rise to generally larger plastic strains and larger relative density, it appears that 45° rotation is better than 75° rotation. Even though it is not taken into account in the ranking analysis, it also appears from the figures displaying the contours of the final ingot shape (Fig. 12.4-Fig. 12.13) that the ingots forged with 45° rotation has a more circular shape, hence requiring less subsequent machining.

Based on the evaluation it seems that the 90° lower die angle is the best, however also the 120°, 150° and 180° give good results.

The author finds it interesting that when applying a porous plasticity model, the 90° is predicted to be best as compared to the 120° when applying uncoupled ductile damage as a measure (see Chapter 11) of the effect of the forging operation. This difference could stem from the fact that the change in relative density is only influenced by the volumetric strain rate (see Eq. 8.77). The uncoupled ductile damage model does also take shear deformation into account when computing damage. The uncoupled ductile damage model is therefore, in the opinion of the author, a more conservative damage estimator. One way of determining whether the uncoupled ductile damage or the porous plasticity approach is most suited for predicting crack formation in manufacturing, could be to perform simulations based on formability experiments, such as found in Gouveia et al. [38] or Rosa et al. [85], and see whether simulations with porous plasticity or ductile damage would provide simulations in best agreement with experiments.

The simulations indicate that the optimum lower die angle is a bit smaller than predicted by the single stroke forging simulations in Chapter 10.

12.5 Conclusion

Multi stroke forging of porous ingot cross-sections have been performed. Different lower die angles and two different rotation angles between forging strokes have been examined. Based on a quantitative ranking scheme, the 90° lower die angle, when performing 45° rotations in between strokes, appears to yield the best results. It is interesting to notice that the process seems to be somewhat more sensitive to the choice of rotation angle than the choice of lower die angle when modelling the ingot forging process by porous plasticity. When applying 45° rotations, all the tested lower die angles, except for 60°, yielded a high average score.

13 Preliminary investigation of feed size

13.1 Introduction

When a cross-section of the ingot has been forged, the ingot is displaced between the opened dies and then a new cross-section is forged. As mentioned in 6.6 the internal soundness of the ingot depends on applying an appropriate displacement (labelled as feed). On one hand the feed should be large enough to ensure a greater part of the ingot to be forged, and on the other hand due to the nature of the deformation process, too large feed may result in dead zone formation in the center of the ingot. The purpose of this chapter is to illustrate the result of different feed sizes and different lower die angles. A porous finite element formulation is utilized and a full 3D simulation is performed using DEFORM®. However due to this, the computational time also increases. These simulations consequently take approximately four days (14 hours working day) each to perform on a 2.8GHz Intel core i7 laptop with 8GB RAM. Therefore only a limited number of lower die angles and feed sizes are included and the results should only be interpreted as preliminary and not as a systematic investigation.

13.2 Numerical simulation layout

An ingot, 2000mm in diameter and 2800mm long, is discretized by 6680 8-node brick elements (7455 nodes). The ingot is then compressed 200mm (10% of the initial ingot diameter) 17 times by a pair of dies. The ingot is subsequently displaced axially between the dies. The displacement is either 400mm or 800mm. The next cross-section is then forged as the first one. It should be noticed that in the industrial production, a couple of extra forging strokes are performed with small stroke length in order to smoothen the final ingot surface. These extra steps are not modelled. The ingot is prevented from longitudinal displacement at one end in order to avoid excessive misalignment in between the dies. This can to some extent also be physically justified because in the real forging process, a manipulator (see Fig. 5.2 and Fig. 5.3a) is attached to one end of the ingot and thereby, to some degree, prevents displacement of the ingot.

The die pair consists of a flat upper die and a 120° or a 180° lower die. The edges of the dies are rounded with a radius of 80mm, which is a value similar to a real forging operation. The simulation layout is seen in Fig. 13.1, where an intermediate stage is shown in Fig. 13.1b after forging one cross-section of the ingot and then displacing the ingot 800mm in axial direction.

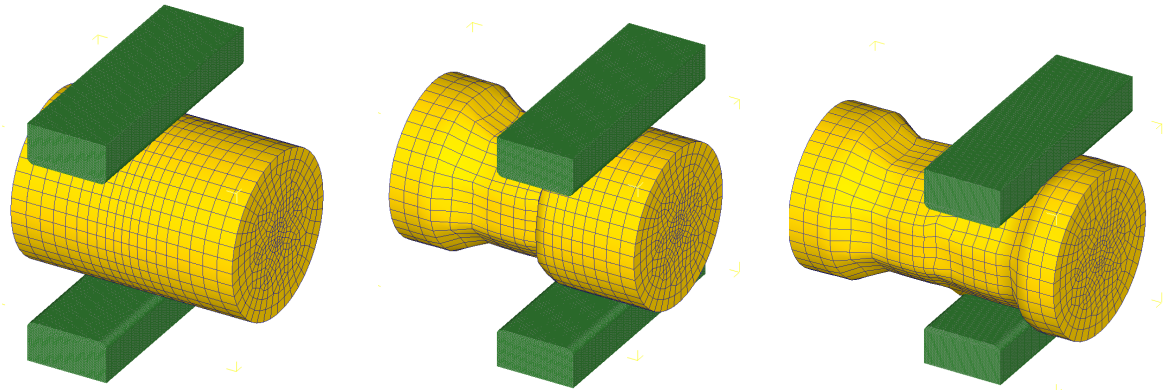

(a) Initial. **(b)** Intermediate. **(c)** Final.

Fig. 13.1. Simulation layout when utilizing a 180° lower die.

As it can be seen from Fig. 13.1, the mesh is somewhat coarse, however it was necessary to use such a mesh in order to have an acceptable computation time.

Damage is modelled both by porous plasticity and the uncoupled normalized Cockcroft & Latham criterion. The initial relative density is the same as applied in Chapter 12 and can be seen in Fig. 13.2. Both a full and a cross sectional view of the ingot is seen.

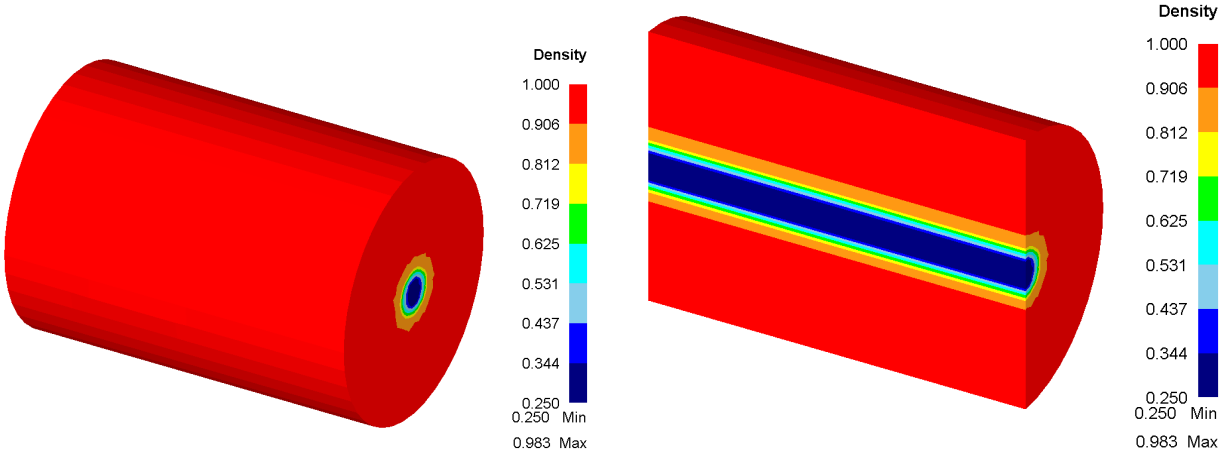

(a) Full model. **(b)** Cut model.

Fig. 13.2. Initial relative density.

A summary of the FEM-simulation settings are found in Table 13.1.

Table 13.1. FEM-simulation settings.

Ingot diameter	2000mm
Ingot length	2800mm
Penalty factor	$K = 10^6$
Mesh	6680 8-node brick elements (7455 nodes)
Number of time steps	200
Convergence criteria	$\frac{\|\triangle \mathbf{v}\|}{\|\mathbf{v}\|} \leq 0.01$ and $\frac{\|\triangle \mathbf{f}\|}{\|\mathbf{f}\|} \leq 0.1$
Press speed	50mm/s
Friction	$m_f = 0.5$
Ingot material	42CrMo4 (Flow stress data from DEFORM® database)
Damage modelling	Relative density and uncoupled normalized Cockcroft & Latham
Dies	Rigid-contact surface elements
Heat transfer coefficient ingot-dies	5kW/(m^{2}K)
Forging procedure	17 strokes, 200mm comp., 45° rotation, 400mm or 800mm feed

13.3 Simulation results

Due to the limited number of performed simulations, quantitative data treatment is not performed. Selected field variables are presented graphically to give an impression of the influence of feed size for the two different lower die angles of 120° and 180°.

13.3.1 Relative density

The relative density after forging the first cross-section and the second cross-section using a 120° lower die are seen in Fig. 13.3-Fig. 13.5.

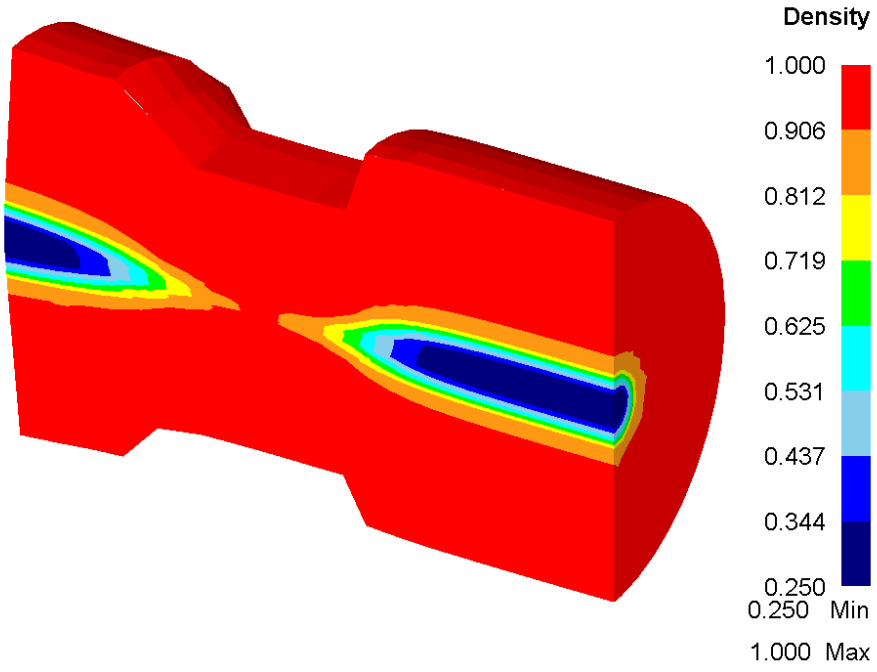

Fig. 13.3. Relative density. 1st forging. 120° lower die.

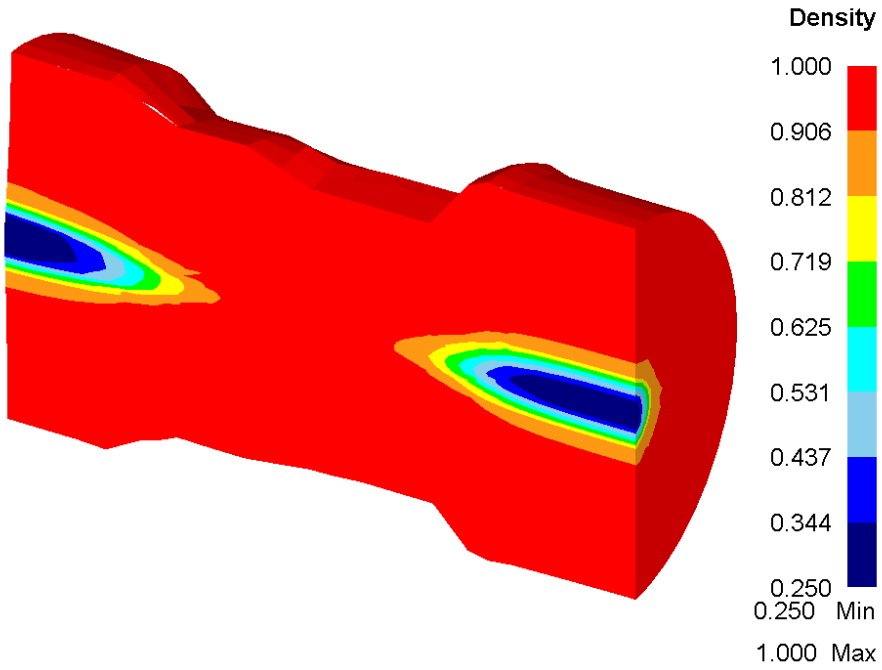

Fig. 13.4. Relative density. 2nd forging. 120° lower die. 400mm feed.

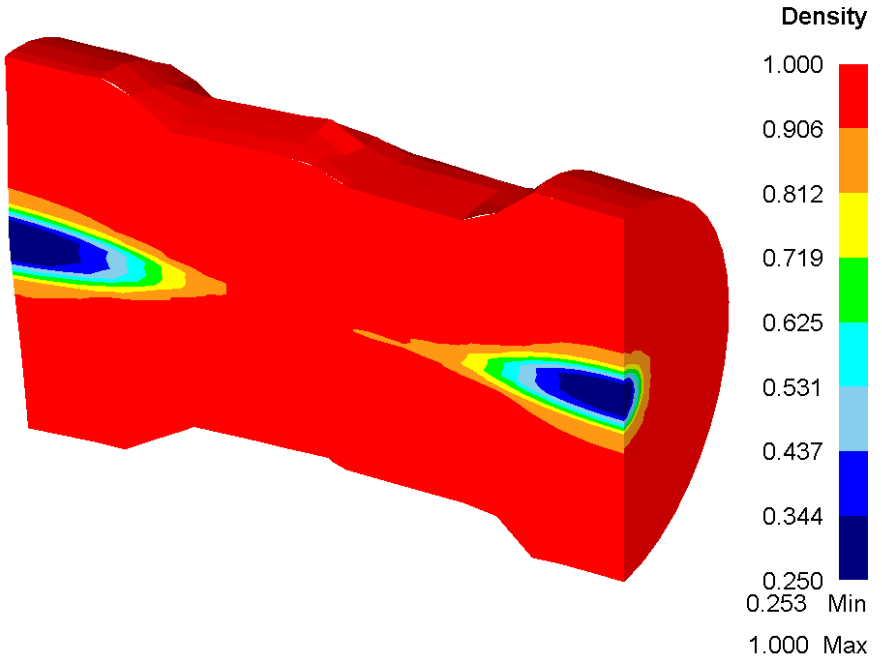

Fig. 13.5. Relative density. 2nd forging. 120° lower die. 800mm feed.

It is interesting to notice how a 800mm feed results in an extension of a less dense zone into the cross-section being forged as seen in Fig. 13.5 as compared to 400mm feed seen in Fig. 13.4.

The relative density after having forged the first cross-section and the second cross-section using a 180° lower die are seen in Fig. 13.6-Fig. 13.8.

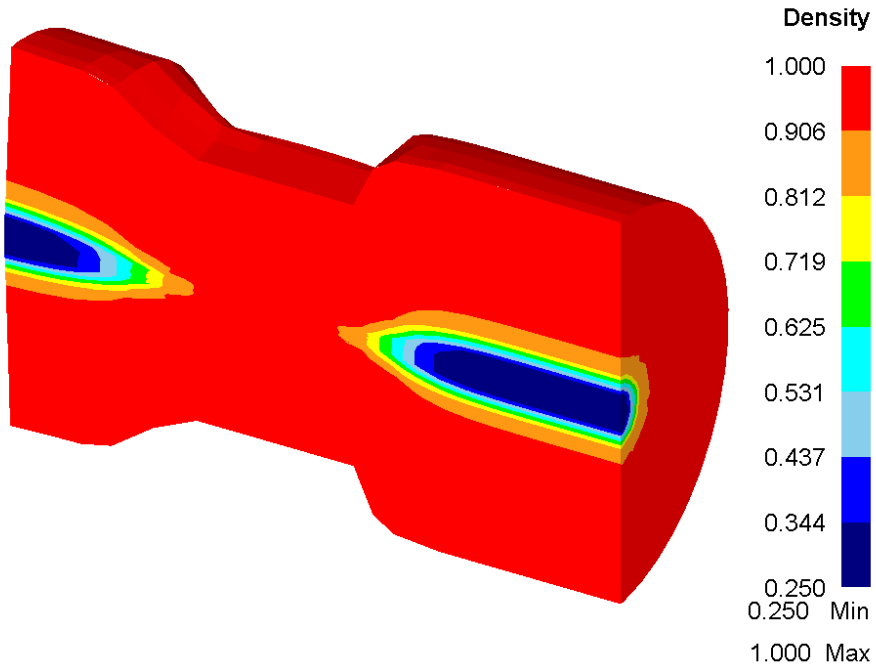

Fig. 13.6. Relative density. 1st forging. 180º lower die.

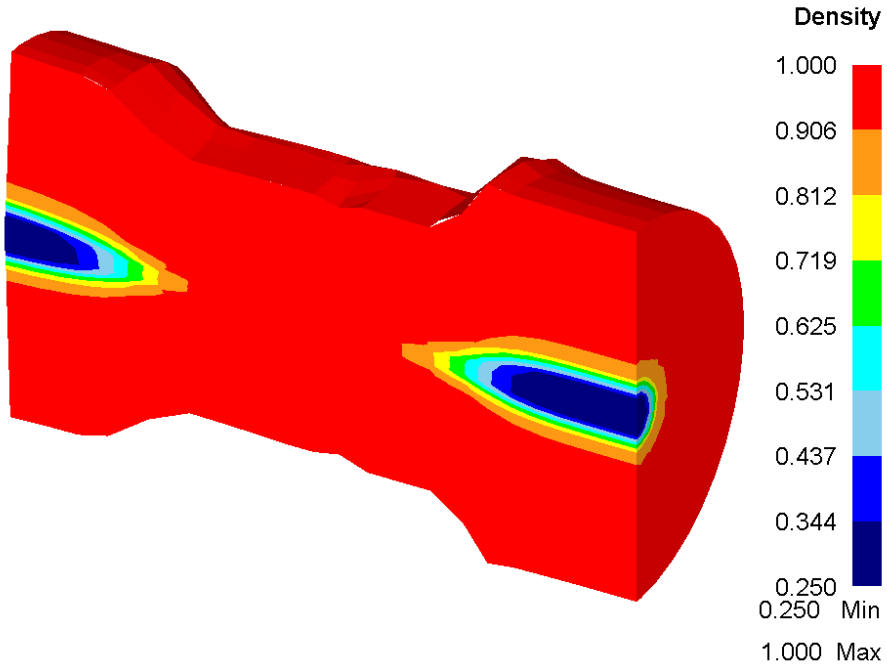

Fig. 13.7. Relative density. 2nd forging. 180º lower die. 400mm feed.

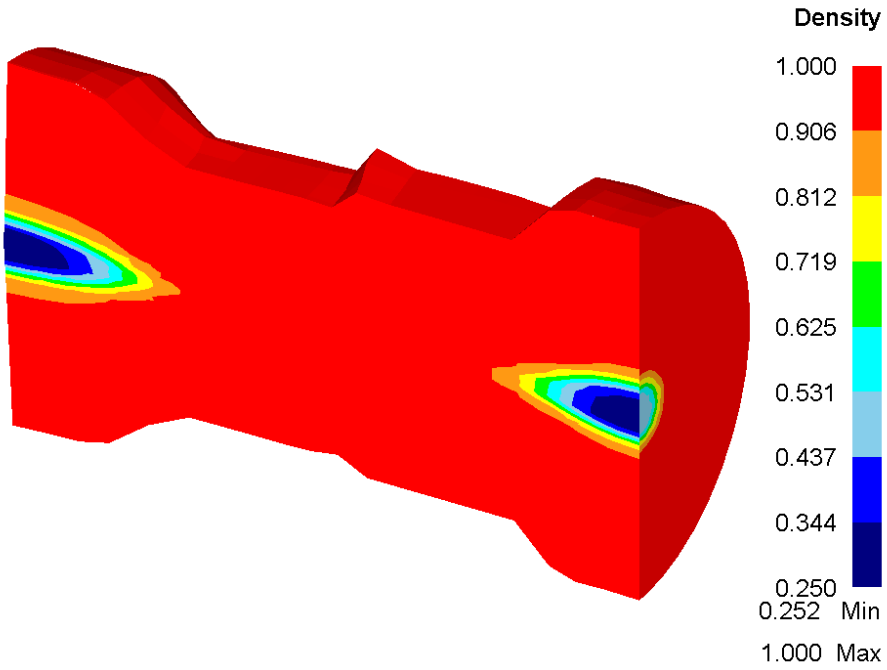

Fig. 13.8. Relative density. 2nd forging. 180° lower die. 800mm feed.

It also appears that a part of the ingot is moving outside the dies (see Fig. 13.8) when forging with a 180° lower die and a feed of 800mm. This is due to the elongation of the ingot due to forging. This problem is reduced by applying a feed of 400mm whereby less material is extruded forward.

13.3.2 Effective plastic strain

The effective plastic strains after forging the first cross-section and the second cross-section using a 120° lower die are seen in Fig. 13.9-Fig. 13.11.

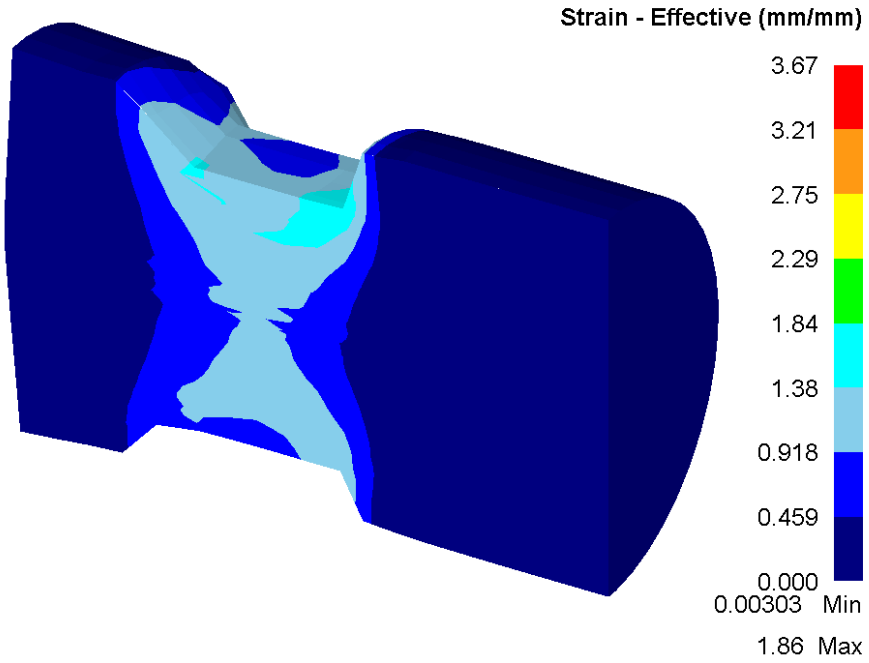

Fig. 13.9. Effective plastic strain. 1st forging. 120º lower die.

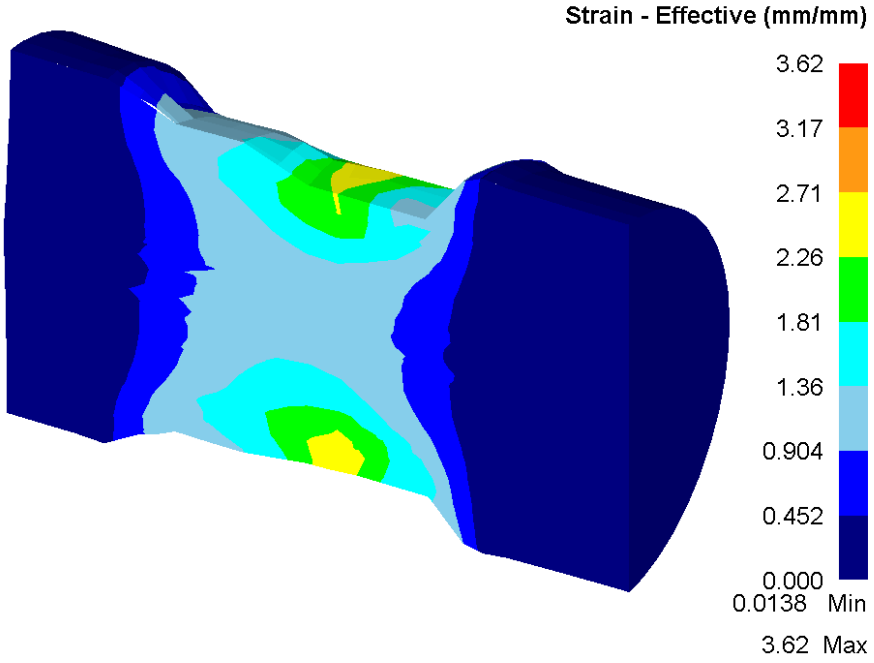

Fig. 13.10. Effective plastic strain. 2nd forging. 120º lower die. 400mm feed.

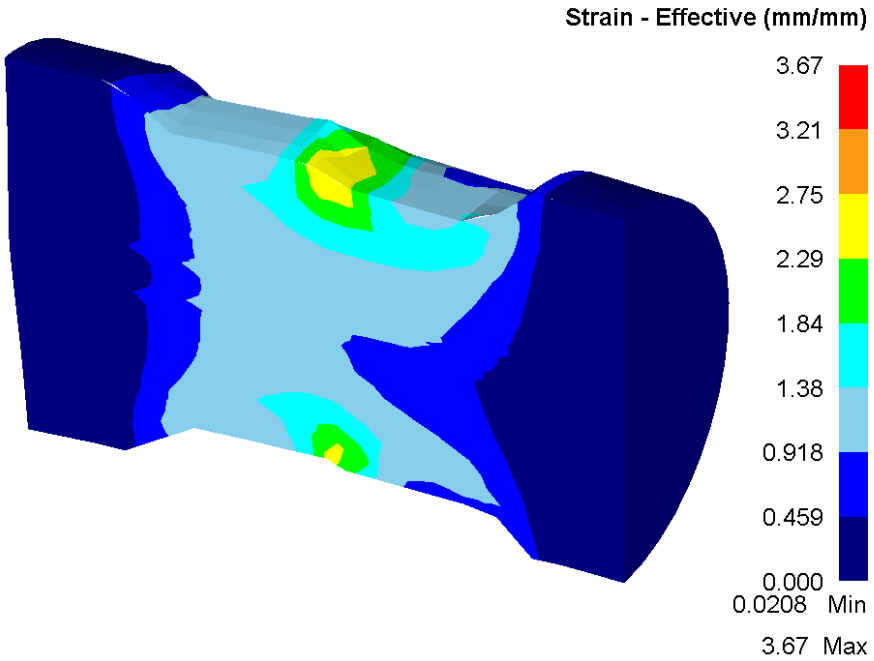

Fig. 13.11. Effective plastic strain. 2nd forging. 120° lower die. 800mm feed.

Fig. 13.9 shows that the forming zone become somewhat narrow in the center of the ingot. One could therefore suspect that a large feed size would result in a dead zone in the center. A zone containing less strain is in fact seen in Fig. 13.11 as compared to Fig. 13.10. The zone does however contain effective plastic strain values larger than approximately 0.5, so quite some deformation is occurring, but it is less than in the remaining deformation zone. A feed of 400mm (0.4 times die width) seems to result in a more homogeneous deformation when forging with a 120° lower die. This is in agreement with Lange [64], who recommends to use a feed size less than 0.5 times the die width.

The effective plastic strain after forging the first cross-section and the second cross-section using a 180° lower die are seen in Fig. 13.12-Fig. 13.14.

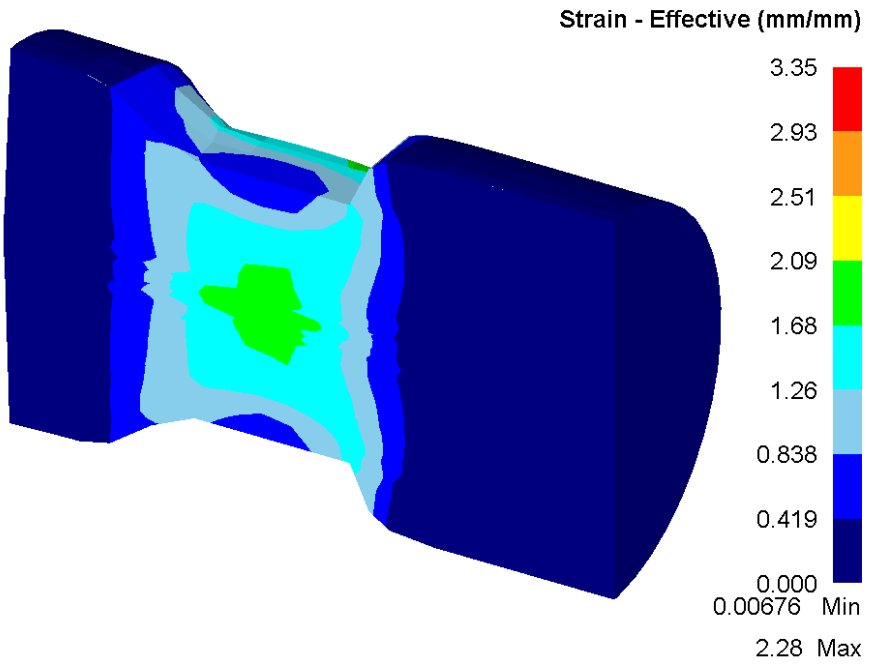

Fig. 13.12. Effective plastic strain. 1st forging. 180° lower die.

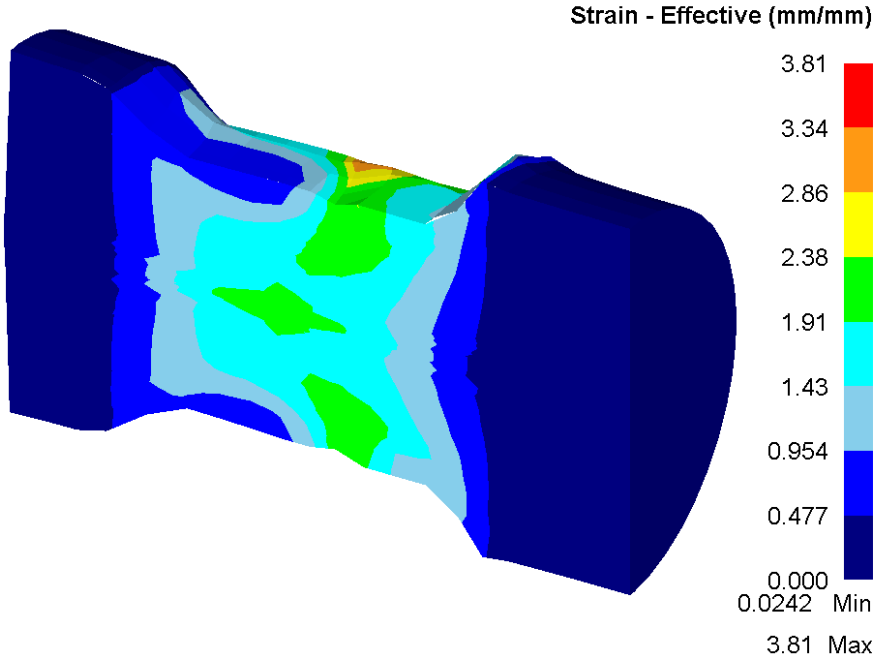

Fig. 13.13. Effective plastic strain. 2nd forging. 180° lower die. 400mm feed.

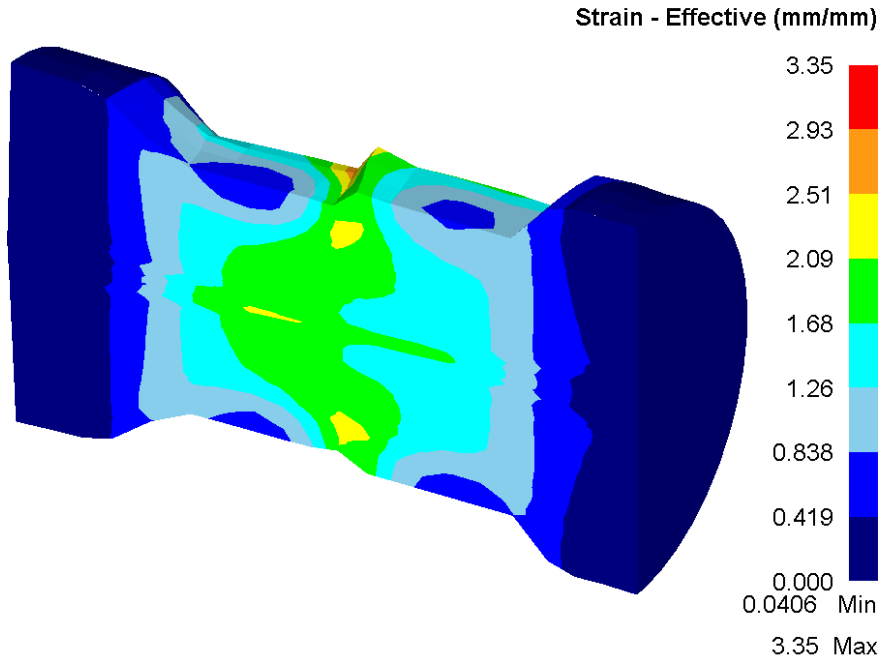

Fig. 13.14. Effective plastic strain. 2nd forging. 180° lower die. 800mm feed.

When forging with a 180° lower die, the effective plastic strain is in general larger but also more inhomogeneous than when forging with a 120° lower die.

13.3.3 Ductile damage

Although the simulations were performed using a porous plasticity model, ductile damage was computed at the same time. These results are also presented but are in essence not concurrent with the analysis in Chapter 11 because the current deformation is influenced by the porous plasticity formulation.

The calculated damage according to the normalized Cockcroft & Latham criterion after forging the first cross-section and the second cross-section using a 120° lower die is seen in Fig. 13.15-Fig. 13.17.

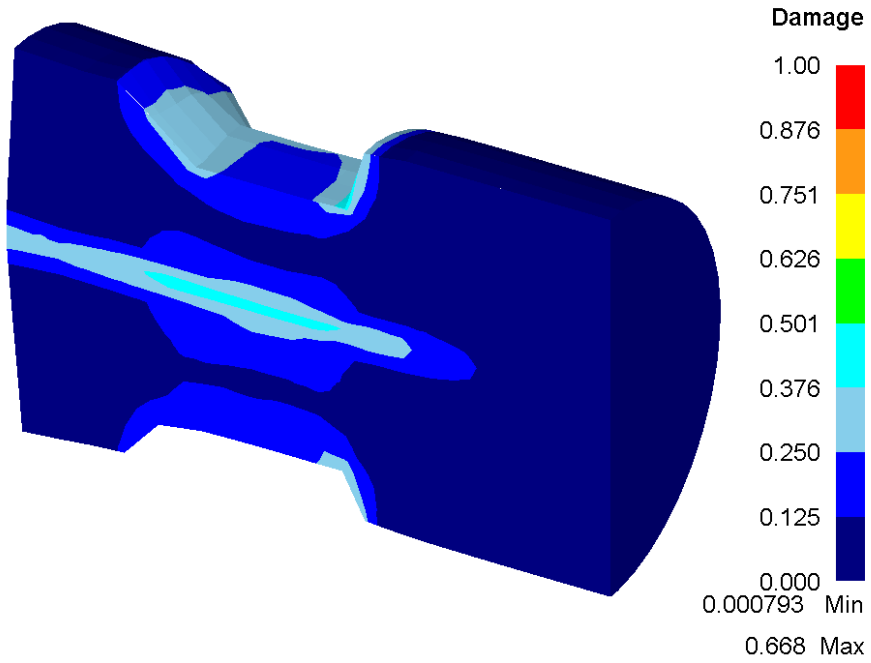

Fig. 13.15. Ductile damage. 1st forging. 120º lower die.

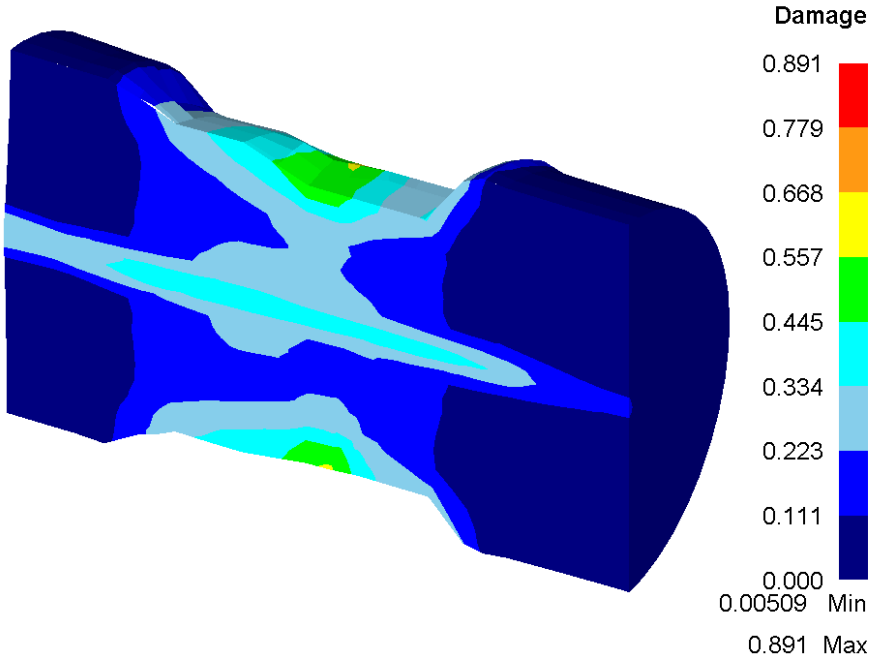

Fig. 13.16. Ductile damage. 2nd forging. 120º lower die. 400mm feed.

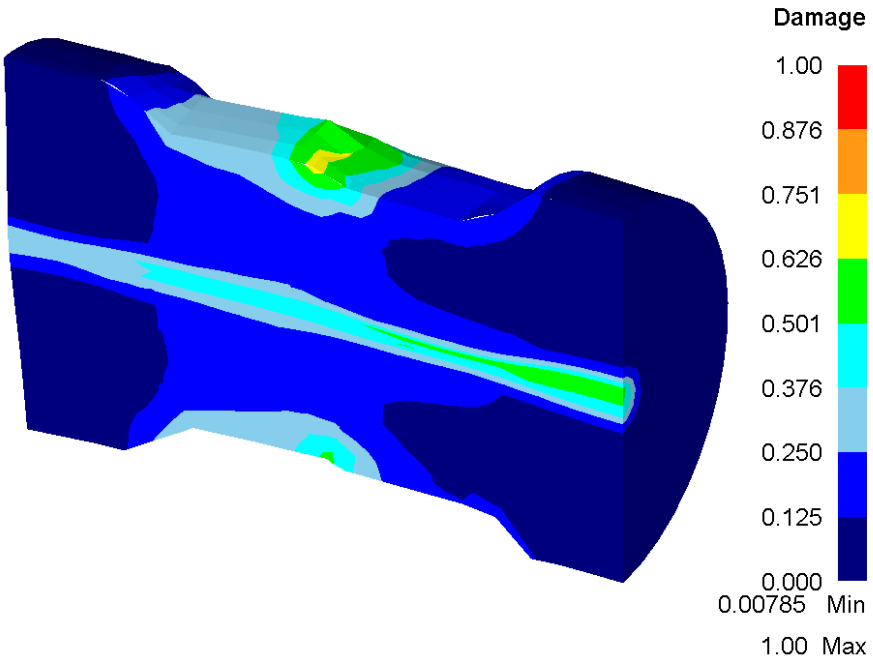

Fig. 13.17. Ductile damage. 2nd forging. 120° lower die. 800mm feed.

It is seen in Fig. 13.15-Fig. 13.17 that mainly two regions are experiencing ductile damage, that is the porous centerline and the surface of the ingot. Damage seems especially to occur in the surface where the neighbouring forging sections meet one another. The smaller feed of 400mm results in less damage in the surface than a feed of 800mm.

The calculated damage according to the normalized Cockcroft & Latham criterion after forging the first cross-section and the second cross-section using a 180° lower die is seen in Fig. 13.18-Fig. 13.20.

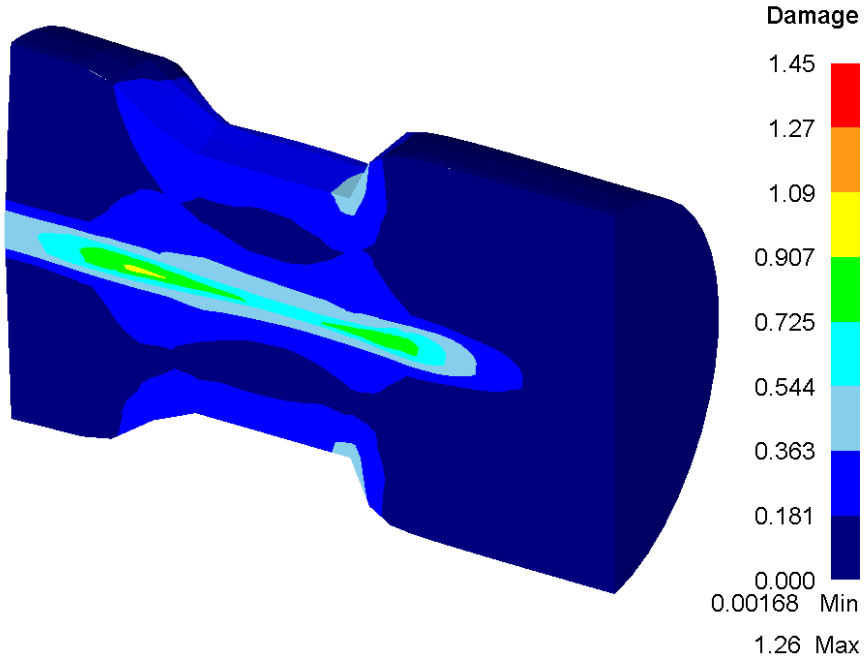

Fig. 13.18. Ductile damage. 1st forging. 180° lower die.

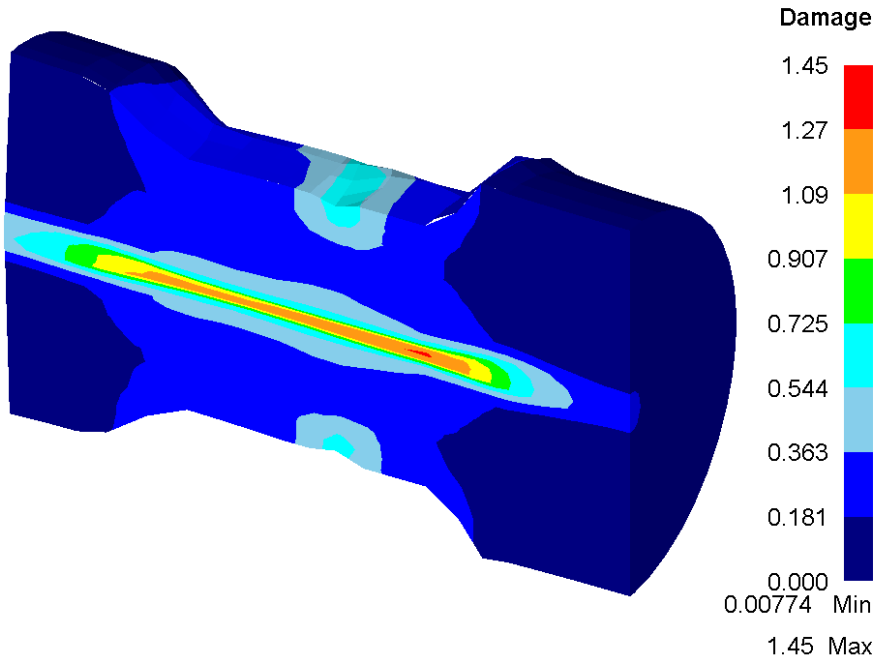

Fig. 13.19. Ductile damage. 2nd forging. 180° lower die. 400mm feed.

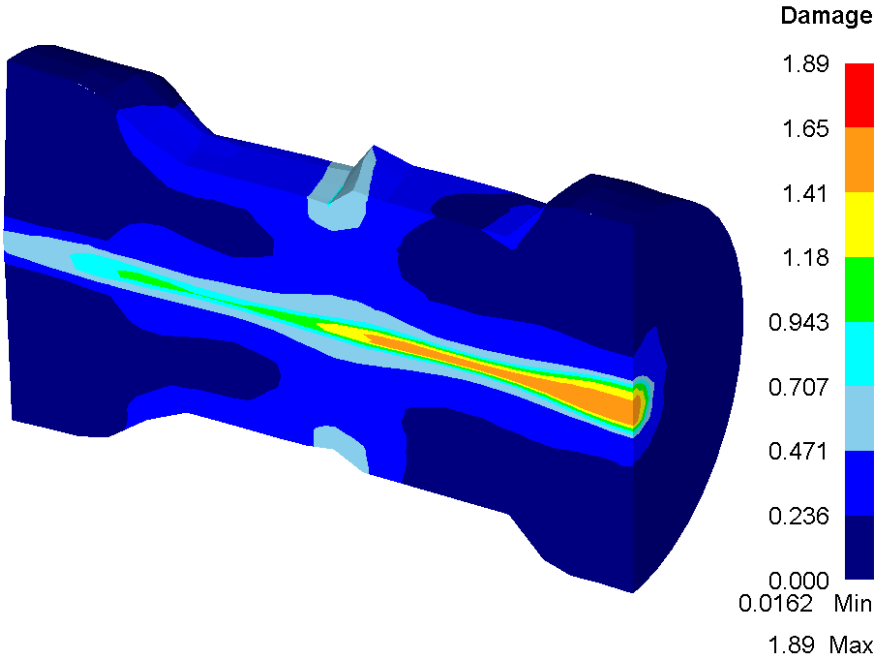

Fig. 13.20. Ductile damage. 2nd forging. 180° lower die. 800mm feed.

From Fig. 13.18-Fig. 13.20 it is seen that forging with a 180° lower die results in substantially more damage along the centerline of the ingot as compared to forging with a 120° lower die (see Fig. 13.15-Fig. 13.17). This is in agreement with the results in Chapter 11. The difference, based on maximum damage value, is seen in Table 13.2.

Table 13.2. Comparison of maximum predicted damage.

	Max. damage, 120° lower die	Max. damage, 180° lower die	Rel. diff. [%]
1st forging	0.668	1.26	88.6
2nd forging, 400mm feed	0.891	1.45	62.7
2nd forging, 800mm feed	1.00	1.89	89.0

It is also interesting to note that ductile damage is predicted to appear along the porous centerline of the ingot. This is in contrast to the porous plasticity modelling, where only limited damage was predicted along the centerline for the case of 800mm displacement when forging with a 120° lower die (see Fig. 13.8). The author noticed when inspecting the different shear strain components, that one component was particularly concentrated along the porous centerline of the ingot.

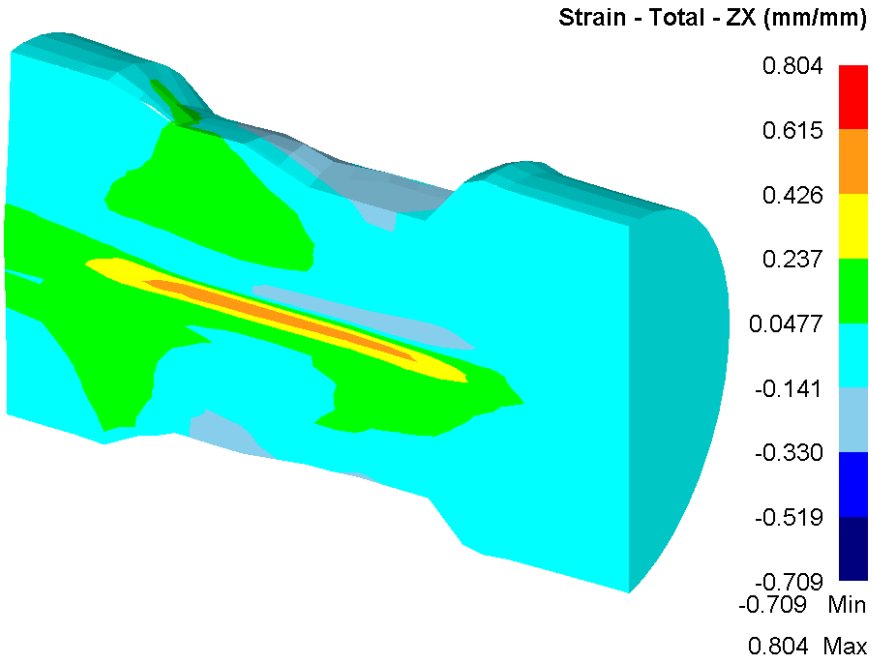

Fig. 13.21. Shear strain ε_{zx}^{pl} after forging. 120° lower die, 400mm feed.

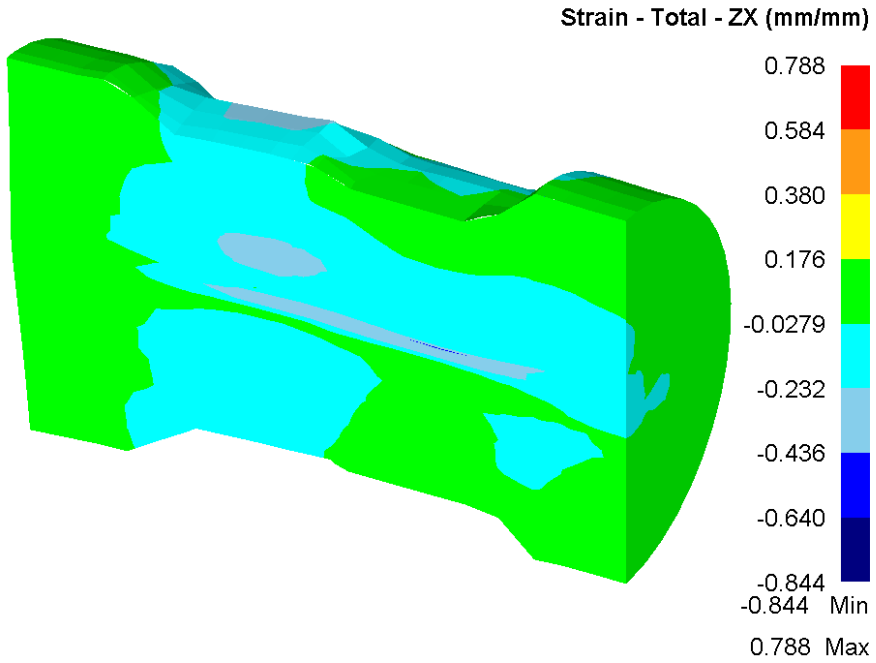

Fig. 13.22. Shear strain ε_{zx}^{pl} after forging. 120°lower die, 800mm feed.

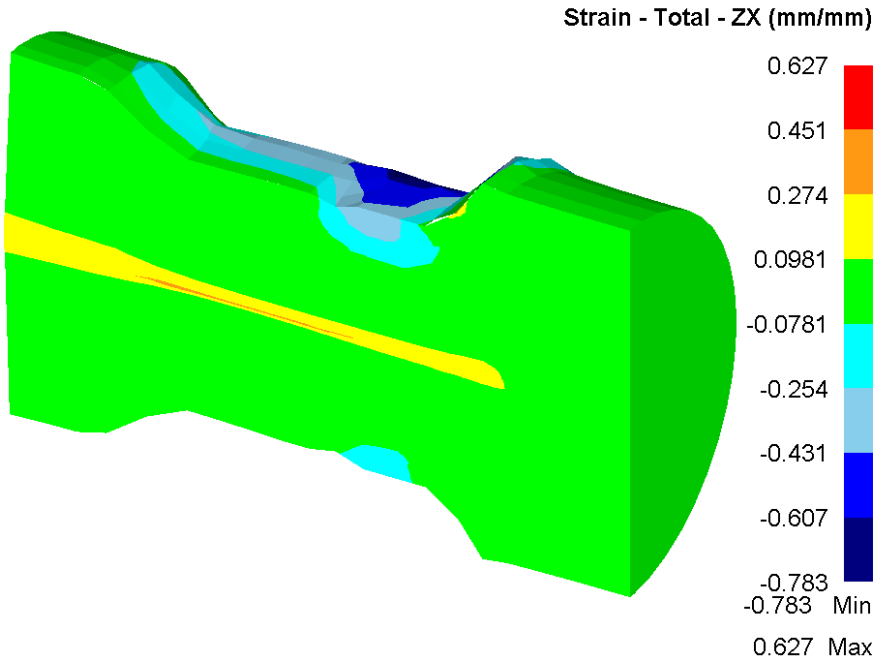

Fig. 13.23. Shear strain ε_{zx}^{pl} after forging. 180°lower die, 400mm feed.

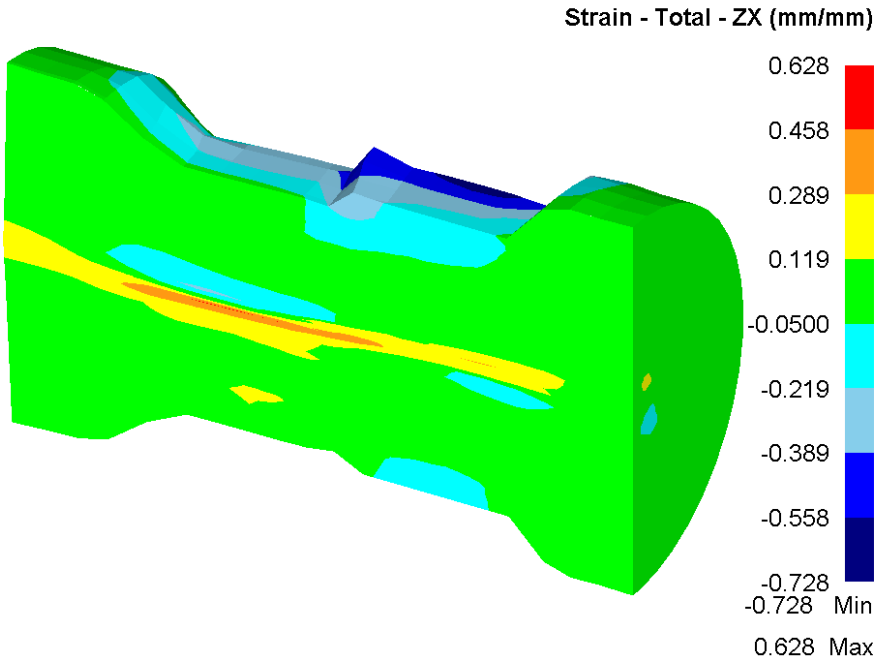

Fig. 13.24. Shear strain ε_{zx}^{pl} after forging. 180°lower die, 800mm feed.

From Fig. 13.21-Fig. 13.24 it is seen that a concentrated shear strain appears along the centerline of the ingot. Since shear strain is not taken into account when computing the relative density R, which is used as a measure of damage in porous plasticity, this might be the reason for the difference in damage based on porous plasticity or ductile damage, respectively. This indicates that an evaluation of the soundness of an ingot being hot forged should not be based only on relative density. Another damage model taking shear into account should also be included.

13.4 Conclusion

The influence of feed size has been investigated by simulation using porous plasticity for a limited number of lower die angles and feed sizes. It is found that when applying a relative density $R = \dfrac{\rho}{\rho_o}$ as a measure of damage, not much difference in the closure of an initial porosity distribution is predicted. This is somewhat different from predictions based on slipline analysis and practical experience (see 6.6) where it is recommended to have a feed size of maximum 0.5 times the width of the dies.

When evaluating damage by the normalized Cockcroft & Latham criterion, larger damage is predicted for a feed of 800mm as compared to 400mm and a 120° lower die results in less damage than forging with a 180° lower die. These results are in better agreement with the generally accepted characteristics of the process.

14 Analysis of uncoupled ductile damage

14.1 Introduction

As a supplement to the literature survey of uncoupled ductile damage criteria (see Section 7.3), this chapter introduces some of the thoughts and findings by the author during his investigation on how to model ductile damage. Some of the findings were done late in the project and could therefore not be utilized in simulations of ingot forging.

14.2 Physical interpretation of uncoupled ductile damage criteria

It is noticed that several of the listed criteria in Section 7.3 (Cockcroft & Latham, Brozzo, McClintock, Ayada, Oyane) have the possibility of accumulating negative damage values. This rises, according to the author, an interesting question: What is the physical interpretation of negative damage?

If one is inspired by the porous plasticity models, one could imagine a negative damage value to conform with densification. Hence if one first compresses a porous solid and thereafter stretches it by the same amount again, the material should return to its initial state. The principle is seen in Fig. 14.1.

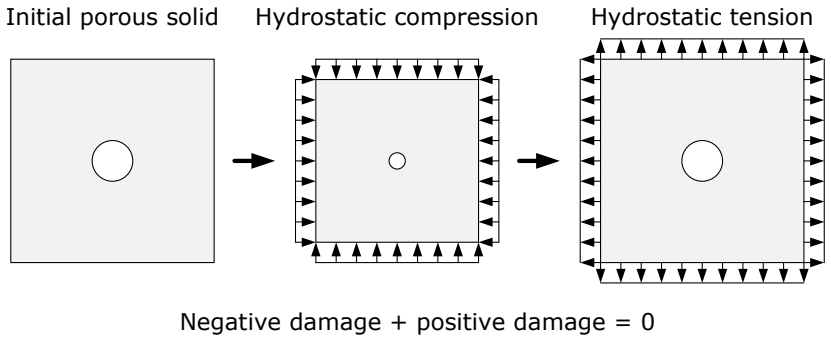

Fig. 14.1. Reversibility of damage analogous to porous metal plasticity.

If one interpretates ductile damage as the compression and expansion of porosities, accumulation of negative ductile damage may therefore seem reasonable.

Negative ductile damage may also be interpreted as porosities welding together after being compressed in hot metal forming. Thereby the initial porosities have disappeared and if loaded in tension again, a porosity may nucleate and grow to same size as the

original one and the initial material is reached again. Therefore the damage model should be able both to predict negative and positive values to be fully reversible. The principle of welding a porosity is seen in Fig. 14.2.

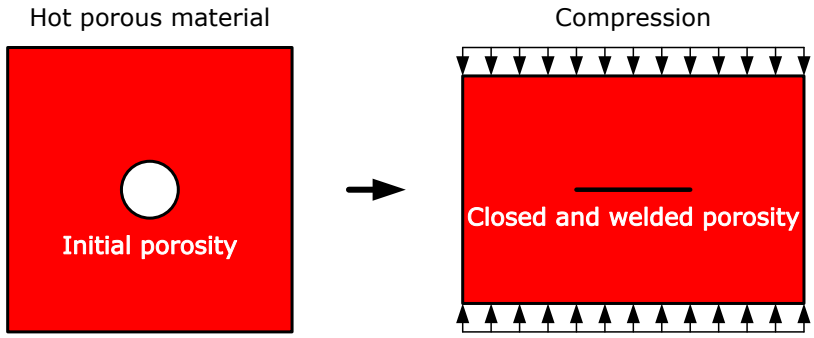

Fig. 14.2. Welding of porosity in hot metal forming.

Both of the above mentioned interpretations have some degree of truth. Increased strength of porous metals due to compaction is found experimentally in for instance Shima & Oyane [90]. It is also reported in Semiatin [88] p. 102 that porosities may be healed due to hot forging.

The question is however how to interpretate negative ductile damage in other metal forming processes such as uniaxial compression of porous free metals in cold condition? In this case the negative damage cannot be viewed as compression of porosities nor welding of them since there are none present and they are not induced during the operation if the stress state remains uniaxial compression. It was noticed in Fig. 7.3 that apparently a threshold exists for $\beta \approx -\frac{1}{3}$ where the formability approaches infinity, hence no ductile damage should be predicted. Therefore negative damage can, in the opinion of the author, in general not be assigned to a specific physical interpretation. Accumulation of negative damage in computational models for ductile damage should therefore, in the authors opinion, not be performed. This is also reflected in the commercial finite element code DEFORM®, which allows the user to choose whether or not to accumulate negative damage for some of the available ductile damage criteria.

What should be implemented in numerical codes is only accumulation of positive damage. This implies that for some stress situations, depending on the damage criterion, damage will not be accumulated for some uncoupled ductile damage criteria while other criteria will accumulate positive damage. The principle is seen in Table 14.1. Green color of a cell indicates accumulation of damage while red indicates no accumulation of damage.

Table 14.1. Accumulation of damage depending on stress triaxiality β for plane stress loading.

Damage criterion		$\beta \leq -1$	$-1 < \beta \leq -\frac{1}{3}$	$-\frac{1}{3} < \beta \leq 0$	$0 < \beta$
$C = \int \frac{\sigma_1}{\bar{\sigma}} d\bar{\varepsilon}^{pl}$	Normalized C&L	No	No	Yes	Yes
$C = \int \frac{\sigma_m}{\bar{\sigma}} d\bar{\varepsilon}^{pl}$	Ayada	No	No	No	Yes
$C = \int \left(1 + \frac{1}{a_0}\frac{\sigma_m}{\bar{\sigma}}\right) d\bar{\varepsilon}^{pl}$	Oyane $\left(a_0 = \frac{1}{3}\right)$	No	No	Yes	Yes
$C = \int exp\left(\frac{3}{2}\frac{\sigma_m}{\bar{\sigma}}\right) d\bar{\varepsilon}^{pl}$	Rice & Tracey	Yes	Yes	Yes	Yes

It can be seen from Table 14.1 that the Rice & Tracey criterion predicts accumulation of damage for all stress triaxiality values since $exp(x) > 0$. However since $exp(x) \to 0$ for $x \to -\infty$ it does, to some extent, reflect the findings of Vujovic & Shabaik [100], see 7.1.2.

The Ayada criterion only predicts damage for $\beta > 0$. This is too conservative since the formability diagram (Fig. 7.3) predicts fracture at a finite strain for slightly negative values of β.

Accumulation of damage according to the Oyane criterion varies with the choice of the constant a_0. If $a_0 = \frac{1}{3}$, the Oyane criterion predicts no positive damage for $\beta < -\frac{1}{3}$. Thereby the criterion would be in agreement with the formability diagram in Fig. 7.3. The Oyane criterion could therefore, with proper choice of the constant a_0, be suited for modelling ductile damage by an uncoupled criterion.

The normalized Cockcroft & Latham criterion depends on the largest principal stress. In uniaxial compression the largest principal stress becomes zero when the stress triaxiality becomes $-\frac{1}{3}$. The normalized Cockcroft & Latham criterion is therefore in agreement with the formability diagram, as regards infinite formability for $\beta < -\frac{1}{3}$.

Both the normalized Cockcroft & Latham criterion and the Ayada criterion are investigated further in Section 14.3 where they are related to the forming fracture limit diagram.

The analysis of differences in the different damage criteria as regards accumulation of damage, in relation to ingot forging, was published in Christiansen et al. [18].

14.3 Analysis of some uncoupled ductile damage criteria seen in relation to the forming fracture limit diagram

It was mentioned in 7.3 that the damage criteria should be able to predict the same degree of damage at fracture irrespectively of the process. Two damage criteria are investigated further, namely the normalized Cockcroft & Latham criterion and the Ayada criterion. The normalized Cockcroft & Latham criterion is investigated because it has been found in experiments to give a fairly small deviation of predicted value at fracture for several different bulk metal forming operations. The Ayada criterion is selected partly because of its simplicity, partly because it is directly dependent of the stress triaxiality level, which has been experimentally found to influence formability significant. The analysis may be explained using Fig. 14.3. The first part of the analysis is concurrent with chapter 12 in Rodrigues & Martins [84] and can also be found in Oh et al. [77].

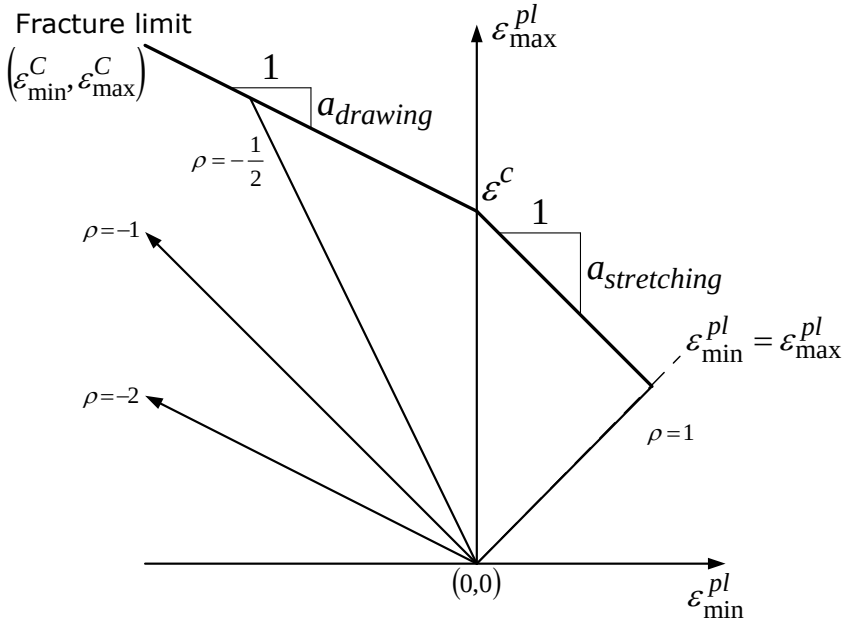

Fig. 14.3. Forming fracture limit diagram with linear strain path.

It is assumed that the material to be formed has zero initial plastic strain, hence the starting point of deformation is in $(0, 0)$ in the in-plane principal strain coordinate system, see Fig. 14.3. It is further assumed that a constant ratio between ε^{pl}_{min} and ε^{pl}_{max} is maintained throughout the deformation. The strain ratio ρ is defined as:

$$\rho = \frac{d\varepsilon^{pl}_{min}}{d\varepsilon^{pl}_{max}} \tag{14.1}$$

which for the assumption of a constant ratio of the principal strains becomes $\rho = \dfrac{\varepsilon^{pl}_{min}}{\varepsilon^{pl}_{max}}$. It is also noticed that $\dfrac{1}{\rho} = \dfrac{d\varepsilon^{pl}_{max}}{d\varepsilon^{pl}_{min}}$ is the slope of the linear strain paths from origo to the intersection with the fracture limit line. The material is assumed to be isotropic and yielding is described using a von Mises yield surface. Plane stress is assumed. The analysis is therefore relevant for surface cracks appearing due to plastic deformation. Fracture is considered to occur when the $\left(\varepsilon^{pl}_{min}, \varepsilon^{pl}_{max}\right)$-coordinates reach the fracture limit. The fracture limit is assumed to consist of two straight lines possibly having different slopes in the drawing and stretching region of the forming limit diagram. The loading situation for some values of ρ can be seen in Table 14.2.

Table 14.2. Different strain paths and their corresponding stress situation.

$\rho = -2$	Uniaxial compression
$\rho = -1$	Pure shear
$\rho = -\frac{1}{2}$	Uniaxial tension
$\rho = 0$	Plane strain tension
$\rho = 1$	Balanced biaxial tension

Useful for the analysis is the stress ratio α defined as:

$$\alpha = \frac{\sigma_{min}}{\sigma_{max}} \tag{14.2}$$

where σ_{min} is the smallest in-plane stress and σ_{max} is the largest in-plane stress.
Levy-Mises flow rule (Eq. 8.82) yields:

$$\begin{aligned} d\varepsilon^{pl}_{min} &= \frac{d\bar{\varepsilon}^{pl}}{\bar{\sigma}}\left[\sigma_{min} - \frac{1}{2}\left(\sigma_{max} + \sigma_n\right)\right] \\ d\varepsilon^{pl}_{max} &= \frac{d\bar{\varepsilon}^{pl}}{\bar{\sigma}}\left[\sigma_{max} - \frac{1}{2}\left(\sigma_{min} + \sigma_n\right)\right] \end{aligned} \tag{14.3}$$

where σ_{min} and σ_{max} are the minimum and maximum in-plane stresses and $\sigma_n = 0$ is the normal stress to the surface, which is assumed to be zero.

The strain ratio can then be expressed as:

$$\rho = \frac{d\varepsilon^{pl}_{min}}{d\varepsilon^{pl}_{max}} = \frac{\sigma_{min} - \frac{1}{2}\sigma_{max}}{\sigma_{max} - \frac{1}{2}\sigma_{min}} = \frac{2\alpha - 1}{2 - \alpha} \tag{14.4}$$

Then the stress ratio α is:

$$\alpha = \frac{2\rho + 1}{2 + \rho} \tag{14.5}$$

Using the aforementioned ratios α and ρ, Rodrigues & Martins [84] writes in their chapter 12 expressions for the normalized Cockcroft & Latham criterion and the Ayada criterion as function of loading path ρ and the fracture limit line. They only investigate the drawing region of the forming limit diagram and assumes a slope of the fracture limit line of $a_{drawing} = -\frac{1}{2}$. This value of the slope has been found in for instance Kuhn et al. [62]. Both Rodrigues & Martins [84] and Oh et al. [77] have noticed that the normalized Cockcroft & Latham criterion is constant along a line with slope $a = -\frac{1}{2}$ in the principal strain diagram.

The author wishes to expand this analysis to both the drawing and the stretching region and to include forming limit lines having arbitrary values of $a_{drawing}$ and $a_{stretching}$.

14.3.1 Expressions for stresses

Since the normalized Cockcroft & Latham criterion involves the ratio of $\frac{\sigma_1}{\bar{\sigma}}$ and the Ayada criterion involves the ratio $\frac{\sigma_m}{\bar{\sigma}}$, it is necessary to express the stresses as a function of strain ratio ρ.

$$\sigma_1 = \sigma_{max} \tag{14.6}$$

$$\bar{\sigma} = \sqrt{\sigma^2_{max} + \sigma^2_{min} - \sigma_{max}\sigma_{min}} = \sqrt{1 - \alpha + \alpha^2} \mid \sigma_{max} \mid = \sqrt{3}\frac{\sqrt{1 + \rho + \rho^2}}{\mid 2 + \rho \mid} \mid \sigma_{max} \mid \tag{14.7}$$

$$\sigma_m = \frac{\sigma_{max} + \sigma_{min}}{3} = \frac{(1+\alpha)}{3}\sigma_{max} = \frac{1+\rho}{2+\rho}\sigma_{max} \tag{14.8}$$

$$\frac{\sigma_1}{\bar{\sigma}} = \frac{\sigma_{max}}{\sqrt{3}\frac{\sqrt{1+\rho+\rho^2}}{|\,2+\rho\,|}\,|\,\sigma_{max}\,|} = \frac{|\,2+\rho\,|}{\sqrt{3}\sqrt{1+\rho+\rho^2}}\frac{\sigma_{max}}{|\,\sigma_{max}\,|} \tag{14.9}$$

$$\frac{\sigma_m}{\bar{\sigma}} = \frac{\frac{1+\rho}{2+\rho}\sigma_{max}}{\sqrt{3}\frac{\sqrt{1+\rho+\rho^2}}{|\,2+\rho\,|}\,|\,\sigma_{max}\,|} = \frac{1+\rho}{\sqrt{3}\sqrt{1+\rho+\rho^2}}\frac{|\,2+\rho\,|}{2+\rho}\frac{\sigma_{max}}{|\,\sigma_{max}\,|} \tag{14.10}$$

14.3.2 Expressions for strains

Fracture is assumed to occur when the in-plane plastic strains $\left(\varepsilon^{pl}_{min}, \varepsilon^{pl}_{max}\right)$ reach the critical values $\left(\varepsilon^{C}_{min}, \varepsilon^{C}_{max}\right)$, which lie on the fracture limit line. The fracture limit may be described generally as:

$$\begin{aligned} \varepsilon^{C}_{max} &= a\varepsilon^{C}_{min} + \varepsilon^{C} \\ &= a\rho\varepsilon^{C}_{max} + \varepsilon^{C} \\ &= \frac{\varepsilon^{C}}{1-a\rho} \end{aligned} \tag{14.11}$$

where $a = a_{drawing}$ in the drawing region of the forming limit diagram and $a = a_{stretching}$ in the stretching region of the forming limit diagram (see Fig. 14.3). The condition for fracture is $a\rho < 1$.

The effective strain increment, which is integrated in the damage formulation, may be expressed using volume constancy as:

$$\begin{aligned} d\bar{\varepsilon}^{pl} &= \sqrt{\frac{2}{3}\left[\left(d\varepsilon^{pl}_{max}\right)^2 + \left(d\varepsilon^{pl}_{min}\right)^2 + \left(-d\varepsilon^{pl}_{max} - d\varepsilon^{pl}_{min}\right)^2\right]} \\ &= \frac{2}{\sqrt{3}}\sqrt{\left(d\varepsilon^{pl}_{max}\right)^2 + \left(d\varepsilon^{pl}_{min}\right)^2 + d\varepsilon^{pl}_{max}d\varepsilon^{pl}_{min}} \\ &= \frac{2}{\sqrt{3}}\sqrt{1+\rho+\rho^2}\;|\,d\varepsilon^{pl}_{max}\,| \end{aligned} \tag{14.12}$$

When assuming proportional loading until fracture $\left(\varepsilon^{pl}_{max} = \varepsilon^{C}_{max}\right)$, $a\rho < 1$ and $\varepsilon^{C} > 0$, combining Eq. 14.11 and Eq. 14.12 yields:

$$\bar{\varepsilon}^{C} = \frac{2}{\sqrt{3}}\sqrt{1+\rho+\rho^2}\frac{\varepsilon^{C}}{1-a\rho} \tag{14.13}$$

where $\bar{\varepsilon}^{C}$ is the effective plastic strain at fracture.

By using Eq. 14.10 and Eq. 14.13 it is possible to plot the effective strain at fracture $\bar{\varepsilon}^{C}$ as function of stress triaxiality β for different values of ρ. Such a plot may be seen in

Fig. 14.4. Values used for the constants are $\varepsilon^C = 0.5$, $a = -0.5$ and $-1.5 \leq \rho \leq 1$.

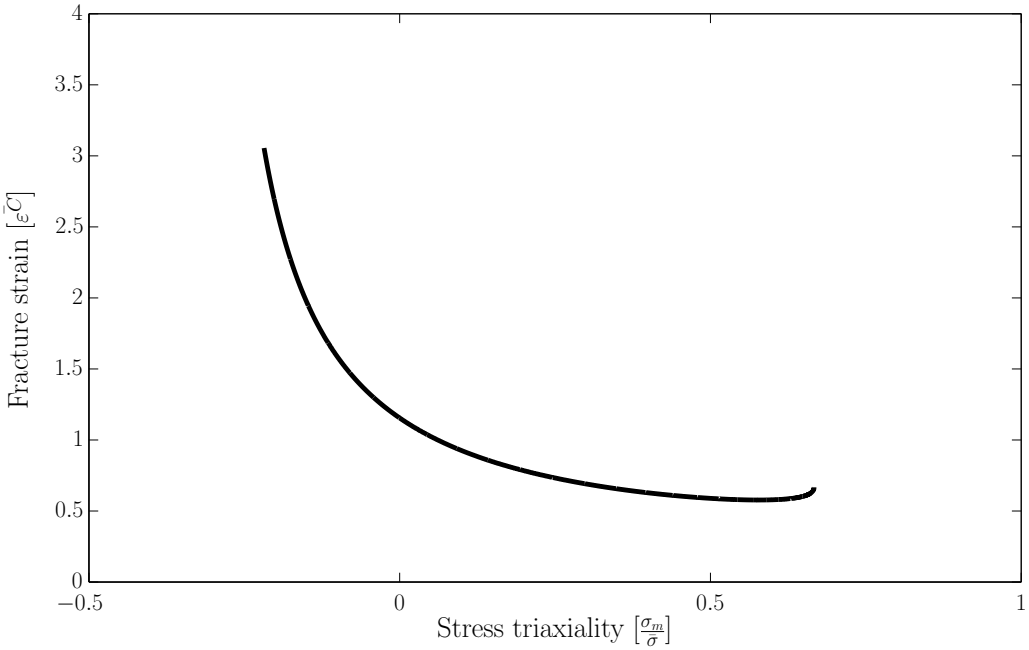

Fig. 14.4. Formability diagram based on FFLD.

Fig. 14.4 shows agreement between the formability diagram suggested in Vujovic & Shabaik [100], Fig. 7.3, and the forming fracture limit diagrams of Kuhn et al. [62], hence, in the opinion of the author, this indicates that they both represent the same physical phenomenon.

14.3.3 Expression for the normalized Cockcroft & Latham criterion

$$\begin{aligned} C &= \int_0^{\bar{\varepsilon}^C} \frac{\sigma_1}{\bar{\sigma}} d\bar{\varepsilon}^{pl} \\ &= \frac{\sigma_1}{\bar{\sigma}} \bar{\varepsilon}^C \\ &= \frac{\mid 2+\rho \mid}{\sqrt{3}\sqrt{1+\rho+\rho^2}} \frac{\sigma_{max}}{\mid \sigma_{max} \mid} \frac{1}{\sqrt{3}} \sqrt{1+\rho+\rho^2} \frac{\varepsilon^C}{1-a\rho} \\ &= \frac{4}{3} \frac{\mid 1+\frac{1}{2}\rho \mid}{1-a\rho} \frac{\sigma_{max}}{\mid \sigma_{max} \mid} \varepsilon^C \end{aligned} \tag{14.14}$$

Assuming $\sigma_{max} > 0$, Eq. 14.14 further reduces to:

$$C = \frac{4}{3} \frac{\mid 1+\frac{1}{2}\rho \mid}{1-a\rho} \varepsilon^C \tag{14.15}$$

It is seen that if $a = -\frac{1}{2}$ and $\rho > -2$, Eq. 14.15 reduces to:

$$C = \frac{4}{3} \varepsilon^C \tag{14.16}$$

which implies that if the slope of the fracture limit line is $-\frac{1}{2}$, the normalized Cockcroft & Latham criterion predicts the same damage value independent of the proportional loading path.

Since the slope of the fracture limit line was found by Kuhn et al. [62] to be $-\frac{1}{2}$ in bulk forming operations, the analysis illustrates why the normalized Cockcroft & Latham criterion should predict damage with little variation in accumulated damage value C, independent of the loading path in plane stress bulk forming operations. It was found in Landre et al. [63] that among the criteria of Brozzo, normalized Cockcroft & Latham and McClintock, the normalized Cockcroft & Latham criterion gave the smallest deviation of the value of C from the average value of the investigated metal forming operations, which consisted of upsetting of cylindrical, tapered and flanged carbon steel cylinders.

The slope $-\frac{1}{2}$ of the fracture limit line corresponds to infinite formability if the strain ratio $\rho = -2$, hence infinite formability is predicted in uniaxial compression. This is in agreement with Fig. 7.3 where the threshold value of stress triaxiality for infinite formability is $\beta = -\frac{1}{3}$, which corresponds to uniaxial compression. The normalized Cockcroft & Latham criterion is therefore in agreement with the findings of Kuhn et al. [62] and Vujovic & Shabaik [100].

14.3.4 Expression for the Ayada criterion

$$\begin{aligned} C &= \int_0^{\bar{\varepsilon}^C} \frac{\sigma_m}{\bar{\sigma}} d\bar{\varepsilon}^{pl} \\ &= \frac{\sigma_m}{\bar{\sigma}} \bar{\varepsilon}^C \\ &= \frac{1+\rho}{\sqrt{3}\sqrt{1+\rho+\rho^2}} \frac{\mid 2+\rho \mid}{2+\rho} \frac{\sigma_{max}}{\mid \sigma_{max} \mid} \frac{2}{\sqrt{3}} \sqrt{1+\rho+\rho^2} \frac{\varepsilon^C}{1-a\rho} \\ &= \frac{2}{3} \frac{\mid 2+\rho \mid}{2+\rho} \frac{\sigma_{max}}{\mid \sigma_{max} \mid} \frac{1+\rho}{1-a\rho} \varepsilon^C \end{aligned} \tag{14.17}$$

Assuming $\sigma_{max} > 0$, Eq. 14.17 further reduces to:

$$C = \frac{2}{3} \frac{\mid 2+\rho \mid}{2+\rho} \frac{1+\rho}{1-a\rho} \varepsilon^C \tag{14.18}$$

Assuming $\rho > -2$, Eq. 14.18 can be reduced to:

$$C = \frac{2}{3} \frac{1+\rho}{1-a\rho} \varepsilon^C \tag{14.19}$$

If $a = -1$, Eq. 14.19 reduces to:

$$C = \frac{2}{3} \varepsilon^C \tag{14.20}$$

Since the slope of the fracture line in the bulk metal forming region of the forming fracture limit diagram has a value of $-\frac{1}{2}$, the Ayada criterion is less suitable than the normalized Cockcroft & Latham criterion for predicting damage of the material because the damage value C at fracture will vary with the strain ratio ρ even for proportional loading. However in the stretching region, where mainly sheet metal forming operations

take place, forming fracture limit diagrams in Embury & Duncan [30] indicate that the slope of the fracture limit line in general is smaller than or equal to the slope in the drawing region, hence $a_{drawing} \geq a_{stretching}$. If the slope in the stretching region becomes equal to -1, the Ayada criterion would be better suited for modelling ductile damage than the normalized Cockcroft & Latham criterion because the Ayada criterion would then be strain ratio independent and predict the same amount of damage at fracture for all the loading paths in the stretching region of the forming fracture limit diagram.

14.4 Derivation of damage criterion independent of proportional loading path and slope of fracture line

The general form of an uncoupled ductile damage criterion is assumed to be $C = \int f(\sigma_{ij})\, g\left(d\varepsilon_{ij}^{pl}\right)$. Assuming $g\left(d\varepsilon_{ij}^{pl}\right) = d\bar{\varepsilon}^{pl}$, proportional plane stress loading, $a\rho < 1$ and $\varepsilon^C > 0$ it follows from Eq. 14.13 that an expression for uncoupled ductile damage is:

$$C = f(\sigma_{ij})\, \frac{2}{\sqrt{3}} \sqrt{1+\rho+\rho^2}\, \frac{\varepsilon^C}{1-a\rho} \tag{14.21}$$

Eq. 14.21 is strain path independent if:

$$\begin{aligned} f(\sigma_{ij}) &= \frac{1-a\rho}{\sqrt{1+\rho+\rho^2}} \\ &= \frac{\sqrt{3}}{2} \frac{1-a\rho}{\mid 1+\frac{1}{2}\rho \mid} \frac{\mid \sigma_{max} \mid}{\bar{\sigma}} \end{aligned} \tag{14.22}$$

where $\bar{\sigma} = \sqrt{3} \frac{\sqrt{1+\rho+\rho^2}}{\mid 2+\rho \mid} \mid \sigma_{max} \mid \Leftrightarrow \sqrt{1+\rho+\rho^2} = \frac{2}{\sqrt{3}} \mid 1+\frac{1}{2}\rho \mid \frac{\bar{\sigma}}{\mid \sigma_{max} \mid}$ is substituted into $f(\sigma_{ij})$.

Inserting the path dependent part of the expression for $f(\sigma_{ij})$ into the general form of the damage criterion yields the ductile damage criterion independent of slope of the fracture line:

$$C = \int \frac{1-a\rho}{\mid 1+\frac{1}{2}\rho \mid} \frac{\mid \sigma_{max} \mid}{\bar{\sigma}} d\bar{\varepsilon}^{pl} \tag{14.23}$$

Assuming $\rho > -2$ and $\sigma_{max} > 0$ Eq. 14.23 becomes:

$$C = \int \frac{1-a\rho}{1+\frac{1}{2}\rho} \frac{\sigma_{max}}{\bar{\sigma}} d\bar{\varepsilon}^{pl} \tag{14.24}$$

It is seen from Eq. 14.24 that in the case of $a = -\frac{1}{2}$, the normalized Cockcroft & Latham criterion is recovered.

A plot of the damage criterion (Eq. 14.24) plotted with some other damage criteria can be seen in Fig. 14.5. $\bar{\varepsilon}^C = 0.5$ in the calculations. The graphs show accumulated damage at fracture depending on strain path, fracture criteria and fracture limit slopes. Eq. 14.24 is labeled as $C_{Slope-independent}$ in the graphs.

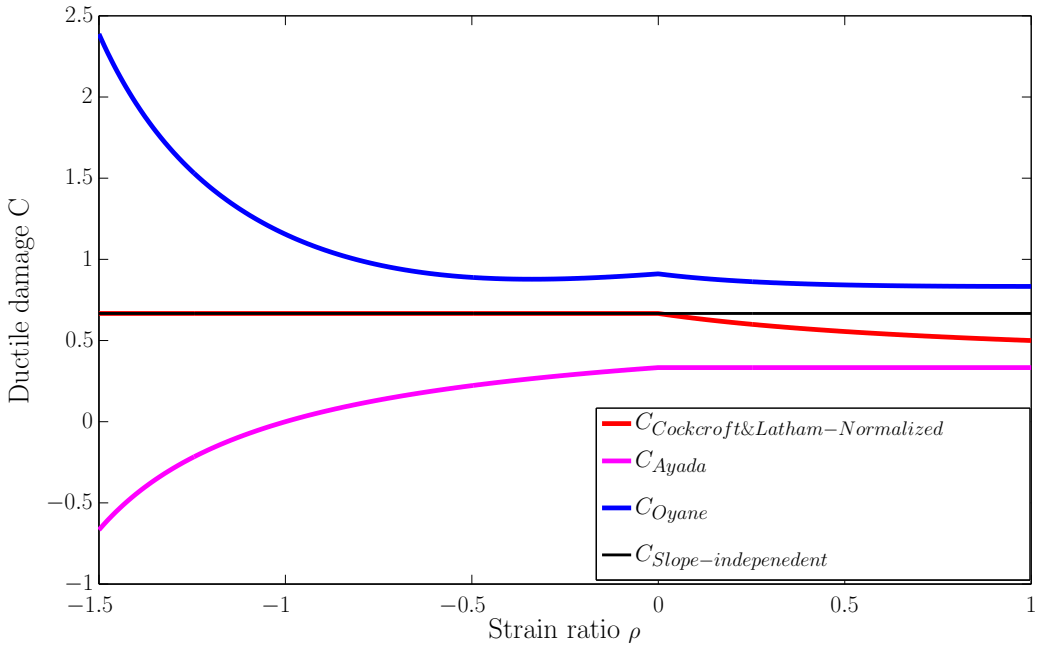

(a) $a_{drawing} = -0.5$ and $a_{stretching} = -1.0$

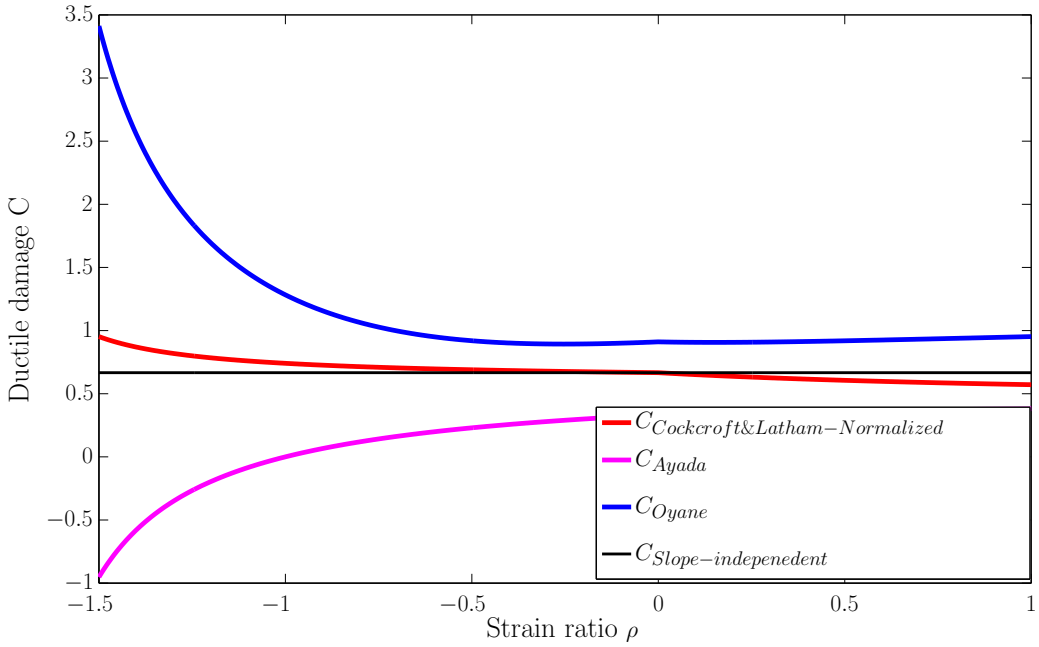

(b) $a_{drawing} = -0.45$ and $a_{stretching} = -0.75$

Fig. 14.5. Different ductile damage values C at fracture for different slopes of the fracture limit line.

It can be seen in Fig. 14.5 that when implementing Eq. 14.24 the damage at fracture is constant for fracture lines having slopes different from $a = -\frac{1}{2}$.

14.5 Derivation of accumulated ductile damage being constant for nonlinear plane stress loading paths

Although linear loading paths may be experienced in metal forming operations, nonlinear loading paths are also frequently encountered. Therefore it would be beneficial if the accumulated damage value C was independent of the loading path. This is illustrated by a bilinear loading path, which is compared to a linear loading path. The situation is seen in Fig. 14.6. In this section a detailed analysis of the normalized Cockcroft & Latham criterion for non-linear strain paths is carried out.

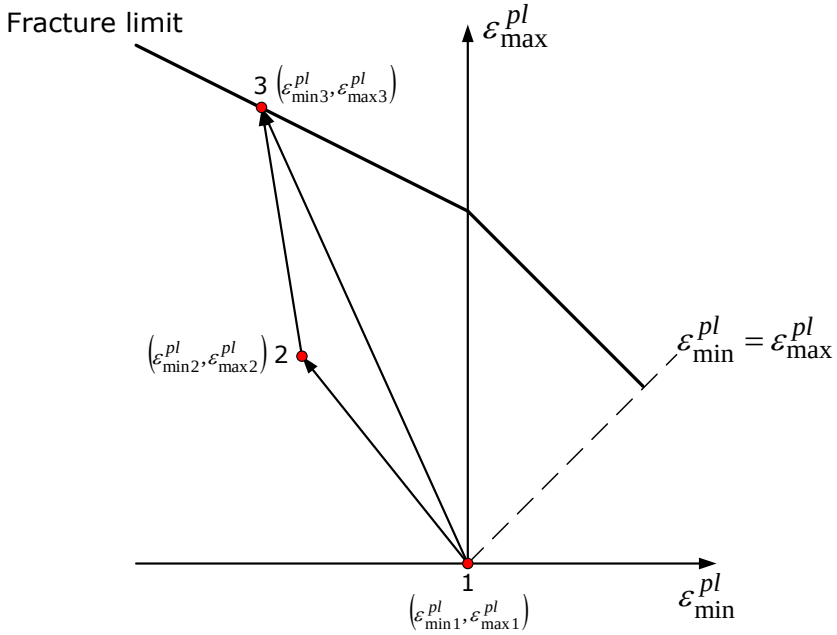

Fig. 14.6. Linear and bilinear loading paths.

In Fig. 14.6 two different loading paths from point 1 to point 3 are indicated by arrows. One is a constant loading path from point 1 to 3, while the other is a bilinear loading path from point 1 to 2 and then from point 2 to 3. For a damage criterion to be more suitable to model ductile damage, it should be independent of loading path. In Oh et al. [77] it is written that in the case of plane stress loading, the normalized Cockcroft & Latham criterion is independent of loading path. This is illustrated by the following derivation.

The ductile damage criterion is the normalized Cockcroft & Latham:

$$C = \int \frac{\sigma_1}{\bar{\sigma}} d\bar{\varepsilon}^{pl} \tag{14.25}$$

It was found in Eq. 14.9 that if $\rho > -2$ and $\sigma_1 > 0$ then

$$\frac{\sigma_1}{\bar{\sigma}} = \frac{2+\rho}{\sqrt{3}\sqrt{1+\rho+\rho^2}} \tag{14.26}$$

Inserting Eq. 14.26 into Eq. 14.25 yields:

$$C = \int \frac{2+\rho}{\sqrt{3}\sqrt{1+\rho+\rho^2}} d\bar{\varepsilon}^{pl} \tag{14.27}$$

The effective strain, when assuming $d\varepsilon^{pl}_{max} \geq 0$, was found in Eq. 14.12 to be:

$$d\bar{\varepsilon}^{pl} = \frac{2}{\sqrt{3}}\sqrt{1+\rho+\rho^2}d\varepsilon^{pl}_{max} \tag{14.28}$$

Inserting Eq. 14.28 into Eq. 14.27 gives:

$$\begin{aligned} C &= \int \frac{2+\rho}{\sqrt{3}\sqrt{1+\rho+\rho^2}}\frac{2}{\sqrt{3}}\sqrt{1+\rho+\rho^2}d\varepsilon^{pl}_{max} \\ &= \int \left(\frac{4}{3}+\frac{2}{3}\rho\right)d\varepsilon^{pl}_{max} \\ &= \frac{4}{3}\int d\varepsilon^{pl}_{max} + \frac{2}{3}\int \rho d\varepsilon^{pl}_{max} \end{aligned} \tag{14.29}$$

The strain ratio was defined as $\rho = \dfrac{d\varepsilon^{pl}_{min}}{d\varepsilon^{pl}_{max}}$. Inserting into Eq. 14.29 yields:

$$\begin{aligned} C &= \frac{4}{3}\int d\varepsilon^{pl}_{max} + \frac{2}{3}\int \frac{d\varepsilon^{pl}_{min}}{d\varepsilon^{pl}_{max}}d\varepsilon^{pl}_{max} \\ &= \frac{4}{3}\int d\varepsilon^{pl}_{max} + \frac{2}{3}\int d\varepsilon^{pl}_{min} \end{aligned} \tag{14.30}$$

With the aforementioned assumptions, Eq. 14.30 shows that the normalized Cockcroft & Latham criterion is path independent. It only depends on the beginning and end values of ε^{pl}_{min} and ε^{pl}_{max}.

A plot of the accumulated ductile damage, when applying the normalized Cockcroft & Latham criterion, can be seen in Fig. 14.7-Fig. 14.10a. The figures contain strain paths (black lines) from origo to the fracture line, which is marked by the red line. It has a slope of $a = -\dfrac{1}{2}$ with $\varepsilon^C = \dfrac{1}{2}$ implying a theoretical value for the normalized Cockcroft & Latham criterion of $C = \dfrac{4}{3}\varepsilon^C = \dfrac{4}{3}\dfrac{1}{2} = \dfrac{2}{3} \approx 0.66$. The numerically computed damage value C at fracture is also plotted for the different strain paths.

The curves are produced using a small, purpose written Matlab program. It is based on an explicit scheme where ε^{pl}_{max} is increased incrementally. From a specified initial value of ρ, the other variables such as ε^{pl}_{min}, $\bar{\varepsilon}^{pl}$ and $\dfrac{\sigma_1}{\bar{\sigma}}$ can be calculated when assuming $\sigma_{max} =\mid \sigma_{max} \mid$. Thereby it is also possible to calculate the accumulated damage C.

For the strain paths in Fig. 14.7, the initial value of ρ is maintained constant for each loading path until the critical value $C = \dfrac{2}{3}$ is reached. The fracture line is marked in red.

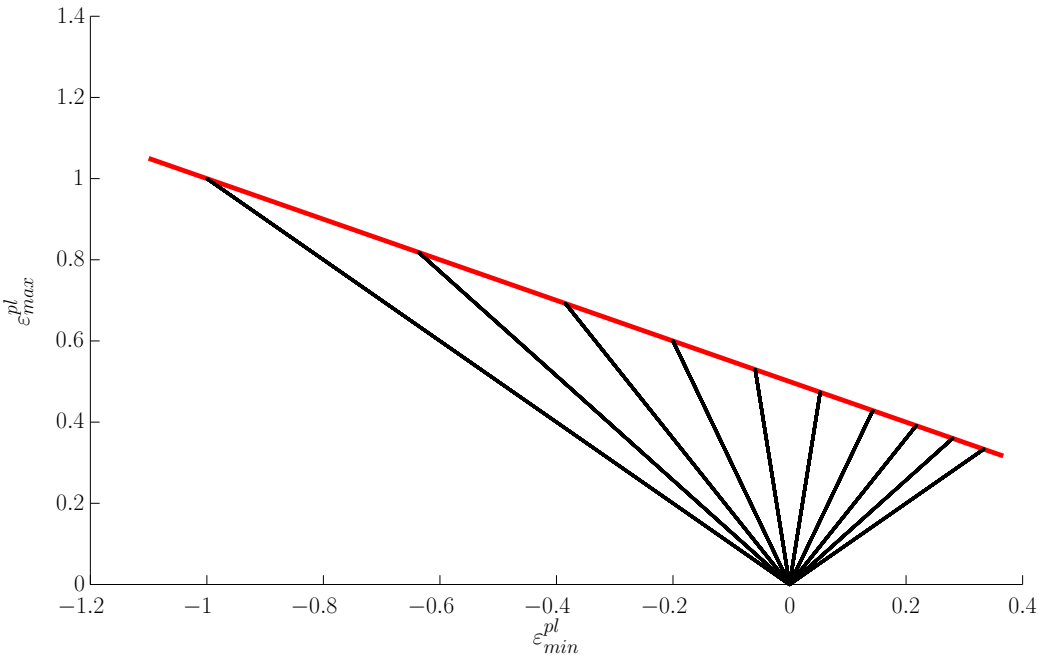

(a) Strain paths.

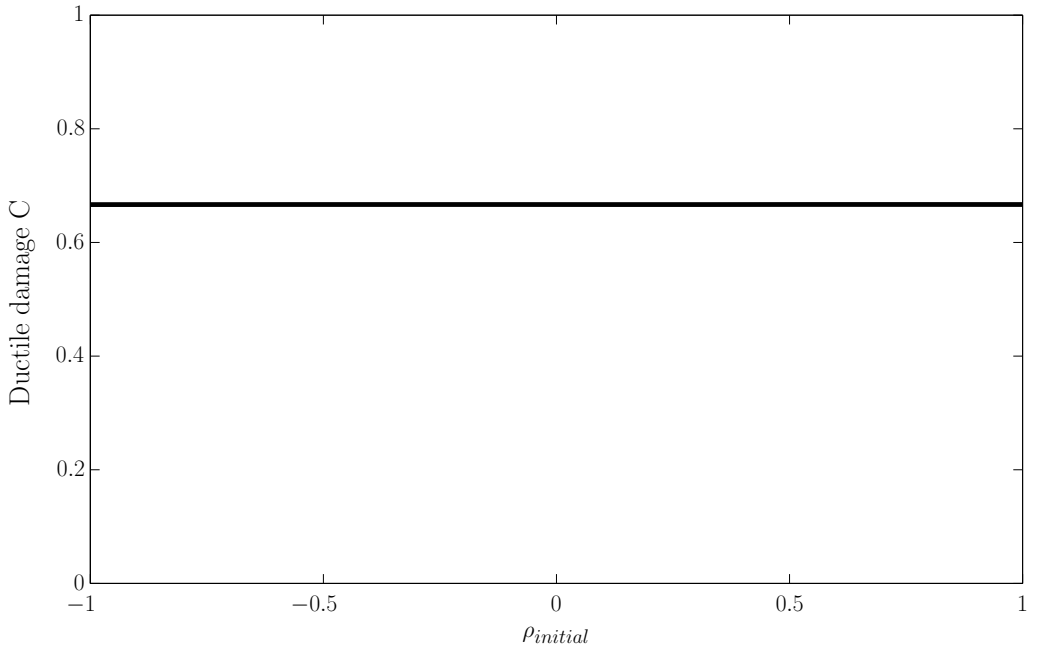

(b) Damage at fracture.

Fig. 14.7. Linear strain paths until fracture and damage value at fracture, normalized Cockcroft & Latham criterion.

In Fig. 14.8, ρ is set to zero when $\bar{\varepsilon}^{pl} = 0.3$ and maintained until the different strain paths reach the critical value $C = \dfrac{2}{3}$.

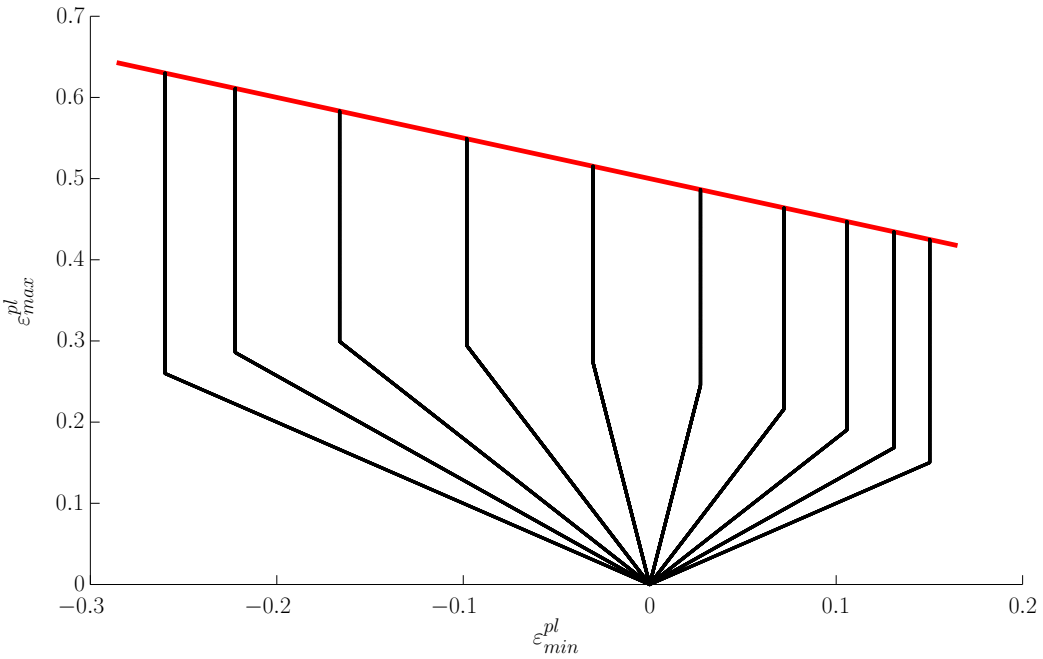

(a) Bilinear strain path.

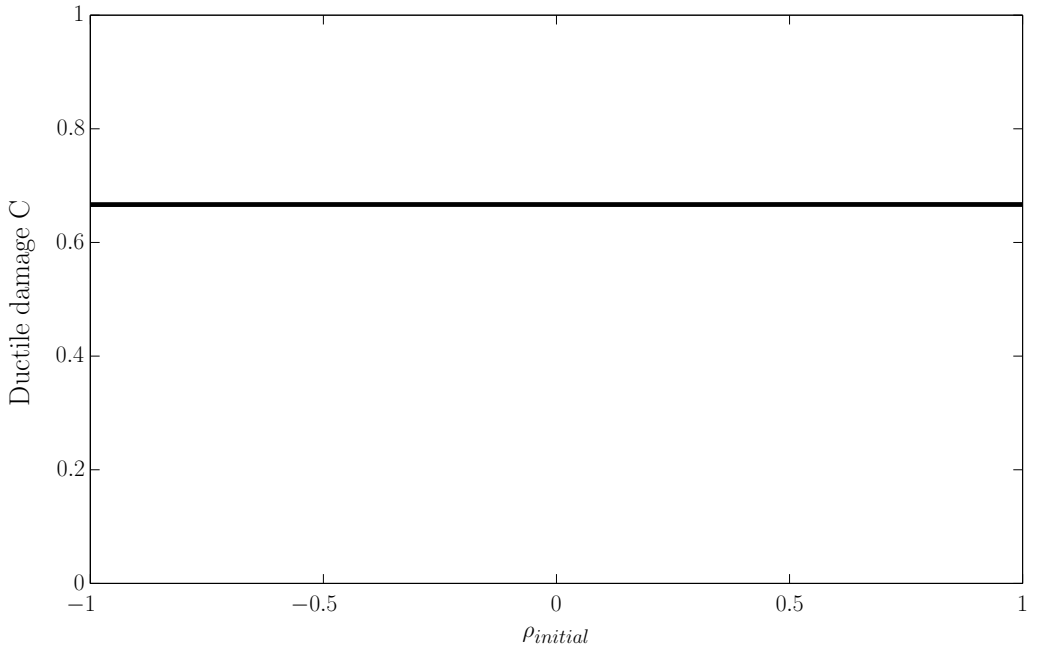

(b) Damage at fracture.

Fig. 14.8. Bilinear strain paths until fracture and damage value at fracture, normalized Cockcroft & Latham criterion.

In Fig. 14.9 the strain paths are initially the same as in Fig. 14.8 but when $\bar{\varepsilon}^{pl} = 0.5$, ρ is set to its initial value $\rho_{initial}$ until reaching the critical value $C = \frac{2}{3}$.

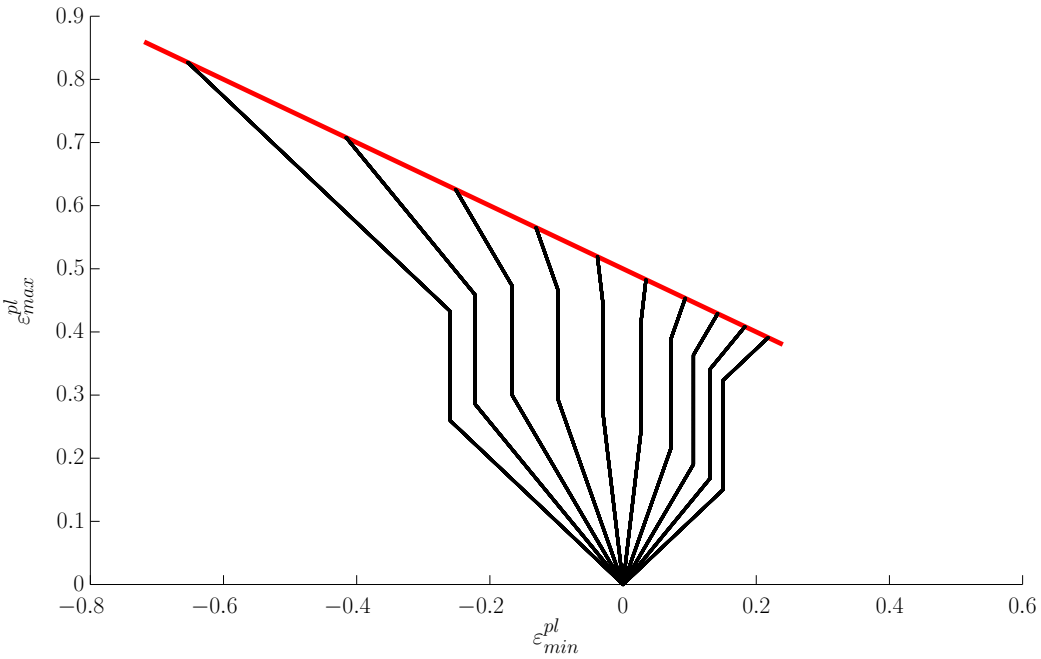

(a) Trilinear strain path.

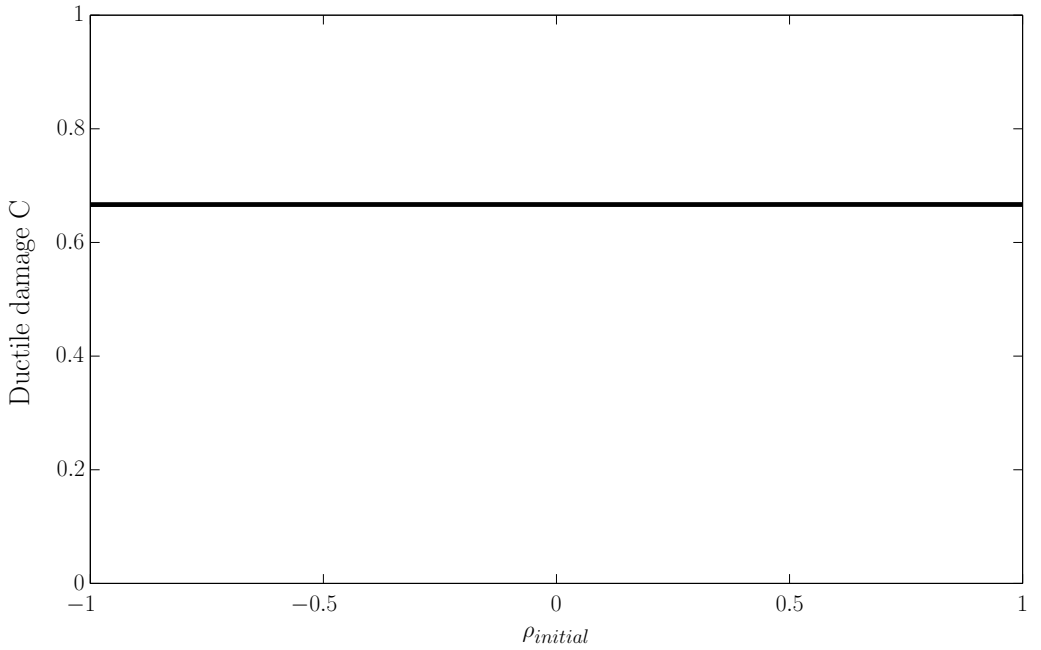

(b) Damage at fracture.

Fig. 14.9. Trilinear strain paths until fracture and damage value at fracture, normalized Cockcroft & Latham criterion.

The strain paths in Fig. 14.10a are the same as in Fig. 14.9 except that when $\bar{\varepsilon}^{pl} = 0.5$ $\rho = -\rho_{initial}$.

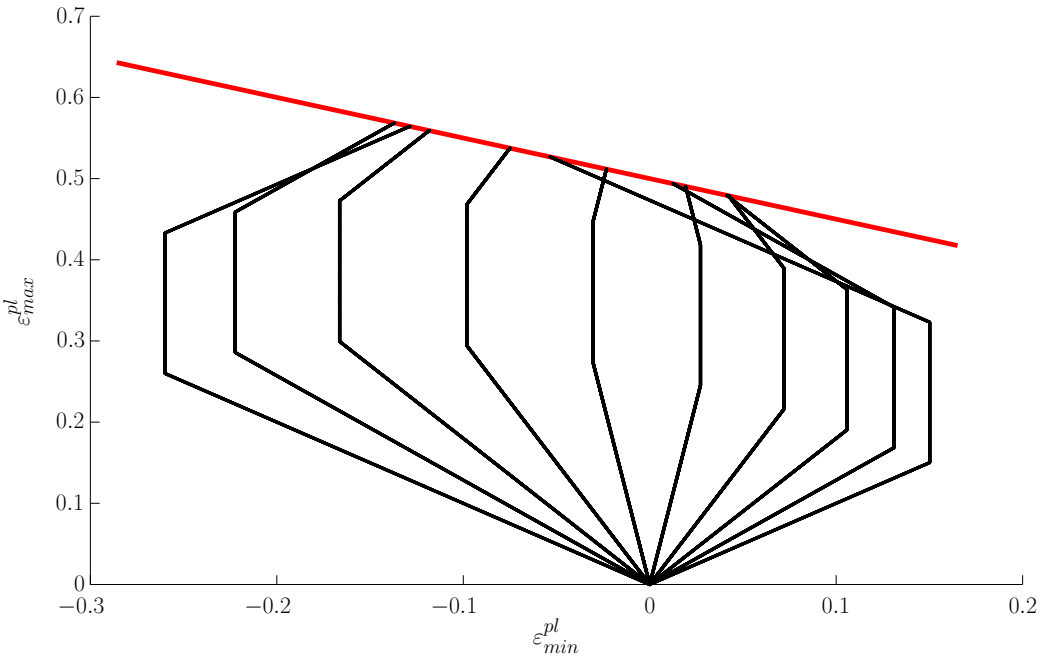

(a) Trilinear strain path.

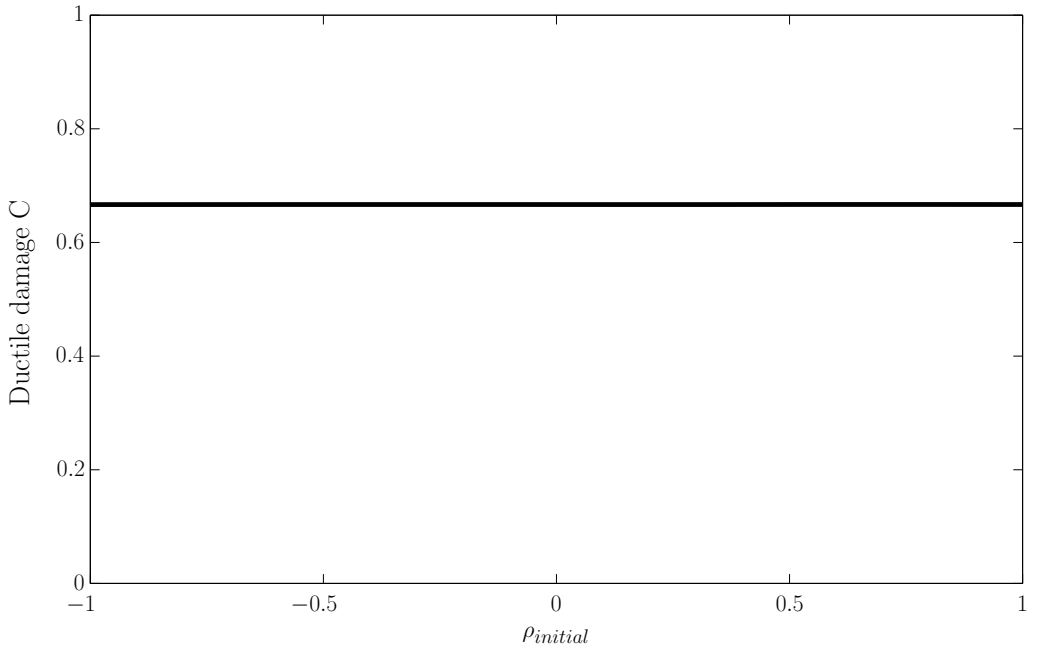

(b) Damage at fracture.

Fig. 14.10. Trilinear strain paths until fracture and damage value at fracture, normalized Cockcroft & Latham criterion.

From Fig. 14.7-Fig. 14.10 it is seen that the strain paths resulting in an amount of accumulated damage at fracture of $C \approx 0.66$ all end on the fracture line independent of the strain path. However it is noticed in Oh et al. [77] that the accumulated normalized Cockcroft & Latham damage at fracture is only constant for plane stress loading, but not for a general stress state.

One important assumption for strain path independence is also that only the formability line described by the slope $-\frac{1}{2}$ may be reached when straining the material. If

one reaches a formability line with a slope of for instance -1, the damage value C of the normalized Cockcroft & Latham criterion is not constant along such a formability line and therefore not path independent.

It should also be emphasized that other damage criteria may not be path independent. For instance the Rice & Tracey criterion, which is plotted in Fig. 14.11. Linear and bilinear loading paths from origo to the fracture line are assumed as indicated in Fig. 14.6, hence both the linear and bilinear strain paths start and end at the same points.

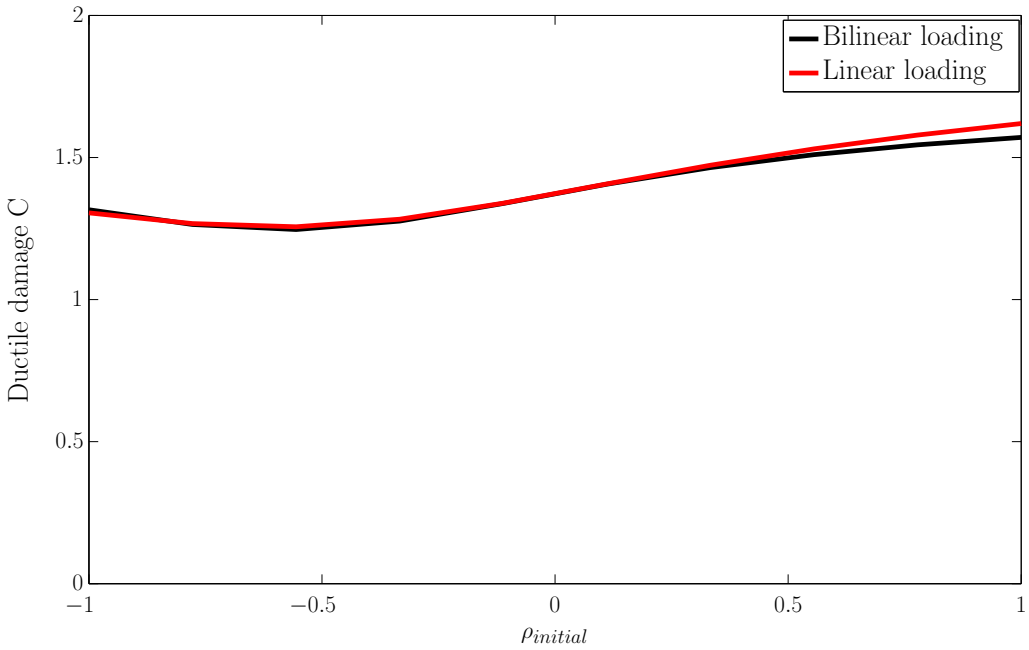

Fig. 14.11. Rice & Tracey damage for linear and bilinear loading paths for different values of ρ.

It is seen in Fig. 14.11 that some difference in the predicted ductile damage occurr for Rice & Tracey criterion depending on whether the strain path is linear or bilinear between the same start and finish points in the strain diagram. The difference seems however to be relatively small for the investigated bilinear strain path.

14.6 Analysis of uncoupled ductile damage criteria for a general stress-strain state

In the previous part of the chapter, the focus has mainly been on plane stress states. However other stress states are also frequently encountered in metal forming operations. For instance plane strain rolling of sheets. Therefore it is interesting to derive expressions for $\frac{\sigma_1}{\bar{\sigma}}$ and $\frac{\sigma_m}{\bar{\sigma}}$ for more general stress states. The analysis is performed for the principal stresses $\sigma_1 \geq \sigma_2 \geq \sigma_3$ and principal plastic strains ε_1^{pl}, ε_2^{pl} and ε_3^{pl}.

First the two stress ratios α_1 and α_2 are introduced:

$$\alpha_1 = \frac{\sigma_2}{\sigma_1} \tag{14.31}$$

$$\alpha_2 = \frac{\sigma_3}{\sigma_1} \tag{14.32}$$

Then the two strain ratios ρ_1 and ρ_2:

$$\rho_1 = \frac{d\varepsilon_2^{pl}}{d\varepsilon_1^{pl}} \tag{14.33}$$

$$\rho_2 = \frac{d\varepsilon_3^{pl}}{d\varepsilon_1^{pl}} \tag{14.34}$$

14.6.1 Expression for stresses

The effective von Mises stress $\bar{\sigma}$ is then:

$$\begin{aligned} \bar{\sigma} &= \sqrt{\sigma_1^2 + \sigma_2^2 + \sigma_3^2 - \sigma_1\sigma_2 - \sigma_1\sigma_3 - \sigma_2\sigma_3} \\ &= \sqrt{1 + \alpha_1^2 + \alpha_2^2 - \alpha_1 - \alpha_2 - \alpha_1\alpha_2}\mid \sigma_1 \mid \end{aligned} \tag{14.35}$$

In case of plane stress, where for instance $\alpha_2 = 0$, Eq. 14.35 reduces to:

$$\bar{\sigma} = \sqrt{1 - \alpha_1 + \alpha_1^2}\mid \sigma_1 \mid \tag{14.36}$$

leading both to Eq. 14.7.
The mean stress σ_m is:

$$\begin{aligned} \sigma_m &= \frac{\sigma_1 + \sigma_2 + \sigma_3}{3} \\ &= \frac{1 + \alpha_1 + \alpha_2}{3}\sigma_1 \end{aligned} \tag{14.37}$$

Again for plane stress, Eq. 14.8 is recovered.
The stress ratio $\frac{\sigma_1}{\bar{\sigma}}$ then becomes:

$$\frac{\sigma_1}{\bar{\sigma}} = \frac{1}{\sqrt{1 + \alpha_1^2 + \alpha_2^2 - \alpha_1 - \alpha_2 - \alpha_1\alpha_2}} \frac{\sigma_1}{\mid \sigma_1 \mid} \tag{14.38}$$

The stress ratio $\frac{\sigma_m}{\bar{\sigma}}$ becomes:

$$\frac{\sigma_m}{\bar{\sigma}} = \frac{1 + \alpha_1 + \alpha_2}{3\sqrt{1 + \alpha_1^2 + \alpha_2^2 - \alpha_1 - \alpha_2 - \alpha_1\alpha_2}} \frac{\sigma_1}{\mid \sigma_1 \mid} \tag{14.39}$$

14.6.2 Expressions for strains

The effective plastic strain increment $d\bar{\varepsilon}^{pl}$ is:

$$\begin{aligned} d\bar{\varepsilon}^{pl} &= \sqrt{\frac{2}{3}\left[\left(d\varepsilon_1^{pl}\right)^2+\left(d\varepsilon_2^{pl}\right)^2+\left(d\varepsilon_3^{pl}\right)^2\right]} \\ &= \sqrt{\frac{2}{3}\left[1+\rho_1^2+\rho_2^2\right]}\mid d\varepsilon_1^{pl}\mid \end{aligned} \tag{14.40}$$

Volume constancy yields:

$$\begin{aligned} d\varepsilon_1^{pl}+d\varepsilon_2^{pl}+d\varepsilon_3^{pl} &= 0 \quad \Leftrightarrow \\ 1+\rho_1+\rho_2 &= 0 \quad \Leftrightarrow \\ \rho_2 &= -\left(1+\rho_1\right) \end{aligned} \tag{14.41}$$

Inserting Eq. 14.41 into Eq. 14.40 gives:

$$\begin{aligned} d\bar{\varepsilon}^{pl} &= \sqrt{\frac{2}{3}\left[1+\rho_1^2+\left(-\left(1+\rho_1\right)\right)^2\right]}\mid d\varepsilon_1^{pl}\mid \\ &= \frac{2}{\sqrt{3}}\sqrt{1+\rho_1+\rho_1^2}\mid d\varepsilon_1^{pl}\mid \end{aligned} \tag{14.42}$$

It is seen that Eq. 14.42 is in accordance with Eq. 14.12.

14.6.3 Expression for the normalized Cockcroft & Latham criterion

$$\begin{aligned} C &= \int \frac{\sigma_1}{\bar{\sigma}} d\bar{\varepsilon}^{pl} \\ &= \int \frac{1}{\sqrt{1+\alpha_1^2+\alpha_2^2-\alpha_1-\alpha_2-\alpha_1\alpha_2}} \frac{\sigma_1}{\mid \sigma_1 \mid} \frac{2}{\sqrt{3}}\sqrt{1+\rho_1+\rho_1^2}\mid d\varepsilon_1^{pl}\mid \end{aligned} \tag{14.43}$$

14.6.4 Expression for the Ayada criterion

$$\begin{aligned} C &= \int \frac{\sigma_m}{\bar{\sigma}} d\bar{\varepsilon}^{pl} \\ &= \int \frac{1+\alpha_1+\alpha_2}{3\sqrt{1+\alpha_1^2+\alpha_2^2-\alpha_1-\alpha_2-\alpha_1\alpha_2}} \frac{\sigma_1}{\mid \sigma_1 \mid} \frac{2}{\sqrt{3}}\sqrt{1+\rho_1+\rho_1^2}\mid d\varepsilon_1^{pl}\mid \end{aligned} \tag{14.44}$$

Other damage criteria such as for instance the Oyane or Rice & Tracey can be derived in a similar manner.

14.6.5 Comment to the derived damage criteria

Basically the analysis conducted in this section is an expansion of the analysis for plane stress loading. The concept of introducing dimensionless numbers α and ρ is the same. The main difference is that for a general stress state, there is no unique relationship between stresses and strains. The constitutive law, given by the Levy-Mises flow rule for incompressible materials (Eq. 8.82), relates deviatoric stresses S_{ij} to plastic strain increments $d\varepsilon_{ij}^{pl}$ through the plastic multiplier $d\lambda$: $d\varepsilon_{ij}^{pl} = d\lambda S_{ij}$. Hence a unique relationship between deviatoric stresses and plastic strain increments exists but not between stresses and plastic strain increments. It therefore follows that the same plastic strains may be

imposed on a component in a metal forming operation but the predicted accumulated damage, predicted by damage criteria based on Eq. 14.38 or Eq. 14.39, is depending on which stress state that gave rise to the plastic strain. Therefore the formulas for a general stress state includes both α_1, α_2 and ρ_1.

14.6.6 Forming fracture limit diagrams for different damage criteria and stress states

The strain at fracture $\bar{\varepsilon}^C$ may be plotted in a diagram for different damage criteria. The procedure is as follows. One assumes a fixed value C at fracture for a given damage criterion. If there is proportional loading, the damage integral is simply the stress function multiplied by the effective plastic strain. For a constant value of C at fracture, $\bar{\varepsilon}^C$ is then found by dividing C with the stress function. The stress function is evaluated for different values of α_1 and α_2, and the resulting $\bar{\varepsilon}^C$ is then plotted in a forming fracture limit diagram. A principal sketch of such a diagram is seen in Fig. 14.12. A diagram similar in nature is found in Nahshon & Hutchinson [73].

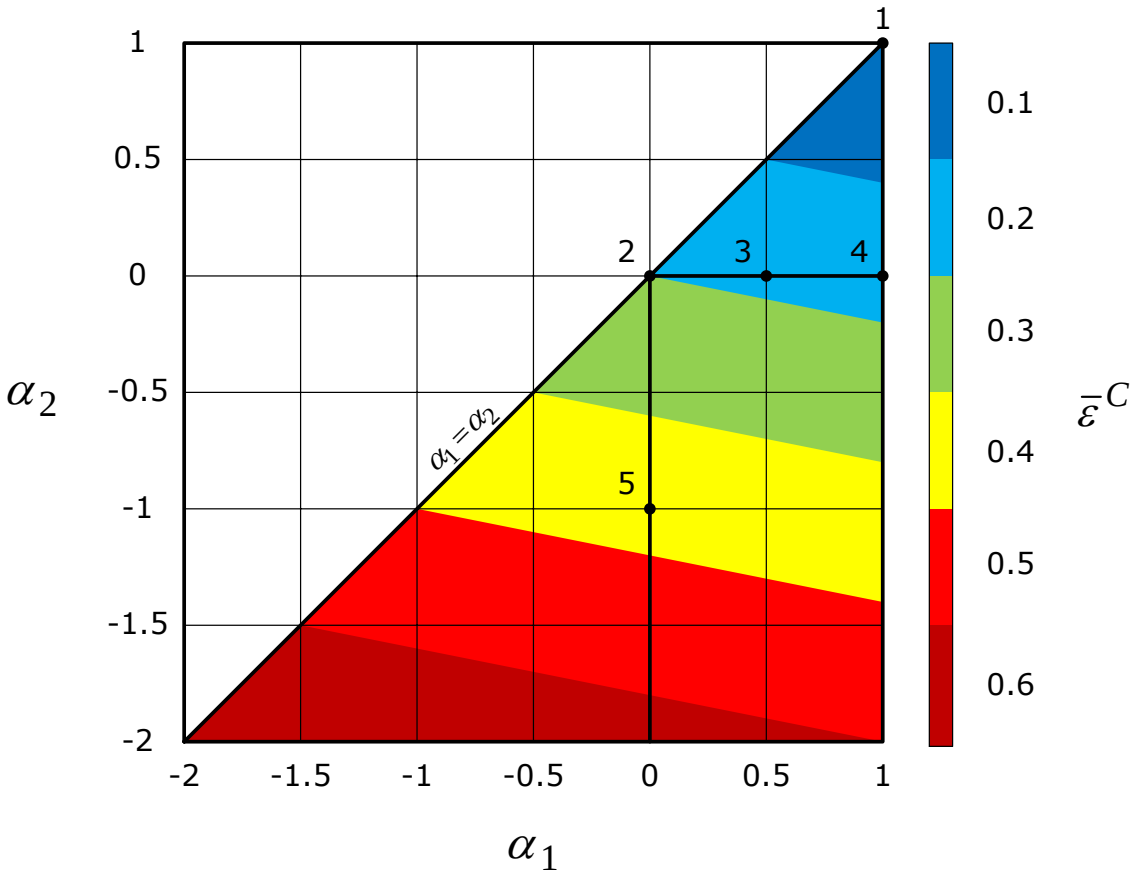

Fig. 14.12. Forming fracture limit diagram for 3 dimensional stress situations.

Fig. 14.12 shows the effective plastic strain at fracture $\bar{\varepsilon}^C$, as a function of α_1 and α_2, presented as a contourplot. It is assumed that $\sigma_1 > 0$. The area above the line $\alpha_1 = \alpha_2$ is not admissible due to the convention $\sigma_1 \geq \sigma_2 \geq \sigma_3$ implying $1 \geq \alpha_1 \geq \alpha_2$ if $\sigma_1 > 0$.

A number of points are plotted in the diagram with black dots. They are as follows:

1: Hydrostatic tension ($\sigma_1 = \sigma_2 = \sigma_3$)
2: Uniaxial tension ($\sigma_2 = \sigma_3 = 0$)
3: Plane strain tension $\left(\sigma_2 = \frac{1}{2}\sigma_1, \sigma_3 = 0\right)$
4: Balanced biaxial tension ($\sigma_1 = \sigma_2, \sigma_3 = 0$)
5: Pure shear ($\sigma_1 = -\sigma_3, \sigma_2 = 0$)

The black line starting in point 4 and going through points 3-5 and ending in $(\alpha_1, \alpha_2) = (0, -2)$ is indicating plane stress.

Principally similar figures are presented for four different damage criteria, see Fig. 14.13-Fig. 14.16. For each criterion, $C = 1$ is used as fracture limit.

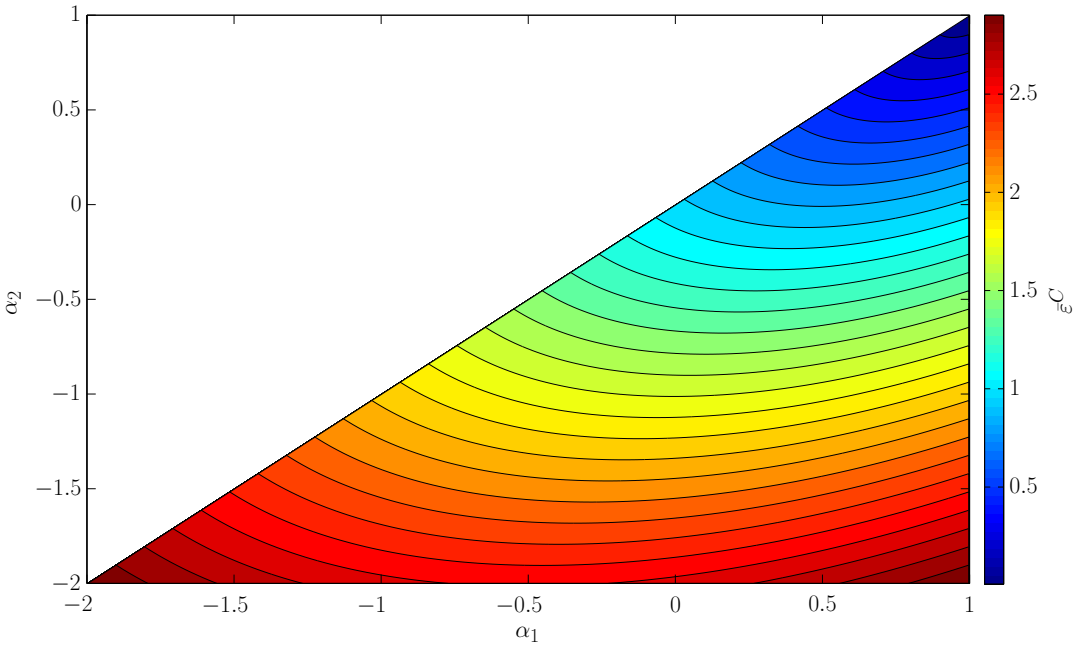

Fig. 14.13. Normalized Cockcroft & Latham.

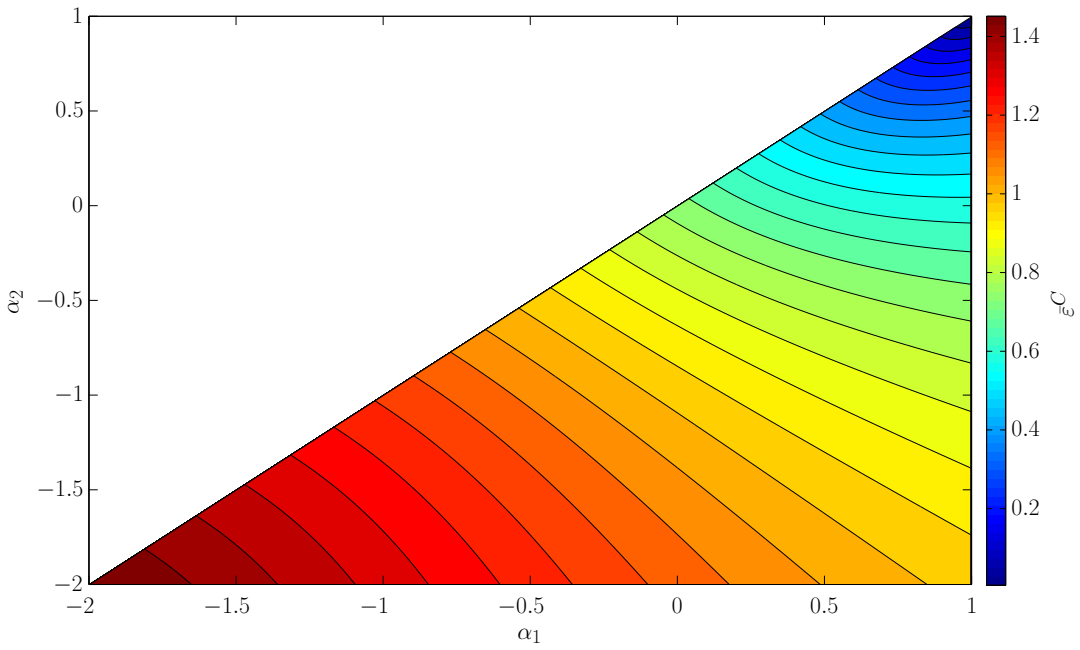

Fig. 14.14. Oyane.

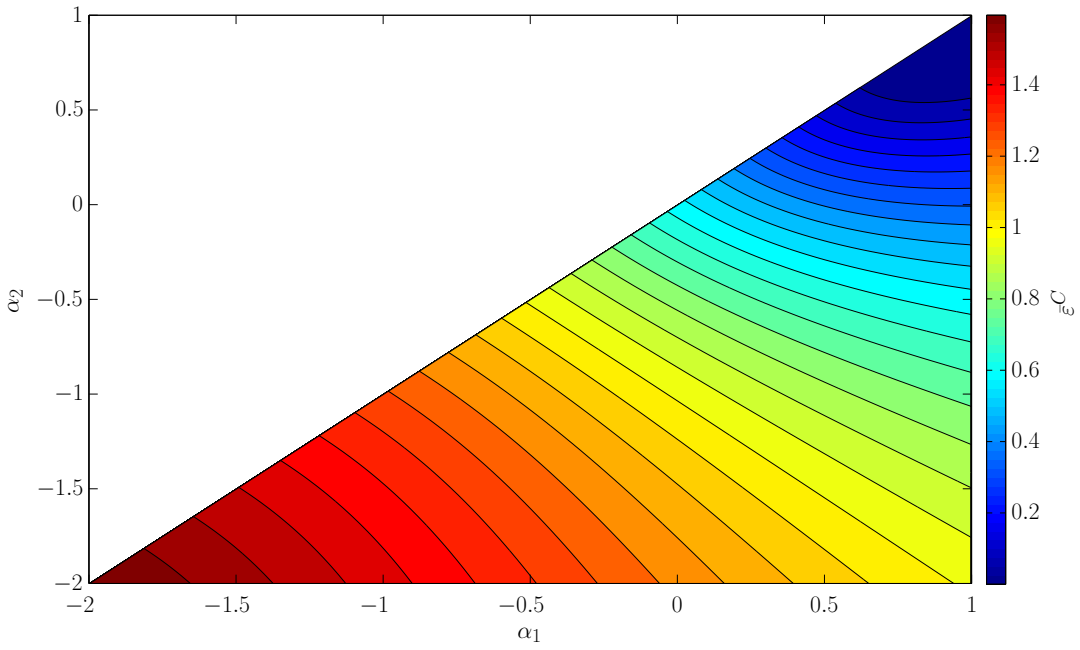

Fig. 14.15. Rice & Tracey.

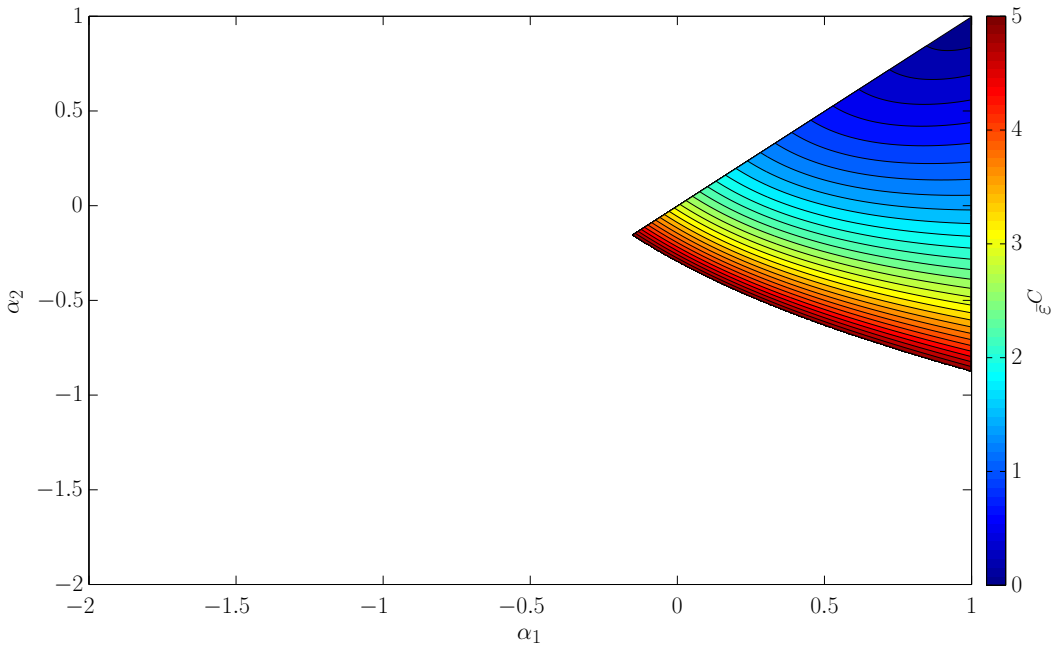

Fig. 14.16. Ayada.

From Fig. 14.13-Fig. 14.16 the predicted forming fracture limit is seen. It is noticed that Oyane and Rice & Tracey are very similar, as was also found in 7.3.7. For the Ayada criterion, only fracture strains less than 5 are plotted. As it was found for the plane stress case, the Ayada criterion predicts infinite formability when approaching pure shear stress state.

The slope independent damage criterion, Eq. 14.24, drawn for two different values of a, is seen in Fig. 14.17.

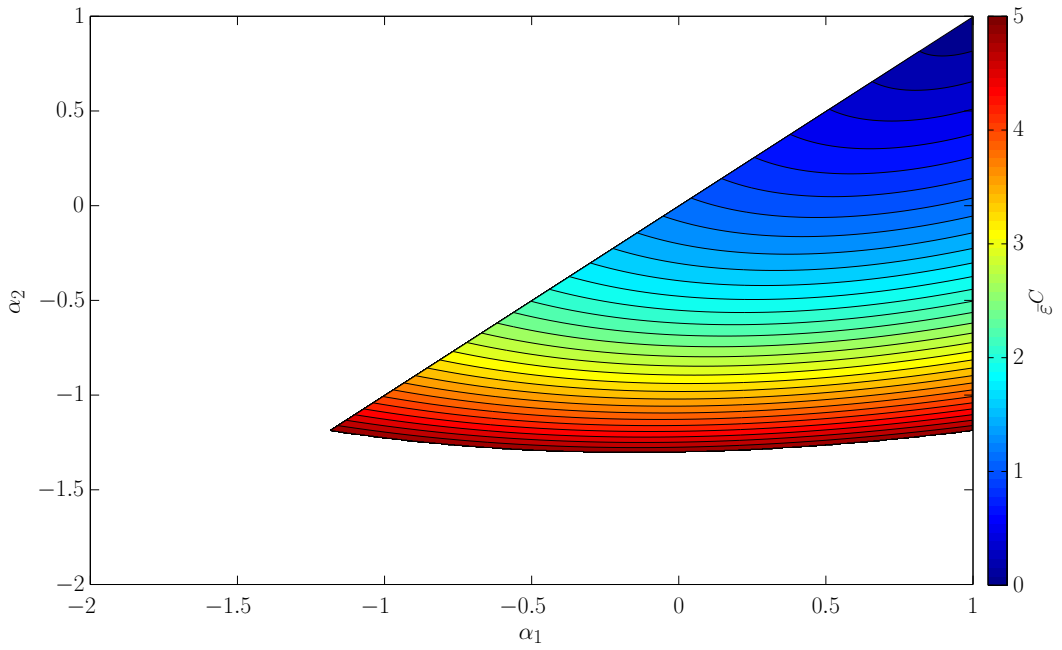

(a) $a = -\frac{3}{4}$

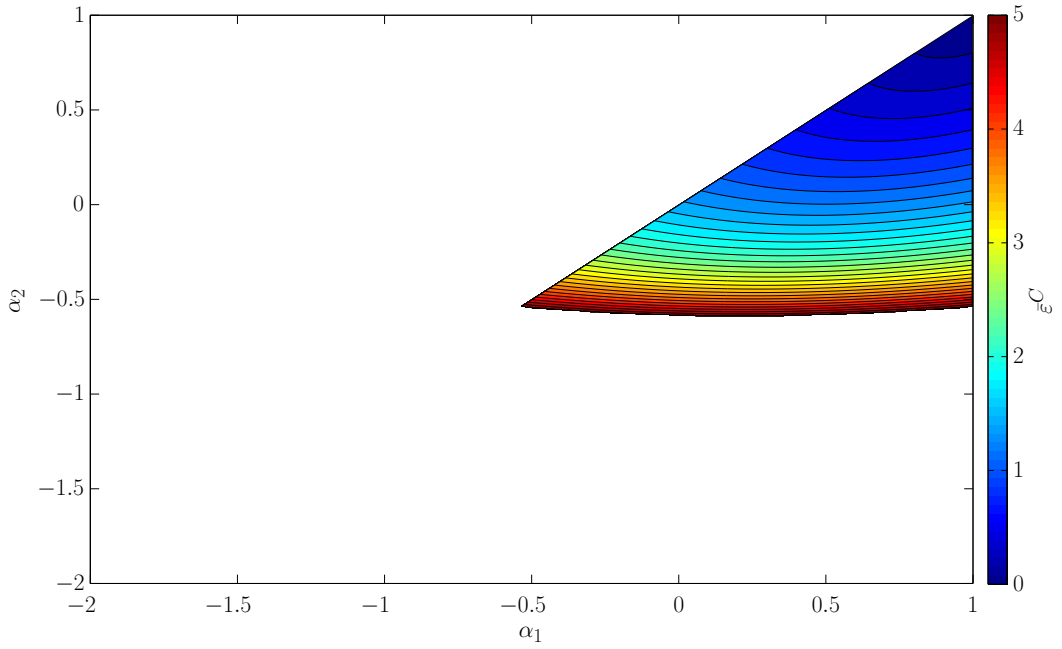

(b) $a = -1$

Fig. 14.17. Slope independent damage criterion with different values of the slope of the forming fracture limit line a.

Again only fracture strains less than 5 are plotted. It is seen that the criterion starts to be somewhat similar to the Ayada criterion in terms of stress range with a large formability ($\bar{\varepsilon}^{pl} > 5$). However it is also seen that isolines of same formability lie more horizontally for decreasing a. For the Ayada criterion, lines of equal formability are more inclined.

14.7 Proposal for a new damage criterion

It was noticed in Section 14.3 that the normalized Cockcroft & Latham criterion predicted a constant value of damage C if the slope of the forming fracture limit line was equal to -1/2. It was also noticed that the Ayada criterion gave a constant damage value C if the slope of the fracture line was equal to -1. Both of these slopes may be encountered in metal forming operations as seen in Fig. 7.5. In order to couple the two criteria into a single, general one, a common damage value C at fracture is assumed.

The damage value may be evaluated at the intersection point between the two curves. As previously mentioned, this point could appear for plane strain tension or for uniaxial tension. Based on the different forming fracture limit diagrams examined by the author, it seems most likely that the shift occurs for uniaxial tension. The normalized Cockcroft & Latham criterion and the Ayada criterion are therefore both evaluated for uniaxial tension:

$$C_{Cockcroft\&Latham} = \int \frac{\sigma_1}{\bar{\sigma}} d\bar{\varepsilon}^{pl} = \int 1 d\bar{\varepsilon}^{pl} \tag{14.45}$$

$$C_{Ayada} = \int \frac{\sigma_m}{\bar{\sigma}} d\bar{\varepsilon}^{pl} = \int \frac{1}{3} d\bar{\varepsilon}^{pl} \tag{14.46}$$

Since both criteria are integrated to the same final value $\bar{\varepsilon}^C$ it can be seen that the two criteria do not predict the same value C at fracture, as would be preferable. The author suggests the following uncoupled ductile damage criterion based on the principal stresses σ_1, σ_2 and σ_3, when positive:

- If $\sigma_1 \geq \sigma_2 \geq \sigma_3 > 0$

$$C = \int \frac{\sigma_1 + \sigma_2 + \sigma_3}{\bar{\sigma}} d\bar{\varepsilon}^{pl} \tag{14.47}$$

- If $\sigma_1 \geq \sigma_2 > 0$ and $\sigma_3 \leq 0$

$$C = \int \frac{\sigma_1 + \sigma_2}{\bar{\sigma}} d\bar{\varepsilon}^{pl} \tag{14.48}$$

- If $\sigma_1 > 0$ and $\sigma_3 \leq \sigma_2 \leq 0$

$$C = \int \frac{\sigma_1}{\bar{\sigma}} d\bar{\varepsilon}^{pl} \tag{14.49}$$

- If $0 \geq \sigma_1 \geq \sigma_2 \geq \sigma_3$

$$C = \int 0 d\bar{\varepsilon}^{pl} = 0 \tag{14.50}$$

It is seen that this damage criterion predicts the same value of C for fracture lines having a slope of -1/2 or -1. C can therefore be viewed as a material property independent of loading. It may be dependent on temperature, thermal hardening, strain rate etc.

A plot of the suggested criterion is seen in Fig. 14.18 with $\alpha_1 = \frac{\sigma_2}{\sigma_1}$ and $\alpha_2 = \frac{\sigma_3}{\sigma_1}$.

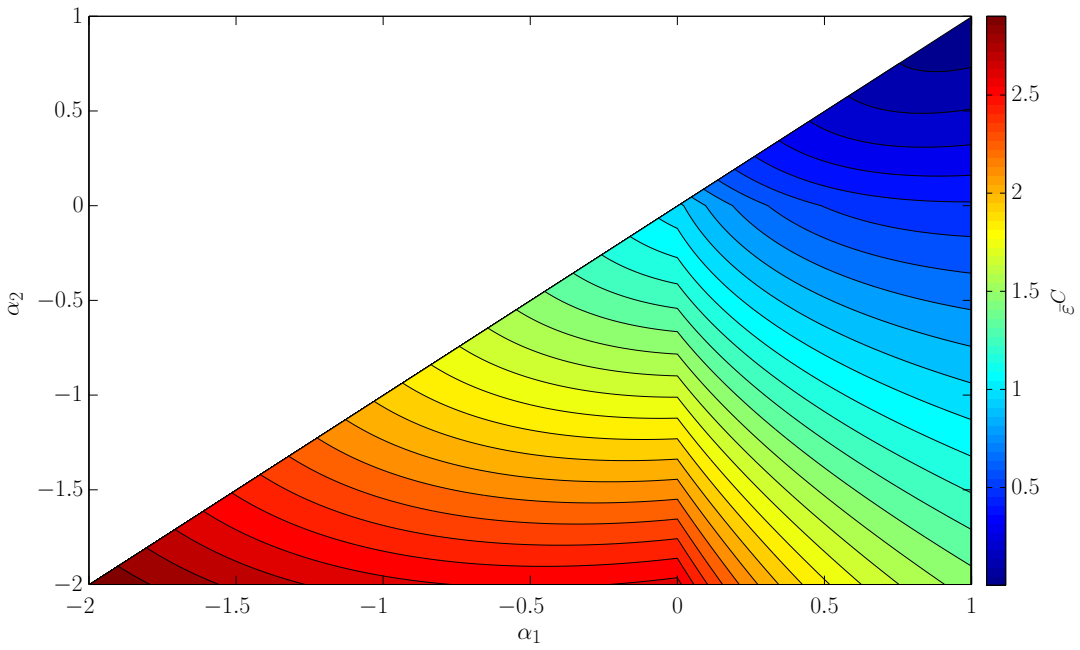

Fig. 14.18. Principal stress damage criterion.

A physical motivation for defining the criterion in terms of principal stresses stems from the observation that growing cracks in a material tend to grow in a direction perpendicular to the applied normal stresses according to Anderson [4] p. 81. The influence of crack growth direction will be explained more elaborate in the following.

14.8 Crack growth predicted by linear elastic fracture mechanics

In the following comparison between ductile damage and linear elastic fracture mechanics is done. Although being substantially different in nature, the linear elastic fracture mechanics offers closed form solutions for crack growth, thus giving some indication of the kinematics of cracks growing in a solid. The analysis shall only be viewed as a qualitative hypothesis.

First a comparison of uniaxial tension and pure shear is performed in order to address which loading is more severe regarding fracture. It is assumed that both stress states give rise to the same effective von Mises stress. The body being loaded is assumed to contain a through thickness crack of length $2a$, see Fig. 14.19. Plane stress is assumed.

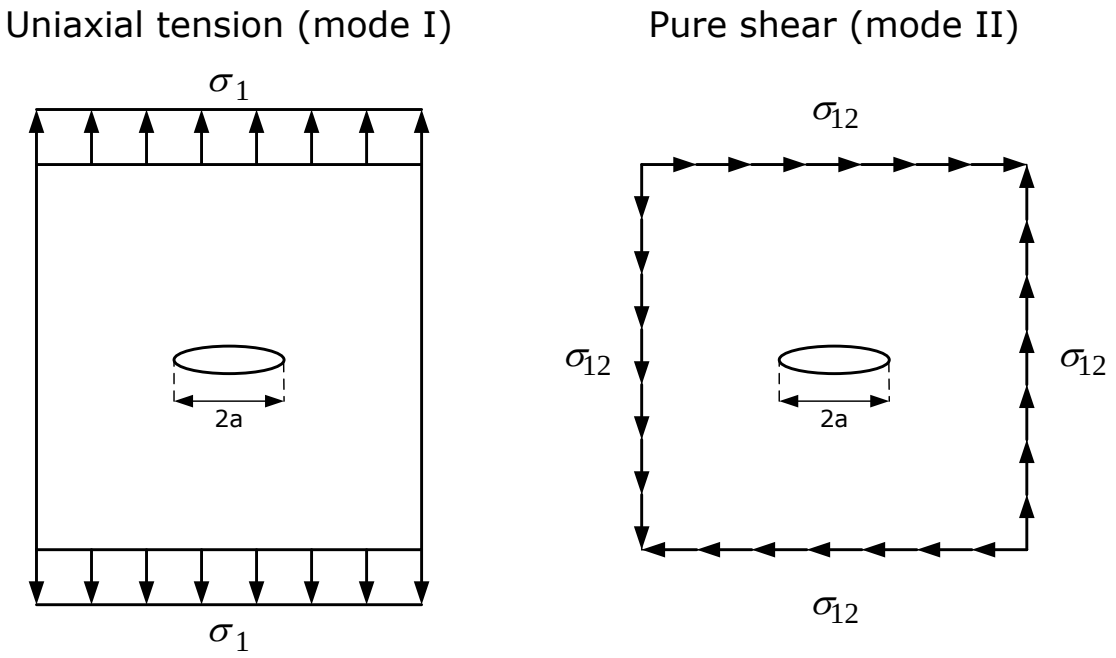

Fig. 14.19. Loading of body with through thickness crack.

- Uniaxial tension

$$\bar{\sigma} = \sigma_1 \tag{14.51}$$

- Pure shear

$$\bar{\sigma} = \sqrt{3}\sigma_{12} \tag{14.52}$$

Setting the expressions equal to one another yields:

$$\sigma_{12} = \frac{\sigma_1}{\sqrt{3}} \tag{14.53}$$

Solutions for the stress intensity factor K are given in Sundström [95] p. 239:

$$K_I = \sigma_1\sqrt{\pi a} \tag{14.54}$$

$$K_{II} = \sigma_{12}\sqrt{\pi a} = \frac{\sigma_1\sqrt{\pi a}}{\sqrt{3}} = \frac{K_I}{\sqrt{3}} \tag{14.55}$$

As seen, normal stresses result in a larger value of the stress intensity factor when loading to same effective von Mises stress, thus indicating earlier fracture for Mode I loading (in-plane normal stress) than mode II loading (in-plane shear).

It is noticed that when evaluating the damage criterion proposed for both uniaxial tension and pure shear, resulting in the same effective von Mises stress, one obtains:

$$C_I = \int \frac{\sigma_1}{\bar{\sigma}} d\bar{\varepsilon}^{pl} = \int 1 d\bar{\varepsilon}^{pl} \tag{14.56}$$

$$C_{II} = \int \frac{\sigma_1}{\bar{\sigma}} d\bar{\varepsilon}^{pl} = \int \frac{\sigma_{12}}{\bar{\sigma}} d\bar{\varepsilon}^{pl} = \int \frac{1}{\sqrt{3}} d\bar{\varepsilon}^{pl} = \frac{C_I}{\sqrt{3}} \tag{14.57}$$

It is noticed that the ratio of predicted ductile damage C_I/C_{II}, when loading to the same effective plastic strain, is the same as the ratio of the stress intensity factors K_I/K_{II}.

14.8.1 Crack growth in uniaxial tension

In the following is studied how a crack grows when being loaded by an external stress, when the crack is not perpendicular to the normal direction of the stress as it was assumed for mode I loading in Fig. 14.19. Such a situation is seen in Fig. 14.20.

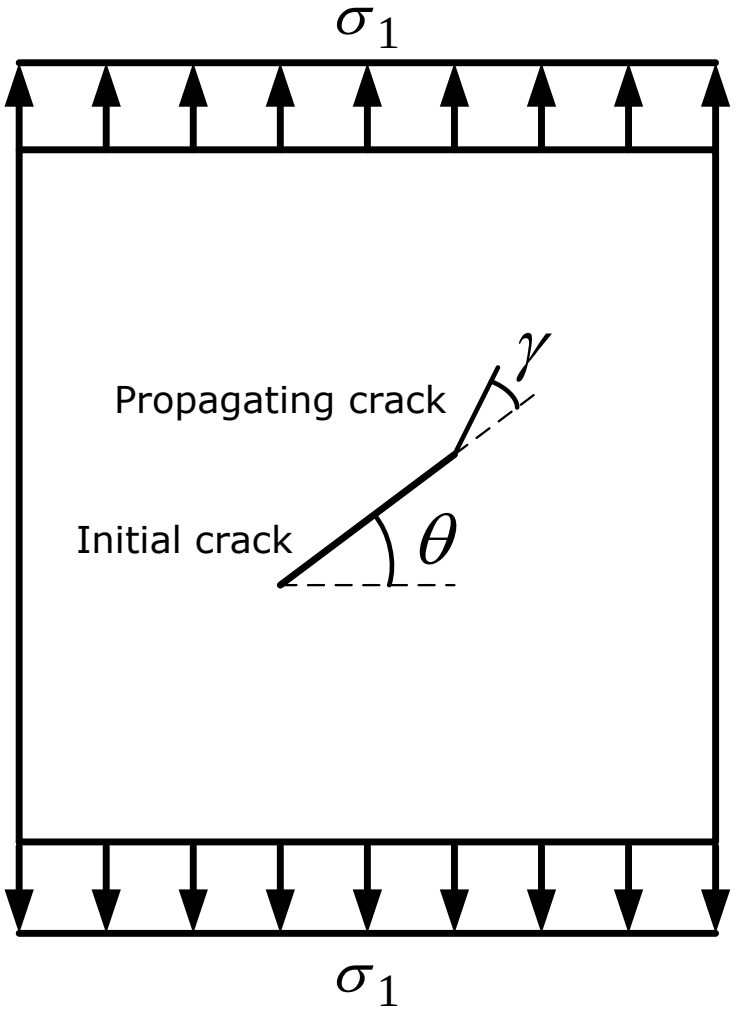

Fig. 14.20. Inclined crack growth in uniaxial tension.

In Fig. 14.20 an initial crack form the angle θ with the direction perpendicular to the loading direction. Due to the loading, the crack grows. The propagating crack then forms the angle γ with the initial crack. A solution for the preferred crack growth direction γ,

as a function of initial crack orientation θ, is given in Anderson [4] p. 81-84 by finding the angle γ^*, which maximizes the energy release rate G.

The computational procedure is as follows:

- First compute K_{Io}, which is the stress intensity factor when $\theta = 0$.
- Compute K_I and K_{II} given by:

$$K_I = K_{Io} \cos^2 \theta \tag{14.58}$$

$$K_{II} = K_{Io} \cos \theta \sin \theta \tag{14.59}$$

- Compute the coefficients C_{11}, C_{12}, C_{21} and C_{22} given by:

$$C_{11} = \frac{3}{4} \cos\left(\frac{\gamma}{2}\right) + \frac{1}{4} \sin\left(\frac{3\gamma}{2}\right) \tag{14.60}$$

$$C_{12} = -\frac{3}{4} \left[\sin\left(\frac{\gamma}{2}\right) + \sin\left(\frac{3\gamma}{2}\right)\right] \tag{14.61}$$

$$C_{21} = \frac{1}{4} \left[\sin\left(\frac{\gamma}{2}\right) + \sin\left(\frac{3\gamma}{2}\right)\right] \tag{14.62}$$

$$C_{22} = \frac{1}{4} \cos\left(\frac{\gamma}{2}\right) + \frac{3}{4} \cos\left(\frac{3\gamma}{2}\right) \tag{14.63}$$

- Compute the local stress intensity factors k_I and k_{II}:

$$k_I = C_{11} K_I + C_{12} K_{II} \tag{14.64}$$

$$k_{II} = C_{21} K_I + C_{22} K_{II} \tag{14.65}$$

- Since the energy release rate of the propagating crack is given by $G(\gamma) = \dfrac{k_I^2(\gamma) + k_{II}^2(\gamma)}{E}$, where E is Young's modulus, the maximum energy release rate occurs, when k_I has a maximum and k_{II} is zero:

$$G_{max} = \frac{k_I^2(\gamma^*)}{E} \tag{14.66}$$

where γ^* is the propagation angle of the growing crack. A plot of the propagation angle, as a function of the initial crack orientation angle θ, is given in Fig. 14.21.

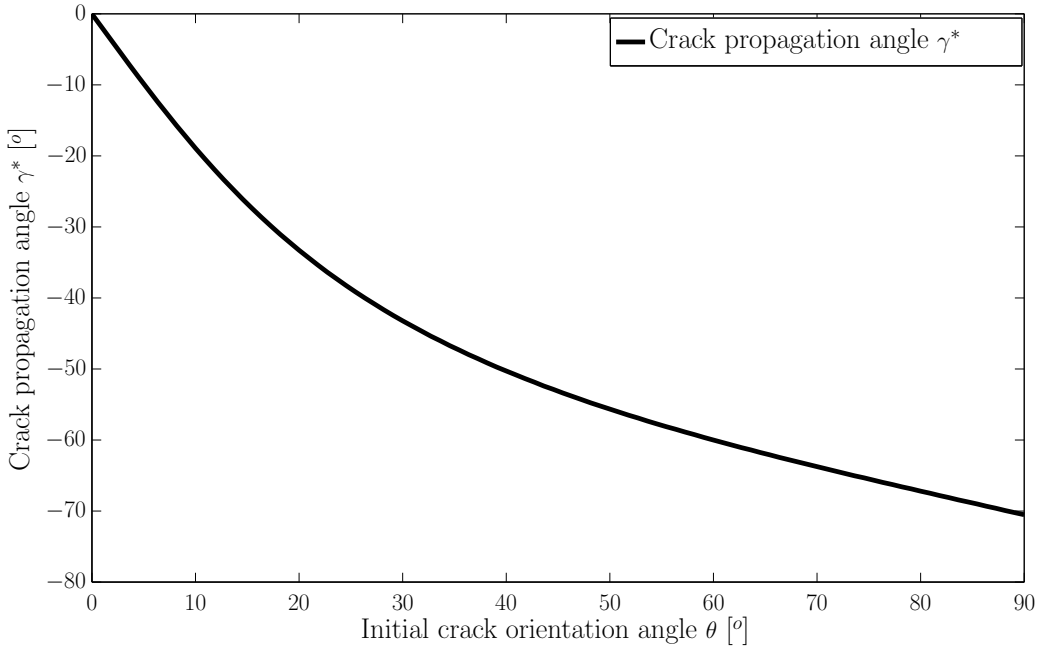

Fig. 14.21. Propagation angle of crack tip growth as function of initial crack orientation angle.

It is seen from Fig. 14.21 that the crack growth direction tends to be transverse to the initial crack orientation for most initial crack angles θ. Therefore it seems to the author reasonable to assume that after some crack growth, the resulting crack will tend to align perpendicular to the applied stress direction. The principle is seen schematically in Fig. 14.22.

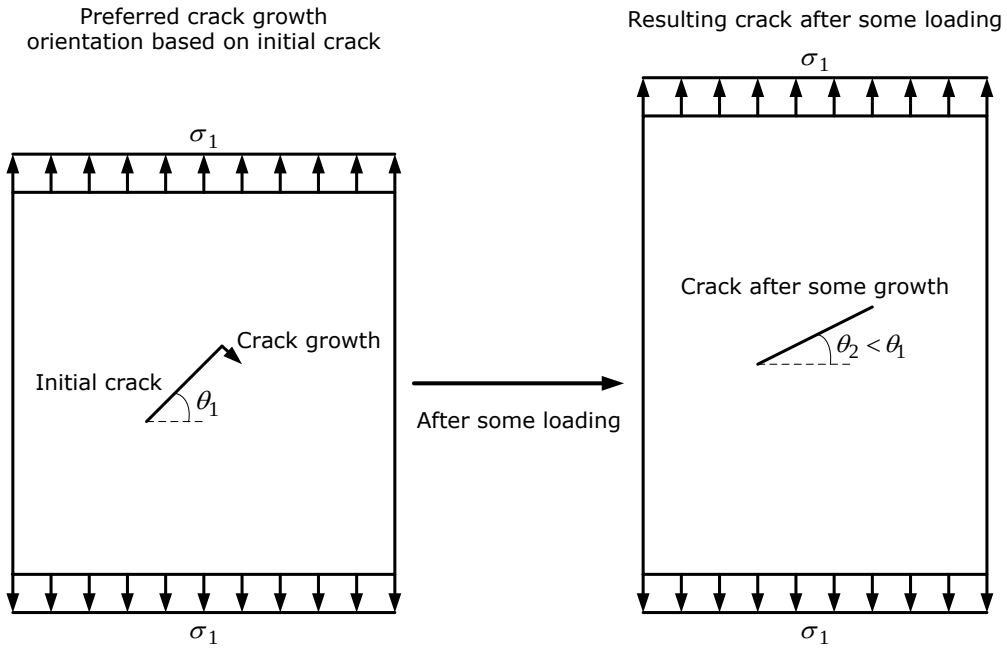

Fig. 14.22. Resulting crack due to crack tip propagation.

Fig. 14.22 shows a crack with the initial orientation θ_1. The crack growth direction is transverse to the initial crack direction, which can be calculated from the previously described procedure. Qualitatively the crack growth direction will be as indicated. After some loading, a larger crack will be established comprising both the initial crack and the developed part due to crack growth. If one represents this larger, kinked crack by a simple line model, this crack will have an orientation $\theta_2 < \theta_1$, hence the crack tends to align perpendicular to the direction of applied stress. Thereby the crack eventually only experiences mode I fracture, which is governed by the principal stress σ_1.

14.8.2 Crack growth in biaxial loading

Solutions, based on linear elastic fracture mechanics, of crack growth orientation for biaxial loading, are also available in Anderson p. 84-85.

The loading situation can be seen in Fig. 14.23.

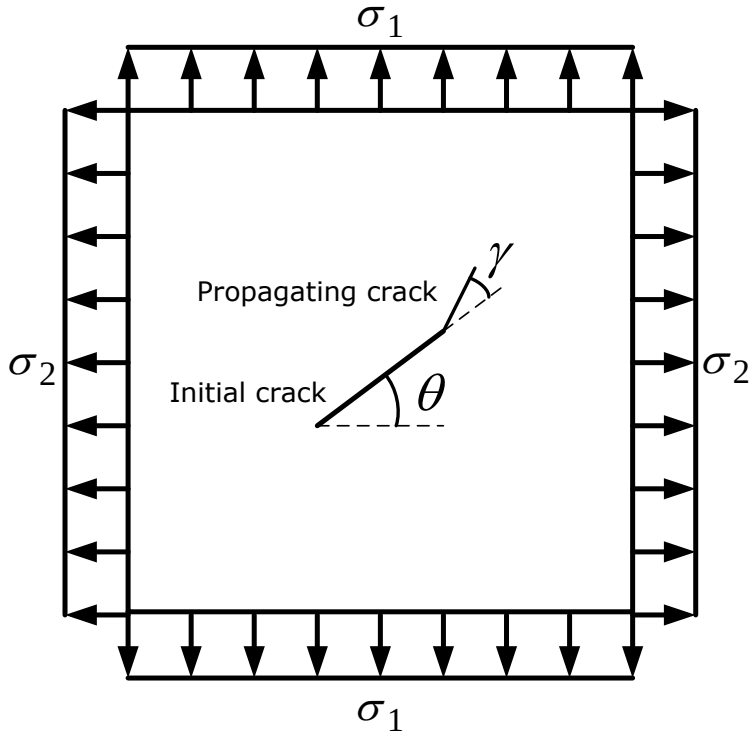

Fig. 14.23. Inclined crack growth in biaxial tension.

The energy release rate G is computed by the following procedure:

- The stress intensity factors K_1 and K_{II} are given by:

$$K_I = K_{Io}\left(\cos^2\theta + \alpha\sin^2\theta\right) \tag{14.67}$$

$$K_{II} = K_{Io}\left(\sin\theta\cos\theta\right)(1-\alpha) \tag{14.68}$$

where $\alpha = \dfrac{\sigma_2}{\sigma_1} \leq 1$.

- The local mode I and mode II stress intensity factors k_I and k_{II} are computed using the coefficients C_{11}, C_{12}, C_{21} and C_{22} as previously described.
- The energy release rate is computed by:

$$G(\gamma) = \frac{k_I^2(\gamma) + k_{II}^2(\gamma)}{E} \tag{14.69}$$

where γ is the crack propagation angle.

- The angle of propagation is found by maximizing the energy release rate:

$$G_{max} = \frac{k_I^2(\gamma^*)}{E} \tag{14.70}$$

where γ^* is the propagation angle of the growing crack.

A simple, qualitative investigation is performed to obtain some intuitive feeling of how the cracks grow when loaded in different biaxial stress states. The following assumptions are made: The Young's modulus E is set equal to unity for all computations. The purpose is not to evaluate any specific material but to obtain some general knowledge of the trends governing linear elastic crack growth. The material is assumed to be loaded to the von Mises yield stress, which is set equal to 1, hence:

$$\bar{\sigma} = \sqrt{\sigma_1^2 + \sigma_2^2 - \sigma_1\sigma_2} = \sqrt{1 - \alpha + \alpha^2}\sigma_1 = 1 \Leftrightarrow \sigma_1 = \frac{1}{\sqrt{1 - \alpha + \alpha^2}} \tag{14.71}$$

σ_1 is utilized when computing K_{Io}.
The following stress ratios are applied: $\alpha = \dfrac{\sigma_2}{\sigma_1} = [-2.0,\ -1.5,\ -1.0,\ 0.0,\ 0.25,\ 0.5,\ 1.0]$
The crack propagation angle γ^* is computed for the different initial crack orientations and stress ratios to obtain the preferred growth direction. This is seen in Fig. 14.24.

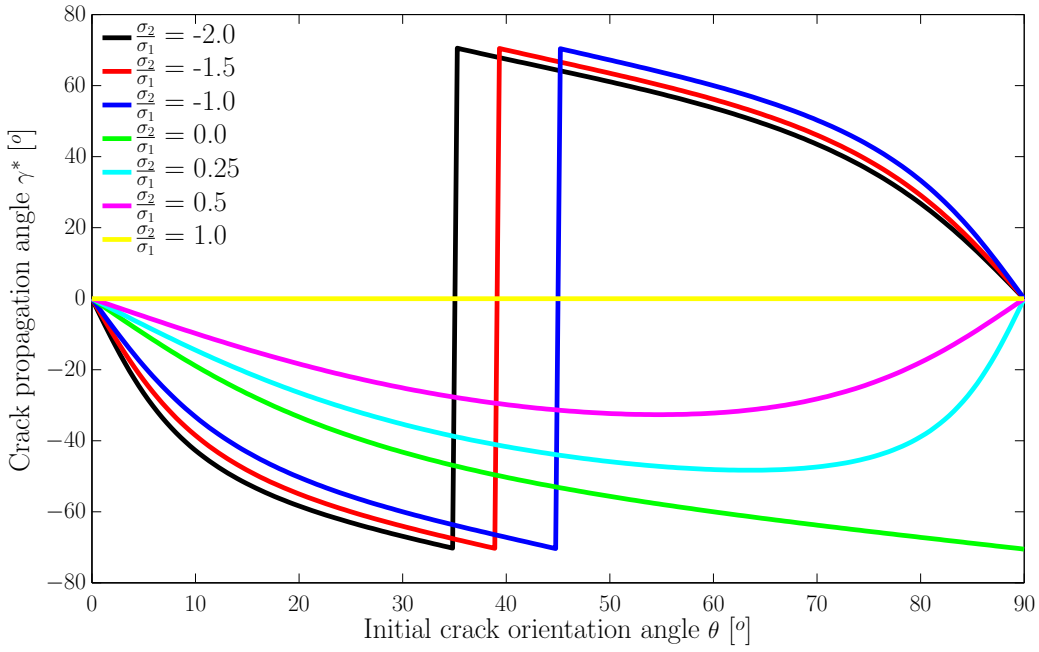

Fig. 14.24. Crack growth direction.

Several interesting observations can be made from Fig. 14.24.

It is seen that when applying a negative stress ratios, implying $\sigma_2 < 0$, the crack growth direction divides depending on the initial crack orientation. If the initial crack orientation is smaller than approximately 45°, the cracks grow in negative direction. Using the same argumentation as in 14.8.1, this implies that these cracks will tend to become perpendicular to the applied normal stress σ_1. On the other hand cracks that are initially having an inclination larger than approximately 45°, will tend to align in a direction parallel to σ_1. Since $\sigma_2 < 0$, these cracks will then not contribute to fracture, hence the process is canceling out an increasing amount of the initial cracks when decreasing the stress ratio α.

If however the stress ratio is positive, hence $\sigma_2 > 0$, it is seen that there is a tendency for all cracks, except the ones with initial orientation of 0° or 90°, to align in a direction perpendicular to the largest applied stress σ_1, thus increasing the onset of fracture because more cracks become loaded in pure mode I. Since both σ_1 and σ_2 are positive, it is expected that the stress intensity factors are larger than when σ_2 is negative, hence fracture happens earlier.

It is also interesting to notice the discontinous behaviour of the crack growth direction for negative stress ratios ($\alpha < 0$).

The principle of aligning cracks, depending on stress ratio α, can be seen in Fig. 14.25.

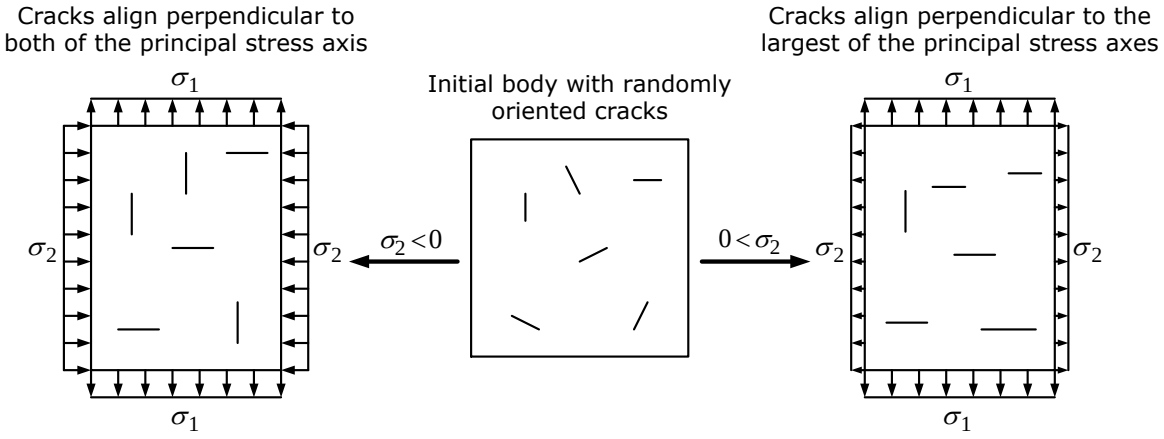

Fig. 14.25. Crack alignment depending on σ_2 being compressive or tensile.

The proposed hypothesis regarding crack growth direction suggests a physical mechanism responsible for the differences in formability observed in Kuhn et al. [62] and Vujovic & Shabaik [100], depending on the stresses applied.

14.9 Conclusion

A mathematical analysis of some uncoupled ductile damage criteria has been performed. It is shown that the agreement between the forming fracture limit diagram of Kuhn et al. [62] and the formability diagram of Vujovic & Shabaik [100] seems to express the same physical phenomenon.

It is shown that the normalized Cockcroft & Latham criterion predicts a constant damage value for fracture, if the forming limit line has a slope of -1/2 in the principal

strain diagram. If the slope is -1, the Ayada criterion predicts a constant value of damage at fracture. Both criteria are independent of the strain path.

A damage criterion for plane stress is derived, which is independent of the slope of the fracture line.

A damage criterion is proposed, which predicts a constant damage value at fracture for a bilinear forming fracture line with the slopes -1/2 and -1.

A physical mechanism is proposed qualitatively explaining why different degrees of formability are to be expected depending on the stress state applied.

15 Conclusions and future work

15.1 Conclusion

In the present thesis, a number of defects occurring due to casting of large ingots have been presented based on literature survey. It is noticed that many different phenomena can occur, an that their origin may be of both micro- and macro-scale. Some of the defects occurring when casting an ingot may be subsequently healed by hot forging the cast ingot. A number of guidelines, based on older analysis methods like the slipline or the upper bound method, as well as guidelines from practical experience have been presented. Due to the findings regarding curing of defects by hot forging, emphasis was put on investigating the influence of the lower die angle on the soundness of the final ingot after the forging process. A literature study on how to quantify damage during forging was performed with its main emphasis on uncoupled ductile damage models. Based on experimental findings presented in the literature, the normalized Cockcroft & Latham criterion was selected for modelling uncoupled ductile damage in the ingot forging process.

Physical experiments forging down scaled model ingots made of lead were performed. The lead billets, some with drilled centreline holes to mimic centreline porosities, were compressed using a die tool enabling the utilization of different lower die angles. The experiments showed that marked differences in centreline hole closure were occurring depending on the lower die angle. A pixel recognition software was developed in order to quantify the cross-sectional area reduction of the drilled centreline holes due to the forging operation. Numerical computation of the final area size was performed using both an in-house 2D FEM program developed by the author, and the commercial FEM program DFORM-3D®. 2D plane strain was found to model the loads in the forging process reasonably well whereas a 2D plane stress model gave reasonable prediction of centreline hole closure, which was measured at the billet ends. It was found that 2D models are sufficiently accurate for reductions up to approximately 10-15%. 3D FEM simulations gave good agreement between measured and computed centreline hole closure and loads. However the computational time was approximately 5 times longer than for the 2D models.

During the development of the 2D FEM code, a derivation of the finite element equations based on the static force equilibrium equations and the Galerkin method was developed. This is a different approach than what is most often encountered in text books regarding the finite element flow formulation, where the finite element equations are derived based on variational methods and the equilibrium of virtual work rate. The author finds the variational method to have little intuitive character and therefore prefers utilization of a physical principle like force equilibrium as foundation for deriving the finite element equations.

Based on the successful utilization of 2D FEM models in predicting centreline hole closure, a number of simulations using different ingot material hardening behaviours and

two different friction factors were performed. The purpose was to investigate, whether the lower die angle, at which maximum centreline hole closure occurs, was affected by ingot material and the magnitude of friction. It was found that for all the different material hardening behaviours investigated, maximum closure, for a given constant degree of compression, was occurring for a constant lower die angle of approximately 130°-140°. Friction was found only to have minor influence when utilizing very inclined lower dies. The forging load is greatly affected by the ingot material properties.

Since the ingot forging operation is comprised by a large number of forging strokes, multi stroke forging operations was also modelled numerically using the commercial software program DEFORM®. The lower die angles investigated were ranging from 60° to 180° with 30° intervals. Two different approaches were utilized, either using uncoupled ductile damage or using a porous plasticity model. When using the uncoupled ductile damage model, an optimum lower die angle of 120° was found. The evaluation was based on a primitive average of damage and effective plastic strain. The utilization of a porous plasticity model predicted 90° to be the optimum followed closely by the other lower die angles larger than 90°. Again the evaluation was based on a primitive average of relative density and effective plastic strain. It is noticed that the utilization of a solid ingot and multi stroke forging operations have shifted the optimum lower die angle towards smaller angles as compared to the optimum found using single stroke compression of an ingot containing a centreline porosity. It was furthermore noticed, that at least four compressions where often required before a stable ranking of the lower die angles emerged.

A preliminary investigation of the influence of feed size was performed using lower die angles of 120° and 180°. Feed sizes were 400mm or 800mm. Damage was modelled using porous plasticity with simultaneous computation of uncoupled normalized Cockcroft & Latham damage. When evaluating damage based on relative density alone, all the different combinations of lower die angles and feed sizes were found to result in an approximately fully dense cross-section of the ingot. This is in contrast to most recommendations, where a relatively small feed size should be used and where a 180° lower die should be unsuited for forging. When evaluating the simulations, considerable shear straining along the centreline of the ingot was noticed. Since shear strains are not causing damage according to the porous plasticity model, the shear strains were not taken into account when evaluating damage based on porous plasticity. However the shear strains are taken into account by the normalized Cockcroft & Latham criterion, which suggests such a criterion should be included when evaluating damage in ingot forging. When adopting this damage criterion, the simulations indicated that the small feed size and the 120° lower die gave the best results, in accordance with the generally accepted characteristics of ingot forging.

In order to further understand why the normalized Cockcroft & Latham criterion is found to be suitable to model ductile damage in bulk forming operations, an analysis of the criterion seen in relation to forming fracture limit diagrams of Kuhn et al. [62] and Vujovic & Shabaik [100] was made. It was found that for a slope of the fracture limit line of -1/2, the normalized Cockcroft & Latham criterion predicts a constant damage value at fracture. However a slope of the fracture line of -1 is also encountered in the forming fracture limit diagram. For this slope, it was found that the Ayada criterion gives a constant damage value. A new damage criterion was proposed predicting the same damage value along the two formability lines if the two formability lines meet when intersecting the strain path line corresponding to pure tension in the principal strain

forming fracture limit diagram. A physical reasoning, based on the growth of cracks, as to why differences in the fracture limit are to be expected depending on the applied stresses was also presented.

15.2 Future work

Four major fields of interest for further investigation of the ingot forging process can be pointed out.

Different die geometries should be investigated

Only variations of a very simple die geometry, namely a v-shaped die, where investigated. It could therefore be of interest to investigate whether a more advanced die layout could result in more sound forgings.

Linking of forging simulations to casting simulations

Only very simple representations of initial defects in the ingot, such as a cylindrical hole along the centreline or a porosity distribution constant along the centreline of the ingot were applied. Both assumptions must be viewed as ideal cases since in reality the distributions of casting defects are 3-dimensional. Therefore linking between casting simulations and forging simulations would be beneficial. Here, two challenges are foreseen: often it is difficult to link two different softwares due to differences in file formats, and it requires a research group both skilled within numerical casting and numerical forging modelling.

Damage modelling & quantification

During the investigation, it was realized that quantification of damage due to forging is a somewhat immature science. There is a general lack of experimental formability diagrams, for plane stress stretching as well as 3-dimensional stress states. The challenge of including high-temperature effects like welding of porosities remains a novel scientific field to be investigated. A primitive ranking scheme for evaluating different die geometries based on an average of damage and effective plastic strain was suggested. Further development is needed for the quantification of the soundness of the final forgings. For instance instead of assuming larger plastic strain to be more beneficial regarding microstructure, actual models of microstructure should be utilized. Here it should be mentioned that for instance DEFORM® has the possibility to include microstructure in the simulations.

Bibliography

[1] **Altan, T.**, *Cold and Hot Forging: Fundamentals and Applications*, ASM International, 2005, ISBN 9781615030941.

[2] **Altan, T.**, **Henning, H.J.**, **Sabroff, A.M.**, *The Use of Model Materials in Predicting Forming Loads in Metalworking*, Journal of Engineering for Industry, vol. 92 (2) p. 444–451, 1970.

[3] **Amontons, G.**, *Historie de l'Académie Royale des Sciences avec Mémoires de Mathématique et de Physique*, 1699.

[4] **Anderson, T.L.**, *Fracture Mechanics - Fundamentals and Applications*, Taylor & Francis Group, 3. ed., 2005, ISBN 978-0-8493-1656-2.

[5] **ASM Handbook Vol. 14**, *Forming and Forging*, vol. 14 of *ASM Handbook*, ASM International, 9. ed., 1998, ISBN 0-87170-007-7, electronic version.

[6] **ASM Handbook Vol. 15**, *Casting*, vol. 15 of *ASM Handbook*, ASM International, 9. ed., 1998, ISBN 0-87170-007-7, electronic version.

[7] **ASM Handbook Vol. 4**, *Heat Treatment*, vol. 4 of *ASM Handbook*, ASM International, 10. ed., 1998, ISBN 0-87170-379-3, electronic version.

[8] **Atkins, A.G.**, *Encyclopedia of Materials: Science and Technology*, chap. Metal forming: Formability, p. 5401–5408, Elsevier, 2001, ISBN 0-08-043152-6.

[9] **Ayada, M.**, **Higashino, T.**, **Mori, K.**, *Central bursting in extrusion of inhomogeneous materials*, Proceedings of the First ICTP. Adv. Technol. of Plast., vol. 1 p. 553–558, 1984.

[10] **Bathe, K.J.**, *Finite Element Procedures*, Prentice Hall, 1996, ISBN 0-13-301458-4.

[11] **Bay, N.**, **Gerved, G.**, *Tool/workpiece interface stresses in simple upsetting*, Journal of Mechanical Working Technology, vol. 14 p. 263–282, 1987.

[12] **Bridgman, P.W.**, *Effects of high hydrostatic pressure on the plastic properties of metals*, Rev. Mod. Phys. (USA), vol. 17 p. 3–14, 1945.

[13] **Brozzo, P.**, **Deluca, B.**, **Rendina, R.**, *A new method for the prediction of formability limits of metal sheets*, Sheet Metal Forming and Formability - Proceedings of the Seventh Biennial Congress of International Deep Drawing Research Group, 1972.

[14] **Budiansky, B.**, **Hutchinson, J.W.**, **Slutsky, S.**, *Void growth and collapse in viscous solids*, p. 13–45, Pergamon Press, 1982.

[15] **Campbell, G.T.**, **Abrahamson, E.P.**, **Grant, N.J.**, *The Recrystalliation Behaviour of an Austenitic Stainless Steel Ingot Structure Due to Hot Deformation*, Metallurgical Transactions, vol. 5 p. 1875–1881, 1974.

[16] **Cardarelli, F.**, *Materials Handbook - A concise desktop reference*, Springer-Verlag London Ltd., 1. ed., 2008, ISBN 978-0-470-01514-8.

[17] **Christiansen, P.**, **Hattel, J.H.**, **Bay, N.**, **Alves, L.M.**, **Martins, P.A.F.**, *Open Die Forging of Large Shafts with Defects - Physical and Numerical Modelling*, Key Engineering Materials, vol. 2443 (554) p. 2145–2155, 2013.

[18] **Christiansen, P.**, **Hattel, J.H.**, **Bay, N.**, **Martins, P.A.F.**, *Modelling of Damage During Hot Forging of Ingots*, STEELSIM 2013 - the 5th International Conference, 2013.

[19] **Christiansen, P.**, **Hattel, J.H.**, **Bay, N.**, **Martins, P.A.F.**, *Numerical optimization of die geometry in open die forging*, Proceedings of International Conference on Advanced Manufacturing Engineering and Technologies (NEWTECH 2013), vol. 2 p. 59–68, 2013.

[20] **Christiansen, P.**, **Hattel, J.H.**, **Bay, N.**, **Martins, P.A.F.**, *Physical modeling and numerical simulation of V-die forging ingot with central void*, Journal of Mechanical Engineering Science, vol. 228 p. 2347–2356, 2014.

[21] **Chu, C.C.**, **Needleman, A.**, *Void Nucleation Effects In Biaxially Stretched Sheets*, Journal of Engineering Materials and Technology, vol. 102 p. 249–256, 1980.

[22] **Cockcroft, M.C.**, **Latham, D.J.**, *Ductility and workability of metals*, Journal of the Institute of Metals, vol. 96 p. 33–39, 1968.

[23] **Cook, R.D.**, **Malkus, D.S.**, **Plesha, M.E.**, **Witt, R.J.**, *Concepts and Applications of Finite Element Analysis*, John Wiley & Sons Inc., 4. ed., 2002, ISBN 978-0-471-35605-9.

[24] **Coulomb, C.A.**, *Mémoires de Mathématique et de Physique de l'Académie Royale de Sciences*, 1785.

[25] **Culver, W.J.**, *On the existence and uniqueness of the real logarithm of a matrix*, Proceedings of the American Mathematical Society, vol. 17.5 p. 1146–1151, 1966.

[26] **Danckert, J.**, **Wanheim, T.**, *Slipline wax*, Experimental Mechanics, vol. 16 p. 318–320, 1976.

[27] **Drucker, D.C.**, *A more fundamental approach to plastic stress-strain relations*, Proceedings of the first U.S. congress of applied mechanics, American Society of Mechanical Engineers, vol. 18 p. 487–491, 1951.

[28] **Dunne, F.**, **Petrinic, N.**, *Introduction to Computational Plasticity*, Oxford U, 2005, ISBN 978-0-19-856826-1.

[29] **Eldén, L.**, **Wittmeyer-Koch, L.**, **Nielsen, H.B.**, *Introduction to Numerical Computation - analysis and MATLAB illustrations*, Studentlitteratur, 1. ed., 2004, ISBN 978-91-44-03727-1.

[30] **Embury, J.D.**, **Duncan, J.L.**, *Formability Maps*, Annual Review of Materials Science, vol. 11 p. 505–521, 1981, ISSN 00846600.

[31] **Erman, E.**, **Kuhn, H.**, **Fitzsimons, G.**, *Novel Test Specimens for Workability Testing*, Compression Testing of Homogeneous Materials and Composites, vol. 1983 p. 279–290, 1983.

[32] **Fields, D.S.**, **Bachofen, W.A.**, *Determination of strain hardening characteristics by torsion testing*, Proceedings of the American Society for Testing and Materials, vol. 57 p. 1259–1272, 1957.

[33] **Flemings, M.C.**, *Principles of control of soundness and homogenity of large ingots*, Scandinavian Journal of Metallurgy, vol. 5 p. 1–15, 1976.

[34] **Fredriksson, H.**, **Åkerlind, U.**, *Materials Processing during Casting*, John Wiley & Sons Ltd., 1. ed., 2006, ISBN 978-87-502-0969-0.

[35] **Freudenthal, A.M.**, *The inelastic behavior of engineering materials and structures*, John Wiley & Sons Ltd., 1. ed., 1950.

[36] **Goodwin, G.M.**, *Application of strain analysis to sheet metal forming problems in press shop*, Metallurgia Italiana, vol. 60 (8) p. 767–774, 1968, ISSN 00260843.

[37] **Gouveia, B.P.P.A.**, **Rodrigues, J.**, **Martins, P.A.F.**, *Technologia Mecânica - Vol. III Exercícios resolvidos*, vol. 3 of *Tecnologia da Deformacão Plástica*, Escolar Editora, 2 ed., 2011, ISBN 978-972-5592-321-4.

[38] **Gouveia, B.P.P.A.**, **Rodrigues, J.M.C.**, **Martins, P.A.F.**, *Fracture prediction in bulk metal forming*, Int. J. Mech. Sci., vol. 38 p. 361–372, 1996.

[39] **Green, A.P.**, *The compression of a ductile material between smooth dies*, Phil. Mag., vol. 42 p. 900–918, 1951.

[40] **Green, A.P.**, *On the use of hodographs in problems of plane plastic strain*, Journal of the Mechanics and Physics of Solids, vol. 2 (2) p. 73–80, 1954, ISSN 00225096.

[41] **Green, R.**, *A plasticity theory for porous solids*, Int. J. of Mech. Sci., vol. 14 (4) p. 215–224, 1972, ISSN 18792162.

[42] **Gurson, A.L.**, *Continuum Theory of Ductile Rupture by Void Nucleation and Growth: Part 1 - Yield Criteria and Flow Rules for Porous Ductile Media*, ASME Journal of Engineering Materials and Technology, vol. 99 p. 2–15, 1977.

[43] **Hattel, J.H.**, *Fundamentals of Numerical Modelling of Casting Processes*, Polyteknisk Forlag, 1. ed., 2005, ISBN 978-87-502-0969-0.

[44] **Hencky, H.**, *Über einige statisch bestimmte Fälle des Gleichgewichts in plastischen Körpern*, Z. Angew. Math. Mech., vol. 3 p. 241–251, 1923.

[45] **Hensel, A.**, **Spittel, T.**, *Kraft- und Arbeitsbedarf bildsamer Formgebungsverfahren*, VEB Deutscher Verlag für Grundstoffindustrie, Leipzig, 1978.

[46] **Hill, R.**, *The Mathematical Theory of Plasticity*, Clarendon Press, Oxford, 1950.

[47] **Hoff, N.J.**, *Approximate analysis of structures in the presence of moderately large creep deformations*, Quarterly of Applied Mathematics, vol. 12 p. 49–55, 1954.

[48] **Hollomon, J.H.**, *Tensile Deformation*, Transactions of the American Institute of Mining and Metallurgical Engineers, vol. 162 p. 268–290, 1945.

[49] **Hosford, W.F.**, **Caddell, R.M.**, *Metal Forming, Mechanics and Metallurgy*, Cambridge University Press, 4. ed., 2011, ISBN 978-1-107-00452-8.

[50] **Johnson, G.R.**, **Cook, W.H.**, *Fracture characteristics of three metals subjected to various strains, strain rates, temperatures and pressures*, Engineering Fracture Mechanics, vol. 21 (1) p. 31–48, 1985, ISSN 18737315.

[51] **Johnson, W.**, *Indentation and forging and action of Nasmyth's Anvil*, Engineer, vol. 205 (5328) p. 348–350, 1958.

[52] **Johnson, W.**, **Mellor, P.**, *Engineering Plasticity*, Van Nostrand Reinhold Company Ltd., 1973, ISBN 0442041519.

[53] **Kachanov, L.**, *Time of the rupture process under creep conditions*, Isv. Akad. Nauk. SSR. Otd Tekh. Nauk, vol. 8 p. 26–31, 1958.

[54] **Kalpakjian, S.**, **Schmid, S.R.**, *Manufacturing, Engineering and Technology*, Pearson Prentice Hall, 5. ed., 2006, ISBN 0-13-148965-8.

[55] **Kawaguchi, S.**, **Tsukada, H.**, **Suzuki, K.**, **Sato, I.**, **Onodera, S.**, *Manufacturing of Large and Integral-Type Steel Forgings for Nuclear Steam Supply System Components*, Steel Forgings, vol. 1986 p. 398–409, 1986.

[56] **Keeler, S.**, **Backofen, W.**, *Plastic instability and fracture in sheets stretched over rigid punches*, ASM Transactions, vol. 56 p. 25–48, 1963.

[57] **Kim, Y.D.**, **Cho, J.R.**, **Bae, W.B.**, *Efficient forging process to improve the closing effect of the inner void on an ultra-large ingot*, Journal of Materials Processing Technology, vol. 211 (6) p. 1005–1013, 2011, ISSN 09240136.

[58] **Kobayashi, S.**, **Oh, S.**, **Altan, T.**, *Metal forming and the finite element method*, Oxford University Press, 1. ed., 1989, ISBN 0-19-504402-9.

[59] **von Kármán, T.**, *Beitrag zur Theorie des Walzvorges*, Z. Angew. Math. Mech., vol. 5 p. 139–141, 1925.

[60] **Kudo, H.**, *Some analytical and experimental studies of axi-symmetric cold forging and extrusion*, Int. J. Mech. Sci., vol. 2 p. 102–127, 1960.

[61] **Kuhn, H.A.**, **Downey, C.L.**, *Deformation characteristics and plasticity theory of sintered powder materials*, International Journal of Powder Metallurgy, vol. 7 (1) p. 15–25, 1971.

[62] **Kuhn, H.A.**, **Lee, P.W.**, **Erturk, T.**, *Fracture criterion for cold forming*, Journal of Engineering Materials and Technology, vol. 95 (73) p. 213–218, 1973.

[63] **Landre, J.**, **Pertence, A.**, **Cetlin, P.R.**, **Rodrigues, J.M.C.**, **Martins, P.A.F.**, *On the utilisation of ductile fracture criteria in cold forging*, Finite Elements in Analysis and Design, vol. 39 (3) p. 175–186, 2003, ISSN 18726925.

[64] **Lange, K.**, *Massivumformung*, Springer, 2. ed., 1988.

[65] **Lee, B.**, **Mear, M.**, *Axisymmetric deformation of power-law solids containing a dilute concentration of aligned spheroidal voids*, Journal of the Mechanics and Physics of Solids, vol. 40 (8) p. 1805–1836, 1992, ISSN 00225096.

[66] **Lemaitre**, *A continuous damage mechanics model for ductile fracture*, Trans. ASME, J. Eng. Mater. Technol., vol. 107 (1) p. 83–89, 1985, ISSN 15288889.

[67] **Li, Y.**, **Onodera, E.**, **Chiba, A.**, *Friction Coefficient in Hot Compression of Cylindrical Sample*, Materials Transactions, vol. 51 (7) p. 1210, 2010, ISSN 13459678.

[68] **Ludwik, P.**, *Elemente der Technologishen Mechanik*, Springer Verlag, 1. ed., 1909.

[69] **Marciniak, Z.**, *Assessment of material formability*, Advanced Technology of Plasticity, vol. 1 p. 685–694, 1984.

[70] **McClintock, F.A.**, *A Criterion for Ductile Fracture by Growth of Holes*, Journal of Applied Mechanics, vol. 35 p. 363–371, 1968.

[71] **Melander, A.**, **Ståhlberg, U.**, *The effect of void size and distribution on ductile fracture*, International Journal of Fracture, vol. 16 (5) p. 431–440, 1980, ISSN 03769429, 15732673.

[72] **Meyer, L.W.**, **Herzig, N.**, **Halle, T.**, **Hahn, F.**, **Krueger, L.**, **Staudhammer, K.P.**, *A basic approach for strain rate dependent energy conversion including heat transfer effects: An experimental and numerical study*, Journal of Materials Processing Technology, vol. 182 p. 319–326, 2007, ISSN 09240136.

[73] **Nahshon, K.**, **Hutchinson, J.**, *Modification of the Gurson Model for shear failure*, European Journal of Mechanics / A Solids, vol. 27 p. 1–17, 2008, ISSN 18737285.

[74] **Nasmyth, J.**, *Improvements in forging iron*, Journal of The Franklin Institute, vol. 50 (6) p. 404–408, 1850.

[75] **Nielsen, C.V.**, **Zhang, W.**, **Alves, L.M.**, **Bay, N.**, **Martins, P.A.F.**, *Modeling of Thermo-Electro-Mechanical Manufacturing Processes*, Springer, 1. ed., 2013, ISBN 978-1-4471-4642-1.

[76] **Norton, F.H.**, *The Creep of Steel at High Temperatures*, McGraw-Hill, 1. ed., 1929.

[77] **Oh, S.I.**, **Chen, C.C.**, **Kobayashi, S.**, *Ductile Fracture in Axisymmetric Extrusion and Drawing - Part 2 Workability in Extrusion and Drawing*, Journal of Engineering for Industry, vol. 101 p. 36–44, 1979.

[78] **Oh, S.I.**, **T., W.W.**, **Park, W.W.**, *Application of the finite element method to P/M forming processes*, Advanced Technology of Plasticity 1987, vol. 2 p. 961–968, 1987.

[79] **Oyane, M.**, *Criteria of ductile fracture strain*, Bull. Jpn. Soc. Mech. Eng. (Japan) Bulletin of JSME, vol. 15 (90) p. 1507–1513, 1972.

[80] **Porter, D.A.**, **Easterling, K.E.**, **Sherif, M.S.**, *Phase Transformations in Metals and Alloys*, John Wiley & Sons Ltd., 3. ed., 2009, ISBN 978-1-4200-6210-6.

[81] **Prager, W.**, **Hodge, P.**, *Theory of Perfectly Plastic Solids*, John Wiley & Sons, 1951.

[82] **Rabotnov, Y.N.**, *Creep rupture*, *Proceedings of the XII congress on applied mechanics*, p. 342–349, 1968.

[83] **Rice, J.R.**, **Tracey, D.M.**, *On the ductile enlargement of voids in triaxial stress fields*, Journal of the Mechanics and Physics of Solids, vol. 17 p. 201–17, 1969.

[84] **Rodrigues, J.**, **Martins, P.A.F.**, *Technologia Mecânica - Vol. I Fundamentos teóricos*, vol. 1 of *Tecnologia da Deformacão Plástica*, Escolar Editora, 2. ed., 2010, ISBN 978-972-592-279-8.

[85] **Rosa, P.A.R.**, **Rodrigues, J.M.C.**, **Martins, P.A.F.**, *External inversion of thin-walled tubes using a die: experimental and theoretical investigation*, International Journal of Machine Tools and Manufacture, vol. 43 (8) p. 787–796, 2003, ISSN 08906955.

[86] **Saanouni, K.**, *Damage Mechanics in Metal Forming - Advanced Modeling and Numerical Simulation*, Wiley, 2012, ISBN 978-1-84821-348-1.

[87] **San-Martin, A.**, **Manchester, F.D.**, *The Fe-H (Iron-Hydrogen) System*, Bulletin of Alloy Phase Diagrams, vol. 11 (2) p. 173–184, 1990.

[88] **Semiatin, S.** (ed.), *ASM Handbook - Volume 14A, Metalworking: Bulk Forming*, ASM, 2005.

[89] **SFTC**, *DEFORM v10.2.1 - INTEGRATED 2D3D SYSTEM MANUAL*, Scientific Forming Technologies Corporation, 2012.

[90] **Shima, S.**, **Oyane, M.**, *Plasticity theory for porous metals*, International Journal of Mechanical Science, vol. 18 p. 285–291, 1976, ISSN 18792162.

[91] **Siebel, E.**, *Untersuchungen über bildsame Formänderung unter besonderer Berücksichtigung des Schmiedens*, Maschinenbau, vol. 9 p. 307–312, 1923.

[92] **Sowerby, R.**, **Chandrasekaran, N.**, **Dung, N.L.**, **Mahrenholtz, O.**, *The prediction of damage accumulation during upsetting tests based on McClintock's model*, Forschung im Ingenieurwesen, vol. 51 (5) p. 147–150, 1985, ISSN 14340860.

[93] **Spittel, M.**, **Spittel, T.**, *Steel symbol/number: 42CrMo4/1.7225*, *Landolt-Börnstein - Group VIII Advanced Materials and Technologies*, p. 1–5, Springer-Verlag Berlin Heidelberg, 2009.

[94] **Ståhlberg, U.**, **Keife, H.**, **Lundberg, M.**, **Melander, A.**, *A study of void closure during plastic deformation*, Journal of Mechanical Working Technology, vol. 4 (1) p. 51–63, 1980, ISSN 03783804.

[95] **Sundström, B.** (ed.), *Handbok och formelsamling i Hållfasthetslära*, Institutionen för hållfasthetslära, Kungliga Tekniska högskolan, 2005.

[96] **Swift, H.W.**, *Plastic instability under plane strain*, Journal of the Mechanics and Physics of Solids, vol. 1 p. 1–18, 1952.

[97] **Tibbetts, G.G.**, *Diffusivity of carbon in iron and steels at high temperatures*, Journal of Applied Physics, vol. 51 p. 4813–4816, 1980.

[98] **Tvergaard, V.**, *Influence of voids on shear band instabilities under plane strain conditions*, International Journal of Fracture, vol. 17 p. 389–407, 1981, ISSN 15732673.

[99] **Voce, E.**, *The relationship between stress and strain for homogeneous deformation*, Journal of the Institute of Metals, vol. 74 p. 537–562, 1948, ISSN 00202975.

[100] **Vujovic**, **Shabaik**, *A new workability criterion for ductile metals*, J. Eng. Mater. Technol., vol. 108 (3) p. 245–249, 1986, ISSN 15288889.

[101] **Wang, J.**, **Fu, P.**, **Liu, H.**, **Li, D.**, **Li, Y.**, *Shrinkage porosity criteria and optimized design of a 100-ton 30Cr2Ni4MoV forging ingot*, Materials and Design, vol. 35 p. 446–456, 2012, ISSN 02613069.

[102] **Wanheim, T.**, **Bay, N.**, **Petersen, A.S.**, *A theoretically determined model for friction in metal working processes*, Wear, vol. 28 (2) p. 251–258, 1974, ISSN 00431648, 18732577.

[103] **Wanheim, T.**, **Ravn, B.G.**, **Bay, N.**, *Teknologisk Plasticitetslære: Grundlaget*, Lecture notes [in danish], IPL-DTU, 2007.

[104] **Wanheim, T.**, **Ravn, B.G.**, **Bay, N.**, *Teknologisk Plasticitetslære: Snitelementmetoden*, Lecture notes [in danish], IPL-DTU, 2007.

[105] **Wanheim, T.**, **Schreiber, M.P.**, **Grønbæk, J.**, **Danckert, J.**, *Physical modelling of metal forming processes*, Journal of Applied Metalworking, vol. 1 (3) p. 5–14, 1970, ISSN 01629700.

[106] **Whitehead, J.R.**, *Surface Deformation and Friction of Metals at Light Loads*, Proceedings of the Royal Society of London. Series A, Mathematical and Physical Sciences, vol. 201 p. 109–124, 1950.

[107] **Xue, L.**, *Damage accumulation and fracture initiation in uncracked ductile solids subject to triaxial loading*, International Journal of Solids and Structures, vol. 44 (16) p. 5163–5181, 2007, ISSN 18792146.

[108] **Zener, C.**, **Hollomon, J.H.**, *Effect of strain rate upon plastic flow of steel*, Journal of Applied Physics, vol. 15 p. 22–32, 1944, ISSN 10897550.

[109] **Zhang, W.**, **Peeters, M.J.A.**, **Bay, N.**, *Numerical Modelling of Cold Rolling of Metal Plate Adopting a General Friction Model*, 5th Int. Conf. on Numerical Methods in Industrial Forming Processes, NUMIFORM95, p. 997–1004, 1995.

[110] **Zhang, X.X.**, **Cui, Z.S.**, **Chen, W.**, **Li, Y.**, *A criterion for void closure in large ingots during hot forging*, Journal of Materials Processing Technology, vol. 209 (4) p. 1950–1959, 2009, ISSN 09240136.

[111] **Zienkiewicz, O.C.**, **Taylor, R.L.**, *The Finite Element Method - Fluid Dynamics*, Butterworth-Heinemann, 5. ed., 2000, ISBN 978-0470395066.

16 Published publications

The author has published the following publications during his Ph.D-study.
The publications are not part of the thesis.

Christiansen, P., Hattel, J.H., Kotas, P., László, V., *Modelling the void deformation and closure by hot forging of ingot castings*, 1st International Conference on Ingot Casting, Rolling and Forging, vol. 1 pp. 1–9, 2012.

Christiansen, P., Hattel, J.H., Bay, N., Alves, L.M., Martins, P.A.F., *Open Die Forging of Large Shafts with Defects - Physical and Numerical Modelling*, Key Engineering Materials, vol. 2443 (554) pp. 2145–2155, 2013.

Christiansen, P., Hattel, J.H., Bay, N., Martins, P.A.F., *Modelling of Damage During Hot Forging of Ingots*, STEELSIM 2013 - the 5th International Conference, 2013.

Christiansen, P., Hattel, J.H., Bay, N., Martins, P.A.F., *Numerical optimization of die geometry in open die forging*, Proceedings of International Conference on Advanced Manufacturing Engineering and Technologies (NEWTECH 2013), pp. 59–68, 2013.

Christiansen, P., Hattel, J.H., Bay, N., Martins, P.A.F., *Physical modeling and numerical simulation of V-die forging ingot with central void*, Journal of Mechanical Engineering Science, pp. 1-10, January 2014

DTU Mechanical Engineering
Section of Manufacturing Engineering
Technical University of Denmark

Produktionstorvet, Bld. 427S
DK- 2800 Kgs. Lyngby
Denmark
Phone (+45) 4525 4763
Fax (+45) 4593 0190
www.mek.dtu.dk
ISBN: 978-87-7475-391-9